Activation of Nitric Oxide and Water by Transition Metal Clusters Relevant to Active Sites in Biology

Thesis by
Christopher John Reed

In Partial Fulfillment of the Requirements
for the Degree of Doctor of Philosophy

CALIFORNIA INSTITUTE OF TECHNOLOGY
Division of Chemistry and Chemical Engineering
Pasadena, California
2019
(Defended on May 30th, 2019)

Christopher John Reed
ORCID: 0000-0002-8774-5106

ACKNOWLEDGEMENTS

I would like to thank Theo for his mentorship over the past five years. I would not be the scientist that I am without your advice, patience, and motivation. I also thank the rest of my PhD committee, Profs. Jonas Peters, Dennis Dougherty, and Harry Gray, who were an excellent source of advice and insight during my studies, and pushed me to think critically of my research. It has been a great opportunity to study chemistry at Caltech.

I would like to thank all the members of the Agapie group, particularly the ones who shared their expertise and resources with me over the years, which was crucial for my development as a chemist; I thank Dr. Graham de Ruiter for training me, and instilling a level-headed approach to working in a synthetic lab.

I want to acknowledge Dr. Kyle Horak for beginning the work on the unsubstituted pyrazolate and hydrogen-bonding pyrazolate clusters in the last year of his PhD. This served as a footing for my later graduate research.

Special thanks to the members of the Peters and Gray groups who had allowed me to use their reagents and instruments, especially the Mössbauer spectrometer, these were invaluable aids in my studies. I would also like to thank the people who ran the facilities in the division, including the NMR (David VanderVelde), Mass spectrometry (Mona Shagoli), X-Ray Crystallography (Mike Takase and Larry Henling), and EPR facilities (Paul Oyala), along with the BILRC (Prof. Harry Gray and Jay Winkler). There were countless times I turned to them for advice on my experiments.

I am grateful for the Resnick Sustainability Institute at Caltech for supporting the last two years of my graduate education, and giving me the opportunity to share my chemistry at the Resnick Fellow Day Seminar.

ABSTRACT

This dissertation discusses the synthesis, characterization, and reactivity of site-differentiated tetranuclear clusters containing Fe and Mn with NO and H_2O-derived ligands. The motivation of this work was to conduct a detailed examination of structure-property relationships in well-defined molecular systems focused on unique features of multinuclear systems, such as bridging ligands, neighboring metal identity, and cluster oxidation state. Reactivity towards NO and H_2O-derived ligands was targeted due to their relevance to biological multinuclear transition metal active sites that promote multi-electron small molecule transformations.

Chapter 2 discusses the synthesis of Fe-nitrosyl clusters bearing an interstitial μ_4-F atom. These clusters were prepared to compare their reactivity to previously synthesized [Fe_3OFeNO] clusters with an analogous structure. A redox series of the [Fe_3FFe] and [Fe_3FFeNO] clusters were accessed, with the nitrosyl clusters displaying five cluster oxidation states, from $Fe^{II}_3\{FeNO\}^8$ to $Fe^{III}_3\{FeNO\}^7$. Overall, the weaker bonding of the F^- ligand resulted in attenuation of the activation and reactivity of the $\{FeNO\}^7$, relative to the corresponding μ_4-O clusters. Furthermore, the ability of distal Fe oxidation state changes to influence the activation of NO was decreased, demonstrating lower cooperativity between metals in clusters linked by a weaker μ_4-atom This represents a rare case where the effects of bridging atom ligands could be compared in isostructural multinuclear complexes and decoupled from changes in metal ion coordination number, oxidation states, or geometry.

Chapter 3 describes the synthesis of site-differentiated heterometallic clusters of [Fe_3OMn], displaying facile ligand substitution at the five-coordinate Mn. This system was able to coordinate H_2O and thermodynamic parameters of the proton and electron transfer processes from the Mn^{II}–OH_2 to form a Mn^{III}–OH moiety were studied. The oxidation state

distribution of the neighboring Fe centers had a significant influence on these thermodynamic parameters, which was similar to the analogous parameters for mononuclear Mn systems, demonstrating that oxidation state changes in neighboring metals of a cluster can perturb the reactivity of a Mn–OH_x unit nearly as much as an oxidation state change at the Mn–OH_x. Subsequent experiments attempted to find spectroscopic or electrochemical evidence for formation of a terminal Mn-oxo in this system; however, that was not obtained, even in relatively extreme conditions. This established a lower limit for the bond dissociation enthalpy of the Mn^{III}–OH of ca. 93 kcal/mol, which makes formation of a terminal Mn-oxo cluster unfavorable in most organic solvents, due to expected facile hydrogen atom abstraction of a solvent C–H bond.

The insights obtained on the reactivity of these tetranuclear metal-hydroxide clusters was applied towards stabilizing a terminal metal-oxo in a multinuclear complex, as outlined in Chapter 4. Through the use of pendant hydrogen bond donors with *tert*-butyl-aminopyrazolate ligands, tetranuclear Fe clusters bearing terminal-hydroxide and -oxo ligands could be stabilized and structurally characterized. A similar thermodynamic analysis of the Fe^{III}–OH bond dissociation enthalpy was conducted, which demonstrated Fe^{III}-oxo clusters could be accessed with a range of reactivity at the terminal-oxo ligand, based on the redox distribution of the neighboring Fe centers. The kinetics of C–H activation for the [$Fe^{II}_2Fe^{III}_2$]-oxo cluster redox state were analyzed, demonstrating a strong dependence of the C–H bond pK_a on the rate of proton coupled electron transfer.

Lastly, Chapter 5 describes the synthesis and reactivity of tetranuclear Fe clusters bearing unsubstituted pyrazolate ligands, focusing on attempts to observe evidence for a terminal Fe-oxo or Fe-imido motif. Clusters bearing a labile trifluoromethanesulfonate ligand at the five-coordinate Fe center could be prepared, and would react with oxygen atom transfer reagents

to produce a terminal Fe-hydroxide cluster, which, upon dehydration, led to isolation of an octanuclear μ_2-O cluster. The pathway for Fe-hydroxide formation was investigated, but could not conclusively determine whether reactivity occurred from a transient terminal Fe-oxo. Similarly, the reduced tetra-iron cluster, in the [$Fe^{II}_3Fe^{III}$], redox state was prepared, and demonstrated reactivity towards electron deficient aryl azides. Isolation of aryl amide clusters (Fe-NHAr) was observed, suggesting, again, formation of a reactive Fe-imido which decomposes through formal hydrogen atom abstraction. Efforts to stabilize either of these Fe=O/NR multiply-bonded species through a more acidic Fe were investigated by synthesizing the corresponding pyrazolate bridged μ_4-F clusters. The [Fe^{II}_4] cluster also displayed reactivity towards oxygen atom transfer reagents, and produced a similar octanuclear μ_2-O cluster, but the observation of μ_4-F substitution with oxygen to produce μ_4-O clusters with a terminal F ligand likely precluded formation of a reactive terminal-oxo cluster. Instead, thermodynamically favorable cluster rearrangement to the [Fe_3OFe] structure dominates.

PUBLISHED CONTENT AND CONTRIBUTIONS

Parts of this thesis have been adapted from published articles co-written by the author.

The following articles were reproduced in part with permission from the American Chemical Society:

"Tetranuclear Fe Clusters with a Varied Interstitial Ligand: Effects on the Structure, Redox Properties, and Nitric Oxide Activation" Reed, C. J.; Agapie, T. *Inorganic Chemistry*, **2017**, *56*, 13360-13367.

"Thermodynamics of Proton and Electron Transfer in Tetranuclear Clusters with Mn–OH_2/OH Motifs Relevant to H_2O Activation by the Oxygen Evolving Complex in Photosystem II" Reed, C. J.; Agapie, T. *Journal of the American Chemical Society*, **2018**, *140*, 10900-10908.

"A Terminal Fe^{III}-Oxo in a Tetranuclear Cluster: Effects of Distal Metal Centers on Structure and Reactivity" Reed, C. J.; Agapie, T. *Journal of the American Chemical Society*, **2019**, *Just Accepted Manuscript*. doi: 10.1021/jacs.9b03157.

TABLE OF CONTENTS

CHAPTER 1

GENERAL INTRODUCTION

INTRODUCTION

Multi-Electron Transformations Relevant to Global Biogeochemical Cycles of Oxygen and Nitrogen. The chemical basis of every living organism is centralized around a handful of elements C, H, N, O, P, and S; the transformation of molecules containing these elements occurs ubiquitously and on massive scales, directly affecting life around Earth. The global chemistry of oxygen and nitrogen are particularly relevant to human life. For example, the beginning of production of molecular oxygen eons ago, and its build up in the planet's atmosphere, has been linked to the development of complex eukaryotic organisms.[1] A constant production of O_2 is required to support aerobic life, and is intimately involved in biochemical processes related to the oxidation of other biological elements. Similarly, ammonium (NH_4^+) serves as the crucial building block to all biological nitrogen-containing molecules, which includes amino acids and nucleotides, and the combination of manmade and natural ammonium synthesis is directly tied to the production of sufficient supplies of food for humans and other animals.[2]

The global cycles of oxygen and nitrogen revolve around electron transfer; the formal oxidation state of oxygen commonly varies from -2 (i.e. H_2O) to 0 (O_2), and nitrogen can vary from -3 (NH_4^+) to +5 (NO_3^-).[1] The four-electron reduction of dioxygen by cellular respiration constitutes a key component of the global oxygen cycle. The consumed dioxygen is replaced by photosynthesis through the analogous four-electron oxidation of water (Scheme 1). In a similar way, multi-electron redox processes of nitrogen provide access to its various biologically relevant forms (i.e. N_2, NH_4^+, NO, N_2O) and processes to regenerate them. The global redox transformations of oxygen and nitrogen typically occur through multi-electron pathways. This is because, often, the partially reduced/oxidized molecule is less thermodynamically stable (Figure 1).

Scheme 1. Multi-Electron Redox Processes of Oxygen and Nitrogen Relevant to Their Global Biogeochemical Cycles.

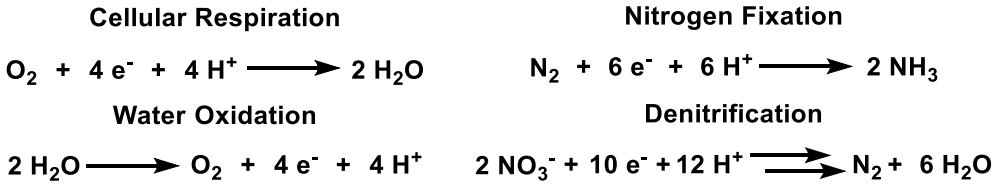

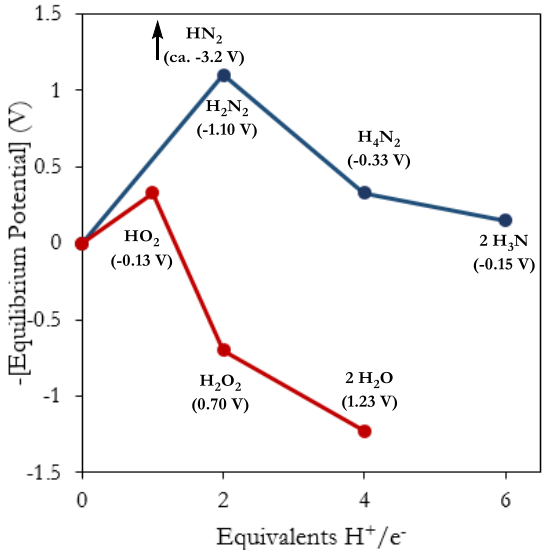

Figure 1. Equilibrium standard potentials of forms of oxygen (red) and nitrogen (blue).[3]

Biological Catalysts for Multi-Electron Redox Transformations of Oxygen and Nitrogen. Nature contains a variety of catalysts which constitute major steps in the global cycles of oxygen and nitrogen. For example, yearly, 300 tetragrams of N_2 are reduced to NH_4^+ by nitrogen-fixing microbes through a metalloenzyme called nitrogenase; this process is considered to be responsible for more than half the amount of bio-available nitrogen in the environment.[2] These enzymes display remarkable efficiency towards their native reactions and are capable of effecting complex, challenging multi-electron transformations under relatively mild, and sustainable, conditions. For this reason, researchers have examined these biological systems to gain insight into the features of these enzymes that promote efficient catalysis.

Biological enzymes responsible for redox transformations of oxygen and nitrogen are all metalloenzymes, containing either Fe, Mn, and/or Cu ions in their active site.[4] Within this set of enzymes, many of the active sites contain complex transition metal clusters (Figure 2). The structural diversity of these multinuclear active sites is notable, displaying various transition metals, nuclearities, bridging ligands, and geometric arrangements. Detailed mechanistic study of these globally relevant metalloenzymes has been a culmination of efforts from biochemists, crystallographers, spectroscopists, and theoreticians, which remain at the frontier of bioinorganic research, leading to developments in enzymology, metal ion spectroscopy, and computational techniques.

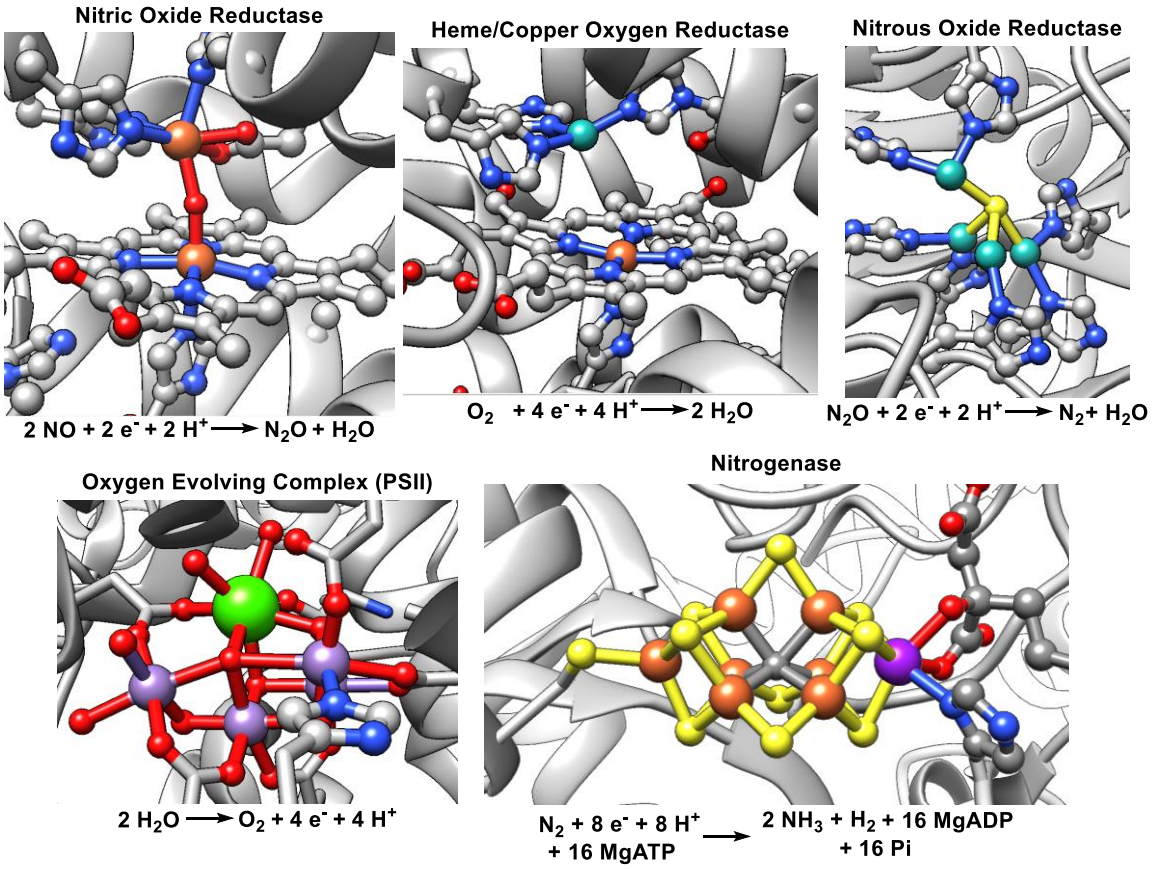

Figure 2. Active site structures of metalloenzymes competent for multi-electron redox transformations of oxygen and nitrogen: nitric oxide reductase (PDB code: 3O0R),

heme/Cu oxygen reductase (1V54), nitrous oxide reductase (1FWX), photosystem II (3WU2), and nitrogenase (1M1N). Fe (light brown), Cu (cyan), Mn (light purple), Mo (purple), Ca (green), S (yellow), O (red), N (blue).

Case Study: Mechanistic Insight to the Oxygen-Ovolving Complex (OEC) in Photosystem II. Photosynthetic organisms use the energy in sunlight to drive the reduction of plastoquinol and produce energy in the form of adenosine triphosphate (ATP). The reducing equivalents obtained are derived from water, one of the most abundant sources of electrons in the environment.[4b, 5] In a separate process, the energy and reducing equivalents are used for reduction of CO_2 and production of carbohydrates in the Calvin cycle. Water oxidation occurs in a protein assembly known as photosystem II (PSII), at a multinuclear active site composed of a heterometallic [Mn_4CaO_5] cluster, called the OEC.[6] Incoming photons induce a charge separated state at by a nearby heme center (P_{680}), which transfers a single electron through a series of mediators until reaching plastoquinone. P_{680} is regenerated by reduction from a nearby tyrosine residue (Tyr_Z). This resulting organic radical oxidizes the OEC, which translates four separate electron transfer events by P_{680} to one catalytic turnover, producing dioxygen from two molecules of water.[4b] The molecular model of OEC turnover is considered within the framework of the Kok cycle, which describes five distinct so-called S-states (S_0, S_1, …, S_4) of the OEC (Figure 3).[4c, 7] Electrons, and protons from coordinated H_xO ligands, are removed from the OEC during each S-state transition; states S_0 through S_3 have been observed spectroscopically (principally through advanced EPR and X-ray absorption techniques), and in some cases structurally characterized by X-ray diffraction. These investigations have established a number of important characteristics of the OEC catalytic cycle, including (i) the lowest oxidation state of the OEC during turnover is [$Mn^{III}_3Mn^{IV}$] and

this cluster undergoes four subsequent oxidations to reach a formal [$Mn^{VI}_3Mn^{V}$] redox state, responsible for O–O bond formation (S_4);[4b, 8] (ii) EPR spectroscopy of the OEC has shown a dynamic structure within the cluster, where at least one of the bridging oxygen atoms is exchangeable (and implicated as one of the substrate oxygen atoms);[9] (iii) recent X-ray techniques have captured structural snapshots of the OEC in the S_3 state, which displays coordination of the second substrate H_xO molecule to one of the cubane Mn centers;[10] and (iv) extensive computational studies based on experimental structural and spectroscopic parameters for the OEC suggest a high-valent terminal Mn-oxo is the key O–O bond forming intermediate in the unobserved S_4 state.[11]

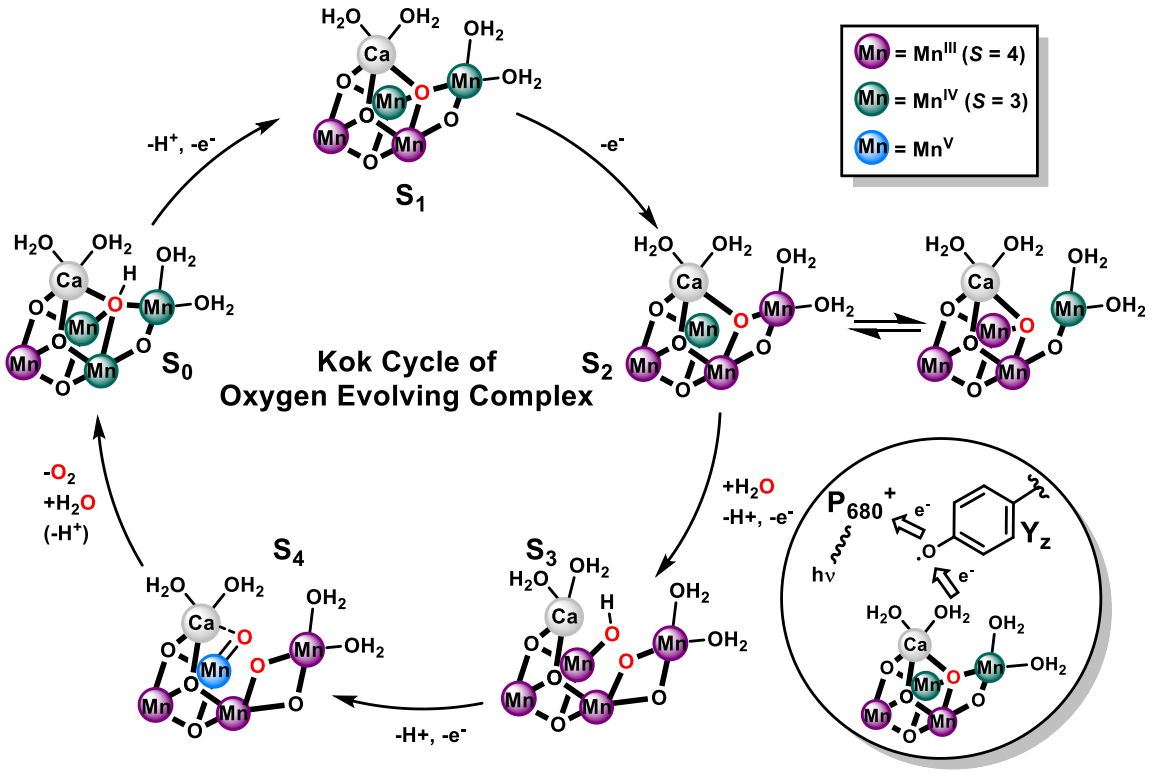

Figure 3. Contemporary proposed structures of the OEC in each stage of the Kok cycle.

These studies provide a remarkably detailed picture of water oxidation by the OEC; however, due to the inherent complexity of studying this massive protein (700 kDa), with its

multiple subunits and cofactors, there are a number of challenges to realizing a complete mechanistic understanding of the OEC. For example, the precise protonation state of the OEC, and its neighboring protein environment, is not well-understood for any S-state.[11b] Also, since PSII is necessarily studied in aqueous conditions, the OEC is always present in a large excess of substrate, which complicates isolation and characterization of the oxidized states of the cluster.

Our mechanistic understanding of the OEC exemplifies a number of possible functional roles for multiple transition metals arranged within a multinuclear active site. The presence of many redox active transition metals allows for the storage of multiple oxidizing equivalents, without requiring a large buildup of charge at a single site. This has been implicated as a cause for the high selectivity of the OEC, which produces little to no partially oxidized forms of oxygen, i.e. H_2O_2 or O_2^-, which would be detrimental to the organism. One can also envision how the relatively unique dangling cubane geometry of the metal centers in the OEC promotes reactivity between specific metal-bound oxygen atoms. Furthermore, the coupling of unpaired spins in the Mn centers may be crucial for efficient release of dioxygen, avoiding the production of reactive singlet oxygen. In general, a number of functions for neighboring metal centers in various catalytic systems can be proposed: (i) storage of redox equivalents, (ii) structurally directing reactive moieties, and (iii) tuning the electronic characteristics of a reactive metal or coordinated ligand.

Biologically Inspired Transition Metal Complexes Relevant to Small Molecule Chemistry of Oxygen and Nitrogen. Due to the potential complexity and constraints of studying metalloenzymes directly, the complementary development of well-defined small molecule transition metal complexes has provided significant chemical insight related to these biological processes. The synthetic inorganic chemistry of Fe, Mn, and Cu complexes has been

studied extensively, including chemistry related to the global oxygen and nitrogen cycles through reactions involving relevant O- and N-containing small molecules such as H_2O, O_2, N_2, and NO. A majority of these studies are performed with mononuclear, or binuclear, transition metal complexes; the development of multinuclear systems with greater complexity that bear closer resemblance to biological active sites remains a challenge for synthetic chemists. The following survey of relevant synthetic metal complexes is by no means exhaustive, but its discussion will place this work within the wider context of previously reported synthetic transition metal complexes that are relevant to biological transformations of oxygen and nitrogen.

Synthetic Inorganic Chemistry Related to Water Oxidation by the OEC. Efforts towards a full structural model of the OEC were undertaken with the goal of elucidating the structure-property relationships of a well-defined [Mn_4CaO_5] cluster with spectroscopic and/or functional relevance to the native metalloenzyme. A variety of di- and tetramanganese oxo clusters have been reported with relevance to the OEC; notable early achievements within this field include the isolation of high-valent [Mn_4O_4] cubane clusters from the groups of Dismukes (**1**) and Christou, and the incorporation of Ca into high nuclearity Mn-oxo clusters by Christou and co-workers.[12] In 2011, Agapie and co-workers reported a [Mn_3CaO_4] cluster analogous to the cubane subunit of the OEC, **3**.[13] Since then, a more complete structural model of the OEC, with the dangler Mn has been reported by Zhang, Dong, Dau, and co-workers (**4**).[14] With these complexes, a great deal of insight has been obtained, towards understanding the electronic interactions between Mn centers in cubane clusters, and the influence of the redox-inactive Ca ion on redox and reactivity properties.[15] Most structural models of the OEC display coordinatively saturated Mn centers (Scheme 2), precluding extensive reactivity studies with

exogenous H_2O; however, these and related systems have been used to study the reactivity of the bridging oxo ligands of high valent Mn complexes with relevance to the OEC.[16]

Scheme 2. Selected Structural Models of the OEC.[12b, 13-14, 15b]

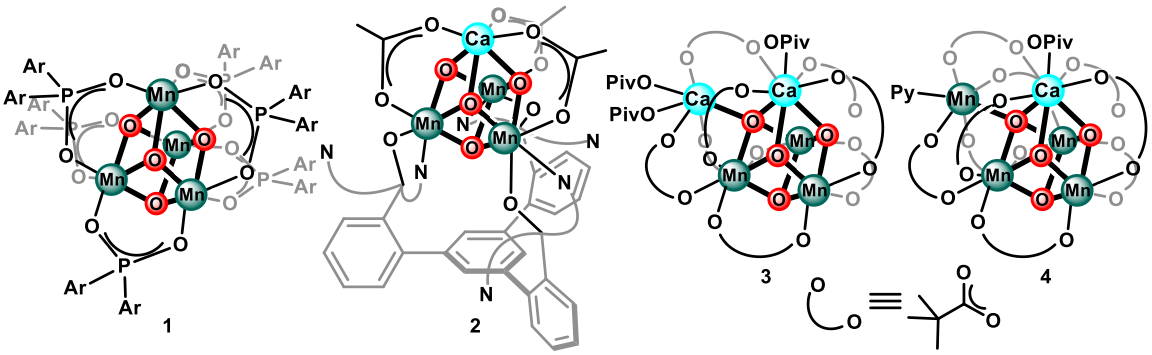

Numerous lower nuclearity metal complexes have been examined for their relevance to the OEC (Scheme 3). For example, Borovik and co-workers have studied the reactivity and electronic structure of mononuclear Mn-OH, Mn-oxo, and Mn–(OH)–Ca motifs, which are related to possible intermediates of the OEC; a unique ligand capable of hydrogen bonding to the Mn–OH_x moiety facilitated characterization of a series of Mn^{III}-, Mn^{IV}-, and Mn^{V}-oxo complexes (**5** – **7**).[17] Particularly relevant to the biological system are understanding aspects that affect the homolytic bond dissociation enthalpy (BDE) of Mn–OH_x motifs; proton coupled electron transfer (PCET) has been implicated as a crucial aspect of OEC catalysis, as it avoids charge built up at the active site, promoting progression to the fully oxidized state of the cluster.[18] Along these lines, other groups have examined the PCET reactivity of mononuclear Mn–OH and -oxo complexes to understand the influence of Mn oxidation state, ligand, field, and protonation state on reactivity.[19] Examples of these types of studies with multinuclear Mn complexes are less common;[16b, 16c, 20] a binuclear Mn system has been reported by Pecoraro and co-workers (**9**), which is able to support –aquo and –hydroxide ligands in multiple Mn oxidation states, and access a reactive terminal Mn-oxo.[21]

O–O bond formation of synthetic Mn-oxo complexes has also been examined, predominantly with porphyrin ligands. Nucleophilic attack of Mn^{V}-oxo (**10**) by hydroxide produces peroxo- intermediates in Mn-corrole systems.[22] In some cases, subsequent oxidation of this intermediate releases dioxygen. The reactivity of related corrole complexes in the presence of a redox-inactive metal has shown significant perturbations to the Mn–O bonding, which could be relevant to Mn–O–Ca motifs in the OEC.[23]

Scheme 3. Selected Examples of PCET and O–O Bond Formation with Synthetic Complexes Relevant to the OEC.

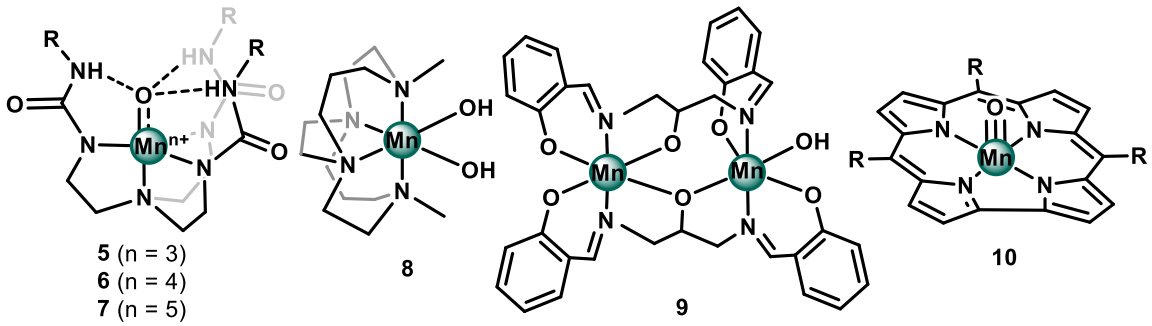

Synthetic Complexes Relevant to Heme/Cu Oxygen Reductase (HCO). Dioxygen reduction by the bimetallic active site of HCO is a key step in cellular respiration that drives transmembrane proton pumping to ultimately obtain ATP from cellular reducing equivalents.[4e] HCO enzymes are part of a wider class of metalloenzymes that reduce dioxygen; other enzymes of this class employ mono- and binuclear active sites of Fe and Cu with O_2 to oxidize organic molecules for a variety of metabolic pathways. A common element between HCO (and other Fe-containing O_2 reducing enzymes) and the OEC is the key role of a putative high-valent terminal metal-oxo intermediate. In HCO, O–O bond cleavage of a Fe–(O_2)–Cu intermediate is proposed to produce Cu^{II}–OH and Fe^{IV}-oxo, which is further reduced and protonated to afford two molecules of H_2O.

The synthetic chemistry of heme and non-heme Fe-oxo complexes has been extensively investigated, due to their relevance to members of O_2-reducing metalloenzymes.[24] Groves and co-workers have recently reviewed this topic for heme Fe-oxo complexes.[25] Close structural mimics of the bimetallic HCO active site have also been prepared (i.e. **11**); a survey of these, and related synthetic Fe/Cu systems, has been reviewed recently by Karlin and co-workers.[26] Biosynthetic approaches to study the mechanism of O_2-reduction by binuclear heme/non-heme active sites has provided great insight to structure-property relationships in HCO; Lu and co-workers have used protein scaffolds to produce close structural models of the HCO active site, through mutagenesis studies of a simpler heme protein. With a single protein scaffold, they were able to introduce binding sites for various non-heme metals (Zn, Fe, Cu) and investigate their effect on the activity and selectivity for HCO-like activity.[27]

Scheme 4. Synthetic HCO Model Complex[26b]

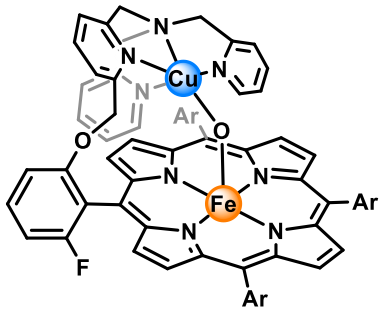

11

Synthetic Complexes Related to the Fe-Mo Cofactor (FeMoCo) of Nitrogenase. The FeMoco cluster of nitrogenase is a [MFe_7S_9C] cluster with a fused-cubane geometry (M = Mo);[28] versions of nitrogenase where the eighth metal is V, Mo, or Fe have been observed, but the Fe-Mo cofactor is the most well-studied. One of the unique structural features of this cluster is the interstitial μ_6-C ligand, which is not observed in any other biological cluster, and a rare motif in reported synthetic complexes. Extensive mechanistic investigations of nitrogenase by EPR

spectroscopy has characterized a number of reduced oxidation states of the cluster;[29] however the precise binding mode of the FeMoco substrate, N_2, has not been established. Peters and co-workers have examined a series of mononuclear Fe–N_2 complexes, bearing different *trans*-ligand donors (**12** – **14**), including an anionic carbon donor;[30] notably, **13** is the first example of an Fe-based molecular N_2-reduction catalyst.[31] The identity of the *trans*-donor had a strong influence on the Fe–N_2 bonding and reactivity. More recently, crystal structures of FeMoco with a displace μ_2-S between to Fe centers have been obtained, suggesting a possible substrate binding site.[32] This has led to the investigation of binuclear Fe complexes as models of FeMoco.[33] The N_2-activation chemistry of higher nuclearity Fe complexes have also been investigated, although well-characterized high-spin Fe clusters (of more than two Fe centers) with a bound N_2 ligand have yet to be reported in the literature. Despite this, reduction of multinuclear Fe complexes in the presence of N_2 has led to the isolation of a number of Fe-nitride and –imido clusters (**15** and **16**), with relevance to putative intermediates in FeMoco.[34]

Scheme 5. Selected Functional Models of FeMoco.[30, 34]

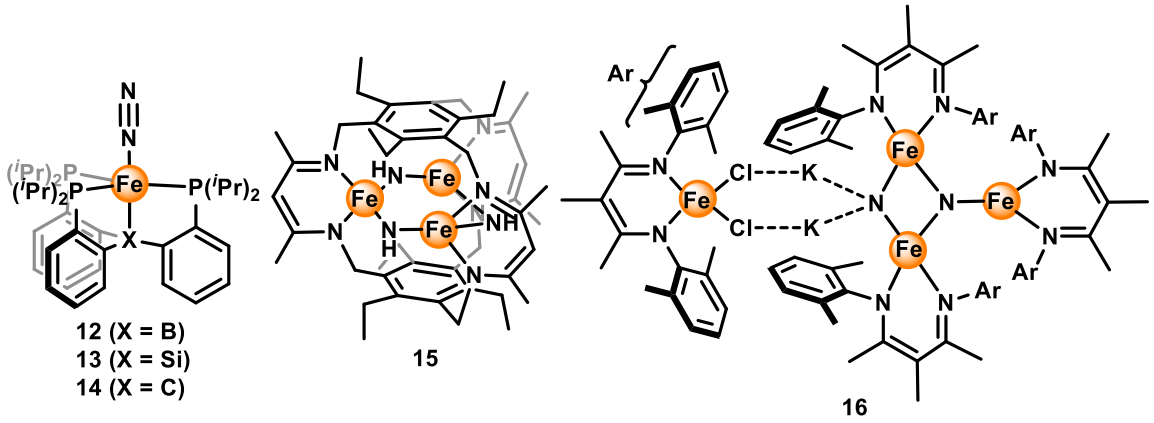

Like the OEC, efforts to make rigorous structural mimics of FeMoco are motivated by a desire to prepare well-defined molecular models for spectroscopic and structure-property investigations. Many fused-cubane clusters reminiscent of FeMoco have been reported by the

research groups of Holm and Ohki, including a [Fe_8S_{10}] cluster bearing a μ_6-S (**17**).[35] Although the small molecule chemistry of these clusters has not been reported, related [Fe_6S_9] clusters have been combined with apo-nitrogenase proteins to produce artificial metalloproteins competent for reductive coupling of CO, $^-$CN, and C_2H_4.[36]

Scheme 6. Structural Models of FeMoco and Related Nitrogenase Clusters.[37]

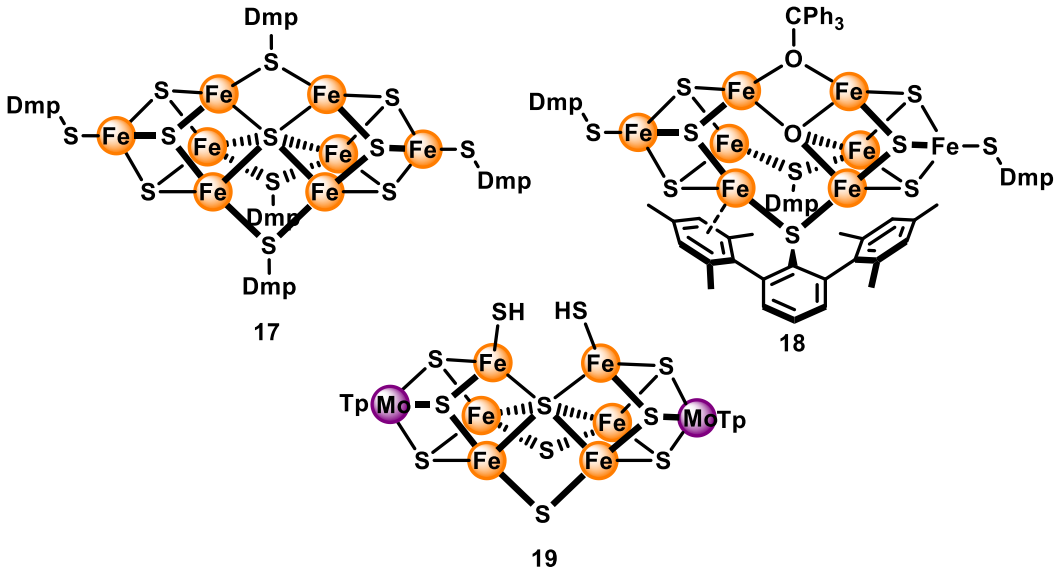

Synthetic Metal Complexes Related to Biological Denitrification. The process of denitrification is an important part of the global nitrogen cycle, nitrate (NO_3^-) is reduced to N_2 over four steps, via nitrite (NO_2^-), nitric oxide (NO), and nitrous oxide (N_2O) intermediates, as a terminal electron acceptor for an anaerobic analogue to cellular respiration.[4a] The NO and N_2O reducing steps are accomplished by multinuclear active sites of Fe and Cu, respectively.

Nitric oxide reductase (NOR) contains an active site structure similar to HCO, with a non-heme Fe center instead of Cu; similar molecular and biosynthetic systems that have been used to understand HCO have been applied to NOR, as well.[38] NO-reducing metalloenzymes with a binuclear non-heme Fe active site are also present in pathogenic bacteria for NO

detoxification. A faithful structural and functional model of this active site has recently been reported by Lehnert and co-workers (**20**).[39]

Nitrous oxide reductase (N_2O) is composed of a tetranuclear Cu active site, containing a bridging S ligand.[40] Mankad and co-workers have reported a tetranuclear Cu complex bearing a μ_4-S with a square pyramidal geometry (**21**); this complex is capable of reducing N_2O to N_2, structurally and functionally mimicking the native enzyme.[41] The proposed mechanism of N_2OR suggests N_2O is activated across two Cu centers; further mechanistic investigations of **21** or the native enzyme are required to establish the precise role of the four Cu centers in the cluster's ability to drive this transformation.

Scheme 8. Multinuclear Model Complexes of NOR and N_2OR[39, 41]

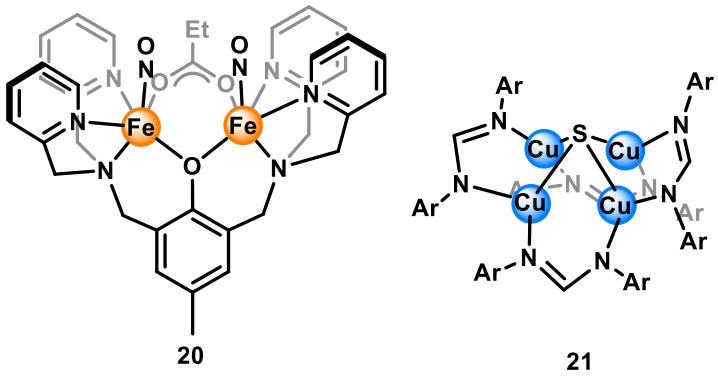

20 21

CONSPECTUS

The oxidation and reduction of small molecules of oxygen and nitrogen occurs on a global scale and has relevance to many of the chemical processes that encompass life. In organisms across all domains of life, the metalloenzymes that catalyze the multi-electron transformations of molecules such as H_2O, O_2, N_2, and NO_3^- contain active sites with diverse, complex multinuclear transition metal structures. Mechanistic investigations of these metalloenzymes have sought to elucidate the functional purpose of these unique multinuclear arrangements; and come with a number of inherent challenges, due to difficulties in preparation and

manipulation of large protein assemblies, or the limitations of aqueous conditions. For this reason, complementary studies of synthetic transition metal complexes and their chemistry towards O- and N-based small molecules is useful for understanding mechanistic details of native biological systems. While a majority of the reported literature has focused on the synthetic chemistry of mononuclear and binuclear transition metal complexes, the synthesis and study of higher nuclearity clusters comprises an important development towards a more complete understanding of the multi-electron redox transformations of globally relevant molecules. The work detailed in this dissertation addresses the development of tetranuclear clusters of biologically relevant transition metals Fe and Mn, in particular their chemistry towards NO and H_2O, with relevance to biological multinuclear active sites responsible for multi-electron transformations of small molecules.

References

1. Falkowski Paul, G.; Godfrey Linda, V. *Philosophical Transactions of the Royal Society B: Biological Sciences* **2008,** *363*, 2705-2716.
2. Kuypers, M. M. M.; Marchant, H. K.; Kartal, B. *Nature Reviews Microbiology* **2018,** *16*, 263.
3. van der Ham, C. J. M.; Koper, M. T. M.; Hetterscheid, D. G. H. *Chem. Soc. Rev.* **2014,** *43*, 5183-5191.
4. (a) Wasser, I. M.; de Vries, S.; Moënne-Loccoz, P.; Schröder, I.; Karlin, K. D. *Chem. Rev.* **2002,** *102*, 1201-1234; (b) Yano, J.; Yachandra, V. *Chem. Rev.* **2014,** *114*, 4175-4205; (c) Vinyard, D. J.; Brudvig, G. W. *Annu. Rev. Phys. Chem.* **2017,** *68*, 101-116; (d) Maia, L. B.; Moura, J. J. G. *Chem. Rev.* **2014,** *114*, 5273-5357; (e) Yoshikawa, S.; Shimada, A. *Chem. Rev.* **2015,** *115*, 1936-1989.
5. (a) Shen, J.-R. *Annual Review of Plant Biology* **2015,** *66*, 23-48; (b) Lee, H. B.; Oyala, P. H.; Agapie, T. Synthesis, Electronic Structure, and Spectroscopy of Multinuclear Mn Complexes Relevant to the Oxygen Evolving Complex of Photosystem II. In *Oxygen Production and Reduction in Artificial and Natural Systems*, World Scientific: 2018; pp 259-283.
6. (a) Umena, Y.; Kawakami, K.; Shen, J.-R.; Kamiya, N. *Nature* **2011,** *473*, 55-60; (b) Ferreira, K. N.; Iverson, T. M.; Maghlaoui, K.; Barber, J.; Iwata, S. *Science* **2004,** *303*, 1831-1838.
7. Kok, B.; Forbush, B.; McGloin, M. *Photochem. Photobiol.* **1970,** *11*, 457-475.
8. (a) Zaharieva, I.; Dau, H.; Haumann, M. *Biochemistry* **2016,** *55*, 6996-7004; (b) Zaharieva, I.; Chernev, P.; Berggren, G.; Anderlund, M.; Styring, S.; Dau, H.; Haumann, M. *Biochemistry* **2016,** *55*, 4197-4211; (c) Kubin, M.; Kern, J.; Gul, S.; Kroll, T.; Chatterjee, R.; Löchel, H.; Fuller, F. D.; Sierra, R. G.; Quevedo, W.; Weniger, C.; Rehanek, J.; Firsov, A.; Laksmono, H.; Weninger, C.; Alonso-Mori, R.; Nordlund, D. L.; Lassalle-Kaiser, B.; Glownia, J. M.; Krzywinski, J.; Moeller, S.; Turner, J. J.; Minitti, M. P.; Dakovski, G. L.; Koroidov, S.; Kawde, A.; Kanady, J. S.; Tsui, E. Y.; Suseno, S.; Han, Z.; Hill, E.; Taguchi, T.; Borovik, A. S.; Agapie, T.; Messinger, J.; Erko, A.; Föhlisch, A.; Bergmann, U.; Mitzner, R.; Yachandra, V. K.; Yano, J.; Wernet, P. *Structural Dynamics* **2017,** *4*, 054307.
9. (a) Oyala, P. H.; Stich, T. A.; Stull, J. A.; Yu, F.; Pecoraro, V. L.; Britt, R. D. *Biochemistry* **2014,** *53*, 7914-7928; (b) Cox, N.; Retegan, M.; Neese, F.; Pantazis, D. A.; Boussac, A.; Lubitz, W. *Science* **2014,** *345*, 804-808; (c) Pantazis, D. A.; Ames, W.; Cox, N.; Lubitz, W.; Neese, F. *Angew. Chem. Int. Ed.* **2012,** *51*, 9935-9940; (d) Rapatskiy, L.; Cox, N.; Savitsky, A.; Ames, W. M.; Sander, J.; Nowaczyk, M. M.; Rögner, M.; Boussac, A.; Neese, F.; Messinger, J.; Lubitz, W. *J. Am. Chem. Soc.* **2012,** *134*, 16619-16634.
10. (a) Suga, M.; Akita, F.; Hirata, K.; Ueno, G.; Murakami, H.; Nakajima, Y.; Shimizu, T.; Yamashita, K.; Yamamoto, M.; Ago, H.; Shen, J.-R. *Nature* **2015,** *517*, 99-103; (b) Suga, M.; Akita, F.; Sugahara, M.; Kubo, M.; Nakajima, Y.; Nakane, T.; Yamashita, K.; Umena, Y.; Nakabayashi, M.; Yamane, T.; Nakano, T.; Suzuki, M.; Masuda, T.; Inoue, S.; Kimura, T.; Nomura, T.; Yonekura, S.; Yu, L.-J.; Sakamoto, T.; Motomura, T.; Chen, J.-H.; Kato, Y.; Noguchi, T.; Tono, K.; Joti, Y.; Kameshima, T.; Hatsui, T.; Nango, E.; Tanaka, R.; Naitow, H.; Matsuura, Y.; Yamashita, A.; Yamamoto, M.; Nureki, O.; Yabashi, M.; Ishikawa, T.; Iwata, S.; Shen, J.-R. *Nature* **2017,** *543*, 131-135; (c) Kern, J.; Chatterjee, R.; Young, I. D.; Fuller, F. D.; Lassalle, L.; Ibrahim, M.; Gul, S.; Fransson, T.; Brewster, A. S.; Alonso-Mori, R.; Hussein, R.; Zhang, M.; Douthit, L.; de Lichtenberg, C.; Cheah, M. H.; Shevela, D.; Wersig, J.; Seuffert, I.; Sokaras, D.; Pastor, E.; Weninger, C.; Kroll, T.; Sierra, R. G.; Aller, P.; Butryn, A.; Orville, A. M.; Liang, M.; Batyuk, A.; Koglin, J. E.; Carbajo, S.; Boutet, S.; Moriarty, N. W.; Holton, J. M.; Dobbek, H.; Adams, P. D.; Bergmann, U.; Sauter, N. K.; Zouni, A.; Messinger, J.; Yano, J.; Yachandra, V. K. *Nature* **2018,** *563*, 421-425.
11. (a) Siegbahn, P. E. M. *BBA - Bioenergetics* **2013,** *1827*, 1003-1019; (b) Ames, W.; Pantazis, D. A.; Krewald, V.; Cox, N.; Messinger, J.; Lubitz, W.; Neese, F. *J. Am. Chem. Soc.* **2011,** *133*, 19743-19757.
12. (a) Li, Q.; Vincent, J. B.; Libby, E.; Chang, H.-R.; Huffman, J. C.; Boyd, P. D. W.; Christou, G.; Hendrickson, D. N. *Angewandte Chemie International Edition in English* **1988,** *27*, 1731-1733; (b) Dismukes, G. C.; Brimblecombe, R.; Felton, G. A. N.; Pryadun, R. S.; Sheats, J. E.; Spiccia, L.; Swiegers, G. F. *Acc. Chem. Res.* **2009,** *42*, 1935-1943; (c) Mishra, A.; Wernsdorfer, W.; Abboud, K. A.; Christou, G. *Chem. Commun.* **2005**, 54-56.
13. Kanady, J. S.; Tsui, E. Y.; Day, M. W.; Agapie, T. *Science* **2011,** *333*, 733-736.
14. Zhang, C.; Chen, C.; Dong, H.; Shen, J.-R.; Dau, H.; Zhao, J. *Science* **2015,** *348*, 690-693.

15. (a) Tsui, E. Y.; Agapie, T. *Proc. Natl. Acad. Sci.* **2013,** *110*, 10084-10088; (b) Mukherjee, S.; Stull, J. A.; Yano, J.; Stamatatos, T. C.; Pringouri, K.; Stich, T. A.; Abboud, K. A.; Britt, R. D.; Yachandra, V. K.; Christou, G. *Proceedings of the National Academy of Sciences of the United States of America* **2012,** *109*, 2257-2262; (c) Tsui, E. Y.; Kanady, J. S.; Agapie, T. *Inorg. Chem.* **2013,** *52*, 13833-13848.
16. (a) Lionetti, D.; Suseno, S.; Tsui, E. Y.; Lu, L.; Stich, T. A.; Carsch, K. M.; Nielsen, R. J.; Goddard, W. A.; Britt, R. D.; Agapie, T. *Inorg. Chem.* **2019,** *58*, 2336-2345; (b) Carrell, T. G.; Bourles, E.; Lin, M.; Dismukes, G. C. *Inorg. Chem.* **2003,** *42*, 2849-2858; (c) Baldwin, M. J.; Stemmler, T. L.; Riggs-Gelasco, P. J.; Kirk, M. L.; Penner-Hahn, J. E.; Pecoraro, V. L. *J. Am. Chem. Soc.* **1994,** *116*, 11349-11356; (d) Kanady, J. S.; Mendoza-Cortes, J. L.; Tsui, E. Y.; Nielsen, R. J.; Goddard, W. A.; Agapie, T. *J. Am. Chem. Soc.* **2013,** *135*, 1073-1082.
17. (a) Gupta, R.; MacBeth, C. E.; Young, V. G.; Borovik, A. S. *J. Am. Chem. Soc.* **2002,** *124*, 1136-1137; (b) Parsell, T. H.; Yang, M.-Y.; Borovik, A. S. *J. Am. Chem. Soc.* **2009,** *131*, 2762-2763; (c) Gupta, R.; Taguchi, T.; Lassalle-Kaiser, B.; Bominaar, E. L.; Yano, J.; Hendrich, M. P.; Borovik, A. S. *Proc. Natl. Acad. Sci.* **2015,** *112*, 5319-5324; (d) Park, Y. J.; Ziller, J. W.; Borovik, A. S. *J. Am. Chem. Soc.* **2011,** *133*, 9258-9261.
18. (a) Weinberg, D. R.; Gagliardi, C. J.; Hull, J. F.; Murphy, C. F.; Kent, C. A.; Westlake, B. C.; Paul, A.; Ess, D. H.; McCafferty, D. G.; Meyer, T. J. *Chem. Rev.* **2012,** *112*, 4016-4093; (b) Migliore, A.; Polizzi, N. F.; Therien, M. J.; Beratan, D. N. *Chem. Rev.* **2014,** *114*, 3381-3465; (c) Amin, M.; Vogt, L.; Szejgis, W.; Vassiliev, S.; Brudvig, G. W.; Bruce, D.; Gunner, M. R. *J. Phys. Chem. B* **2015,** *119*, 7366-7377.
19. (a) Yin, G.; Danby, A. M.; Kitko, D.; Carter, J. D.; Scheper, W. M.; Busch, D. H. *J. Am. Chem. Soc.* **2008,** *130*, 16245-16253; (b) Yin, G. *Acc. Chem. Res.* **2013,** *46*, 483-492; (c) Zaragoza, J. P. T.; Baglia, R. A.; Siegler, M. A.; Goldberg, D. P. *J. Am. Chem. Soc.* **2015,** *137*, 6531-6540; (d) Lassalle-Kaiser, B.; Hureau, C.; Pantazis, D. A.; Pushkar, Y.; Guillot, R.; Yachandra, V. K.; Yano, J.; Neese, F.; Anxolabehere-Mallart, E. *Energy & Environmental Science* **2010,** *3*, 924-938; (e) Kurahashi, T.; Kikuchi, A.; Shiro, Y.; Hada, M.; Fujii, H. *Inorg. Chem.* **2010,** *49*, 6664-6672.
20. Caudle, M. T.; Pecoraro, V. L. *J. Am. Chem. Soc.* **1997,** *119*, 3415-3416.
21. Yu, F.; Pecoraro, V. L. *Polyhedron* **2013,** *64*, 99-105.
22. (a) Gao, Y.; Åkermark, T.; Liu, J.; Sun, L.; Åkermark, B. *J. Am. Chem. Soc.* **2009,** *131*, 8726-8727; (b) Kim, S. H.; Park, H.; Seo, M. S.; Kubo, M.; Ogura, T.; Klajn, J.; Gryko, D. T.; Valentine, J. S.; Nam, W. *J. Am. Chem. Soc.* **2010,** *132*, 14030-14032; (c) Guo, M.; Lee, Y.-M.; Gupta, R.; Seo, M. S.; Ohta, T.; Wang, H.-H.; Liu, H.-Y.; Dhuri, S. N.; Sarangi, R.; Fukuzumi, S.; Nam, W. *J. Am. Chem. Soc.* **2017**.
23. Leeladee, P.; Baglia, R. A.; Prokop, K. A.; Latifi, R.; de Visser, S. P.; Goldberg, D. P. *J. Am. Chem. Soc.* **2012,** *134*, 10397-10400.
24. (a) McDonald, A. R.; Que Jr, L. *Coord. Chem. Rev.* **2013,** *257*, 414-428; (b) Olivo, G.; Cussó, O.; Borrell, M.; Costas, M. *JBIC Journal of Biological Inorganic Chemistry* **2017,** *22*, 425-452; (c) Kovaleva, E. G.; Lipscomb, J. D. *Nat Chem Biol* **2008,** *4*, 186-193.
25. Huang, X.; Groves, J. T. *Chem. Rev.* **2018,** *118*, 2491-2553.
26. (a) Adam, S. M.; Wijeratne, G. B.; Rogler, P. J.; Diaz, D. E.; Quist, D. A.; Liu, J. J.; Karlin, K. D. *Chem. Rev.* **2018,** *118*, 10840-11022; (b) Ju, T. D.; Ghiladi, R. A.; Lee, D.-H.; van Strijdonck, G. P. F.; Woods, A. S.; Cotter, R. J.; Young, V. G.; Karlin, K. D. *Inorg. Chem.* **1999,** *38*, 2244-2245.
27. Bhagi-Damodaran, A.; Michael, M. A.; Zhu, Q.; Reed, J.; Sandoval, B. A.; Mirts, E. N.; Chakraborty, S.; Moënne-Loccoz, P.; Zhang, Y.; Lu, Y. *Nature Chemistry* **2016,** *9*, 257.
28. (a) Einsle, O.; Tezcan, F. A.; Andrade, S. L. A.; Schmid, B.; Yoshida, M.; Howard, J. B.; Rees, D. C. *Science* **2002,** *297*, 1696-1700; (b) Spatzal, T.; Aksoyoglu, M.; Zhang, L.; Andrade, S. L. A.; Schleicher, E.; Weber, S.; Rees, D. C.; Einsle, O. *Science* **2011,** *334*, 940; (c) Lancaster, K. M.; Roemelt, M.; Ettenhuber, P.; Hu, Y.; Ribbe, M. W.; Neese, F.; Bergmann, U.; DeBeer, S. *Science* **2011,** *334*, 974-977.
29. Hoffman, B. M.; Lukoyanov, D.; Yang, Z.-Y.; Dean, D. R.; Seefeldt, L. C. *Chem. Rev.* **2014,** *114*, 4041-4062.
30. Creutz, S. E.; Peters, J. C. *J. Am. Chem. Soc.* **2014,** *136*, 1105-1115.
31. Anderson, J. S.; Rittle, J.; Peters, J. C. *Nature* **2013,** *501*, 84-87.
32. Spatzal, T.; Perez, K. A.; Einsle, O.; Howard, J. B.; Rees, D. C. *Science* **2014,** *345*, 1620-1623.

33. (a) Creutz, S. E.; Peters, J. C. *J. Am. Chem. Soc.* **2015,** *137*, 7310-7313; (b) Rittle, J.; McCrory, C. C. L.; Peters, J. C. *J. Am. Chem. Soc.* **2014,** *136*, 13853-13862; (c) McWilliams, S. F.; Bill, E.; Lukat-Rodgers, G.; Rodgers, K. R.; Mercado, B. Q.; Holland, P. L. *J. Am. Chem. Soc.* **2018,** *140*, 8586-8598; (d) Geri, J. B.; Shanahan, J. P.; Szymczak, N. K. *J. Am. Chem. Soc.* **2017,** *139*, 5952-5956.
34. (a) Lee, Y.; Sloane, F. T.; Blondin, G.; Abboud, K. A.; García-Serres, R.; Murray, L. J. *Angew. Chem. Int. Ed.* **2015,** *54*, 1499-1503; (b) McWilliams, S. F.; Holland, P. L. *Acc. Chem. Res.* **2015,** *48*, 2059-2065.
35. Lee, S. C.; Lo, W.; Holm, R. H. *Chem. Rev.* **2014,** *114*, 3579-3600.
36. (a) Tanifuji, K.; Sickerman, N.; Lee, C. C.; Nagasawa, T.; Miyazaki, K.; Ohki, Y.; Tatsumi, K.; Hu, Y.; Ribbe, M. W. *Angew. Chem. Int. Ed.* **2016,** *55*, 15633-15636; (b) Tanifuji, K.; Lee, C. C.; Ohki, Y.; Tatsumi, K.; Hu, Y.; Ribbe, M. W. *Angew. Chem. Int. Ed.* **2015,** *54*, 14022 - 14025.
37. (a) Zhang, Y.; Holm, R. H. *J. Am. Chem. Soc.* **2003,** *125*, 3910-3920; (b) Ohki, Y.; Ikagawa, Y.; Tatsumi, K. *J. Am. Chem. Soc.* **2007,** *129*, 10457-10465; (c) Ohta, S.; Ohki, Y.; Hashimoto, T.; Cramer, R. E.; Tatsumi, K. *Inorg. Chem.* **2012,** *51*, 11217-11219.
38. (a) Bhagi-Damodaran, A.; Reed, J. H.; Zhu, Q.; Shi, Y.; Hosseinzadeh, P.; Sandoval, B. A.; Harnden, K. A.; Wang, S.; Sponholtz, M. R.; Mirts, E. N.; Dwaraknath, S.; Zhang, Y.; Moënne-Loccoz, P.; Lu, Y. *Proc. Natl. Acad. Sci.* **2018,** *115*, 6195-6200; (b) Yeung, N.; Lin, Y.-W.; Gao, Y.-G.; Zhao, X.; Russell, B. S.; Lei, L.; Miner, K. D.; Robinson, H.; Lu, Y. *Nature* **2009,** *462*, 1079-1082; (c) Collman, J. P.; Dey, A.; Yang, Y.; Decréau, R. A.; Ohta, T.; Solomon, E. I. *J. Am. Chem. Soc.* **2008,** *130*, 16498-16499; (d) Collman, J. P.; Yang, Y.; Dey, A.; Decréau, R. A.; Ghosh, S.; Ohta, T.; Solomon, E. I. *Proc. Natl. Acad. Sci.* **2008,** *105*, 15660-15665.
39. White, C. J.; Speelman, A. L.; Kupper, C.; Demeshko, S.; Meyer, F.; Shanahan, J. P.; Alp, E. E.; Hu, M.; Zhao, J.; Lehnert, N. *J. Am. Chem. Soc.* **2018,** *140*, 2562-2574.
40. Brown, K.; Djinovic-Carugo, K.; Haltia, T.; Cabrito, I.; Saraste, M.; Moura, J. G.; Moura, I.; Tegoni, M.; Cambillau, C. *J. Biol. Chem.* **2000,** *275*, 41133-41136.
41. Johnson, B. J.; Antholine, W. E.; Lindeman, S. V.; Graham, M. J.; Mankad, N. P. *J. Am. Chem. Soc.* **2016,** *138*, 13107-13110.

CHAPTER 2

TETRANUCLEAR IRON CLUSTERS WITH A VARIED INTERSTITIAL LIGAND: EFFECTS ON STRUCTURE, REDOX PROPERTIES, AND NITRIC OXIDE ACTIVATION

The text for this chapter was reproduced in part from:

Reed, C. J.; Agapie, T. *Inorg. Chem.*, **2017**, *56*, 13360-13367

ABSTRACT

A new series of tetranuclear Fe clusters displaying an interstitial μ_4-F ligand was prepared for a comparison to previously reported μ_4-O analogues. With a single nitric oxide (NO) coordinated as a reporter of small-molecule activation, the μ_4-F clusters were characterized in five redox states, from $Fe^{II}_3\{FeNO\}^8$ to $Fe^{III}_3\{FeNO\}^7$, with NO stretching frequencies ranging from 1680 to 1855 cm^{-1}, respectively. Despite accessing more reduced states with an F^- bridge, a two-electron reduction of the distal Fe centers is necessary for the μ_4-F clusters to activate NO to the same degree as the μ_4-O system; consequently, NO reactivity is observed at more positive potentials with μ_4-O than μ_4-F. Moreover, the μ_4-O ligand better translates redox changes of remote metal centers to diatomic ligand activation. The implication for biological active sites is that the higher-charge bridging ligand is more effective in tuning cluster properties, including the involvement of remote metal centers, for small-molecule activation.

INTRODUCTION

Transition metal clusters perform diverse functions in proteins, including metal storage, sensing, electron transfer, and multi-electron small molecule conversions (such as H_2O oxidation, CO_2 fixation, and N_2 reduction).[1] A common element of these multinuclear sites is the presence of highly bridged ($\geq \mu_3$-binding) single atom ligands, such as sulfide,[2] oxide,[3] or carbide.[4] Quantitative measures of the effects these ligands play in small molecule activation remain rare. This is particularly relevant to understanding the role the interstitial μ_6-C ligand in the FeMo cofactor (FeMoco) of nitrogenase (Figure 1A). Synthetic clusters suitable for structure-function studies of bridging ligands with respect to the activation of a small molecule are rare, likely because of design constraints that are difficult to overcome by self-assembly, which is the route typically employed in cluster synthesis. Maintaining the exact same structure while changing the bridging ligands and redox states while limiting ligand binding to a single small molecule, desirable for quantification of the effect and for mimicking substrate activation by protein active sites, are two major challenges. A host of iron carbonyl clusters have been synthesized with a variety of bridging ($\geq \mu_3$) single-atom ligands, including μ_6-C clusters, such as $[(\mu_6\text{-C})Fe_6(CO)_{16}]^{2-}$, with arrangements reminiscent of the FeMoco structure (Figure 1B).[5] While a related cluster has been reported displaying a μ_6-N ligand, $[(\mu_6\text{-N})Fe_6(CO)_{15}]^{3-}$ has been reported, with potential for structure-function studies of the effect of the interstitial ligand, changes in the structure and number of carbon monoxide (CO) ligands complicate interpretations. In the cases where completely isostructural clusters can be prepared with bridging elements of the second row of the periodic table, the large number (≥ 9) of diatomic ligands limits interpretations regarding the activation of a *single* small molecule substrate, which is most relevant to biological systems. Recently, in an elegant demonstration of the effect of the μ_4-ligand (N vs C) on reactivity, the hydride ligands in $[HFe_4C(CO)_{12}]^{2-}$ and $[HFe_4N(CO)_{12}]^{-}$

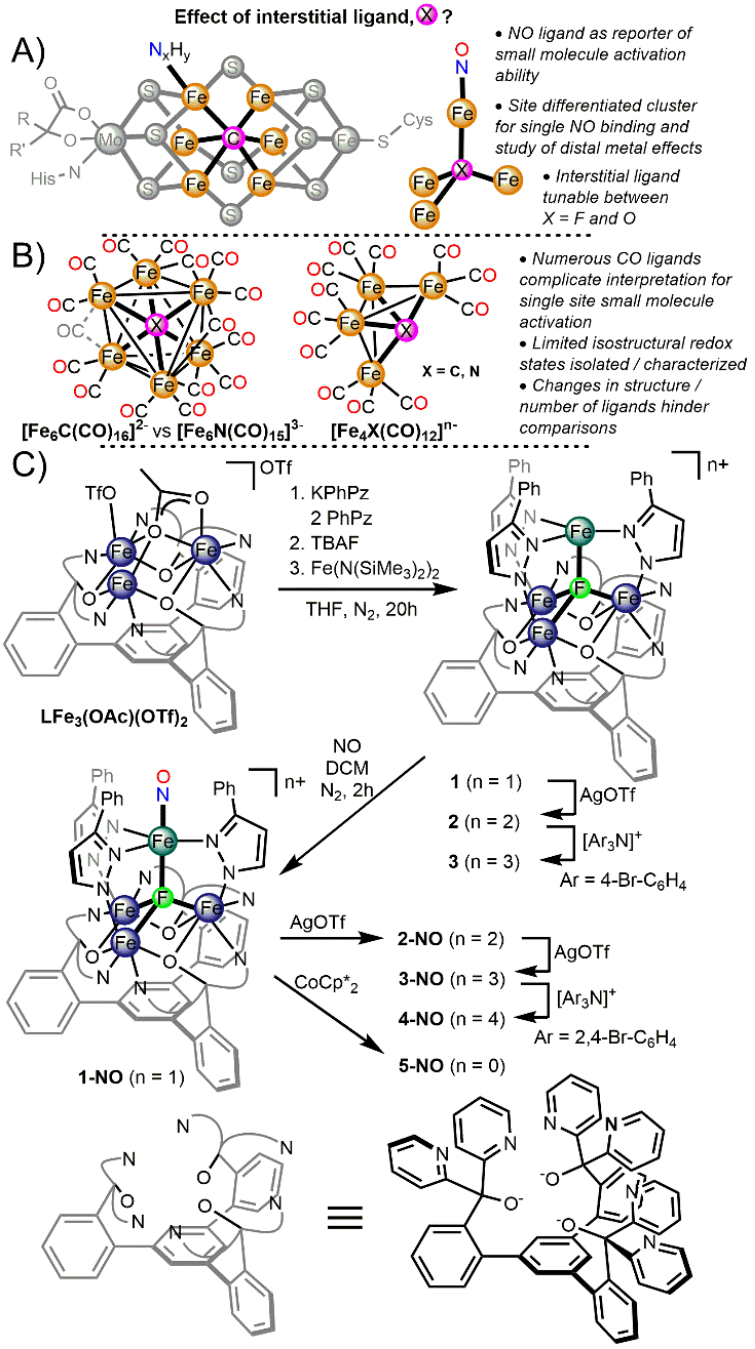

Figure 1 (A) Depiction of FeMoco cluster of nitrogenase with putative binding of nitrogenous ligand and design elements of the clusters reported herein (B) Reported Fe clusters with different interstitial (or psedo-interstitial, X) and diatomic (CO) ligands; right, limitations of these clusters for determining the effect of interstitial ligand on small molecule activation (C) Synthesis of tetranuclear iron clusters.

have been shown to have distinct behavior for H_2 and formate generation.[6] Other synthetic clusters have been studied to address effects of a bridging ligand on reduction potentials or to model FeMoco, but small molecule binding by the clusters with different bridging ligands has not been reported.[7]

Toward directly interrogating the effect of a cluster's interstitial ligand on reactivity, we have developed synthetic methodologies to access site-differentiated multinuclear complexes that allow variation of the bridging ligands. Initial studies by Dr. Graham de Ruiter established a synthetic route to tetranuclear Fe clusters arranged in a pseudo-tetrahedral geometry around a μ_4-O ligand. One of these Fe centers displays a trigonal pyramidal coordination geometry, with an open coordination site *trans* to the μ_4-O and the three neighboring Fe centers; this open coordination site is facilitated by steric protection of phenyl-pyrazolate ligands, which preclude binding of most ligands except for small molecules. These clusters, **LFe$_3$O(PhPz)$_3$Fe^{n+}**, were competent to bind and activate nitric oxide (NO; Scheme 1), where redox changes of the distal Fe centers were able to modulate the degree of NO activation and reactivity.[8] In summary, reduction of a distal Fe^{III} to Fe^{II} leads to an average decrease of N–O stretching frequency of ~ 50 – 30 cm^{-1}, where the lowest oxidation state NO cluster observed ($Fe^{II}_2Fe^{III}${FeNO}^{7}) displayed reactivity towards NO disproportionation.

Scheme 1. Related Tetranuclear Clusters Previously Reported by the Agapie Group[8]

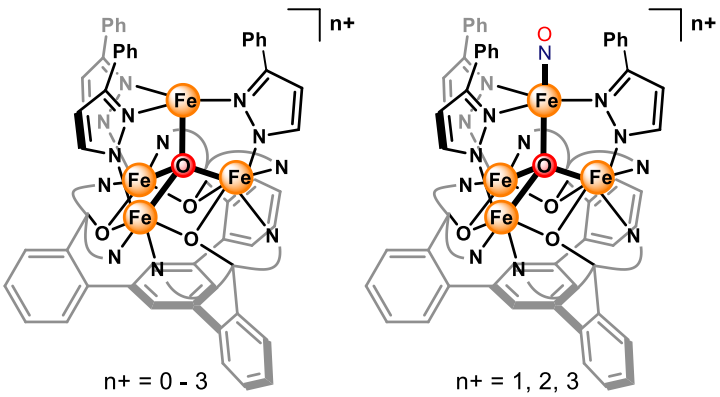

Herein, we present investigations of a series of tetranuclear iron clusters containing a μ_4-F motif, isostructural with the previously reported μ_4-O clusters (Figure 1C).[8-9] These compounds allow for the evaluation of the effects of the nature of the interstitial atom on cluster properties related to the activation of a single diatomic ligand (NO).

RESULTS AND DISCUSSION

We have recently reported the synthesis of site differentiated tetranuclear clusters, where three (basal) metal centers are coordinated by a hexapyridyl trialkoxide framework (**L^{3-}**, Figure 1C) and bridged to a fourth (apical) metal site through three pyrazolate ligands and a μ_4-O ligand.[8-9] The all-ferrous fluoride-bridged cluster, **1**, was synthesized via addition of a 2:1 ratio of phenylpyrazole and potassium phenylpyrazolate along with 1 equiv of anhydrous tetrabutylammonium fluoride to a previously reported trinuclear iron precursor (**$LFe_3(OAc)(OTf)_2$**; Figure 1C).[8, 10] The fourth Fe equivalent was delivered as $Fe(N(SiMe_3)_2)_2$ to complete the tetranuclear cluster (**1**). This redox-neutral route of installing the interstitial F proved to be the most reliable way to avoid the generation of mixtures of clusters, with some μ_4-O clusters likely having formed due to trace moisture. Subsequent chemical oxidations afford two additional redox states, [$Fe^{II}_3Fe^{III}$] (**2**) and [$Fe^{II}_2Fe^{III}_2$] (**3**); cyclic voltammetry of **1** displays two quasi-reversible features for these oxidations at potentials of -0.51 V (all potentials vs Fc/Fc^+) and +0.18 V (Figure 2). Characterization by Mössbauer spectroscopy is consistent with charge localization on each Fe center and with oxidations occurring exclusively in the basal triiron core, the apical Fe remaining Fe^{II} (Figure 3), as was observed for the μ_4-O analogs.[9a] Structural characterization by single crystal X-ray diffraction (XRD) reveals that the most oxidized cluster, **3**, displays a five-coordinate apical Fe^{II}, due to acetonitrile (MeCN) binding (Figure 4). Removal of this ligand under vacuum results in decomposition. This behavior is in contrast to the analogous μ_4-O clusters, which have been isolated in the

[$Fe^{II}_2Fe^{III}_2$] and [$Fe^{II}Fe^{III}_3$] oxidation states, both displaying a four-coordinate apical Fe^{II}. This difference suggests that that the μ_4-F clusters are more Lewis acidic than their μ_4-O analogues. Consistent with this interpretation, μ_4-O clusters with electron withdrawing substituents show increased coordination numbers at the apical metal.[9a]

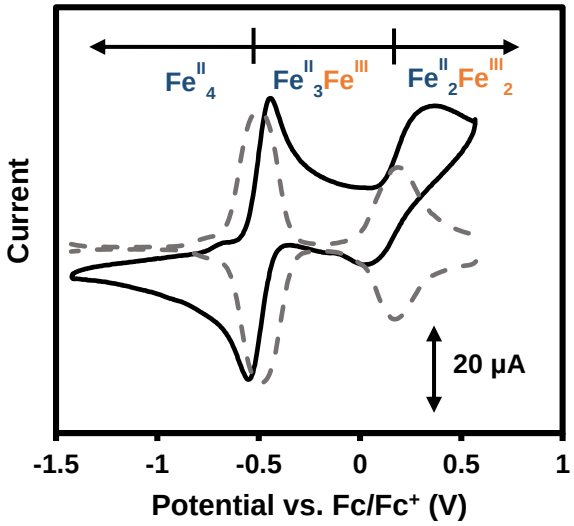

Figure 2. Cyclic voltammogram (black trace) of **1** (3 mM) in MeCN with 85 mM [Bu_4N][PF_6] at a scan rate of 200 mV/s with glassy carbon, Pt-wire, and Ag-wire as working, counter, and reference electrode, respectively. Square wave voltammograms (gray dashed trace) overlaid with 0.1 V amplitude, 1.0 s period, and 0.01 V increment.

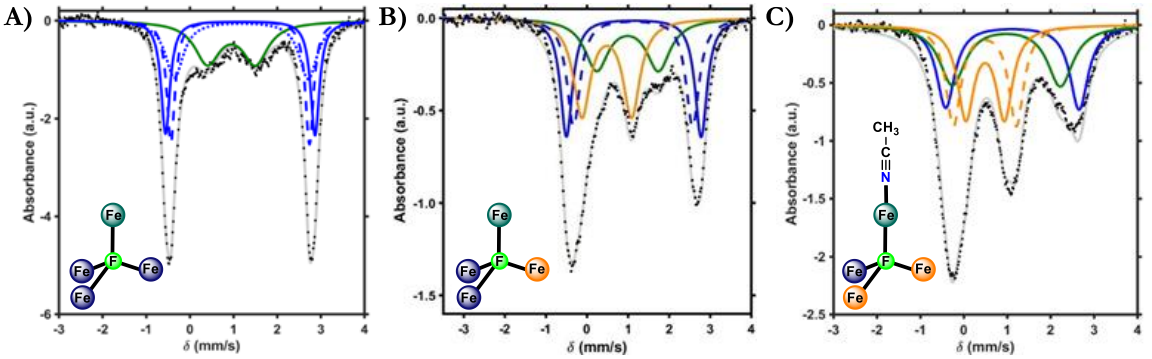

Figure 3. ^{57}Fe Mössbauer spectra at 80K of (A) **1**, (B) **2**, and (C) **3**. Black dots represent the data, gray traces are the sum of the simulated fits, and colored traces represent the individual fits for the Fe centers (See Table 1 for parameters). Blue traces represent assignments made to basal Fe^{II}, orange traces represent basal Fe^{III} assignments, green traces represent apical Fe^{II}.

Table 1. ^{57}Fe Mössbauer Parameters for Complexes 1 – 3 with Oxidation State Assignments

	δ (mm/s)	$\|\Delta E_q\|$ (mm/s)	%	assignment
		1		
———	1.16	3.42	25	h.s. Fe^{II}
– – –	1.15	3.18	25	*h.s.* Fe^{II}
·····	1.18	3.07	25	h.s. Fe^{II}
———	0.95	1.10	25	*h.s.* Fe^{II}
		2		
———	1.14	3.30	25	*h.s.* Fe^{II}
– – –	1.12	2.90	25	*h.s.* Fe^{II}
———	0.48	1.21	29	*h.s.* Fe^{III}
———	0.99	1.50	21	*h.s.* Fe^{II}
		3		
———	1.12	3.07	25	*h.s.* Fe^{II}
———	0.49	0.89	25	*h.s.* Fe^{III}
– – –	0.49	1.45	25	*h.s.* Fe^{III}
———	0.98	2.49	25	*h.s.* Fe^{II}

NO provides a diagnostic vibrational spectroscopic signature for comparing different complexes to address the effects of the multinuclear supporting platform and the interstitial ligand on small-molecule binding.[11] Studies of the chemistry of Fe clusters with NO have been

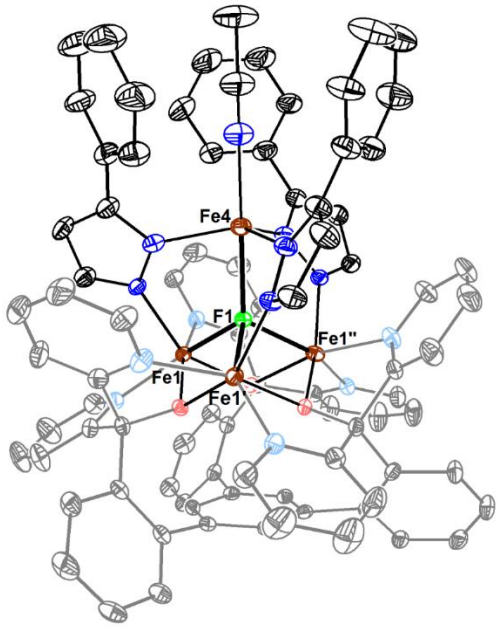

Figure 4. Crystal structure of **3**. Ellipsoids are shown at the 50% probability level. Hydrogen atoms, solvent molecules, and outersphere counterions omitted for clarity.

---

principally focused on understanding the biologically relevant conversion of Fe–S clusters to nitrosylated products.[12] However, there are few examples of multinuclear mononitrosyl complexes containing nearby redox-active metal centers.[8, 13] The clusters targeted here provide insight into the influence of neighboring metal centers on the chemistry of the metal nitrosyl moiety. The addition of NO to compound **1** leads to the formation of the corresponding nitrosyl adduct. Cyclic voltammetry of the monocationic nitrosyl cluster, **1-NO**, displays three electrochemically quasi-reversible oxidations and one quasi-reversible reduction (Figure 5). Each of the five redox states of the nitrosyl clusters observed electrochemically was accessed synthetically (Figure 1C). Stepwise treatment of **1-NO** with AgOTf (**2-NO** and **3-NO**) and $[(2,4\text{-Br-}C_6H_4)_3N][SbCl_6]$ (**4-NO**) provides access to the oxidized NO adducts. **4-NO** decomposes in solution and as a solid on the time scale of attempted crystallizations, preventing structural characterization. Reduction of **1-NO** with decamethylcobaltocene in

MeCN precipitates a purple solid assigned as **5-NO**. Dissolution of **5-NO** in tetrahydrofuran, pyridine, or dichloromethane (CH_2Cl_2), leads to rapid decomposition, preventing structural characterization of this complex as well (Figure 6). Reoxidation of a MeCN suspension of **5-NO** with silver triflate (AgOTf) leads to isolation of the one electron oxidized cluster, **1-NO**, in good yield (Figure 7). Nitrous oxide (N_2O) is detected upon decomposition of **5-NO**, albeit in low yield (~0.1 equiv, gas chromatography-mass spectrometry).

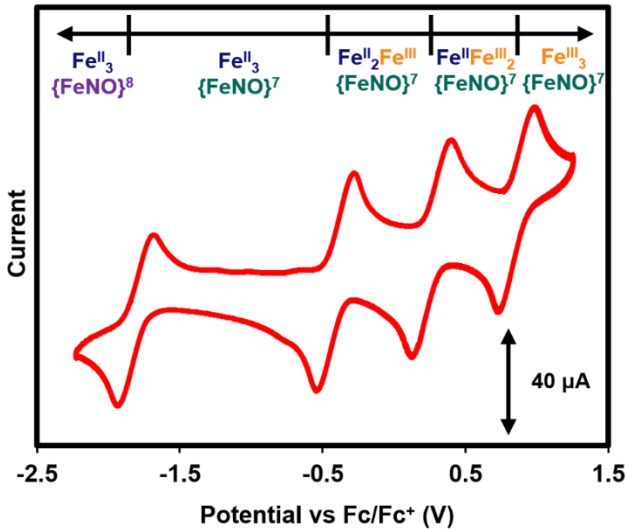

Figure 5. Cyclic voltammogram of monocationic nitrosyl cluster, **1-NO** (2mM) in CH_2Cl_2 with 100 mM $[Bu_4N][PF_6]$ at a scan rate of 200 mV/s with glassy carbon, Pt wire, and Ag wire as working, reference, and counter electrodes, respectively. The measured open-circuit potential was -0.7 V.

Mössbauer spectroscopy was performed on **1-NO** – **5-NO.** As observed in the μ_4-O system, Mössbauer parameters are consistent with oxidations being localized at the basal triiron core as characterized previously.[8-9, 14] In the Mössbauer spectrum of **1-NO**, the Fe–NO signal is readily distinguished from the basal iron centers in the cluster, and was fit with an isomer shift (δ) of 0.62 mm/s and a quadrupole splitting value ($|\Delta E_q|$) of 1.16 mm/s (Figure

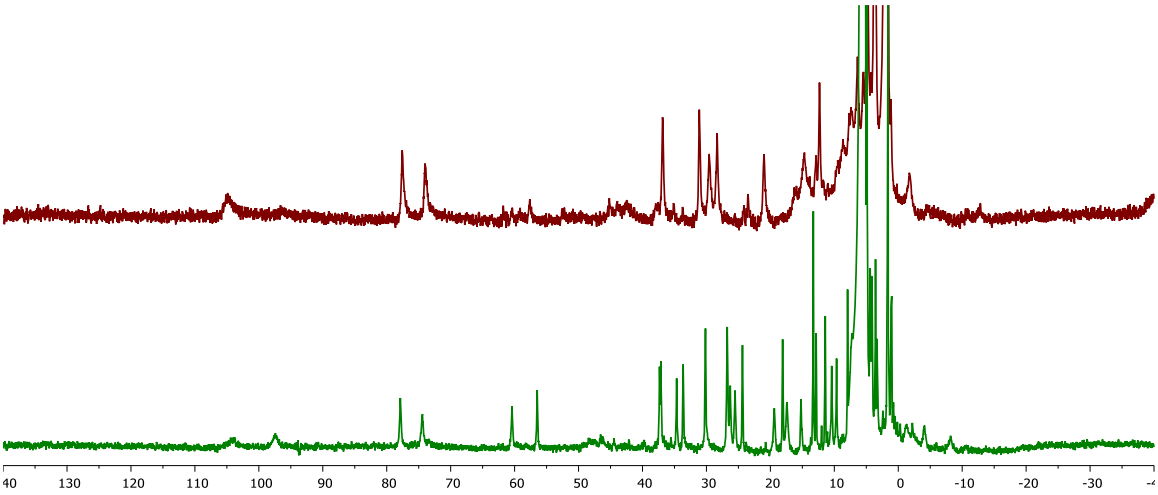

Figure 6. (Top) ^{1}H NMR (300 MHz; CD_3CN) of reaction mixture of **5-NO** in THF over 24 hours. The spectrum of the major species is identical to $[LFe_3F(PhPz)_3Fe][OTf]$ (**1**) in CD_3CN. (Bottom) ^{1}H NMR (300 MHz; CD_2Cl_2) of reaction mixture of **5-NO** in THF over 24 hours. The spectrum of the new species is identical to $[LFe_3O(PhPz)_3Fe][OTf]$. We have previously observed decomposition of $LFe_3O(PhPz)_3Fe$ in dichloromethane to the monocationic cluster. This is consistent with formation of a mixture of $[LFe_3F(PhPz)_3Fe]^{+}$ and $LFe_3O(PhPz)_3Fe$ from the decomposition of **5-NO** in THF.

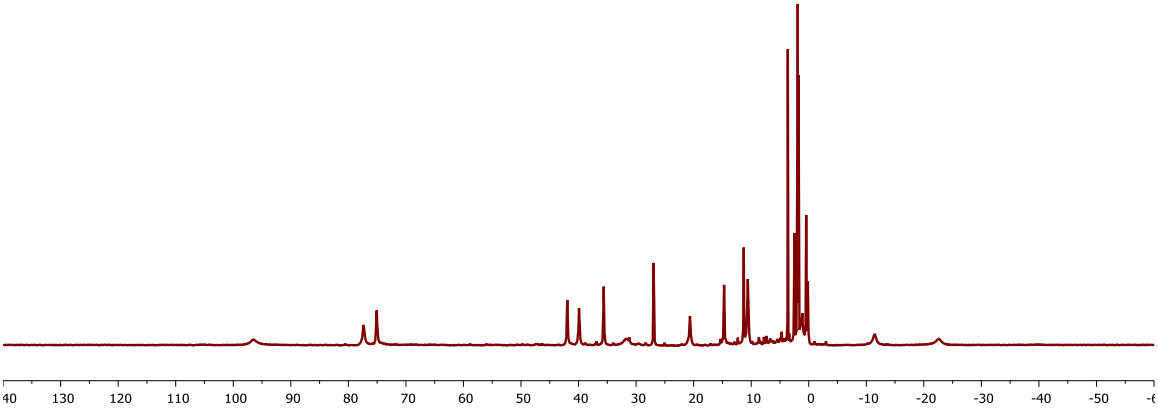

Figure 7. ^{1}H NMR (300 MHz; CD_3CN) of reaction mixture of AgOTf addition to $LFe_3F(PhPz)_3Fe(NO)$ (**5-NO**) in thawing THF. The spectrum is identical to $[LFe_3F(PhPz)_3Fe(NO)][OTf]$ (**1-NO**) in CD_3CN.

8B; Table 2). The exact Mössbauer parameters for the Fe–NO centers in **2-NO** – **4-NO** are more difficult to assign due to spectral overlap with signals from the Fe^{III} centers of the triiron core. The overlap is consistent, however, with only small changes in the Mössbauer parameters for the Fe-NO sites in **1-NO** – **4-NO** (Figures 8C-D and Table 2). These parameters are also similar to the previously reported μ_4-O NO clusters, which have δ values ranging from 0.55 to0.62 mm/s, and $|\Delta E_q|$ values of 1.94 to 2.38 mm/s.[8] Overall, these data, along with the IR spectroscopy data (vide infra), are consistent with the $\{FeNO\}^7$ formulation, according to

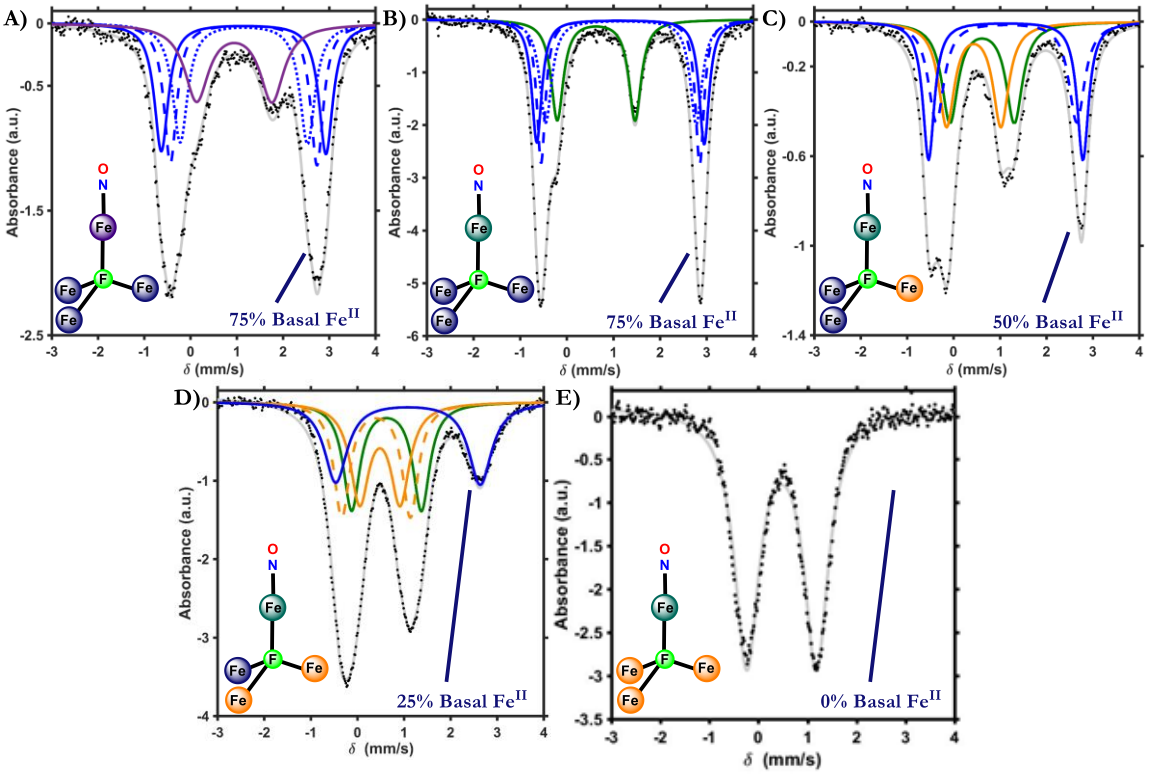

Figure 8. Zero applied field ^{57}Fe Mössbauer spectra at 80K of (A) **5-NO**,(B) **1-NO**, (C) **2-NO**, (D) **3-NO**, and (E) **4-NO**. Black dots represent the data, gray traces are the sum of the simulated fits, and colored traces represent the individual fits for the Fe centers (see Table 2 for parameters). Blue traces represent assignments made to basal Fe^{II}, orange traces represent basal Fe^{III} assignments, green and purple traces represent $\{FeNO\}^7$ and $\{FeNO\}^8$ units, respectively.

Table 2. Fe–μ_4-F Distances and ^{57}Fe Mössbauer Parameters for Complexes 1-NO – 5-NO with Oxidation State Assignments

Fe Center	Fe–μ_4-F distance (Å)	δ (mm/s)	$\lvert\triangle E_q\rvert$ (mm/s)	assignment
		1-NO		
Fe1, Fe2, Fe3	2.129(7); 2.205(6); 2.169(5)	1.15; 1.15; 1.16	3.59; 3.40;3.23	h.s. Fe^{II}
Fe4	2.065(7)	0.63	1.67	$\{FeNO\}^7$
		2-NO		
Fe1	2.030(4)	0.44	1.17	*h.s.* Fe^{III}
Fe2, Fe3	2.237(4); 2.101(4)	1.12; 1.15	3.31; 3.03	*h.s.* Fe^{II}
Fe4	2.093(4)	0.62	1.39	$\{FeNO\}^7$
		3-NO		
Fe1	2.207(3)	1.09	3.10	*h.s.* Fe^{II}
Fe2, Fe3	2.080(3); 2.091(3)	0.48; 0.40	0.87; 1.47	*h.s.* Fe^{III}
Fe4	2.155(3)	0.62	1.51	$\{FeNO\}^7$
		4-NO [a]		
Fe1-Fe4	-	0.47	1.42	*h.s.* Fe^{III} and $\{FeNO\}^7$
		5-NO		
Fe1, Fe2, Fe3	-	1.15; 1.15; 1.15	3.56; 3.17; 3.75	h.s. Fe^{II}
Fe4	-	0.95	1.63	$\{FeNO\}^8$

[a]In this case, the signals for the Fe centers overlap preventing reliable parameter determination for the unique apical $\{FeNO\}^7$ center. The presence of an $\{FeNO\}^7$ moiety is supported via the IR spectroscopy data.

Enemark-Feltham notation.[15] The Mössbauer spectrum of **5-NO** was fit with three Fe^{II} in the triiron core and an apical Fe–NO signal distinct from the ones observed for **1-NO** – **4-NO**; this is assigned as $\{FeNO\}^8$ (δ = 0.94 mm/s and $\lvert\Delta E_q\rvert$ = 1.63 mm/s; Figure 8A), consistent with reduction of the Fe–NO moiety rather than a remote metal site. Compounds **1-NO**, **2-NO**, and **3-NO** were structurally characterized by XRD. In all cases, binding of NO to the apical Fe occurs in a linear fashion (∠Fe4–N40–O40 > 175°, Figure 9A). As observed in the μ_4-O system and from Mössbauer spectra (Figure8B-D), bond metrics are consistent

with oxidations being localized at the basal triiron core of these three clusters (Table 2). The Fe– μ_4-F bonds, which range from 2.07 to 2.24 Å, are longer than the Fe–μ_4-O bonds (1.93 to 2.18 Å) despite the shorter ionic radius of F^- which suggests a significantly weaker interaction with the fluoride resulting in more electron deficient metal centers.[16]

IR spectroscopy reveals a large range of ν_{N-O} for complexes **1-NO** – **5-NO**, from 1680 cm^{-1} to 1855 cm^{-1} (Figure 10). Comparison of ν_{N-O} for **1-NO** – **4-NO** (1799 – 1855 cm^{-1}**)** provides insight into the effect of remote redox changes on NO activation. Oxidation of the Fe centers not bound to NO leads to an average of 19 cm^{-1} per redox change, with redox changes of more reduced clusters having a larger effect. The shift in ν_{N-O} to higher energy upon oxidation is matched by an increase in Fe4-μ_4-F distance, and likely results from a more electron deficient Fe4 center due to this elongation. The nature and type of interaction with axial ligand has been previously demonstrated to effect the level of NO activation in mononuclear Fe complexes.[17] Analogous shifts in the distance between Fe and axial ligands trans to coordinated N_2 have been reported for monoiron models of nitrogenase.[18]

The correlation between the increase in the Fe4-μ_4-ligand distance and the increase in the ν_{N-O} frequency observed previously for μ_4-O and now with μ_4-F interstitial ligands suggests that this structural parameter generally serves to relay the effect of remote redox changes to the metal that binds the small molecule. However, the magnitude of the change in NO activation as a result of these distal redox changes varies with the nature of the interstitial atom. For μ_4-O clusters, the ν_{N-O} changes from 1715/1759 to 1823 cm^{-1} over two redox events with an average change of 54/33 cm^{-1} per electron transfer, in contrast to only 19 cm^{-1} for μ_4-F. The stronger O^{2-} ligand roughly doubles the effect of the remote redox changes on the activation of NO compared to F^-. This is a unique observation, which relies on the ability to access multiple oxidation states of these clusters, and demonstrates that an interstitial ligand

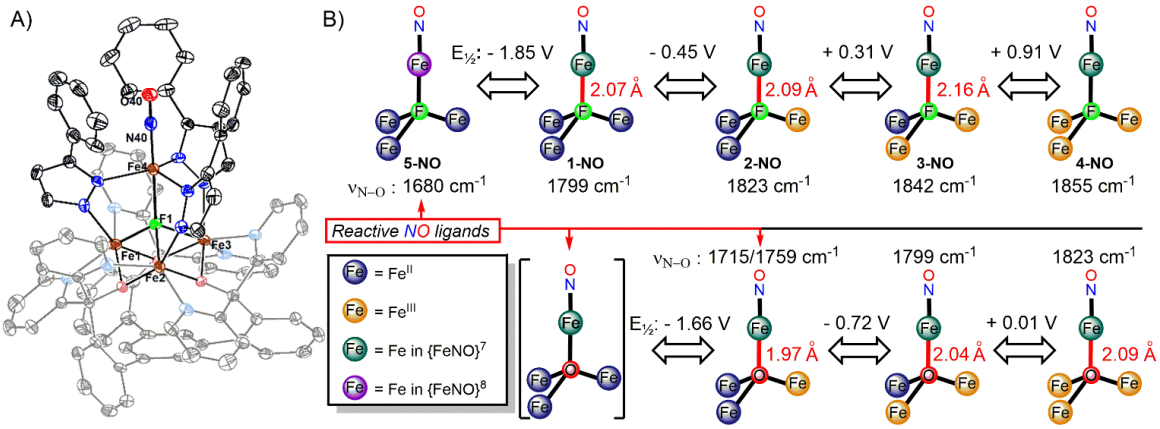

Figure 9. (A) Crystal structure of tetranuclear iron nitrosyl cluster **2-NO** with ellipsoids shown at the 50% probability level. Solvents molecules, outer-sphere counterions, and H atoms are omitted for clarity. (B) Simplified depiction of the tetranuclear iron clusters discussed. Measured redox potentials, NO stretching frequencies, and apical Fe-μ_4-ligand distances are included for comparison. Data for the μ_4-O clusters were previously reported.[8]

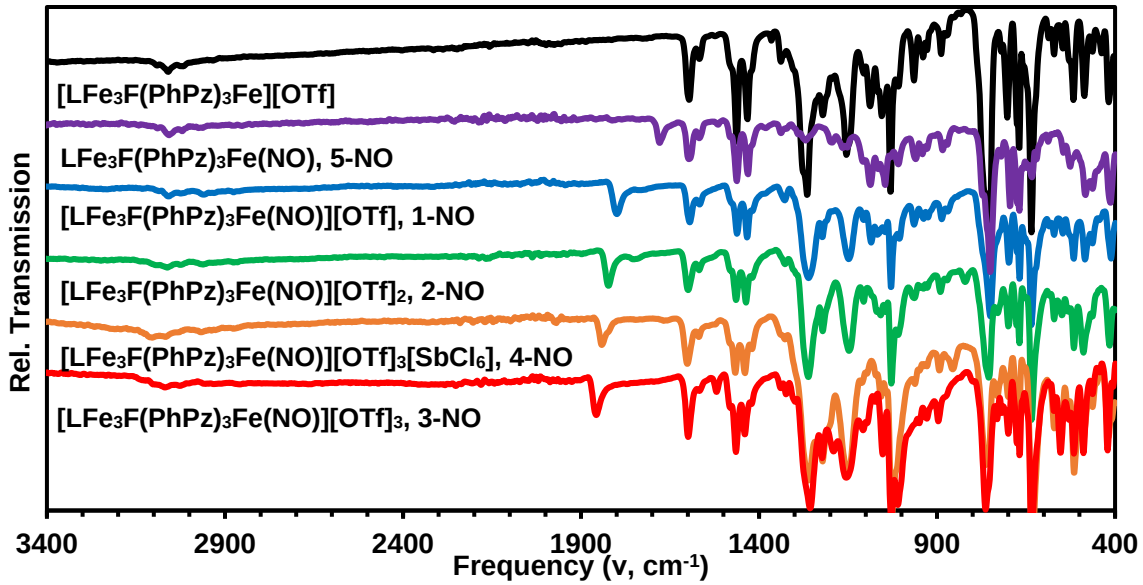

Figure 10. Solid state IR spectra of complexes **1**, **1-NO** - **5-NO**.

---

can influence small molecule activation in two ways: first, by its direct interaction with the small molecule-binding metal center, and second, by modulation of the degree to which other

metals in the cluster can perturb this meta-interstitial ligand interaction. A structural comparison of the Fe4-μ_4-ligand distances over two oxidation states shows that redox changes at the remote Fe centers shift the Fe4-μ_4-F distance by 0.09 Å and the Fe4-μ_4-O bond by 0.12 Å (Figure 9B). The more donating interstitial ligand is able to more efficiently translate remote redox changes in the cluster into NO activation.

A consequence of varying the μ_4-ligand in these clusters is that the weaker F^- donor increases the overall cluster charge of a particular redox state by 1 compared to the O^{2-} version. In reported mononuclear complexes, related modifications of a ligand's charge at a distal site (i.e. R_3BH^- vs R_3CH) leads to observable shifts of bound carbonyl stretching frequencies by ~10 – 40 cm^{-1}.[19] For these clusters, separating the effect of higher positive charge from the effect of the donating abilities of the interstitial ligand on NO activation can be addressed by comparing clusters **2-NO**−**4-NO** and the μ_4-O analogues. For the same cluster redox state, significantly higher ν_{N-O} are observed for the μ_4-F ligand compared to μ_4-O, as expected. The overall cluster charge, which is higher by 1 compared to μ_4-O clusters of the same Fe redox states, is not sufficient to explain the higher NO activation. A comparison of clusters of the same charge for μ_4-O and μ_4-F, but higher overall Fe redox state for μ_4-O (for example, (μ_4-F)$Fe^{II}Fe^{III}_2${FeNO}^{7} (**3-NO**) with ν_{N-O} = 1842 cm^{-1} vs (μ_4-O)Fe^{III}_2{FeNO}^{7} with ν_{N-O} = 1823 cm^{-1}) still shows a higher degree of NO activation with O^{2-}. This difference suggests that the higher-charge interstitial ligand leads to a more electron-rich cluster and a lower ν_{N-O} due to its direct interaction with the metal centers rather than *solely* due to the reduced cluster charge.

IR spectroscopy of **5-NO** corroborates the Mössbauer data and is consistent with the formation of a {FeNO}^{8} motif; the ν_{N-O} at 1680 cm^{-1}, is ~120 cm^{-1} lower than ν_{N-O} for the {FeNO}^{7} moiety of **1-NO**. A similarly large shift was observed upon reduction for a structurally related mononuclear trigonal bipyramidal Fe-NO complex,[20] and more generally

for nonheme $\{FeNO\}^7/\{FeNO\}^8$ complexes.[21] An analogous species is not observable for the μ_4-O clusters. A comparison of the redox potentials of the μ_4-F and the μ_4-O systems (Figure 9B)[8] reveals that the F^- ligand shifts the redox potentials positively by approximately 1 V for the same cluster oxidation states compared to the O^{2-} ligand because of the lower negative charge and weaker electron donating ability of F^-. An analogous effect is observed for other clusters upon changing the bridging ligand to alter the charge of the cluster.[6, 7e] The shift in redox potentials allows access to more reduced states of the μ_4-F clusters within the electrochemical solvent window, which could be beneficial for storing additional reducing equivalents at more positive potentials. However, this is counterbalanced by weaker activation of the diatomic ligand, as reflected by IR spectroscopy (vide supra). In fact, to achieve the same level of NO activation, the μ_4-F clusters need to have Fe oxidation states lower by two levels compared to the μ_4-O clusters. This is in contrast to the behavior observed for certain iron-multicarbonyl clusters, where data is available for isostructural motifs. For example, $[Fe_4C(CO)_{12}]^{2-}$ shows lower average CO activation than the one electron more reduced, but same-charge cluster, $[Fe_4N(CO)_{12}]^{2-}$.[6, 22] The difference is likely a result of distribution of charge and small molecule activation over many (12) CO ligands. In the present system, which displays a more biomimetic, single ligand binding, the NO activation is relayed remotely through the interstitial atom and provides a test for the ability of the $\mu_4$ligand to communicate the redox change at metals not bound to NO. Furthermore, differences in chemical reactivity of the diatomic ligand are observed. The addition of NO to $(\mu_4\text{-O})Fe^{II}_2Fe^{III}\{FeNO\}^7$ leads to NO disproportionation to generate N_2O and the one electron oxidized nitrosyl cluster.[8] In contrast, addition of NO to **1-NO**, which is one electron more reduced $(\mu_4\text{-F})Fe^{II}_3\{FeNO\}^7$, does not result in a reaction. This difference in reactivity as a function of interstitial ligand is likely due to a more activated NO and a 250 mV lower redox potential for the μ_4-O cluster.

Only **5-NO**, with an electronically different, $\{FeNO\}^8$ moiety, undergoes conversion to N_2O with a fluoride interstitial ligand, albeit not cleanly. Overall, despite more negative potentials compared to μ_4-F analogs of the same redox state, reactivity of NO is observed at milder potentials with the μ_4-O cluster.

CONCLUSIONS

In this report, we have demonstrated the significant effects that the change of interstitial ligands (μ_4-O vs μ_4-F) has on the small molecule activation properties of tetranuclear Fe clusters. The more positive redox potentials of μ_4-F clusters allow access to more reduced Fe states. However, this does not result in more efficient activation of small molecule ligands, as inferred from IR spectroscopy and reactivity of NO complexes. The higher ν_{N-O} values of the μ_4-F species for the same Fe oxidation states compared to the μ_4-O analogues are not due to the difference in cluster charge but rather the nature of the interactions with the bridging ligand. To achieve similar NO activation, the cluster needs to be two electrons more reduced with the μ_4-F compared to the μ_4-O ligand. Consequently, NO disproportionation is observed with a μ_4-O ligand at higher Fe oxidation states and more positive potentials than with a μ_4-F ligand. Furthermore, the μ_4-O ligand is a better relay of remote redox changes. The structure-function studies described here suggest that a higher charge interstitial ligand, such as the carbide in FeMoco of nitrogenase, is more efficient at tuning cluster properties in a variety of ways toward the activation of small molecule. Cluster analogs with interstitial C and N moieties are currently being pursued for comparison.

EXPERIMENTAL DETAILS

General Considerations. All reactions were performed at room temperature in an N_2-filled M. Braun glovebox or using standard Schlenk techniques unless otherwise specified. Glassware was oven dried at 140 ºC for at least 2 h prior to use, and allowed to cool under vacuum. **$LFe_3(OAc)(OTf)_2$**,[8] $Fe(N(SiMe_3)_2)_2$,[23] benzyl potassium,[24] 1-*H*-3-phenyl pyrazole (HPhPz),[25] anhydrous $[NBu_4][F]$[26], and $[(2,4\text{-}Br\text{-}C_6H_3)_3N][SbCl_6]$[27] were prepared according to literature procedures. $[(4\text{-}Br\text{-}C_6H_4)_3N][OTf]$ was prepared according to a modified literature procedure.[28] Tetrahydrofuran was dried using sodium/benzophenone ketyl, degassed with three freeze-pump-thaw cycles, vacuum transferred, and stored over 3Å molecular sieves prior to use. CH_2Cl_2, diethyl ether, benzene, acetonitrile, hexanes, and pentane were dried by sparging with nitrogen for at least 15 minutes, then passing through a column of activated A2 alumina under positive N_2 pressure. ^1H and ^{19}F NMR spectra were recorded on a Varian 300 MHz spectrometer. ^{13}C NMR spectra were recorded on a Varian 500 MHz spectrometer. CD_3CN and CD_2Cl_2 was purchased from Cambridge Isotope Laboratories, dried over calcium hydride, degassed by three freeze-pump-thaw cycles, and vacuum transferred prior to use. Infrared (ATR-IR) spectra were recorded on a Bruker ALPHA ATR-IR spectrometer at 4 cm^{-1} resolution. Headspace analysis was conducted on a HP 5972 GC-MS.

Physical Methods. *Mössbauer measurements*. Zero applied field ^{57}Fe Mossbauer spectra were recorded at 80 K in constant acceleration mode on a spectrometer from See Co (Edina, MN) equipped with an SVT-400 cryostat (Janis, Wilmington, WA). The isomer shifts are relative to the centroid of an α-Fe foil signal at room temperature. Samples were prepared by mixing polycrystalline material (20 mg) with boron nitride in a cup fitted with screw cap or freezing a concentrated acetonitrile solution in the cup. The data were fit to Lorentzian lineshapes using WMOSS (www.wmoss.org).

Mössbauer simulation details for compounds 1 – 3 and 1-NO – 5-NO. All spectra were simulated as four pairs of symmetric quadrupole doubles with equal populations and Lorentzian lineshipes (the parameter defining the width, Γ, is reported). They were refined to a minimum via least squares optimization (13 fitting parameters per spectrum). Signals appearing above 2 mm/s were indicative with the presence of high-spin Fe^{II} centers and correspond to species with isomer shifts ~ 1 mm/s. The Mössbauer data were fit to be consistent with our previously reported iron clusters.[8-9, 14] The observed Mossbauer parameters are in agreement with related six-coordinate high-spin Fe^{II}/Fe^{III} centers.[29]

Electrochemical measurements. CVs and SWVs were recorded with a Pine Instrument Company AFCBP1 biopotentiostat with the AfterMath software package. All measurements were performed in a three electrode cell, which consisted of glassy carbon (working; ø = 3.0 mm), silver wire (counter), and bare platinum wire (reference), in a N_2 filled M. Braun glovebox at RT. Dry acetonitrile or CH_2Cl_2 that contained ~85 mM $[Bu_4N][PF_6]$ was used as the electrolyte solution. The ferrocene/ferrocinium (Fc/Fc^+) redox wave was used as an internal standard for all measurements.

X-ray crystallography. X-ray diffraction data was collected at 100 K on a Bruker PHOTON100 CMOS based diffractometer (microfocus sealed X-ray tube, Mo Kα (λ) = 0.71073 Å or Cu Kα (λ) = 1.54178 Å). All manipulations, including data collection, integration, and scaling, were carried out using the Bruker APEXII software. Absorption corrections were applied using SADABS. Structures were solved by direct methods using XS (incorporated into SHELXTL) and refined by using ShelXL least squares on Olex2-1.2.7 to convergence. All non-hydrogen atoms were refined using anisotropic displacement parameters. Hydrogen atoms were placed in idealized positions and refined using a riding model. Due to the size of

the compounds (**1** - **3** and **1-NO** – **3-NO**), most crystals included solvent-accessible voids that contained disordered solvent. In most cases the solvent could be modeled satisfactorily.

Synthetic Procedures. *Synthesis of Potassium 3-phenyl-pyrazolate (KPhPz).* In the glovebox, a solution of 1-*H*-3-phenyl-pyrazole (1.54 g, 11.8 mmol) in THF (5 mL) was stirred while a solution of benzyl potassium (1.70 g, 11.8 mmol) in THF (10 mL) was added drop-wise. Addition caused the solution to change from colorless to pale yellow. After 30 minutes, the solvent was removed under reduced pressure to obtain 1.83 g off-white powder (85% yield). ^{1}H NMR (300 MHz, CD_3CN) δ 7.83 (d, 2H), 7.44 (s, 1H), 7.28 (t, 2H), 7.07 (t, 1H), 6.39 (s, 1H). ^{13}C NMR (500 MHz, CD_3CN) δ 100.01 (Pz NC*C*H), 125.02 (*p*-Ar *C*H), 125.37 (*m*-Ar *C*H), 128.98 (*o*-Ar *C*H), 139.34 (Pz *C*HCHN), 150.27 (Pz N*C*CH). An expected signal ~ 138 ppm (*i*-Ar *C*)[8] could not be observed, likely due to the low solubility of KPhPz.

Synthesis of tris-4-bromo-phenylamininum trifluoromethanesulfonate ([(4-Br-C_6H_4)$_3$N][OTf]). This was prepared through a modification of a literature procedure for [(4-Br-C_6H_4)$_3$N][BF_4].[28] Tris-4-bromo-phenylamine (1.5 g, 3.11 mmol) was dissolved in 30 mL diethyl ether with silver trifluoromethanesulfonate (AgOTf; 1.2 g, 4.67 mmol). This light green solution was added to a 100 mL Schlenk tube and cooled to -40 ºC under N_2 atmosphere. Iodine powder (0.75 g, 2.96 mmol) was added with a counter-flow of N_2 while stirring; addition caused the solution to turn dark blue. The Schlenk tube was warmed to room temperature and filtered over a course porosity frit. The collected precipitate was filtered with 30 mL CH_2Cl_2 in the glovebox. To the resulting dark blue solution, 40 mL diethyl ether was added and the flask was cooled to -40 ºC. [(4-Br-C_6H_4)$_3$N][OTf] was collected as a dark purple solid upon filtration (1.36 g, 69% yield). Anal. Calc. (%) for $C_{19}H_{12}Br_3F_3NO_3S$: C, 36.16; H, 1.92; N, 2.22. Found: C, 36.70; H, 1.94; N, 2.27.

*Synthesis of [LFe$_3$F(PhPz)$_3$Fe][OTf] (**1**).* In the glovebox, a suspension of **LFe$_3$(OAc)(OTf)$_2$** (1047 mg, 0.76 mmol) in THF (3 mL) was frozen in the cold well. To the thawing suspension, solutions of potassium 3-phenyl-pyrazolate (190 mg, 1.04 mmol) in THF (3 mL) and 1-*H*-3-phenyl-pyrzole (220 mg, 1.52 mmol) in THF (3 mL) were added. The suspension changed color from yellow to orange upon addition of the potassium 3-phenyl-pyrazolate. [Bu$_4$N][F] (208 mg, 0.79 mmol) was added as a suspension in THF (3 mL), causing the solution to become dark red. A solution of Fe(N(SiMe$_3$)$_2$)$_2$ (288 mg, 0.76 mmol) in THF (2 mL) was added. The reaction was stirred for 20 h, after which an orange precipitate was observed. The suspension was filtered over a bed of celite on a fine porosity glass frit and washed with 5 mL THF. The orange solid was collected with 60 mL MeCN. The solvent was removed under reduced pressure to obtain [LFe$_3$F(PhPz)$_3$Fe][OTf] as an orange solid (950 mg, 75% yield). ^{1}H NMR (300 MHz, CD_2Cl_2) δ 104.77, 78.57, 75.13, 48.82, 37.46, 30.48, 27.17, 26.44, 25.63, 19.69, 18.42, 11.60, 10.53, 4.54, 4.22, 3.44, 1.99, 1.27, 1.16, -1.13, -2.80, -46.96. ^{19}F NMR (300 MHz, CD_2Cl_2) δ -78.45. UV-vis (CH_2Cl_2) [ε (M^{-1} cm^{-1})]: 251 nm (9.2×10^4), 463 nm (3.9×10^3). Anal. Calcd. (%) for $C_{85}H_{60}F_4Fe_4N_{12}O_6S$: C, 60.88; H, 3.61; N, 10.02. Found: C, 61.16; H, 3.75; N, 9.74.

*Synthesis of [LFe$_3$F(PhPz)$_3$Fe][OTf]$_2$ (**2**).* To a suspension of [LFe$_3$F(PhPz)$_3$Fe][OTf] (**1**; 94 mg, 0.06 mmol) in THF (2 mL), a solution of AgOTf (14 mg, 0.06 mmol) in THF (2 mL) was added. The color of the suspension changed from orange to brown and, after 2 hours, the solvent was removed under reduced pressure. The brown residue was dissolved in CH_2Cl_2 and filtered over a bed of celite on glass filter paper. The solvent was removed under reduced pressure to obtain [LFe$_3$F(PhPz)$_3$Fe][OTf]$_2$ as a brown solid (100 mg, 98% yield). ^{1}H NMR (300 MHz, CD_2Cl_2) δ 101.33, 87.83, 79.33, 47.73, 46.79, 35.24, 34.14, 28.86, 26.35, 18.15, 16.58, 16.33, 12.10, 8.55, 7.28, 6.79, 6.25, 5.25, 4.63, -42.36. ^{19}F NMR (300 MHz, CD_2Cl_2) -

78.19. UV-vis (CH_2Cl_2) [ε (M^{-1} cm^{-1})]: 250 nm (10.9 ×10^4), 432 nm (4.8 ×10^3). Anal. Calcd. (%) for $C_{86}H_{60}F_7Fe_4N_{12}O_9S_2$: C, 56.57; H, 3.31; N, 9.21. Found: C, 56.47; H, 3.13; N, 8.88.

*Synthesis of [LFe₃F(PhPz)₃Fe(MeCN)][OTf]₃ (**3**).* To a stirring solution of [$LFe_3F(PhPz)_3Fe$][OTf]$_2$ (**2**; 78.5 mg, 0.04 mmol) in acetonitrile (2 mL), [(p-Br-C_6H_4)$_3$N][OTf] (27.1 mg, 0.04 mmol) was added as an MeCN solution (2 mL). The brown solution became purple upon addition. After 30 minutes, the solution was filtered. 5 mL of CH_2Cl_2 was added to the filtrate, then 10 mL pentane, to obtain a purple precipitate. The supernatant was decanted and the remaining solid was briefly dried under reduced pressure to obtain [$LFe_3F(PhPz)_3Fe(MeCN)$][OTf]$_3$ as a purple solid (42.3 mg, 50% yield). ^{1}H NMR (300 MHz, CD_3CN) δ 125.15, 91.53, 82.45, 80.10, 61.48, 51.98, 43.99, 15.30, 13.93, 12.33, 8.44, 6.48, 5.67, 5.30, 0.46, -5.74, -18.78. ^{19}F NMR (300 MHz, CD_3CN) -75.66. UV-vis (CH_2Cl_2) [ε (M^{-1} cm^{-1})]: 250 nm (10.3 ×10^4), 465 nm (3.6 ×10^3). Anal. Calcd. (%) for $C_{88}H_{62}Cl_2F_{10}Fe_4N_{12}O_{12}S_3$ (**3** with CH_2Cl_2 instead of MeCN; compound recrystallized in CH_2Cl_2): C, 51.31; H, 3.03; N, 8.16. Found: C, 51.26; H, 3.04; N, 8.43.

*Synthesis of [LFe₃F(PhPz)₃Fe(NO)][OTf] (**1-NO**). Method A.* In the glovebox, a 100 mL Schlenk tube was charged with a solution of [$LFe_3F(PhPz)_3Fe$][OTf] (**1**; 179 mg, 0.11 mmol) in CH_2Cl_2 (5 mL). The solution was degassed by three freeze-pump-thaw cycles. While frozen, gaseous nitric oxide (33 mL, 59 mmHg, 0.11 mmol) was condensed in the tube. The reaction was stirred at room temperature for 2 h and changed color from orange to brown. The solvent was removed under reduced pressure to yield [$LFe_3F(PhPz)_3Fe(NO)$][OTf] as a brown solid (181 mg, 99% yield). ^{1}H NMR (300 MHz, CD_2Cl_2) δ 98.43, 76.64, 74.24, 42.59, 40.12, 35.92, 32.51, 27.06, 20.05, 15.27, 14.16, 11.24, 10.79, 4.27, 2.46, 1.13, 0.58, 0.46, -10.77, -23.61. ^{19}F NMR (300 MHz, CD_2Cl_2) δ -78.71. Anal. Calcd. (%) for $C_{86}H_{62}Cl_2F_4Fe_4N_{13}O_7S$ (**1-NO** ·

CH_2Cl_2; compound recrystallized from CH_2Cl_2/pentane): C, 57.66; H, 3.49; N, 10.16. Found: C, 57.40; H, 3.46; N, 10.01.

Method B. In the glovebox, solid $LFe_3F(PhPz)_3Fe(NO)$ (**5-NO**; 22 mg, 0.014 mmol) was cooled to -196 °C in a cold well in a 20 mL vial with a stir bar. AgOTf (3.7 mg, 0.014 mmol) in 0.5 mL thawing tetrahydrofuran was added to the cooled powder. This reaction was stirred at room temperature for 30 minutes then pumped down. The purple suspension became a brown solution. ^{1}H NMR analysis of the crude reaction showed mostly (>90%) $[LFe_3F(PhPz)_3Fe(NO)][OTf]$ (**1-NO**). The brown solid was filtered in CH_2Cl_2 to obtain 16.8 mg of $[LFe_3F(PhPz)_3Fe(NO)][OTf]$ after recrystallization (69% yield).

*Synthesis of $[LFe_3F(PhPz)_3Fe(NO)][OTf]_2$ (**2-NO**). Method A.* In the glovebox, a 100 mL Schlenk tube was charged with a solution of $[LFe_3F(PhPz)_3Fe][OTf]_2$ (**2**; 163 mg, 0.09 mmol) in CH_2Cl_2 (5 mL). The solution was degassed by three freeze-pump-thaw cycles. While frozen, gaseous nitric oxide (33 mL, 50 mmHg, 0.09 mmol) was condensed in the tube. The reaction was stirred at room temperature for 2 h, changing color from brown to yellow-green. The solvent was removed under reduced pressure to yield $[LFe_3F(PhPz)_3Fe(NO)][OTf]_2$ as a dark green solid (162 mg, 98% yield). ^{1}H NMR (300 MHz, CD_2Cl_2) δ 100.10, 83.22, 80.63, 66.68, 50.74, 46.79, 41.32, 17.25, 14.62, 14.38, 12.35, 11.71, 3.31, 0.30, -3.31, -17.33. ^{19}F (300 MHz, CD_2Cl_2) δ -77.52. Anal. Calcd. (%) for $C_{86}H_{60}F_7Fe_4N_{13}O_{10}S_2$: C, 55.65; H, 3.26; N, 9.81. Found: C, 55.59; H, 3.25; N, 9.53.

Method B. In the glovebox, a solution of $[LFe_3F(PhPz)_3Fe(NO)][OTf]$ (**1-NO**; 160 mg, 0.10 mmol) in MeCN (3 mL) was added to a solution of AgOTf (25 mg, 0.10 mmol) in MeCN (2 mL). The solution changed color from brown to yellow-green. After 1 h, the solvent was removed under reduced pressure. The green residue was dissolved in CH_2Cl_2 and filtered over a bed of celite. The solvent was removed under reduced pressure to obtain

$[LFe_3F(PhPz)_3Fe(NO)][OTf]_2$ as a dark green solid (164 mg, 95% yield). ^1H NMR is identical to that observed for method A.

*Synthesis of $[LFe_3F(PhPz)_3Fe(NO)][OTf]_3$ (**3-NO**).* In the glovebox, a solution of $[LFe_3F(PhPz)_3Fe(NO)][OTf]_2$ (**2-NO**; 27.6 mg, 0.015 mmol) in CH_2Cl_2 (1 mL) was stirred as a solution of $[(4\text{-}Br\text{-}C_6H_4)_3N][OTf]$ (10.0 mg, 0.016 mmol) in CH_2Cl_2 (1 mL) was added. The addition caused the yellow-green solution to turn purple. After 30 minutes, the reaction was filtered and layered under pentane to afford purple crystals of $[LFe_3F(PhPz)_3Fe(NO)][OTf]_3$ (20.3 mg, 68% yield). ^1H NMR (300 MHz, CD_2Cl_2) δ 123.58, 98.80, 89.32, 60.89, 41.42, 14.25, 13.41, 10.34, 5.32, 4.35, 3.93, 3.71, 3.47, 2.07, 1.85, 1.18, -2.45, -8.26. Anal. Calcd. (%) for $C_{87}H_{60}F_{10}Fe_4N_{13}O_{13}S_3$: C, 52.12; H, 3.02; N, 9.08. Found: C, 51.88; H, 2.94; N, 8.74.

*Synthesis of $[LFe_3F(PhPz)_3Fe(NO)][OTf]_3[SbCl_6]$ (**4-NO**).* In the glovebox, a thawing solution of $[LFe_3F(PhPz)_3Fe(NO)][OTf]_3$ (**3-NO**; 25.7 mg, 0.013 mmol) in CH_2Cl_2 (1 mL) was stirred as a solution of $[(2,4\text{-}Br\text{-}C_6H_3)_3N][SbCl_6]$ (13.9 mg, 0.013 mmol) in MeCN (1 mL) was added. The addition caused the purple solution to turn blue. Cold toluene was added until a precipitate was observed. This was kept in a liquid nitrogen-cooled cold well for 2 minutes. The supernatant was decanted and the resulting solid was dried under vacuum. This afforded $[LFe_3F(PhPz)_3Fe(NO)][OTf]_3[SbCl_6]$ as a blue solid (15 mg, 49% yield). This compound decomposes over time in solution and the solid state, even at reduced temperatures. Characterization of this compound was conducted with freshly prepared samples to minimize decomposition. ^1H NMR (300 MHz, CD_3CN) δ 124.54, 97.65, 80.33, 77.50, 74.55, 37.57, 18.30, 15.25, 13.39, 9.04, 0.01, -1.66, -5.71, -6.88. Anal. Calcd. (%) for $C_{101}H_{76}Cl_6F_{10}Fe_4N_{13}O_{13}S_3Sb$ (^{NO}**4** · 2 C_7H_8; compound precipitated with toluene): C, 48.07; H, 3.04; N, 7.21. Found: C, 47.83; H, 2.97; N, 7.88.

*Synthesis of $LFe_3F(PhPz)_3Fe(NO)$ (**5-NO**).* In the glovebox, a solution of $[LFe_3F(PhPz)_3Fe(NO)][OTf]$ (**1-NO**; 82.9 mg, 0.049 mmol) in MeCN was stirred as a solution of $CoCp^*_2$ (16.8 mg, 0.051 mmol) in MeCN was added. The addition caused the brown solution to become a purple suspension. After 2 hours, the solids were collected, washed with minimal MeCN, and dried under vacuum to afford $LFe_3F(PhPz)_3Fe(NO)$ as a purple solid (44.3 mg, 59% yield). This species decomposes upon dissolution in tetrahydrofuran, pyridine, or CH_2Cl_2 and is mostly insoluble in acetonitrile, benzene, and toluene. Therefore, NMR and UV-Vis Absorbance data could not be collected for this complex. Anal. Calcd. (%) for $C_{84}H_{60}FFe_4N_{13}O_4$: C, 64.76; H, 3.88; N, 11.69. Found: C, 64.21; H, 3.86; N, 11.51.

*Decomposition of $LFe_3F(PhPz)_3Fe(NO)$ (**5-NO**).* In the glovebox, solid $LFe_3F(PhPz)_3Fe(NO)$ (26 mg, 0.02 mmol) was added to a 20 mL vial with septum cap and stir bar. 10 mL tetrahydrofuran was added and the vial was quickly sealed. Upon dissolving, the solution appeared brown. After stirring for 24 hr, the headspace was analyzed via GC-MS. A blue precipitate was observed in a brown-orange solution.

ELECTROCHEMICAL DETAILS

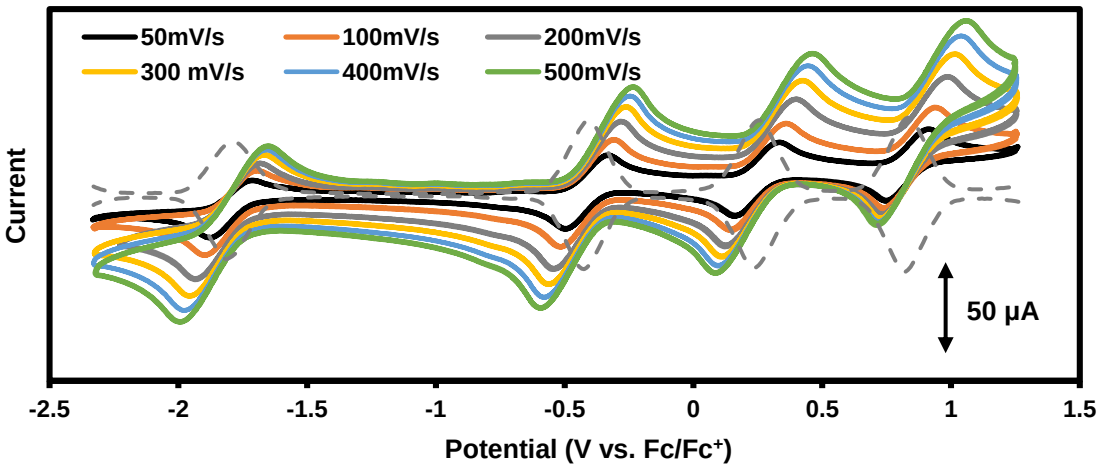

Figure 11. Cyclic voltammogram (solid traces) of $[LFe_3F(PhPz)_3Fe(NO)][OTf]$ (**1-NO**; 2 mM) in CH_2Cl_2 with 100 mM $[Bu_4N][PF_6]$ at various scan rates with glassy carbon, Pt-wire, and Ag-wire as working, reference, and counter electrode, respectively. Square wave voltammograms (gray dashed trace) overlaid with 0.1 V amplitude, 1.0 s period, and 0.01 V increment. The open circuit potential (OCP) was measured to be -0.7 V.

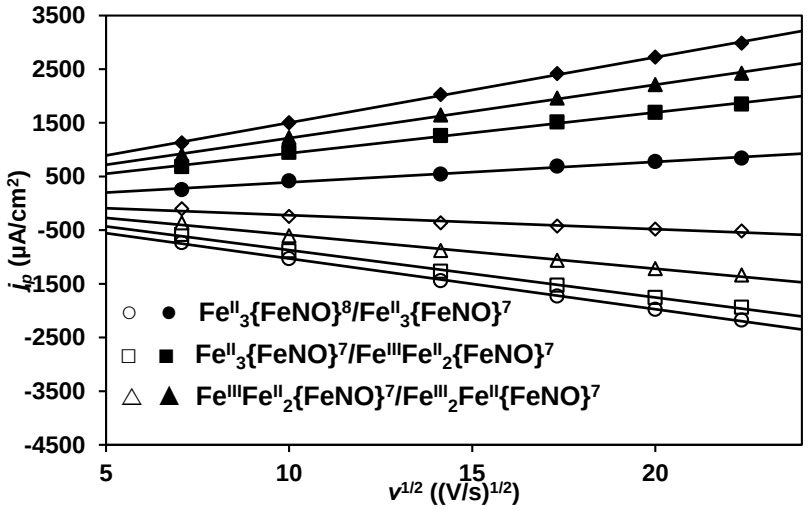

Figure 12. Current density (j_p) dependence of the square root of the scan rate $\nu^{1/2}$ for the electrochemical events observed in the CV of $[LFe_3F(PhPz)_3Fe(NO)][OTf]$, **1-NO**.

CRYSTALOGRAPHIC DETAILS

Crystal and refinement data for complexes 1 – 3 and 1-NO – 3-NO.

	1	2	3	1-NO	2-NO	3-NO
CCDC Number	1554599	1554601	1554596	1554600	1554598	1554597
Empirical formula	$C_{86.75}H_{62}Cl_4F_4Fe_4N_{12}O_6S$	$C_{96}H_{71}Cl_2F_7Fe_4N_{12}O_9S_2$	$C_{101.5}H_{75}F_{10}Fe_4N_{14}O_{12}S_3$	$C_{93}H_{76}Cl_{16}F_4Fe_4N_{13}O_7S$	$C_{93}H_{74}Cl_{14}F_7Fe_4N_{13}O_{10}S_2$	$C_{89.92}H_{64.86}Cl_{5.85}F_{10}Fe_4N_{13}O_{12}S_2$
Formula weight (g/mol)	1837.80	2028.06	2235.21	2386.32	2450.16	2252.38
Radiation	MoKα (λ = 0.71073)	MoKα (λ = 0.71073)	MoKα (λ = 0.71073)	CuKα (λ = 1.54178)	MoKα (λ = 0.71073)	CuKα (λ = 1.54178)
a (Å)	12.4213(18)	40.6924(19)	16.1006(6)	18.7000(7)	20.1692(15)	17.8680(9)
b (Å)	16.108(2)	17.6138(8)	16.1006(6)	16.8237(7)	17.4343(13)	20.4024(11)
c (Å)	20.502(3)	25.6670(13)	67.515(3)	32.4277(11)	28.440(2)	26.3282(15)
α (°)	78.323(6)	90	90	90	90	78.386(4)
β (°)	78.274(7)	114.015(2)	90	103.821(2)	99.091(2)	72.564(3)
γ (°)	85.537(6)	90	120	90	90	82.836(3)
V (Å^3)	3930.6(10)	16804.3(14)	15157.0(13)	9906.5(7)	9874.8(13)	8948.2(9)
Z	2	8	6	4	4	4
Cryst. syst.	triclinic	monoclinic	trigonal	monoclinic	monoclinic	triclinic
Space group	P-1	C2/c	R-3	$P2_1/n$	$P2_1/n$	P-1
ϱ_{calc}g (cm^3)	1.553	1.603	1.469	1.600	1.648	1.672
2 Θ range (°)	2.584 to 61.034	4.626 to 55.754	5.060 to 61.146	5.004 to 130.168	4.464 to 51.356	9.042 to 179.202
μ (mm^{-1})	0.960	0.877	0.712	9.351	1.076	8.167
GOF	0.998	1.026	1.051	1.052	1.060	1.033
R1, wR2 (I>2σ (I))	0.0400, 0.1003	0.0458, 0.0959	0.0835, 0.2216	0.1232, 0.2937	0.0944, 0.2594	0.0786, 0.2045

Special refinement details for [LFe$_3$F(PhPz)$_3$Fe][OTf] (1). The structure contains several co-crystallized solvent molecules, many of which are on special positions. The only complete solvent molecule in the asymmetric unit that could be refined was disordered over two positions refined as 34.1% (C14 through C102) and 65.9% (Cl2 through C101). The two remaining solvent molecules were also disordered over two positions, but on a symmetry element. One disordered dichloromethane was refined as a partially occupied carbon 25% (C103) with ~50% occupied chlorine groups (Cl6 and Cl7). The other disordered dichloromethane was refined as a half occupied molecule, disordered over a symmetry element.

Special refinement details for [LFe$_3$F(PhPz)$_3$Fe][OTf]$_2$ (2). This structure contains two triflate counterions, one of which is positionally disordered over two positions with refined occupancies of 78.5% (S201 through C201) and 21.5% (S202 through C202). The structure also contains a co-crystallized dichloromethane (C0AA through Cl20), and two benzene molceules; one is complete (C101 through C106) the other (C107 through C109) is on a special position. Rigid bond restraints were used on the triflate counterions.

Special refinement details for [LFe$_3$F(PhPz)$_3$Fe(MeCN)][OTf]$_3$ (3). This structure contains the cluster on a C_3 rotation axis, and therefore the three irons in the tri-iron core (Fe1 through Fe1") are indistinct. One triflate counterion is observed in the asymmetric unit along with four solvent molecules, only two of which could be modeled satisfactorily. A toluene molecule (C104 through C107) was disordered over a special position. There was another disordered toluene and acetonitrile that were disordered near special positions, based on residual electron density peaks; however, they could not be satisfactorily modeled. A solvent mask was used to account for the electron density of these molecules.

Special refinement details for [LFe$_3$F(PhPz)$_3$Fe(NO)][OTf] (1-NO). This structure contained numerous co-crystallized solvent molecules (eight dichloromethane molecules). One solvent molecule was disordered and modeled with occupancies of 69% (Cl111 through C105) and 31% (Cl8 through C104). Another dichloromethane contained a disordered chlorine atom that was modeled with occupancies of 63% (Cl15) and 37% (Cl14). The triflate counterion was positionally disordered, whereby the sulfur would point either towards or away from the cluster. It was refined as two molecules with occupancies of 61% (S200 through C200) and 39% (S201 through C201). The standard deviations of some atoms in the phenyl ring of the trinucleating ligand (C34 – C36) were restrained to be the same.

Special refinement details for [LFe$_3$F(PhPz)$_3$Fe(NO)][OTf]$_2$ (2-NO). The structure contains two triflate counterions. One counterion is disordered over two positions with occupancies of 79.3% (S202 through C202) and 20.7% (S201 through C201). Three of the seven co-crystallized dichloromethane molecules are disordered over two positions. The first has occupancies of 59% (Cl11 through C105) and 41% (C103 through C108).

Special refinement details for [LFe$_3$F(PhPz)$_3$Fe(NO)][OTf]$_3$ (3-NO). There are two molecules in the asymmetric unit of the crystal structure. One of the clusters (Fe0A through C199) has a disordered phenyl pyrazolate ligand. Because of this disorder, the bond lengths and angles were not considered with in this molecule and only the other cluster, for which there was no evidence of disorder, (Fe1 through C99) was used for reporting bond metrics. All but two triflate counterions were disordered. Three triflates were positionally disordered; the first two had occupancies of 78% (S303 through C303 and S304 through C304) and 22% (S302 through C302 and S305 through C305). The third triflate had occupancies of 76% (S306 through C306) and 24% (S307 thgouh C307). The two remaining triflates were disordered as a pair. They could be modeled as being adjacent to one another with occupancies of 51%

(S308 through C308) and 62% (S130 through C130). This would be disordered with two triflates, one occupying the same space as the first pair with an occupancy of 37% (S309 through C309), and the other, itself disordered, next to a symmetry element with an occupancy of 50%. There were seven dichloromethane solvent molecules modeled in the structure. Two had positionally disordered chlorine atoms with occupancies of 78% (Cl9) and 22% (Cl16), and 51% (Cl5) and 49% (Cl6). Another dichloromethane was only partially occupied (taking up the same space as the disordered pair of triflates, as discussed above); it had an occupancy of 36% (Cl10 through C205).

Selected bond angles and distances for complexes 1-3, 1-NO – 3-NO.

	Complex					
Bond Distance (Å)	**1**	**2**	**3**	**1-NO**	**2-NO**	**3-NO**
Fe1–F1	2.167(1)	2.024(1)	2.132(2)	2.129(7)	2.030(4)	2.207(3)
Fe2–F1	2.154(1)	2.204(1)	–	2.205(6)	2.237(4)	2.080(3)
Fe3–F1	2.174(1)	2.216(1)	–	2.169(5)	2.101(4)	2.091(3)
Fe4–F1	1.997(1)	2.011(1)	2.172(4)	2.065(7)	2.093(4)	2.155(3)
Fe1–N13	2.170(2)	2.076(2)	2.061(3)	2.118(10)	2.076(5)	2.057(4)
Fe2–N23	2.187(2)	2.125(2)	–	2.122(8)	2.102(5)	2.046(4)
Fe3–N33	2.157(2)	2.108(2)	–	2.116(11)	2.083(6)	2.025(4)
Fe4–N14	2.034(2)	2.063(2)		2.049(10)	2.064(6)	2.020(4)
Fe4–N24	2.056(2)	2.056(2)	–	2.060(9)	2.057(6)	2.049(4)
Fe4–N34	2.046(2)	2.044(2)	–	2.044(10)	2.064(5)	2.025(4)
N13–N14	1.390(2)	1.386(3)	1.387(5)	1.401(15)	1.389(7)	1.369(6)
N23–N24	1.383(2)	1.389(3)	–	1.398(13)	1.380(8)	1.371(6)
N33–N34	1.387(2)	1.388(3)	–	1.384(13)	1.379(8)	1.389(5)
Fe4–N40	–	–	2.112(8)	1.757(10)	1.773(6)	1.754(4)
N40–O40	–	–	–	1.163(13)	1.147(7)	1.133(6)
Bond Angles (º)						
N14–Fe4–N24	119.24(7)	119.34(8)	117.323	118.5(4)	114.6(2)	119.99(2)
N24–Fe4–N34	117.34(7)	120.91(8)	–	117.1(4)	119.8(2)	116.37(2)
N34–Fe4–N14	123.35(7)	119.26(8)	–	119.1(4)	119.6(2)	114.83(2)
Fe4–N40–O40	–	–	–	175.7(9)	177.0(6)	179.2(4)
Torsion Angles (º)						
Fe1–N13–N14–Fe4	3.640	3.40	27.095	23.02	29.86	23.320
Fe2–N23–N24–Fe4	1.317	4.02	-	31.89	30.26	23.035
Fe3–N33–N34–Fe4	4.968	2.14	-	30.32	22.64	25.985
Centroid Distances (Å)						
Fe1|Fe2|Fe3N14|N24|N34	3.090	2.972	2.832	2.889	2.856	2.828
Fe1|Fe2Fe3–O11|O21|O31	0.974	0.945	1.008	0.959	0.987	0.926
Fe1|Fe2|Fe3–F1	1.093	1.051	0.975	1.100	1.063	1.029
N14|N24|N34–Fe4	0.053	0.084	0.344	0.276	0.296	0.353

References

1. Bertini, I.; Gray, H. B.; Stiefel, E. I.; Valentine, J. S. *Biological Inorganic Chemistry: Structure and Reactivity*. 1st ed.; University Science Books: Sausolito, California, 2007.
2. (a) Peters, J. W.; Stowell, M. H. B.; Soltis, S. M.; Finnegan, M. G.; Johnson, M. K.; Rees, D. C. *Biochemistry* **1997,** *36*, 1181-1187; (b) Liu, J.; Chakraborty, S.; Hosseinzadeh, P.; Yu, Y.; Tian, S.; Petrik, I.; Bhagi, A.; Lu, Y. *Chem. Rev.* **2014,** *114*, 4366-4469; (c) Brown, K.; Djinovic-Carugo, K.; Haltia, T.; Cabrito, I.; Saraste, M.; Moura, J. G.; Moura, I.; Tegoni, M.; Cambillau, C. *J. Biol. Chem.* **2000,** *275*, 41133-41136; (d) Drennan, C. L.; Heo, J.; Sintchak, M. D.; Schreiter, E.; Ludden, P. W. *Proc. Natl. Acad. Sci.* **2001,** *98*, 11973-11978; (e) Dobbek, H.; Svetlitchnyi, V.; Gremer, L.; Huber, R.; Meyer, O. *Science* **2001,** *293*, 1281-1285.
3. (a) Ferreira, K. N.; Iverson, T. M.; Maghlaoui, K.; Barber, J.; Iwata, S. *Science* **2004,** *303*, 1831-1838; (b) Umena, Y.; Kawakami, K.; Shen, J.-R.; Kamiya, N. *Nature* **2011,** *473*, 55-60.
4. (a) Einsle, O.; Tezcan, F. A.; Andrade, S. L. A.; Schmid, B.; Yoshida, M.; Howard, J. B.; Rees, D. C. *Science* **2002,** *297*, 1696-1700; (b) Lancaster, K. M.; Roemelt, M.; Ettenhuber, P.; Hu, Y.; Ribbe, M. W.; Neese, F.; Bergmann, U.; DeBeer, S. *Science* **2011,** *334*, 974-977; (c) Spatzal, T.; Aksoyoglu, M.; Zhang, L.; Andrade, S. L. A.; Schleicher, E.; Weber, S.; Rees, D. C.; Einsle, O. *Science* **2011,** *334*, 940.
5. (a) Churchill, M. R.; Wormald, J. *J. Chem. Soc., Dalton Trans.* **1974**, 2410-2415; (b) Churchill, M. R.; Wormald, J.; Knight, J.; Mays, M. J. *J. Am. Chem. Soc.* **1971,** *93*, 3073-3074; (c) Kuppuswamy, S.; Wofford, J. D.; Joseph, C.; Xie, Z.-L.; Ali, A. K.; Lynch, V. M.; Lindahl, P. A.; Rose, M. J. *Inorg. Chem.* **2017,** *56*, 5998-6012; (d) Čorić, I.; Holland, P. L. *J. Am. Chem. Soc.* **2016,** *138*, 7200-7211.
6. Taheri, A.; Berben, L. A. *Inorg. Chem.* **2016,** *55*, 378-385.
7. (a) Ohki, Y.; Ikagawa, Y.; Tatsumi, K. *J. Am. Chem. Soc.* **2007,** *129*, 10457-10465; (b) Ohta, S.; Ohki, Y.; Hashimoto, T.; Cramer, R. E.; Tatsumi, K. *Inorg. Chem.* **2012,** *51*, 11217-11219; (c) Chen, X.-D.; Duncan, J. S.; Verma, A. K.; Lee, S. C. *J. Am. Chem. Soc.* **2010,** *132*, 15884-15886; (d) Chen, X.-D.; Zhang, W.; Duncan, J. S.; Lee, S. C. *Inorg. Chem.* **2012,** *51*, 12891-12904; (e) Powers, T. M.; Betley, T. A. *J. Am. Chem. Soc.* **2013,** *135*, 12289-12296; (f) Fout, A. R.; Zhao, Q.; Xiao, D. J.; Betley, T. A. *J. Am. Chem. Soc.* **2011,** *133*, 16750-16753; (g) Cinco, R. M.; Rompel, A.; Visser, H.; Aromí, G.; Christou, G.; Sauer, K.; Klein, M. P.; Yachandra, V. K. *Inorg. Chem.* **1999,** *38*, 5988-5998; (h) Bobrik, M. A.; Laskowski, E. J.; Johnson, R. W.; Gillum, W. O.; Berg, J. M.; Hodgson, K. O.; Holm, R. H. *Inorg. Chem.* **1978,** *17*, 1402-1410; (i) Di Francesco, G. N.; Gaillard, A.; Ghiviriga, I.; Abboud, K. A.; Murray, L. J. *Inorg. Chem.* **2014,** *53*, 4647-4654.
8. de Ruiter, G.; Thompson, N. B.; Lionetti, D.; Agapie, T. *J. Am. Chem. Soc.* **2015,** *137*, 14094-14106.
9. (a) de Ruiter, G.; Thompson, N. B.; Takase, M. K.; Agapie, T. *J. Am. Chem. Soc.* **2016,** *138*, 1486-1489; (b) de Ruiter, G.; Carsch, K. M.; Gul, S.; Chatterjee, R.; Thompson, N. B.; Takase, M. K.; Yano, J.; Agapie, T. *Angew. Chem. Int. Ed.* **2017,** *56*, 4772-4776; (c) Han, Z.; Horak, K. T.; Lee, H. B.; Agapie, T. *J. Am. Chem. Soc.* **2017,** *139*, 9108-9111.
10. Tsui, E. Y.; Kanady, J. S.; Day, M. W.; Agapie, T. *Chem. Commun.* **2011,** *47*, 4189-4191.
11. McCleverty, J. A. *Chem. Rev.* **2004,** *104*, 403-418.
12. (a) Victor, E.; Lippard, S. J. *Inorg. Chem.* **2014,** *53*, 5311-5320; (b) Tran, C. T.; Williard, P. G.; Kim, E. *J. Am. Chem. Soc.* **2014,** *136*, 11874-11877; (c) Harrop, T. C.; Tonzetich, Z. J.; Reisner, E.; Lippard, S. J. *J. Am. Chem. Soc.* **2008,** *130*, 15602-15610.
13. (a) Majumdar, A.; Lippard, S. J. *Inorg. Chem.* **2013,** *52*, 13292-13294; (b) Awasabisah, D.; Xu, N.; Gautam, K. P. S.; Powell, D. R.; Shaw, M. J.; Richter-Addo, G. B. *Eur. J. Inorg. Chem.* **2016,** *2016*, 509-518; (c) Han, B.; Shao, J.; Ou, Z.; Phan, T. D.; Shen, J.; Bear, J. L.; Kadish, K. M. *Inorg. Chem.* **2004,** *43*, 7741-7751; (d) Victor, E.; Minier, M. A.; Lippard, S. J. *Eur. J. Inorg. Chem.* **2014,** *2014*, 5640-5645; (e) Sidebotham, R. P.; Beer, P. D.; Hamor, T. A.; Jones, C. J.; McCleverty, J. A. *J. Organomet. Chem.* **1989,** *371*, C31-C34.
14. Herbert, D. E.; Lionetti, D.; Rittle, J.; Agapie, T. *J. Am. Chem. Soc.* **2013,** *135*, 19075-19078.
15. Enemark, J. H.; Feltham, R. D. *Coord. Chem. Rev.* **1974,** *13*, 339-406.
16. Shannon, R. *Acta Crystallographica Section A* **1976,** *32*, 751-767.

17. (a) Martirosyan, G. G.; Kurtikyan, T. S.; Azizyan, A. S.; Iretskii, A. V.; Ford, P. C. *J. Inorg. Biochem.* **2013,** *121*, 129-133; (b) Praneeth, V. K. K.; Näther, C.; Peters, G.; Lehnert, N. *Inorg. Chem.* **2006,** *45*, 2795-2811; (c) Wyllie, G. R. A.; Schulz, C. E.; Scheidt, W. R. *Inorg. Chem.* **2003,** *42*, 5722-5734; (d) Sharma, S. K.; Kim, H.; Rogler, P. J.; A. Siegler, M.; Karlin, K. D. *JBIC Journal of Biological Inorganic Chemistry* **2016,** *21*, 729-743.
18. (a) Creutz, S. E.; Peters, J. C. *J. Am. Chem. Soc.* **2014,** *136*, 1105-1115; (b) Rittle, J.; Peters, J. C. *Proc. Natl. Acad. Sci.* **2013,** *110*, 15898-15903; (c) Cammarota, R. C.; Clouston, L. J.; Lu, C. C. *Coord. Chem. Rev.* **2017,** *334*, 100-111.
19. (a) Schoenberg, A. R.; Anderson, W. P. *Inorg. Chem.* **1972,** *11*, 85-87; (b) Hallett, A. J.; Angharad Baber, R.; Guy Orpen, A.; Ward, B. D. *Dalton Transactions* **2011,** *40*, 9276-9283; (c) Imai, S.; Fujisawa, K.; Kobayashi, T.; Shirasawa, N.; Fujii, H.; Yoshimura, T.; Kitajima, N.; Moro-oka, Y. *Inorg. Chem.* **1998,** *37*, 3066-3070; (d) Kujime, M.; Kurahashi, T.; Tomura, M.; Fujii, H. *Inorg. Chem.* **2007,** *46*, 541-551; (e) Thomas, J. C.; Peters, J. C. *J. Am. Chem. Soc.* **2003,** *125*, 8870-8888; (f) Thomas, J. C.; Peters, J. C. *Inorg. Chem.* **2003,** *42*, 5055-5073.
20. (a) Speelman, A. L.; Lehnert, N. *Angew. Chem. Int. Ed.* **2013,** *52*, 12283-12287; (b) Speelman, A. L.; Zhang, B.; Krebs, C.; Lehnert, N. *Angew. Chem. Int. Ed.* **2016,** *55*, 6685-6688.
21. (a) Sanders, B. C.; Patra, A. K.; Harrop, T. C. *J. Inorg. Biochem.* **2013,** *118*, 115-127; (b) Kupper, C.; Rees, J. A.; Dechert, S.; DeBeer, S.; Meyer, F. *J. Am. Chem. Soc.* **2016,** *138*, 7888-7898.
22. Taheri, A.; Thompson, E. J.; Fettinger, J. C.; Berben, L. A. *ACS Catalysis* **2015,** *5*, 7140-7151.
23. Rauchfuss, T. B. Bio-Inspired Iron and Nickel Complexes. In *Inorg. Synth.*, John Wiley & Sons, Inc.: 2010; pp 129-147.
24. Izod, K.; Rayner, D. G.; El-Hamruni, S. M.; Harrington, R. W.; Baisch, U. *Angew. Chem. Int. Ed.* **2014,** *53*, 3636-3640.
25. (a) Larina, N. A.; Lokshin, V.; Berthet, J.; Delbaere, S.; Vermeersch, G.; Khodorkovsky, V. *Tetrahedron* **2010,** *66*, 8291-8299; (b) Kiss, L.; David, L.; Da Costa Pereira Rosa, C. P.; De Nornha, R. G.; Palma, P. N. L.; Da Silva, A. S.; Beliaev, A. US Patent 2012/65191, Mar 15, 2012.
26. Sun, H.; DiMagno, S. G. *J. Am. Chem. Soc.* **2005,** *127*, 2050-2051.
27. Yueh, W.; Bauld, N. L. *J. Am. Chem. Soc.* **1995,** *117*, 5671-5676.
28. Barton, D. H. R.; Haynes, R. K.; Leclerc, G.; Magnus, P. D.; Menzies, I. D. *J. Chem. Soc., Perkin Trans. 1* **1975**, 2055-2065.
29. (a) Herold, S.; Lippard, S. J. *Inorg. Chem.* **1997,** *36*, 50-58; (b) Singh, A. K.; Jacob, W.; Boudalis, A. K.; Tuchagues, J.-P.; Mukherjee, R. *Eur. J. Inorg. Chem.* **2008,** *2008*, 2820-2829; (c) Sutradhar, M.; Carrella, L. M.; Rentschler, E. *Eur. J. Inorg. Chem.* **2012,** *2012*, 4273-4278; (d) Schünemann, V.; Hauke, P. Mössbauer Spectroscopy. In *Applications of Physical Methods to Inorganic and Bioinorganic Chemistry*, Scott, R. A.; Lukehart, C. M., Eds. John Wiley & Sons: West Sussex, England, 2007; pp 243-269.

CHAPTER 3

THERMODYNAMICS OF PROTON AND ELECTRON TRANSFER IN TETRANUCLEAR CLUSTERS WITH MN–OH_2/OH MOTIFS RELEVANT TO H_2O ACTIVATION BY THE OXYGEN EVOLVING COMPLEX IN PHOTOSYSTEM II

The text for this chapter was reproduced in part from:

Reed, C. J.; Agapie, T. *J. Am. Chem. Soc.*, **2018**, *140*, 10900 – 10908

ABSTRACT

We report the synthesis of site-differentiated heterometallic clusters with three Fe centers and a single Mn site that binds water and hydroxide in multiple cluster oxidation states. Deprotonation of [$Fe^{III/II}_3Mn^{II}$–OH_2] clusters leads to internal redox reorganization resulting in formal oxidation at Mn to generate [$Fe^{III/II}_3Mn^{III}$–OH]. ^{57}Fe Mössbauer spectroscopy reveals that oxidation state changes (three for [$Fe^{III/II}_3Mn^{II}$–OH_2] and four for [$Fe^{III/II}_3Mn^{III}$–OH] clusters) occur exclusively at the Fe centers; the Mn center is formally Mn^{II} when water is bound and Mn^{III} when hydroxide is bound. Experimentally determined pK_a (17.4) of the [$Fe^{III}_2Fe^{II}Mn^{II}$–OH_2] cluster and the reduction potentials of the [Fe_3Mn–OH_2] and [Fe_3Mn–OH] clusters were used to analyze the O–H bond dissociation enthalpies ($BDE_{O–H}$) for multiple cluster oxidation states. $BDE_{O–H}$ increases from 69, to 78, and 85 kcal/mol for the [$Fe^{III}Fe^{II}_2Mn^{II}$-OH_2], [$Fe^{III}_2Fe^{II}Mn^{II}$-OH_2], and [$Fe^{III}_3Mn^{II}$-OH_2] clusters, respectively. Further insight of the proton and electron transfer thermodynamics of the [Fe_3Mn–OH_x] system was obtained by constructing a potential–pK_a diagram; the shift in reduction potentials of the [Fe_3Mn–OH_x] clusters in the presence of different bases supports the $BDE_{O–H}$ values reported for the [Fe_3Mn–OH_2] clusters. A lower limit of the pK_a for the hydroxide ligand of the [Fe_3Mn–OH] clusters was estimated for two oxidation states. These data suggest $BDE_{O–H}$ values for the [$Fe^{III}_2Fe^{II}Mn^{III}$–OH] and [$Fe^{III}_3Mn^{III}$–OH] clusters are greater than 93 and 103 kcal/mol, which hints to the high reactivity expected of the resulting [Fe_3Mn=O] in this and related multinuclear systems.

INTRODUCTION

During photosynthesis, water oxidation is catalyzed at the active site of Photosystem II (PSII) by a [$CaMn_4O_5$] cluster known as the oxygen evolving complex (OEC).[1] The catalytic mechanism is outlined by the Kok cycle, with the cluster transitioning through five distinct so-called S-states (S_0, S_1, …, S_4).[2] Four sequential oxidations of the cluster occur ($S_0 \rightarrow \rightarrow S_4$), followed by the O–O bond forming step, with concomitant loss of O_2 and binding of H_2O to complete the cycle ($S_4 \rightarrow S_0$). Protons are sequentially released from the active site during the S-state cycle; deprotonation of bound H_2O in this stepwise manner prevents the buildup of significant charge at the active site, facilitating the further oxidation of the [$CaMn_4O_5$] cluster.[3] PSII utilizes a nearby tyrosine radical (Y_z•) as a mediator to transfer electrons/protons away from the OEC during turnover; because of the nature of the tyrosine radical, proton-coupled electron transfer (PCET) of the H_2O-derived ligands bound to the OEC is considered to play an important role in the Kok cycle.[3-4] Due to the wealth of information available in X-ray crystallographic[1b-d, 5], EPR[6], and X-ray absorption[2b, 6d, 7] spectroscopic techniques, much is known about the Mn oxidation states and electronic environment of the OEC in the S_0 through S_3 states of the Kok cycle. More challenging has been understanding the precise protonation state of H_2O ligands and relevant neighboring amino acid residues of any S-state; computational studies of the OEC have considered a variety of possible protonation states.[4c, 8] Experimentally, time-resolved IR spectroscopy has been helpful in gaining insight to the dynamics of protons at the active site during turnover.[6j, 9] Furthermore, multiple computational models of the OEC mechanism invoke a terminal Mn-oxo as a crucial part of the O–O bond forming S_4 intermediate[2c, 10]. Therefore, there is significant interest in understanding the chemistry of a Mn–OH_2 species undergoing multiple proton and electron transfers to reach a reactive terminal Mn-oxo.

The chemistry of synthetic Mn-aquo, -hydroxo, and -oxo motifs has been a subject of interest for inorganic chemists, particularly within the context of gaining insight into the thermodynamic basis of Mn–OH_x PCET reactivity and how it relates to the mechanism of the OEC.[11, 12, 13] Reported mononuclear systems have been able to probe the roles of Mn oxidation state[12c, 12d, 12i], ligand field[11a, 11f, 13b], and oxygen ligand protonation state[11j, 12j] on PCET reactions and the intrinsic O–H bond dissociation enthalpies ($BDE_{O–H}$) of Mn–OH_x moieties. There are fewer examples of such studies with multinuclear Mn complexes, with most of the reports examining the PCET chemistry of bridging oxo moieties,[14] as opposed to terminally bound OH_x ligands.[15] Most of these reports are limited to binuclear Mn complexes or systems where only a single redox couple could be examined. The PCET reactivity of a synthetic $Mn^{III}_3Mn^{IV}O_3(OH)$ cubane cluster has been examined, where the $BDE_{O–H}$ of the μ_3-OH could be estimated to be >94 kcal/mol; however, precise determination of the thermodynamic bond strength was complicated by subsequent decomposition of the protonated cubane.[14d] A report of proton and electron transfer at a terminal Mn-OH_x moiety with an adjacent Mn center over three oxidation states (Mn^{III}_2, $Mn^{III}Mn^{IV}$, and Mn^{IV}_2) represents a very rare example of thermodynamic studies of a terminal Mn-OH_x in a multinuclear system.[15a] Access to a suitable synthetic platform to interrogate the effects of *multiple* neighboring redox-active metal centers on the chemistry of a terminal Mn–OH_x motif may facilitate a more complete picture of the dynamics of proton and electron transfer of the OEC leading up to its reactive S_4 state, and more generally lead to a better understanding of the behavior of metal clusters in reactions involving water, dioxygen, and multi-electron transformations.

Our group has demonstrated the utility of rationally-designed, well-defined molecular clusters for probing structure-function relationships in multinuclear first-row transition metal complexes, acting as models of complex active sites found in biology.[16, 17] Recently, we have

studied a family of tetranuclear Fe and Mn complexes composed of three coordinatively-saturated metal ions bridged to a fourth (apical) metal center through substituted pyrazolate (or imidazolate) ligands and a μ_4-single atom ligand.[18] The apical metal has a coordination site available for exogenous ligands, allowing for the study of substrate binding and reactivity by a molecular cluster. With bulky and nonpolar phenyl substituents in the 3 position of the pyrazolate ligands coordination of bulkier ligands remains inhibited, and intramolecular ligand activation had been observed.[18d-f] In contrast, previous group members, Drs. Zhiji Han and Kyle Horak, have established that amino-phenylpyrazolate ligands, which are more open and facilitate hydrogen bonding interactions, support oxo-bridged tetramanganese clusters bearing a Mn^{III}–OH moiety (Scheme 1; **[$LMn_3O(PzNHPh)_3Mn(OH)$][OTf]**), which are competent for catalyzing electrochemical water oxidation to H_2O_2.[19] Detailed examination of the PCET reactivity of this cluster was challenging, however, which may have been due, in part, to the acidity and possible redox non-innocence of the amino-phenylpyrazolate ligands. Other previous efforts within the Agapie group to examine PCET reactivity of clusters includes studies of related tri-iron-oxo/-hydroxo clusters bearing a pendant redox inactive metal, **[$LFe_3O_2M(OAc)_2(DME)(OTf)]^{n+}$** (Scheme 1), by Dr. Davide Lionetti.[20]

Scheme 1. Previous Multinuclear Complexes Studied by the Agapie Group for PCET Reactivity[19-20]

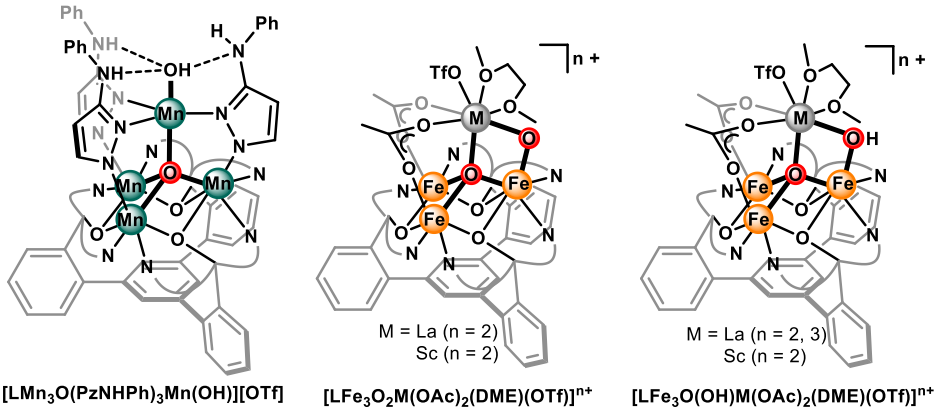

[$LMn_3O(PzNHPh)_3Mn(OH)$][OTf] [$LFe_3O_2M(OAc)_2(DME)(OTf)]^{n+}$ [$LFe_3O(OH)M(OAc)_2(DME)(OTf)]^{n+}$

Here, clusters with unsubstituted bridging pyrazolate ligands (Pz^-) were synthesized to further promote intermolecular reactivity between apical Mn–OH_x groups and external acids, bases, or hydrogen atom donors/acceptors. A heterometallic cluster composition, in this case [Fe_3Mn], was targeted to provide a spectroscopic handle of metal oxidation states within the cluster, via ^{57}Fe Mössbauer spectroscopy. The thermodynamic aspects of the PCET reactivity of these $LFe_3O(Pz)_3Mn(OH_x)^{n+}$ clusters were investigated through examination of the discrete electron and proton transfers taking place over multiple redox states. The results herein establish the significant influence redox changes at distal metal sites in a cluster have on a Mn–OH_x motif and, conversely, how this motif's protonation state can modulate the electron distribution between metals in the cluster.

RESULTS AND DISCUSSION

Synthesis and Characterization of Pyrazolate Bridged [Fe_3Mn] Clusters. The [$Fe^{III}_2Fe^{II}Mn^{II}$] cluster (**2-[OTf]**) can be prepared via one-pot synthesis, starting from previously reported **[LFe_3(OAc)(OTf)][OTf]** complex.[18a] Sequential addition of $Ca(OTf)_2$ (which serves to sequester the equivalent of acetate in the starting material, to avoid mixtures of counterions), potassium pyrazolate, iodosobenzene (PhIO), and manganese (II) trifluoromethanesulfonate bis-acetonitrile solvate ($Mn(OTf)_2$ • 2 MeCN) allows for isolation of the desired complex (Figure 1C). ^{1}H NMR and Mössbauer spectra of **2-[OTf]** are similar to our previously reported $[LFe_3O(PhPz)_3Mn][OTf]_2$ cluster which was synthesized using sodium phenyl pyrazolate, supporting the assignment that the apical metal is Mn (Figure 2).[18e] The structure of **2-[OTf]** was confirmed by single crystal X-ray diffraction (see Figure 1A for isostructural **1-[OTf]**); the cluster geometry is analogous to the substituted pyrazolate and imidizolate tetranuclear clusters, with a single μ_4-interstitital ligand and pyrazolates bridging

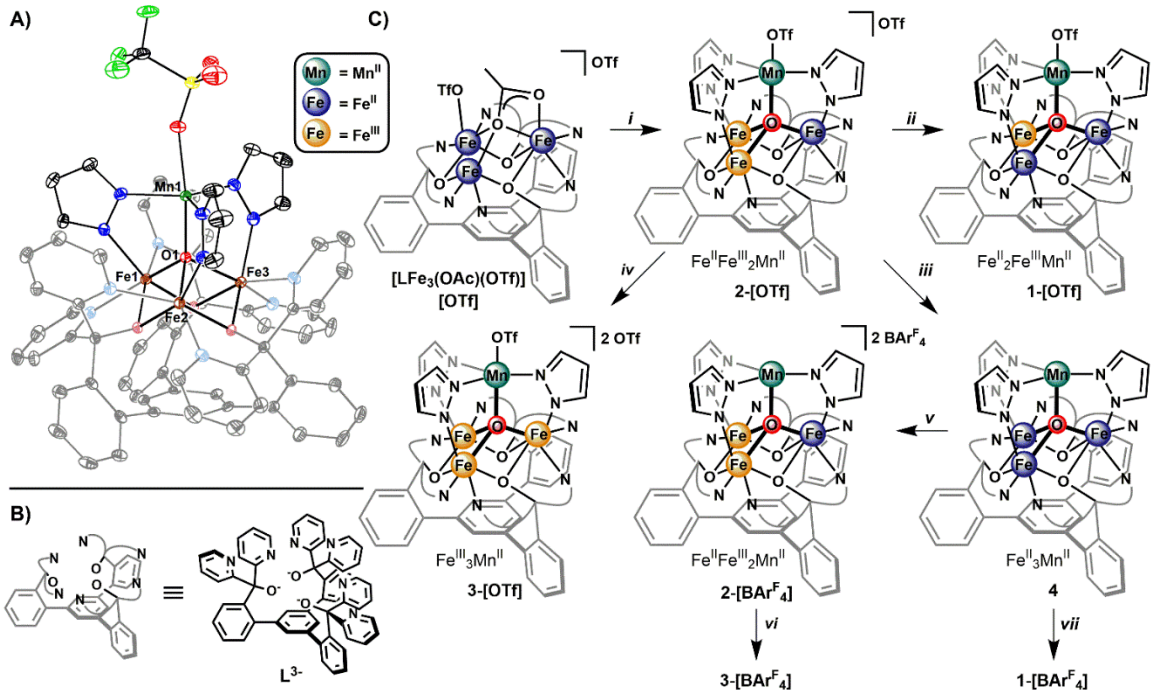

Figure 1. (A) Crystal structure of tetranuclear Fe_3Mn cluster **1-[OTf]** with ellipsoids shown at the 50% probability level. Solvent molecules, outer-sphere counterions, and H atoms are omitted for clarity. (B) 1,3,5-triarylbenzene ligand platform ($\mathbf{L^{3-}}$). (C) Synthetic scheme of Fe_3Mn clusters with triflate and $^{-}[BAr^{F}{}_4]$ counterions. Conditions: (i) One-pot synthesis in THF with (1) $Ca(OTf)_2$ (1 equiv., 60 min), (2) potassium pyrazolate (3.1 equiv., 20 min), (3) PhIO (1 equiv., 90 min), and (4) $Mn(OTf)_2 \bullet 2$ MeCN (1.3 equiv., 18 hr); (ii) $CoCp_2$ (1 equiv.), THF, 60 min; (iii) Na/Hg (2.6 equiv. Na), THF, 4 hr; (iv) AgOTf (1 equiv.), THF, 30 min; (v) $Ag[BAr^{F}{}_4] \bullet 2$ MeCN (2 equiv.), Et_2O, 15 min; (vi) $[^{Ac}Fc][BAr^{F}{}_4]$ (1 equiv.), THF, 10 min; (vii) $Ag[BAr^{F}{}_4] \bullet 2$ MeCN (1 equiv.), Et_2O, 15 min.

---

each Fe center of the tri-nuclear core to the apical Mn.[18] In the case of the previously reported clusters, the apical metal typically adopts a four-coordinate, trigonal pyramidal geometry since the sterics of the substituted pyrazolate ligands disfavor binding of one of the triflate counterions to the apical metal. Here, the apical Mn is ligated by one triflate counterion with

a trigonal bipyramidal geometry, indicative of the increased steric accessibility of the apical metal with the unsubstituted pyrazolates.

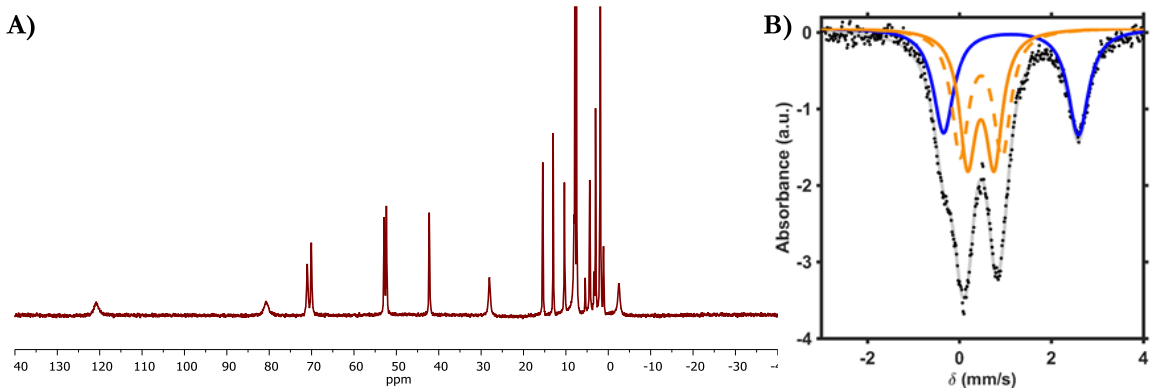

Figure 2. (A) ^{1}H NMR (300 MHz) of **2-[OTf]** in CD_3CN. (B) Zero applied field ^{57}Fe Mössbauer spectrum of **2-[OTf]** (black dots) fit with three equal quadrupole doublets (gray line) with parameters: (i) $\delta = 1.12$ mm/s, $|\Delta E_q| = 2.93$ mm/s (blue trace), (ii) $\delta = 0.47$ mm/s, $|\Delta E_q| = 0.58$ mm/s (solid orange trace), and (iii) $\delta = 0.42$ mm/s, $|\Delta E_q| = 0.91$ mm/s (dashed orange trace).

Cyclic voltammetry (CV) data of **2-[OTf]** in MeCN show a quasi-reversible oxidation at -0.11 V, a quasi-reversible reduction wave at -0.84 V, and an irreversible reductive process below -1.50 V (Figure 3; all potentials vs Fc/Fc^{+}). The one electron reduced (**1-[OTf]**), and one electron oxidized (**3-[OTf]**) clusters were prepared via chemical reduction/oxidation of **2-[OTf]** with cobaltocene ($CoCp_2$) and silver trifluoromethanesulfonate (AgOTf), respectively. The X-ray crystal structures of these three compounds all have identical coordination modes for the metal centers (Figure 1A). Bond distances between the metals and the μ_4-oxo are consistent with the redox processes taking place at the Fe centers, with the apical Mn maintaining a +2 oxidation state across the series **1-[OTf]** – **3-[OTf]** (Table 1). Mössbauer data corroborate these oxidation state assignments, and are similar to our previously characterized clusters.[18a-e]

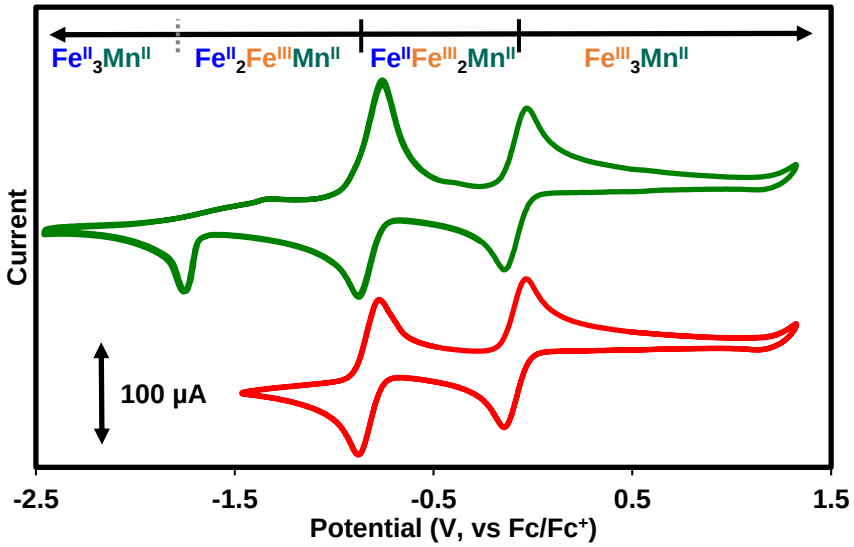

Figure 3. Cyclic voltammogram (green trace) of **2-[OTf]** (2.8 mM) in MeCN and 100 mM $[Bu_4N][PF_6]$ at a scan rate of 200 mV/s with glassy carbon, Pt-wire, and Ag-wire as working, counter, and reference electrode, respectively. The open circuit potential was -0.5 V. (Red trace) Partial CV of **2-[OTf]** of the quasi-reversible electrochemical features.

Table 1. Selected Bond Distances, ^{57}Fe Mössbauer Parameters, and Oxidation State Assignments for Structurally Characterized Compounds

Metal Center	M–μ_4-O1; (*Mn1–O2*) distance (Å)	δ (mm/s)	$\lvert\Delta E_q\rvert$ (mm/s)	Assignment
		1-[OTf]		
Fe1	1.912(2)	0.56	1.32	*h.s.* Fe^{III}
Fe2, Fe3	2.054(2), 2.112(2)	1.14, 1.13	3.51, 3.02	*h.s.* Fe^{II}
Mn1	1.997(2); (*2.249(2)*)			Mn^{II}
		2-[OTf]		
Fe1, Fe2	1.951(2), 1.966(2)	0.47, 0.42	0.58, 0.91	*h.s.* Fe^{III}
Fe3	2.097(2)	1.12	2.93	*h.s.* Fe^{II}
Mn1	2.053(2); (*2.167(3)*)			Mn^{II}
		2-[OTf] (H_2O)		
Fe1, Fe2	1.923(5), 1.984(5)			*h.s.* Fe^{III}
Fe3	2.092(5)			*h.s.* Fe^{II}
Mn1	2.064(5); (*2.163(6)*)			Mn^{II}
		3-[OTf]		
Fe1, Fe2, Fe3	1.980(4), 1.982(4), 1.989(4)	0.44	0.80	*h.s.* Fe^{III}
Mn1	2.107(4); (*2.162(5)*)			Mn^{II}
		6-[OTf]		
Fe1	2.003(7)	0.53	0.76	*h.s.* Fe^{III}
Fe2, Fe3	2.126(7), 2.051(7)	1.09, 1.08	3.09, 2.58	*h.s.* Fe^{II}
Mn1	1.838(8); (*1.843(9)*)			Mn^{III}

Preparation of Mn–OH_2 and Mn–OH Clusters. Binding of water to these clusters was investigated; however, the coordination of triflate to the apical Mn complicates direct access to the Mn–OH_2 moiety for all oxidation states of the cluster. The triflate ligand in **2-[OTf]** is sufficiently labile to allow for isolation of the Mn–OH_2 cluster as single crystals by slow diffusion of Et_2O into a MeCN/5% H_2O solution of the cluster, and its structure was confirmed via X-ray crystallography (**2-[OTf] (H_2O)**; Figure 4B). Attempts to obtain crystals of the analogous reduced Mn-OH_2 cluster (**1-[OTf] (H_2O)**) were unsuccessful; we postulate that the difficulty lies in poor crystallinity of the complex, as opposed to an inability to

coordinate H_2O over triflate. Crystallization attempts of **3-[OTf]** in MeCN/5% H_2O solutions produced crystals of triflate coordinated clusters, demonstrating the complication of preparing Mn–OH_2 clusters across these oxidation states with the triflate counterions. The structure of **2-[OTf] (H_2O)** displays H_2O coordinated to the apical Mn, with a long Mn–O distance of 2.163(6) Å, consistent with a Mn^{II}–OH_2 assignment;[13e, 21] furthermore, both triflate counterions are hydrogen bonding to each proton of the Mn–OH_2 moiety through one of the sulfonate oxygen atoms (O_{aquo}–O_{OTf} distances of 2.787 and 2.695 Å).

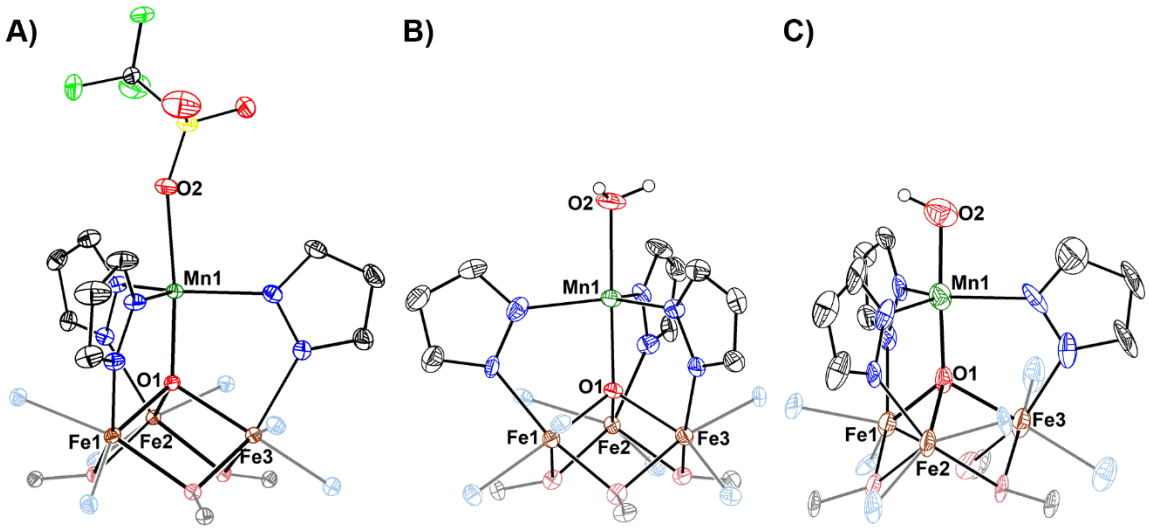

Figure 4. Truncated crystal structures of (A) **1-[OTf]**, (B) **2-[OTf] (H_2O)**, and (C) **6-[OTf]**. Ellipsoids are shown at the 50% probability level with solvent molecules, outersphere counterions, and hydrogen atoms (except for hydrogen atoms on O2) are omitted for clarity.

To ensure that H_2O remained coordinated to the cluster in solution, experiments were performed in THF, a less coordinating solvent than MeCN, and triflate counterions were replaced with the non-coordinating tetrakis[3,5-bis(trifluoromethyl)phenyl]borate ([$BAr^F{}_4$]) anion. This was accomplished by reducing the dicationic cluster, **2-[OTf]**, with Na/Hg amalgam in THF to obtain the neutral all M^{II} cluster, **4**, as a blue solid (Figure 1C). Similar to the related neutral phenyl pyrazolate clusters,[18a] **4** is either insoluble or unstable in most organic

solvents, so its chemistry towards H_2O was not pursued. Oxidation of **4** with 1 and 2 equiv of $Ag[BAr^F_4]$ • 2 MeCN affords **1-[BAr$^F_4$]** and **2-[BAr$^F_4$]**, respectively (Figure 1C). The $[Fe^{III}_3Mn^{II}]$ cluster, **3-[BAr$^F_4$]**, was prepared by oxidation of **2-[BAr$^F_4$]** with acetyl-ferrocenium ($[^{Ac}Fc][BAr^F_4]$). All these clusters are highly soluble in THF and bind H_2O under conditions where it is present in ~100 molar equivalents (Figures 5 - 7). Significant decomposition is observed when H_2O concentrations above ~1000 equivalents were used; therefore, all the studies described herein were performed on ca. 2 mM of a cluster with $^-[BAr^F_4]$ counterions in THF solution with 250 mM H_2O, as these conditions displayed ^{1}H NMR spectra consistent with complete or near complete binding of H_2O to the apical Mn.

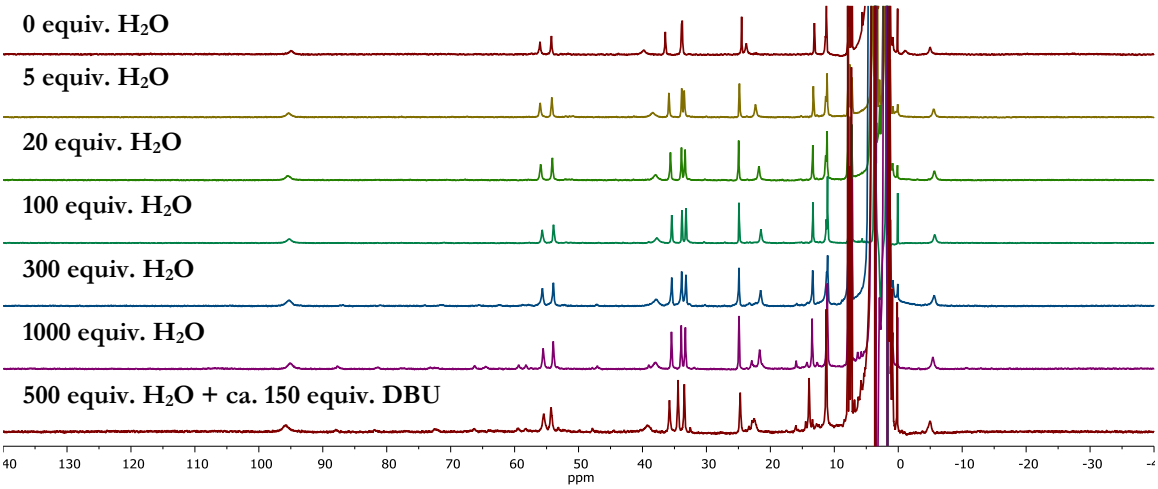

Figure 5. ^{1}H NMR spectra (500 MHz) of 2mM $[LFe_3O(Pz)_3Mn][BAr^F_4]$ (**1-[BAr$^F_4$]**) in THF/C_6D_6 with various equivalents of H_2O. Splitting of the peak at ~35 ppm was used to judge the amount of H_2O coordination, which appeared complete at > 20 equivalents H_2O. Addition of excess 1,8-diazabicyclo(5.4.0)undec-7-ene (DBU) leads to no significant change in the ^{1}H NMR spectrum.

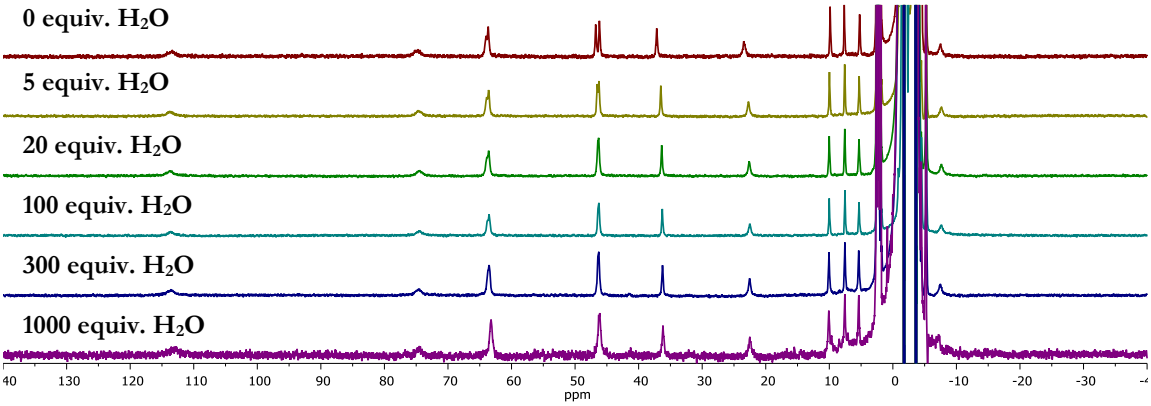

Figure 6. ^{1}H NMR spectra (500 MHz) of 2mM $[LFe_3O(Pz)_3Mn][BAr^F{}_4]_2$ (**2-[BAr$^F{}_4$]**) in THF/C_6D_6 with various equivalents of H_2O. Coalescence of the two peaks at ~45 ppm was used to judge the amount of H_2O coordination, which appeared complete at > 20 equivalents H_2O.

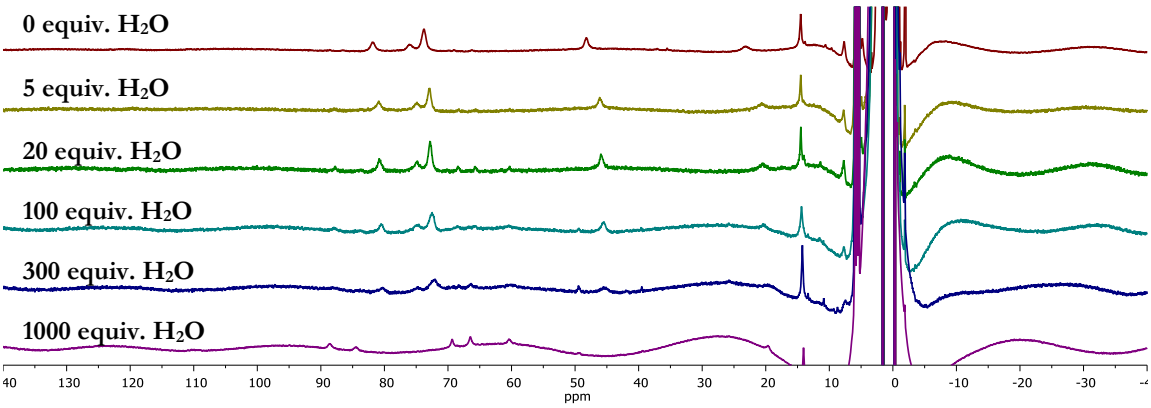

Figure 7. ^{1}H NMR spectra (500 MHz) of $[LFe_3O(Pz)_3Mn][BAr^F{}_4]_3$ (**3-[BAr$^F{}_4$]**) in THF/C_6D_6 with various equivalents of H_2O. The upfield shift of the peak at ~50 ppm was used to judge the amount of H_2O coordination, which appeared complete at > 20 equivalents H_2O.

Deprotonation of the Mn–OH_2 moiety in the $[Fe^{III}{}_2Fe^{II}Mn^{II}]$ cluster, **2-[BAr$^F{}_4$]**, was accomplished by addition of 1 equivalent of a relatively strong organic base, 1,8-diazabicyclo(5.4.0)undec-7-ene (DBU; pK_a(THF) = 19.1)[22], or by stirring a THF solution of **2-[BAr$^F{}_4$]** over solid KOH for 30 minutes. Both reactions lead to the same species based on the

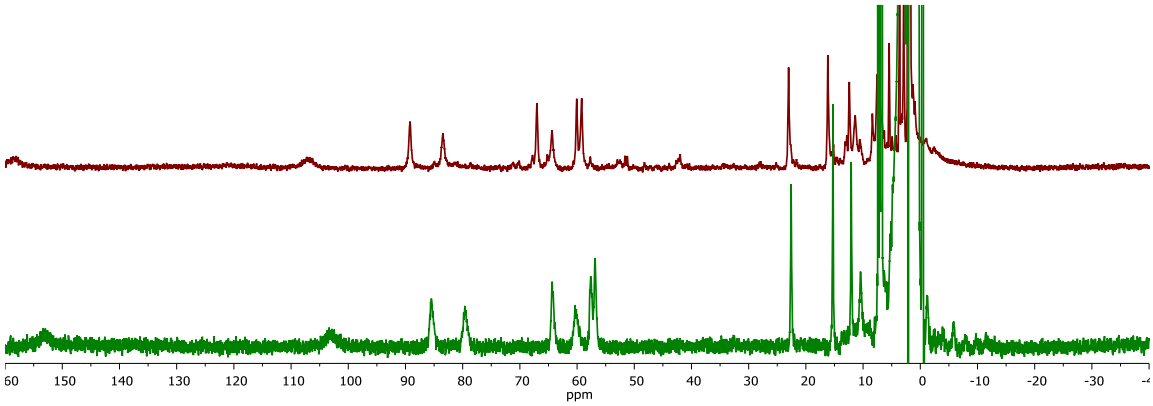

Figure 8. ^{1}H NMR spectrum (300 MHz) of [$LFe_3O(Pz)_3Mn(OH)$][OTf] (**6-[OTf]**; top) and [$LFe_3O(Pz)_3Mn(OH)$][BAr^F_4] (**6-[BAr^F_4]**; bottom) in CD_3CN.

---

^{1}H NMR and UV-Vis absorbance features, assigned to the Mn–OH cluster, **6-[BAr^F_4]**. Structural confirmation of this species was obtained by performing analogous reactions on **2-[OTf]** to prepare the triflate salt, **6-[OTf]**, which displays the same ^{1}H NMR features (Figure 8). This species could be crystallized from MeCN solution by slow diffusion of Et_2O, and was characterized via X-ray diffraction (Figure 4C). The structure of **6-[OTf]** is similar to **2-[OTf] (H_2O)**, displaying Mn binding to the hydroxide ligand with a trigonal bipyramidal geometry. Notably, the Mn–O distance to the hydroxide ligand is contracted by approximately 0.3 Å relative to **2-[OTf] (H_2O)** (1.843(9) vs 2.163(6) Å). Furthermore, the distance of the apical Mn to the interstitial μ_4-O in the cluster is also shortened significantly (1.838(8) vs 2.064(5) Å in **2-[OTf] (H_2O)**; Table 1); both of these observations are consistent with a Mn^{III}–OH assignment.[23] The Mn–OH and Mn–μ_4-O distances of ~1.8 Å are similar to the bond metrics observed in our previously reported hydroxide-bound tetramanganese cluster in the [$Mn^{III}_2Mn^{II}_2$] oxidation state.[19] There, the Mn–OH bond is slightly longer (1.872(2) Å) due to hydrogen bonding to the pendant *tert*-butyl-phenyl-aminopyrazolate ligands. The structural data for **6-[OTf]** are consistent to an oxidation state assignment of [$Fe^{II}_2Fe^{III}Mn^{III}$] for the

cluster; corroborated by the Mössbauer spectrum of **6-[BAr$^{F}_{4}$]** (Figure 9B). Deprotonation of the Mn^{II}–OH_2 in **2** to form **6** leads to rearrangement of the redox states of the metals in the cluster to produce a Mn^{III}–OH site. Similar 'valence tautomerizations' have been observed in Mn^{V}(O)-corrole systems, where protonation or binding a Lewis acid to the oxo moiety leads to reversible formation of a Mn^{IV}(O–X)-(corrole-radical cation) complexes.[24]

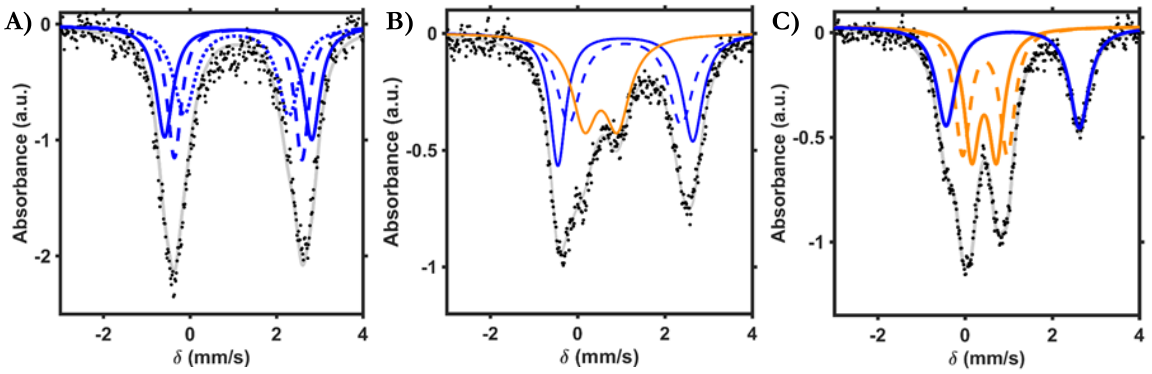

Figure 9. (A) Mössbauer spectrum of **5** (black dots) fit with three equal doublets (gray trace) with parameters: (i) δ = 1.12 mm/s; ΔE_q = 3.40 mm/s (solid blue trace), (ii) δ = 1.12 mm/s; ΔE_q = 2.95 mm/s (dashed blue trace), and (iii) δ = 1.08 mm/s; ΔE_q = 2.42 mm/s (dotted blue trace). (B) Mössbauer spectrum of **6-[BAr$^{F}_{4}$]** (THF solution [250 mM H_2O]; black dots) fit with three equal doublets (gray trace) with parameters: (i) δ = 1.09 mm/s; ΔE_q = 3.09 mm/s (solid blue trace), (ii) δ = 1.08 mm/s; ΔE_q = 2.58 mm/s (dashed blue trace), and (iii) δ = 0.53 mm/s; ΔE_q = 0.76 mm/s (solid orange trace). (C) Mössbauer spectrum of **7-[BAr$^{F}_{4}$]** (THF solution [250 mM H_2O]; black dots) fit with three equal doublets (gray trace) with parameters: (i) δ = 1.10 mm/s; ΔE_q = 3.03 mm/s (solid blue trace), and (ii) δ = 0.43 mm/s; ΔE_q = 0.55 mm/s (solid orange trace), (iii) δ = 0.46 mm/s; ΔE_q = 1.02 mm/s (dashed orange trace).

Electrochemistry. The electrochemistry of the [$Fe_3OMn–OH_2$] and [$Fe_3OMn–OH$] clusters was investigated by cyclic voltammetry of **2-[BAr^F_4]** and **6-[BAr^F_4]**. Two quasi-reversible redox events were observed in **2-[BAr^F_4]**: an oxidation at -0.02 V and a reduction at -0.90 V (all potentials vs Fc/Fc^+; Figure 10, red trace). These redox events were assigned to the $[Fe^{III}_2Fe^{II}Mn^{II}]\rightarrow[Fe^{III}_3Mn^{II}]$ and $[Fe^{III}Fe^{II}_2Mn^{II}]\rightarrow[Fe^{III}_2Fe^{II}Mn^{II}]$ couples. Mössbauer spectra collected on **1-[BAr^F_4]** – **3-[BAr^F_4]** in THF with 250 mM H_2O show that both oxidation state changes occur at the Fe centers (Figure 11), leading to the conclusion that the apical Mn remains divalent when bound to H_2O across all the oxidation states observed in the CV experiment, and only the distal Fe centers change oxidation states. The hydroxide-bound cluster, **6-[BAr^F_4]**, displays two oxidations: a quasi-reversible couple at -0.49 V ($[Fe^{III}Fe^{II}_2Mn^{III}]\rightarrow[Fe^{III}_2Fe^{II}Mn^{III}]$), and an irreversible event at +0.26 V ($[Fe^{III}_2Fe^{II}Mn^{III}]\rightarrow[Fe^{III}_3Mn^{III}]$). A quasi-reversible reduction for the $[Fe^{III}Fe^{II}_2Mn^{III}]\rightarrow[Fe^{II}_3Mn^{III}]$ couple is also observed at -1.34 V. The Mössbauer spectra of **5** - **7-[BAr^F_4]** (Figure 9) are again consistent with redox changes occurring exclusively at Fe. Notably, no catalytic oxidation wave is observed at high potentials for **6-[BAr^F_4]**, in contrast to our previously reported tetramanganese cluster bridged with *tert*-butyl-phenylaminopyrazolates.[19] Reasons for this difference may be the ~100 mV negative shift in reduction potentials for the [$Fe_3Mn–OH$] clusters, along with the lower concentration of H_2O. The lack of electrocatalytic oxidation by **6-[BAr^F_4]** could also suggest the importance of pendant basic groups near the Mn^{III}–OH moiety for water oxidation catalysis.

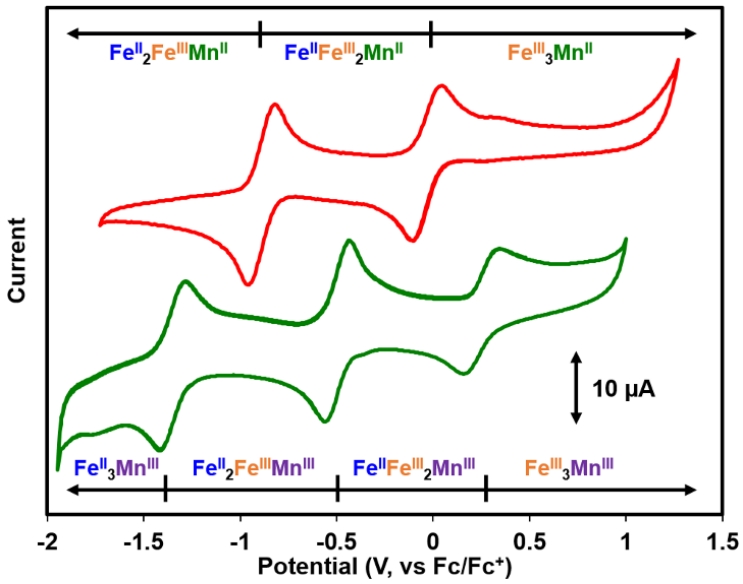

Figure 10. Cyclic voltammograms of **2-[BAr$^F_4$]** (red trace) and **6-[BAr$^F_4$]** (green trace); 2 mM compound in THF with 250 mM H_2O and 100 mM [^{n}Pr$_4$N][BAr$^F_4$] at a scan rate of 50 mV/s with glassy carbon, Pt-wire, and Ag-wire as working, counter, and reference electrodes, respectively. The open circuit potentials were -0.2 V for **2-[BAr$^F_4$]** and -1.0 V for **6-[BAr$^F_4$]**.

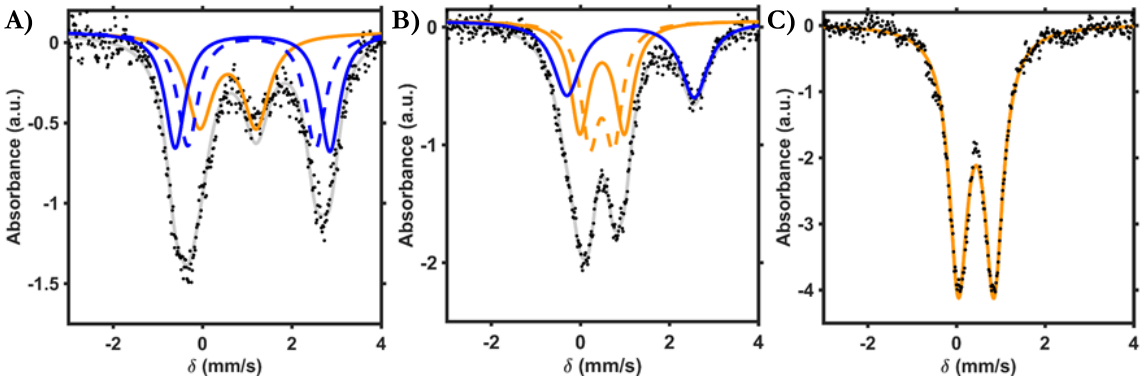

Figure 11. (A) Mössbauer spectrum of **1-[BAr$^F_4$]** (THF solution [250 mM H_2O]; black dots) fit with three equal doublets (gray trace) with parameters: (i) δ = 1.12 mm/s; ΔE_q = 3.46 mm/s (solid blue trace), (ii) δ = 1.10 mm/s; ΔE_q = 2.86 mm/s (dashed blue trace), and (iii) δ = 0.57 mm/s; ΔE_q = 1.27 mm/s (solid orange trace). (B) Mössbauer spectrum of **2-[BAr$^F_4$]** (THF solution [250 mM H_2O]; black dots) fit with three equal doublets (gray trace) with parameters:

(i) δ = 1.13 mm/s; ΔE_q = 2.86 mm/s (solid blue trace), (ii) δ = 0.49 mm/s; ΔE_q = 1.00 mm/s (solid orange trace), and (iii) δ = 0.48 mm/s; ΔE_q = 0.546 mm/s (dashed orange trace). (C) Mössbauer spectrum of **3-[BAr$^F_4$]** (THF solution [250 mM H_2O]; black dots) fit with a single quadrupole doublet (orange trace) with parameters: δ = 0.44 mm/s and ΔE_q = 0.80 mm/s

---

Determination of pK_a of H_2O Ligand in [Fe_3Mn^{II}–OH_2] Clusters. The pK_a of the aquo-ligand bound to 2-[BAr$^F_4$] was measured by mixing this cluster with various concentrations of 1,1,3,3-tetramethyl-2-phenylguanidine (PhTMG; pK_a(THF) = 16.5).[22] The ratio of **2-[BAr$^F_4$]** and **6-[BAr$^F_4$]** was examined by UV-Vis absorbance spectroscopy as a function of PhTMG concentration, and a pK_a value of 17.5 for **2-[BAr$^F_4$]** was obtained (Figure 12). Analogous experiments were attempted on the oxidized aquo-cluster, **3-[BAr$^F_4$]**; however, the changes in UV-Vis spectral features upon deprotonation are minor. The pK_a of **3-[BAr$^F_4$]** could be obtained by examining its ^{1}H NMR resonances in the presence of a suitable exogenous base, 2,6-Me_2-pyridine (Figure 13; pK_a(THF) = 9.5).[22] As expected, the acidity of the [Fe_3Mn–OH_2] cluster increases upon oxidation; a pK_a value of 9.2 was obtained for **3-[BAr$^F_4$].** While a titration on the reduced [$Fe^{III}Fe^{II}_2Mn^{II}$] cluster, **1-[BAr$^F_4$]**, was not conducted, we determined that its pK_a is significantly higher than the other clusters investigated, since it does not react with excess DBU (Figure 5; pK_a(THF) = 19.1).[22]

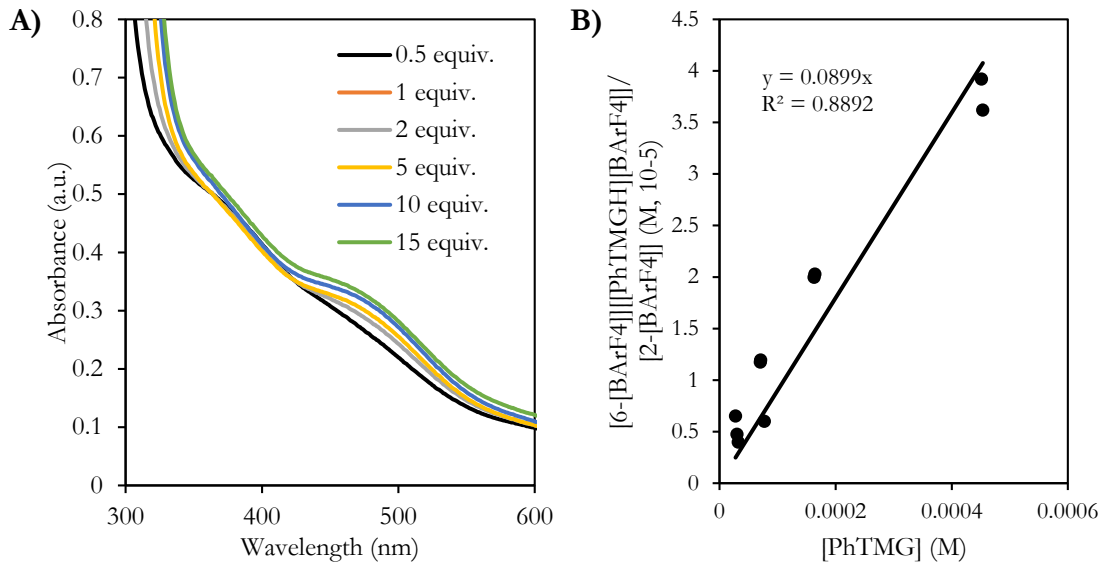

Figure 12. (A) UV-Vis absorbance spectra of $[LFe_3O(Pz)_3Mn][BAr^F{}_4]_2$ (**2-[BAr$^F{}_4$]**; 1 cm cuvette; 100μM) in THF [250 mM H_2O] after addition of various equivalents of 1,1,3,3-tetramethyl-2-phenylguanidine (PhTMG; pK_a(THF) = 16.5).[22] (B) Titration plot for deprotonation of $[LFe_3O(Pz)_3Mn][BAr^F{}_4]_2$ (**2-[BAr$^F{}_4$]**) to $[LFe_3O(Pz)_3Mn(OH)][BAr^F{}_4]$ (**6-[BAr$^F{}_4$]**) based on multiple titrations; the slope of the line represents an equilibrium constant value of $K = 0.09$, where:

$$K = \frac{[\mathbf{6}\text{–}[\mathbf{BAr^F_4}]][(\text{PhTMGH})([BAr^F_4])]}{[\mathbf{2}\text{–}[\mathbf{BAr^F_4}]][\text{PhTMG}]}$$

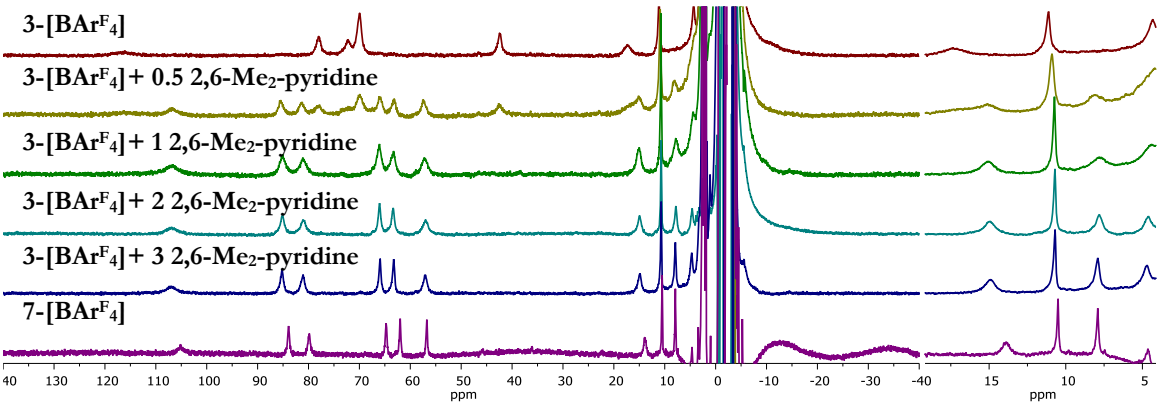

Figure 13. ^{1}H NMR spectrum (500 MHz) of $[LFe_3O(Pz)_3Mn][BAr^F{}_4]_3$ (**3-[BAr$^F{}_4$]**) with various equivalents of 2,6-dimethyl-pyridine in THF/C_6D_6 [250 mM H_2O].

Table 2. pK_a titration of 3-[BAr$^F{}_4$] via ^{1}H NMR spectroscopy with 2,6-dimethyl-pyridine.

^{1}H NMR	δ[a] (ppm)	$X_{\mathbf{3\text{-}[BArF4]}}$[b]	K[c]
3-[BAr$^F{}_4$]	11.12	-	
3-[BAr$^F{}_4$] + 0.5 2,6-Me$_2$-Py	10.90	0.632	1.625
3-[BAr$^F{}_4$] + 1 2,6-Me$_2$-Py	10.72	0.343	3.661
3-[BAr$^F{}_4$] + 2 2,6-Me$_2$-Py	10.70	0.319	1.100
3-[BAr$^F{}_4$] + 3 2,6-Me$_2$-Py	10.69	0.296	0.730
7-[BAr$^F{}_4$]	10.51	-	
		Average K	1.779 (±0.654)

[a]A sharp resonance ~ 11 ppm was selected to measure the mole fraction of **3-[BAr$^F{}_4$]** ($X_{\mathbf{3\text{-}[BArF4]}}$), as **3-[BAr$^F{}_4$]** and **7-[BAr$^F{}_4$]** undergo fast exchange on the NMR time-scale. [b] The concentrations of **3-[BAr$^F{}_4$]**, 2,6-Me$_2$-Py, and [2,6-Me$_2$-PyH][BAr$^F{}_4$] were determined from $X_{\mathbf{3\text{-}[BArF4]}}$ via mass balance. [c]According to the equation below:

$$K = \frac{[\mathbf{7}\text{–}[\mathbf{BAr}_4^F]][(2,6\text{–}\mathrm{Me_2}\text{–}\mathrm{PyH})([\mathrm{BAr}_4^F])]}{[\mathbf{3}\text{–}[\mathbf{BAr}_4^F]][2,6\text{–}\mathrm{Me_2}\text{–}\mathrm{Py}]}$$

BDE$_{O–H}$ and PCET Reactivity of the Different Redox States. The homolytic bond dissociation enthalpy of the aquo O–H (BDE$_{O–H}$) were determined for the three cluster oxidation states observed (**1-[BAr$^F{}_4$]** – **3**-**[BAr$^F{}_4$]**) by analyzing the pK_a and reduction potentials of the aquo- and hydroxide-bound clusters (Figure 14). This calculation combines the energies of the discrete proton and electron transfers involved, along with the energy of formation of the hydrogen atom in THF (C; 66 kcal/mol[25]):[26]

$$\mathrm{BDE_{O–H}}\ (\mathrm{kcal/mol}) = 1.37\ \mathrm{p}K_a + 23.06\ E° + C \qquad (1)$$

Therefore, summing the energy of the oxidation of **1-[BAr$^F{}_4$]** (-0.90 V; -20.6 kcal/mol) and the energy of deprotonation of **2-[BAr$^F{}_4$]** (17.5; 24.0 kcal/mol) with C establishes an energy of 69 kcal/mol for the formal H-atom transfer from **1-[BAr$^F{}_4$]** to **6-[BAr$^F{}_4$]**. Likewise, the oxidation of **2-[BAr$^F{}_4$]** (-0.02 V; -0.5 kcal/mol) followed by the deprotonation of **3-[BAr$^F{}_4$]** (9.2; 12.6 kcal/mol) leads to a BDE$_{O–H}$ of 78 kcal/mol for the aquo-ligand of **2-[BAr$^F{}_4$]** (formal HAT to form **7-[BAr$^F{}_4$]**). An alternate way to determine the BDE$_{O–H}$ of **2-[BAr$^F{}_4$]** is from the pK_a of **2-[BAr$^F{}_4$]** and the reduction potential of **6-[BAr$^F{}_4$]**, leading to a similar bond enthalpy of 78.7 kcal/mol. The same square scheme analysis can be done to obtain a BDE$_{O-H}$

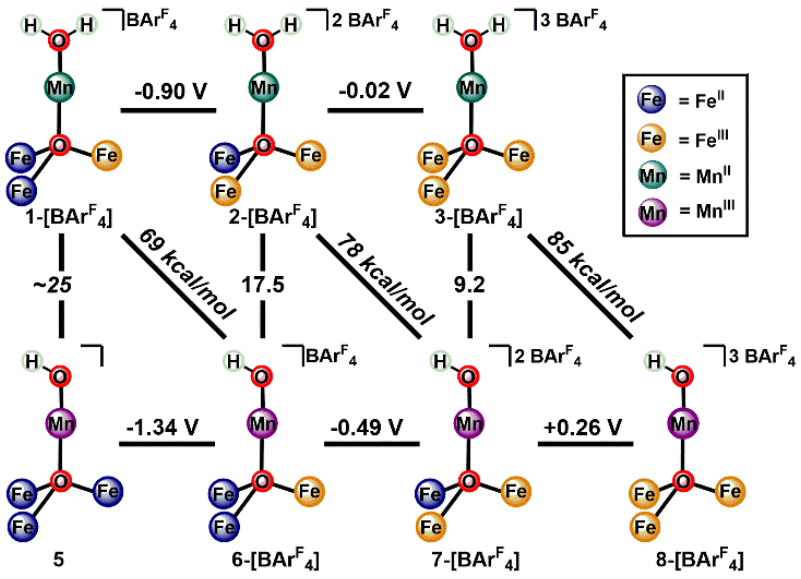

Figure 14. Thermodynamic cycles to evaluate the BDE_{O-H} of Mn–OH_2 clusters **1-[BAr^F_4]** - **3-[BAr^F_4]**. Reduction potentials (horizontal lines) are referenced to Fc/Fc^+. pK_a values (vertical lines) are based on relative pK_a values of acids in THF. Diagonal lines are the BDE_{O-H} values calculated from the reduction potential and pK_a according to the Bordwell equation (equation 1). Approximate values (~) are extrapolated from the Bordwell equation.

---

of 85 kcal/mol for **3-[BAr^F_4]**. With these measured values, the pK_a of **1-[BAr^F_4]** could be estimated; a BDE_{O-H} of 69 kcal/mol for **1-[BAr^F_4]** means the enthalpy of deprotonation for this cluster is expected to be ~34 kcal/mol (pK_a = 24.9), by combining this energy with the oxidation of **5** (-1.34 V; -30.9 kcal/mol).

The BDE_{O-H} values of these clusters were evaluated by investigating their proton-coupled electron transfer (PCET) reactivity towards different organic radicals. The PCET reagents employed were (2,2,6,6,-tetramethylpiperidin-1yl)oxyl (TEMPO; BDE_{O-H} = 70 kcal/mol) and 2,4,6-tri-*tert*-butylphenoxy radical (2,4,6-TBPR; BDE_{O-H} = 82 kcal/mol).[26c] Formal hydrogen atom transfer from **1-[BAr^F_4]** to form **6-[BAr^F_4]** could be accomplished using either one equivalent of TEMPO or 2,4,6-TBPR, consistent with a BDE_{O-H} less than 70 kcal/mol

(Scheme 2). **2-[BAr$^F_4$]** reacts with 1 equivalent 2,4,6-TBPR to form **7-[BAr$^F_4$]**, but no reaction is observed between this cluster and TEMPO, indicative of a BDE_{O-H} that is between 70 and 82 kcal/mol. **3-[BAr$^F_4$]** does not react with either PCET reagent, which supports the assignment of a BDE_{O-H} greater than 82 kcal/mol).

Scheme 2. Proton Coupled Electron Transfer (PCET) Reactions of Mn–OH_2 clusters, 1-[BAr$^F_4$] - 3-[BAr$^F_4$].

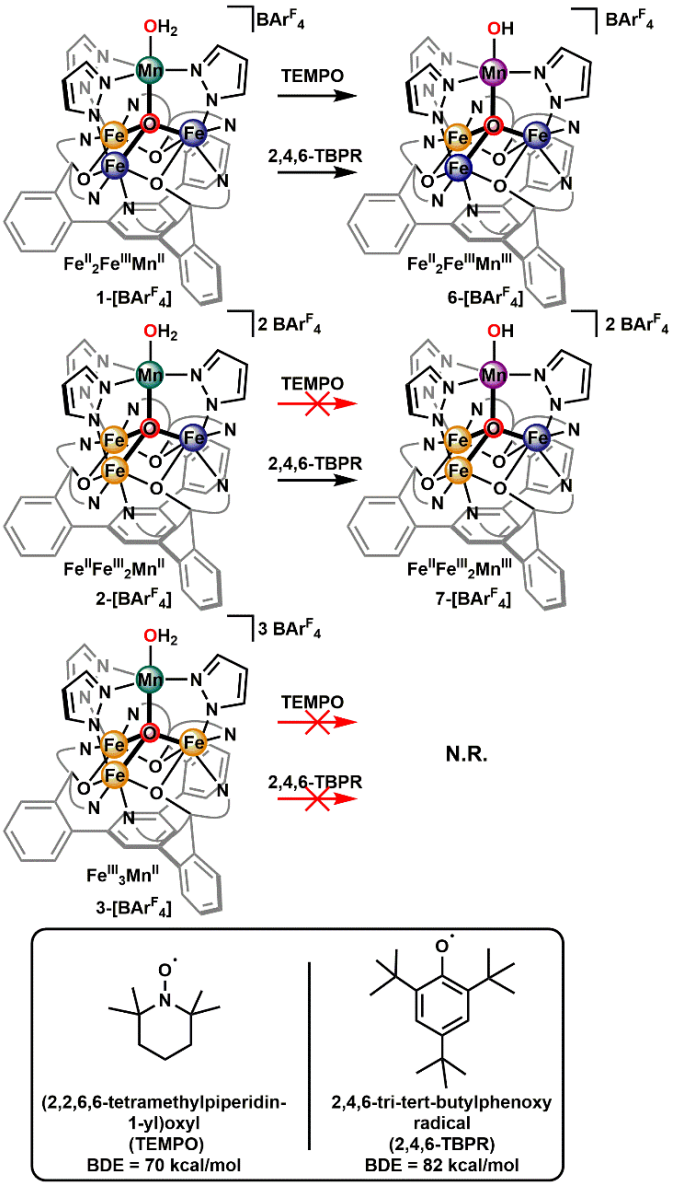

Potential–pK_a Diagram of [$Fe_3Mn–OH_x$] Clusters. Further insight into the basis of PCET reactivity of these clusters was obtained by investigating the effect of external bases on the reduction potentials of the aquo- and hydroxide-bound clusters. Typically, this type of analysis is conducted under aqueous conditions, where the reduction potentials can be measured as a function of solution pH; data are presented as a potential–pH plot, known as a Pourbaix diagram.[27] Aqueous Pourbaix diagrams have been helpful in understanding the speciation of a number of molecular Ru/Mn water oxidation catalysts and related complexes.[15b, 28] Recently, Pourbaix theory has been applied to nonaqueous solvents, where the reduction potential of PCET will depend on the pK_a of an external acid/base (and the concentration of this acid/base relative to its conjugate base/acid at Nernstian equilibrium).[29] For the system reported here, a potential– pK_a plot was constructed as a means of providing experimental support for the aquo-ligand pK_a and $BDE_{O–H}$ values of **1-[BAr^F_4]** - **3-[BAr^F_4]** and to gain information about the thermochemistry of PCET with the Mn–OH clusters to form a terminal Mn-oxo moiety.

Measuring the CV of **2-[BAr^F_4]** with one equivalent of various organic bases, with pK_a values of their conjugate acids in THF ranging from 7.5 to 28.1, produced the potential–pK_a plot depicted in Figure 15 (blue points; see Electrochemical Details section for individual CVs). For relatively weak bases (pK_a < 10), the reduction potentials of **2-[BAr^F_4]** do not significantly deviate from their potentials in the absence of any base. As the strength of the base increases, the reduction potential for the oxidation of **2-[BAr^F_4]** is lowered as a function of the conjugate acid pK_a, consistent with PCET occurring between the pK_a range 10-17. The data points in this pK_a range follow the diagonal line calculated for the **2-[BAr^F_4]→7-[BAr^F_4]** PCET process, based on the reduction potentials of **2-[BAr^F_4]** and **6-[BAr^F_4]** and the pK_a values of **2-[BAr^F_4]** and **3-[BAr^F_4]**. Observing the predicted linear decrease in reduction

potential for **3-[BAr$^{F}_{4}$]** in the pK_a range 10 - 17 supports the pK_a values reported for **2-[BAr$^{F}_{4}$]** and **3-[BAr$^{F}_{4}$]** in Figure 14. Similar support is given to the pK_a of **1-[BAr$^{F}_{4}$]** (24.9) when using strong bases (pK_a > 17.5). Evidence for the **1-[BAr$^{F}_{4}$]→6-[BAr$^{F}_{4}$]** PCET process was observed under these conditions, again with the data roughly matching the diagonal line with an intercept at -1.34 V and a pK_a of 24.9. Furthermore, when a base was employed with a pK_a > 24.9, the reduction potentials observed were nearly identical to the potentials reported for **6-[BAr$^{F}_{4}$]** in the absence of any acid or base.

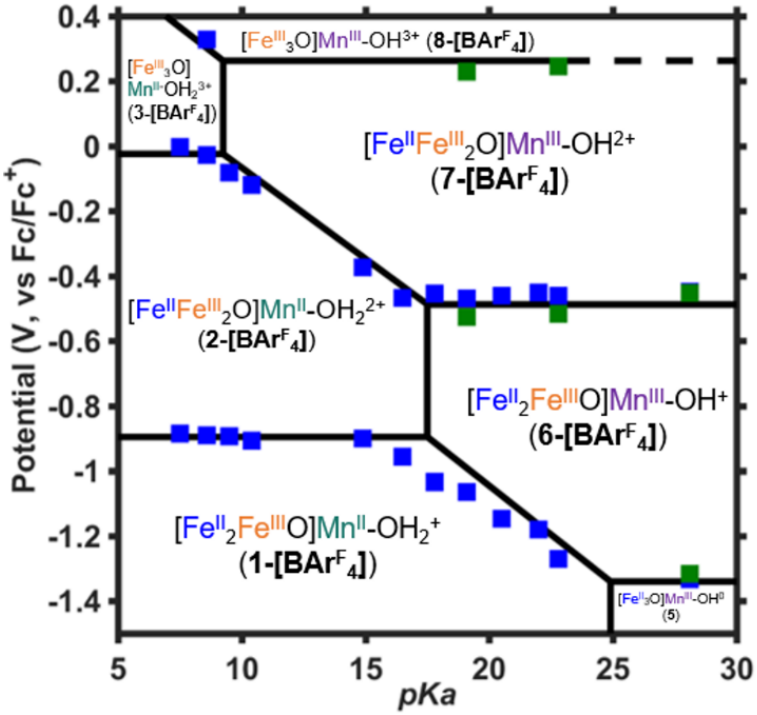

Figure 15. Potential–pK_a diagram of **2-[BAr$^{F}_{4}$]** (blue squares) and **6-[BAr$^{F}_{4}$]** (green squares). Data points are the observed reduction potentials of the compounds (y-axis) in the presence of one equivalent base with various pK_a values in THF (x-axis). The horizontal lines correspond to the measured reduction potentials of **2-[BAr$^{F}_{4}$]** and **6-[BAr$^{F}_{4}$]** in the absence of any external base. Vertical lines correspond to the pK_a values of Mn–OH$_2$ clusters **1-[BAr$^{F}_{4}$]** - **3-[BAr$^{F}_{4}$]**. The horizontal line for the **7-[BAr$^{F}_{4}$]→8-[BAr$^{F}_{4}$]** redox couple is dashed at high pK_a values due to the possibility of PCET from the Mn–OH with a strong enough base.

As expected, deviations of the data from the calculated diagonal line occur as the base pK_a approaches the pK_a of the cluster (see **2-[BAr$^F_4$]→7-[BAr$^F_4$]** around pK_a of 10, for example), based on predicted potential–pK_a relationships for ET-PT or PT-ET reaction mechanisms.[29] Further deviations from the predicted solid lines in Figure 15 could be due to incompatibility of the chosen base with this system (too coordinating, electrochemically unstable, etc.). Ultimately, inconsistencies between the potential–pK_a data of **2-[BAr$^F_4$]** and the BDE$_{O–H}$ values reported in Figure 14 only amount to a difference of ~3 kcal/mol, which is a reasonable uncertainty for these bond energydeterminations.[26c] Based on the PCET reactivity of these complexes towards TEMPO and TBPR (vide supra), it is unlikely that these BDE$_{O–H}$ values could deviate more than a few kcal/mol.

Potential–pK_a data were also obtained for **6-[BAr$^F_4$]** in the presence of relatively strong organic bases in attempts to observe a PCET process accessing Mn=O clusters, since this technique has been previously useful for gaining insight into the proton and electron transfer thermodynamics for unstable species.[29] Based on the potential–pK_a plot constructed in Figure 15, PCET to form a Mn-oxo cluster could be possible at high potentials with a strong base (top right area of the diagram). The CV of **6-[BAr$^F_4$]** with one equivalent *tert*-butylimino-tri(pyrrolidino)phosphorene (*t*-BuP$_1$(pyrr); pK_a(THF) = 22.8)[22] shows no shift in the Mn–OH cluster reduction potentials. Similarly, no change is observed with the **5→6-[BAr$^F_4$]** and **6-[BAr$^F_4$]→7-[BAr$^F_4$]** reduction potentials with 1-ethyl-2,2,4,4,4-pentakis(dimethylamino)2-λ^5,4λ^5-catenadi(phosphazene) (EtP$_2$(dma); pK_a(THF) = 28.1).[22, 30] These experimental observations provide a lower limit to the pK_a values of **8-[BAr$^F_4$]** and **7-[BAr$^F_4$]**, respectively. With these values, the BDE$_{O–H}$ of **7-[BAr$^F_4$]** and **8-[BAr$^F_4$]** are predicted to be greater than 93 and 103 kcal/mol, respectively (Figure 16).[31] These BDE$_{O–H}$ estimates are higher than Mn complexes, where these bond strengths have been reported.[11c, 12d, 12i, 12k] The large BDE$_{O–H}$

values for these hydroxide clusters suggest that if these terminal oxo moieties could be accessed, they would be highly reactive. Indeed, previous attempts to generate a terminal oxo species on related phenyl-pyrazolate bridged multimetallic clusters results in activation of strong bonds, although the identity of the reactive intermediate in these reactions could not be established (terminal metal-oxo or iodosylbenzene adduct).[18d-f]

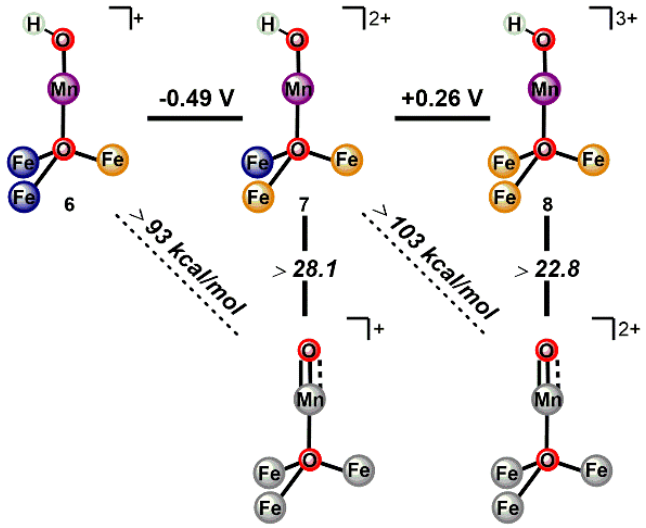

Figure 16. Estimated BDE_{O-H} values for Mn^{III}–OH clusters **6-[BAr$^F_4$]** and **7-[BAr$^F_4$]** based on their oxidation potentials and lower bound of their pK_a (where no PCET occurs in their CV with an external base). The metal oxidation states of the resulting putative Mn-oxo clusters are left ambiguous since multiple oxidation state distributions are possible.

CONCLUSIONS

We have reported the synthesis of tetranuclear [Fe_3Mn–OH_x] clusters bearing bridging unsubstituted pyrazolate ligands, leading to a sterically open coordination environment around the apical Mn center. These clusters were used to investigate the implications of distal metal redox changes on the activation of water by Mn in terms of the aquo-cluster pK_a, reduction potential, and homolytic O–H bond strength. Increasing the oxidation state of a distal Fe

center by one increases the acidity of the aquo ligand by ~7 pKa units (in THF), while raising the $BDE_{O–H}$ 8 kcal/mol, on average. By only changing the redox states of the distal Fe centers, a wide range of $BDE_{O–H}$ values could be measured for the Mn–OH_2 moiety (69 – 85 kcal/mol), which nearly spans the range of the reported $BDE_{O–H}$ measured in reported in mononuclear Mn–OH_2 complexes.[11c, 12e, 12f, 12i] The three different oxidation states of the aquo-cluster (**1-[BAr^F_4]** – **3-[BAr^F_4]**) underwent PCET reactions with TEMPO and 2,4,6-TBPR consistent with their measured $BDE_{O–H}$ values. The increase in $BDE_{O–H}$ of ~8 kcal/mol by increasing distal Fe oxidation state is similar to the increases that have been observed in mononuclear Mn systems where $BDE_{O–H}$ studies could be accomplished over multiple Mn oxidation states.[12d, 12i] This is in contrast to the previous example of a binuclear Mn system, where Mn–OH_2 $BDE_{O–H}$ values could be measured over three oxidation states, where small changes in the bond strength of ~ 4 kcal/mol for the $Mn^{III}Mn^{IV}$–OH_2 complex versus $Mn^{III}{}_2$–OH_2 were observed.[15a]

Importantly, the large effect of the remote metals on the $BDE_{O–H}$ demonstrates that the cluster as a whole has a significant impact in the activation of substrate water molecules. The range of $BDE_{O–H}$ reported here is achieved without change in the redox state of Mn; therefore, consideration of the effect of metal centers not directly supporting the substrate must be taken into account for multimetallic biological active sites as well as synthetic clusters. Additionally, the present findings demonstrate that, in comparison to monometallic complexes, transition metal clusters not only provide the possibility of increased storage of redox equivalents, but also can serve to dynamically tune reactivity through remote oxidation state changes.

EXPERIMENTAL DETAILS

General Considerations. All reactions were performed at room temperature in an N_2-filled M. Braun glovebox or using standard Schlenk techniques unless otherwise specified; reactions of compounds in THF/H_2O mixtures were performed in an N_2-filled VAC wetbox. Glassware was oven dried at 140 ºC for at least 2 h prior to use, and allowed to cool under vacuum. **[LFe$_3$(OAc)(OTf)][OTf]**[18a], Mn(OTf)$_2$ • 2 MeCN[32], benzyl potassium[33], iodosobenzene[34], silver tetrakis[3,5-bis(trifluoromethyl)phenyl]borate bis-acetonitrile (Ag[BAr$^F_4$] • 2 MeCN)[35], 2,4,6-tri-tert-butylphenoxy radical (2,4,6-TBPR)[36], and tetrapropylammnoium tetrakis[3,5-bis(trifluoromethyl)phenyl]borate ([^{n}Pr$_4$N][BAr$^F_4$])[37] were prepared according to literature procedures. All organic solvents were dried by sparging with nitrogen for at least 15 minutes, then passing through a column of activated A2 alumina under positive N_2 pressure. ^{1}H and ^{19}F NMR spectra were recorded on a Varian 300 MHz spectrometer. ^{1}H NMR spectra in THF/C_6D_6 were recorded on a Varian 500 MHz spectrometer using solvent suppression protocols. CD_3CN, CD_2Cl_2, and C_6D_6 were purchased from Cambridge Isotope Laboratories, dried over calcium hydride, degassed by three freeze-pump-thaw cycles, and vacuum transferred prior to use.

Physical Methods. *Mössbauer measurements*. Zero field ^{57}Fe Mossbauer spectra were recorded at 80 K in constant acceleration mode on a spectrometer from See Co (Edina, MN) equipped with an SVT-400 cryostat (Janis, Wilmington, WA). The isomer shifts are relative to the centroid of an α-Fe foil signal at room temperature. Samples were prepared by mixing polycrystalline material (20 mg) with boron nitride in a cup fitted with screw cap or freezing a concentrated solution in MeCN or THF. The data were fit to Lorentzian lineshapes using WMOSS (www.wmoss.org).

Mössbauer simulation details for all compounds. All spectra were simulated by three pairs of symmetric quadrupole doublets with equal populations and Lorentzian lineshapes. They were refined to a minimum via least squares optimization (13 fitting parameters per spectrum). Signals appearing above 2 mm/s were indicative with the presence of high-spin Fe^{II} centers and correspond to species with isomer shifts of ~ 1 mm/s. The Mössbauer data were fit to be consistent with our previously reported iron clusters.[17a, 18a, 18d, 18e] The observed Mossbauer parameters are in agreement with related six-coordinate high-spin Fe^{II}/Fe^{III} centers.[38]

Electrochemical measurements. CVs and SWVs were recorded with a Pine Instrument Company AFCBP1 biopotentiostat with the AfterMath software package. All measurements were performed in a three electrode cell, which consisted of glassy carbon (working; ø = 3.0 mm), silver wire (counter) and bare platinum wire (reference), in a N_2 filled M. Braun glovebox at RT. Either the ferrocene/ferrocinium (Fc/Fc^+) or decamethylferrocene/ decamethylferrocinium (Fc^*/Fc^{*+}; -0.524 V vs Fc/Fc^+ in THF/250 mM H_2O, under our experimental conditions) redox waves were used as an internal standard for all measurements.

X-ray crystallography. X-ray diffraction data was collected at 100 K on a Bruker PHOTON100 CMOS based diffractometer (microfocus sealed X-ray tube, Mo Kα (λ) = 0.71073 Å or Cu Kα (λ) = 1.54178 Å). All manipulations, including data collection, integration, and scaling, were carried out using the Bruker APEXII software. Absorption corrections were applied using SADABS. Structures were solved by direct methods using XS (incorporated into SHELXTL) and refined by using ShelXL least squares on Olex2-1.2.7 to convergence. All non-hydrogen atoms were refined using anisotropic displacement parameters. Hydrogen atoms were placed in idealized positions and refined using a riding model. Due to the size of the compounds most crystals included solvent-accessible voids that contained disordered solvent. In most cases the solvent could be modeled satisfactorily.

Synthetic Procedures. *Synthesis of Potassium pyrazolate (KPz).* 1.09 g (16.0 mmol) pyrazole was dissolved in 2 mL THF. To this stirring solution, a 10 mL THF solution of benzyl potassium, 2.03 g (15.6 mmol), was added dropwise; an off-white precipitate formed. After stirring for 20 minutes, the reaction was concentrated to 10 mL; the solids were collected on a glass frit and washed with 2 mL THF. The white solid was dried completely under vacuum to obtain 1.37 g (83% yield) potassium pyrazolate. Anal. calcd. (%) for $C_3H_3KN_2$: C. 33.94; H, 2.85; N, 26.39. Found: C, 34.12; H, 2.89; N, 25.38.

*Synthesis of [LFe₃O(Pz)₃Mn][OTf]₂ (**2-[OTf]**).* A suspension of 387 mg (0.28 mmol) **[LFe₃(OAc)(OTf)][OTf]** in 7 mL THF was stirred with 98.4 mg (0.29 mmol) $Ca(OTf)_2$ for an hour before being frozen with LN_2. To this mixture, 93.2 mg (0.88 mmol) KPz was added in thawing THF (4 mL) and stirred for 20 minutes at room temperature to obtain a dark red-orange solution. Iodosylbenzene, 63.6 mg (0.29 mmol), was added with 1 mL THF and the reaction was stirred for 90 minutes. 160 mg (0.37 mmol) $Mn(OTf)_2 \bullet 2$ MeCN solution in 2 mL THF was then added to the reaction. After 18 hours, the reaction was concentrated to 10 mL and filtered over a bed of celite; the precipitate was dried under vacuum, extracted with 8 mL DCM, and recrystallized via vapor diffusion of Et_2O into the filtrate. Dark green crystals of **2-[OTf]** were collected on a glass frit and dried (147 mg, 33% yield). Another 69 mg of **2-[OTf]** can be obtained by drying the crude reaction filtrate, extracting with 6 mL DCM and recrystallizing via Et_2O vapor diffusion (46% overall yield). X-ray diffraction quality crystals were obtained via oxidation of $[LFe_3O(Pz)_3Mn][OTf]$ (**1-[OTf]**) with 1 equivalent of $AgBPh_4$; Et_2O vapor diffusion into a DCM/THF solution of the resulting $[LFe_3O(Pz)_3Mn][OTf][BPh_4]$ produced crystals of suitable quality. ^1H NMR (300 MHz, CD_3CN): δ 120.8 (br), 80.8 (br), 71.0, 70.1, 52.9, 52.3, 42.2, 28.0 (br), 15.5, 13.0, 10.4, 8.1 (br), 4.38, 3.01, -2.51 (br). UV-Vis

(MeCN) [ε (M^{-1} cm^{-1})] 241 nm (6.53× 10^4), 368 nm (6.49 × 10^3). Anal. calcd. (%) for $C_{68}H_{48}F_6Fe_3MnN_{12}O_{10}S_2$: C. 51.25; H, 3.04; N, 10.55. Found: C, 50.81; H, 3.12; N, 10.18.

*Synthesis of [LFe₃O(Pz)₃Mn][OTf] (**1-[OTf]**).* A suspension of $[LFe_3O(Pz)_3Mn][OTf]_2$ (**2-[OTf]**; 91.5 mg, 0.057 mmol) in 2 mL THF was stirred as a THF solution of 10.9 mg $CoCp_2$ (0.058 mmol) was added. After 1 hour, the reaction was dried under vacuum. 4 mL DME was added to the purple solid and stirred for 12 hours. The resulting purple precipitate was collected on a bed of celite, washed with 2 mL DME, dried, and eluted with 2:1 THF/MeCN; crystals of $[LFe_3O(Pz)_3Mn][OTf]$ (**1-[OTf]**) were obtained by vapor diffusion of Et_2O into this solution (46.3 mg, 56% yield). ^{1}H NMR (300 MHz, CD_3CN): δ 96.4 (br), 57.8, 55.5, 37.8 (br), 36.4, 34.3, 34.0, 25.2, 13.4, 13.0, 12.0, 11.4, 3.4, 2.6, -6.4 (br). UV-Vis (MeCN) [ε (M^{-1} cm^{-1})] 250 nm (6.08 × 10^4), 517 nm (3.72 × 10^3). Anal. calcd. (%) for $C_{67}H_{48}F_3Fe_3MnN_{12}O_7S$: C, 55.70; H, 3.35; N, 11.63. Found: C, 55.36; H, 3.58; N, 11.20.

*Synthesis of [LFe₃O(Pz)₃Mn][OTf]₃ (**3-[OTf]**).* 9.2 mg (0.036 mmol) of AgOTf in THF was added to a stirring suspension of 56.8 mg (0.036 mmol) $[LFe_3O(Pz)_3Mn][OTf]_2$ (**2-[OTf]**) in THF. The resulting brown suspension was pumped down after 30 minutes. The reaction was filtered over a celite pad using DCM and the solvent was removed under reduced pressure. Crystals of $[LFe_3O(Pz)_3Mn][OTf]_3$ were obtained via vapor diffusion of Et_2O into a concentrated DCM/MeCN solution of the crude product, 57.4 mg (92% yield). ^{1}H NMR (300 MHz, CD_2Cl_2): δ 162.2 (br), 118.9 (br), 81.2, 76.9, 74.4, 73.1, 45.7, 18.8 (br), 16.3, 9.5, 3.34, 1., -6.5 (br). UV-Vis (MeCN) [ε (M^{-1} cm^{-1})] 241 nm (7.84 × 10^4), 411 nm (9.22 × 10^3). Anal. calcd. (%) for $C_{69}H_{48}F_9Fe_3MnN_{12}O_{13}S_3$: C, 47.55; H, 2.78; N, 9.64. Found: C, 47.57; H, 3.07; N, 9.21.

*Synthesis of [LFe₃O(Pz)₃Mn] (**4**).* 4.1 mg (0.18 mmol) sodium metal was mixed ~6 g elemental mercury with a pre-reduced stirbar. After 12 hours, a 5 mL THF suspension of $[LFe_3O(Pz)_3Mn][OTf]_2$ (**2-[OTf]**; 114 mg, 0.07 mmol) was added to the Na/Hg amalgam.

Over 4 hours, a blue precipitate formed; this resulting suspension was decanted from the amalgam and filtered over a fine porosity glass frit. The solids were washed with 5 mL THF and dried under vacuum. The resulting blue material, $[LFe_3O(Pz)_3Mn]$ (78.1 mg; 84% yield), is insoluble or unstable in most typical organic solvents. Anal. calcd. (%) for $C_{66}H_{48}Fe_3MnN_{12}O_4$: C. 61.18; H, 3.73; N, 12.94. Found: C, 60.44; H, 3.82; N, 12.87

Synthesis of $[LFe_3O(Pz)_3Mn][BAr^F{}_4]$ (***1-[BAr$^F{}_4$]***). 14.0 mg (0.013 mmol) $Ag[BAr^F{}_4]$ • 2 MeCN in 2 mL Et_2O was added to a stirring suspension of $[LFe_3O(Pz)_3Mn]$ (**4**; 17.2 mg, 0.013 mmol); the blue suspension changed to a purple solution. After 15 minutes, the solvent was removed under reduced pressure. 3 mL Et_2O was added to the purple residue and filtered over a pad of celite. The filtrate was dried to afford $[LFe_3O(Pz)_3Mn][BAr^F{}_4]$ as a purple solid, 26.5 mg (92% yield). ^{1}H NMR (300 MHz, CD_3CN) is identical to $[LFe_3O(Pz)_3Mn][OTf]$ (**1-[OTf]**). Anal. calcd. (%) for $C_{98}H_{60}BF_{24}Fe_3MnN_{12}O_4$: C. 54.52; H, 2.80; N, 7.79. Found: C, 54.06; H, 2.84; N, 7.33.

Synthesis of $[LFe_3O(Pz)_3Mn][BAr^F{}_4]_2$ (***2-[BAr$^F{}_4$]***). 45.0 mg (0.043 mmol) $Ag[BAr^F{}_4]$ • 2 MeCN in 2 mL Et_2O was added to a stirring suspension of $[LFe_3O(Pz)_3Mn]$ (**4**; 27.6 mg, 0.021 mmol); the blue suspension changed to a brown-green solution. After 15 minutes, the solvent was removed under reduced pressure. 3 mL Et_2O was added to the brown residue and filtered over a pad of celite. 6 mL benzene was added to the filtrate to produce an oily precipitate; after 30 minutes, the supernatant was removed and the remaining brown-green residue was dried under reduced pressure. 36.6 mg (57% yield) of the brown-green solid, **2-[BAr$^F{}_4$]**, was obtained; the ^{1}H NMR (300 MHz, CD_3CN) is identical to $[LFe_3O(Pz)_3Mn][OTf]_2$ (**2-[OTf]**). UV-Vis (THF/250 mM H_2O) [ε (M^{-1} cm^{-1})] 368 nm (5.11×10^3). Anal. calcd. (%) for $C_{130}H_{72}B_2F_{48}Fe_3MnN_{12}O_4$: C. 51.67; H, 2.40; N, 5.56. Found: C, 51.38; H, 2.56; N, 5.46.

*Synthesis of [LFe$_3$O(Pz)$_3$Mn][BAr$^F{}_4$]$_3$ (**3-[BAr$^F{}_4$]**).* 6.4 mg (0.006 mmol) [^{Ac}Fc][BAr$^F{}_4$] in 0.5 mL THF was added to [LFe$_3$O(Pz)$_3$Mn][BAr$^F{}_4$]$_2$ (**2-[BAr$^F{}_4$]**; 18.6 mg, 0.006 mmol). After 10 minutes, 5 mL benzene was added to the solution to produce an oily brown precipitate; after 30 minutes, the yellow supernatant was removed and the remaining brown residue was dried under reduced pressure. 18.4 mg of a brown solid was obtained (77% yield). ^{1}H NMR (500 MHz, THF/C$_6$D$_6$ [250mM H$_2$O]): δ 83.8, 78.2, 75.9, 50.2, 24.9 (br), 16.6, 9.8 (br), 0.1. UV-Vis (THF/250 mM H$_2$O) [ε (M^{-1} cm^{-1})] 405 nm (7.64× 10^3). Anal. calcd. (%) for C$_{162}$H$_{84}$B$_3$F$_{72}$Fe$_3$MnN$_{12}$O$_4$: C. 50.08; H, 2.18; N, 4.33. Found: C, 50.34; H, 2.38; N, 4.29.

*Synthesis of [LFe$_3$O(Pz)$_3$Mn(OH)][BAr$^F{}_4$] (**6-[BAr$^F{}_4$]**).* Addition of 100 μL of a 50 mM solution of DBU in THF/250 mM H$_2$O to 2 mL 2 mM solution of [LFe$_3$O(Pz)$_3$Mn][BAr$^F{}_4$]$_2$ (**2-[BAr$^F{}_4$]**) in THF/250 mM H$_2$O leads to a color change of the solution from green to red. Crystals for X-ray diffraction (**6-[OTf]**) were obtained by conducting the analogous reaction with [LFe$_3$O(Pz)$_3$Mn][OTf]$_2$ (**2-[OTf]**) and DBU in 95:5 MeCN/H$_2$O and crystalizing via vapor diffusion of Et$_2$O into this solution; considerable decomposition occurs on the timescale of crystallization, making crystallization unsuitable for preparing analytically pure solid samples of [LFe$_3$O(Pz)$_3$Mn(OH)][OTf]. Solutions of [LFe$_3$O(Pz)$_3$Mn(OH)][BAr$^F{}_4$] were prepared for electrochemistry experiments by stirring 4 mL of 2.5 mM [LFe$_3$O(Pz)$_3$Mn][[BArF4]]$_2$ (**2-[BAr$^F{}_4$]**) and 0.1 M [^{n}Pr$_4$N][BAr$^F{}_4$] solution in THF/250 mM H$_2$O with ~2 mg of solid KOH pellet for 1 hour; the resulting red solution was decanted off the remaining KOH before electrochemical measurements were conducted. ^{1}H NMR (500 MHz, THF/C$_6$D$_6$ [250mM H$_2$O]): δ 153.1 (br), 102.7 (br), 85.9, 80.0, 64.8, 60.8, 58.1, 57.3, 23.0, 15.7. 12.5, 10.9 (br). UV-Vis (THF/250 mM H$_2$O) [ε (M^{-1} cm^{-1})] 467 nm (3.29 × 10^3).

*Synthesis of [LFe$_3$O(Pz)$_3$Mn(OH)] (**5**).* Addition of 11 mg (0.03 mmol) decamethylcobaltocene in THF/250 mM H$_2$O to 4 mL 7 mM solution of

$[LFe_3O(Pz)_3Mn(OH)][BAr^F{}_4]$ (**6-[$BAr^F{}_4$]**; 0.03 mmol) in THF/250 mM H_2O leads to a color change of the solution from red to blue. The reaction was pumped down after 30 minutes. ^1H NMR (500 MHz, THF/C_6D_6 [250mM H_2O]): δ 126.0 (br), 76.1 (br), 59.6, 49.0, 46.9, 42.7, 37.0, 23.9 (br), 17.2, 15.6, 12.8, -14.9.

*Synthesis of $[LFe_3O(Pz)_3Mn(OH)][BAr^F{}_4]_2$ (**7-[$BAr^F{}_4$]**). Method A.* Addition of 160 μL of a 50 mM solution of Et_3N in THF/250 mM H_2O to 2 mL 2 mM solution of $[LFe_3O(Pz)_3Mn][BAr^F{}_4]_3$ (**3-[$BAr^F{}_4$]**) in THF/250 mM H_2O leads to a color change of the solution from brown to brown-green. ^1H NMR spectroscopy confirms complete conversion to $[LFe_3O(Pz)_3Mn(OH)][BAr^F{}_4]_2$.

Method B. Addition of 200 μL of 6 mM solution of Ag[BArF4] • 2 MeCN in THF/250 mM H_2O to 400 μL of a 3mM solution of $[LFe_3O(Pz)_3Mn(OH)][BAr^F{}_4]$ (**6-[$BAr^F{}_4$]**) in THF/250 mM H_2O leads to formation of a grey precipitate. Filtration of this solution yields a brown-green solution with an identical ^1H NMR obtained from Method A. ^1H NMR (500 MHz, THF/C_6D_6 [250 mM H_2O]: δ 110.2 (br), 89.1, 85.1, 70.0, 67.2, 62.0, 19.1 (br), 15.7, 13.1, 9.8 (br), 8.6 (br), 6.2 (br), 1.1, 0.7, 0. UV-Vis (THF/250 mM H_2O) [ε (M^{-1} cm^{-1})] 389 nm (5.29×10^3).

ELECTROCHEMICAL DETAILS

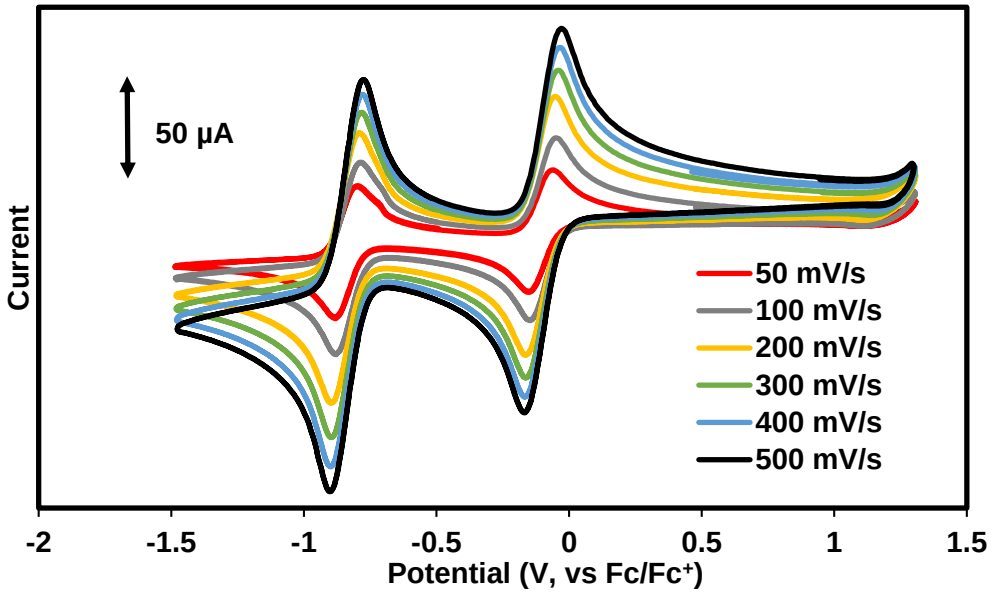

Figure 17. Cyclic voltammograms of $[LFe_3O(Pz)_3Mn][OTf]_2$ (**2-[OTf]**, 2.8 mM) in MeCN and 100 mM $[Bu_4N][PF_6]$ at various scan rates with glassy carbon, Pt-wire, and Ag-wire as working, counter, and reference electrode, respectively.

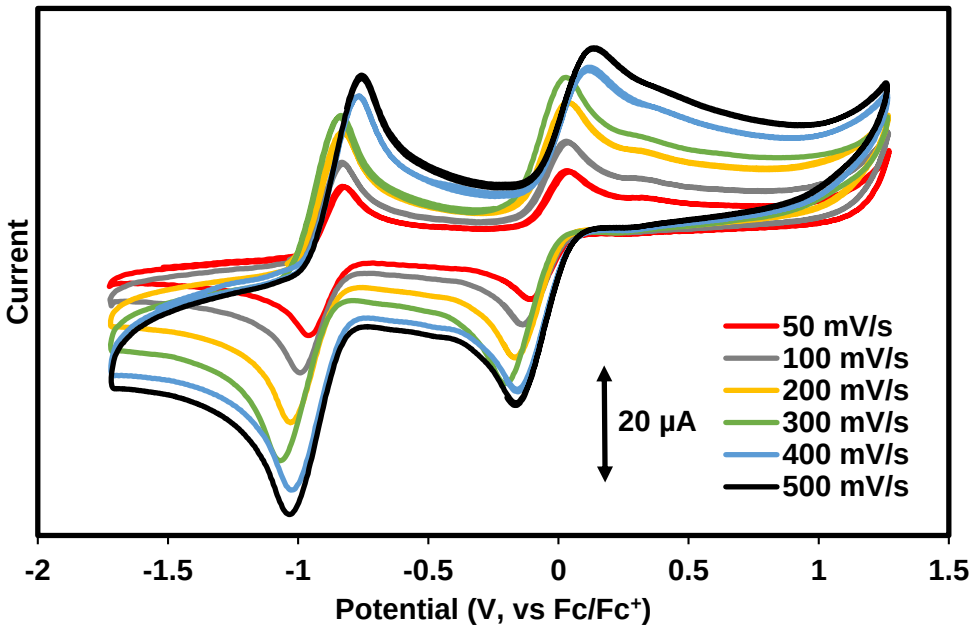

Figure 18. Cyclic voltammograms of $[LFe_3O(Pz)_3Mn(OH_2)][BAr^F{}_4]_2$ (**2-[BAr$^F{}_4$]**, 2.1 mM) in THF [250 mM H_2O] and 100 mM $[^nPr_4N][BAr^F{}_4]$ at various scan rates with glassy carbon, Pt-wire, and Ag-wire as working, counter, and reference electrode, respectively.

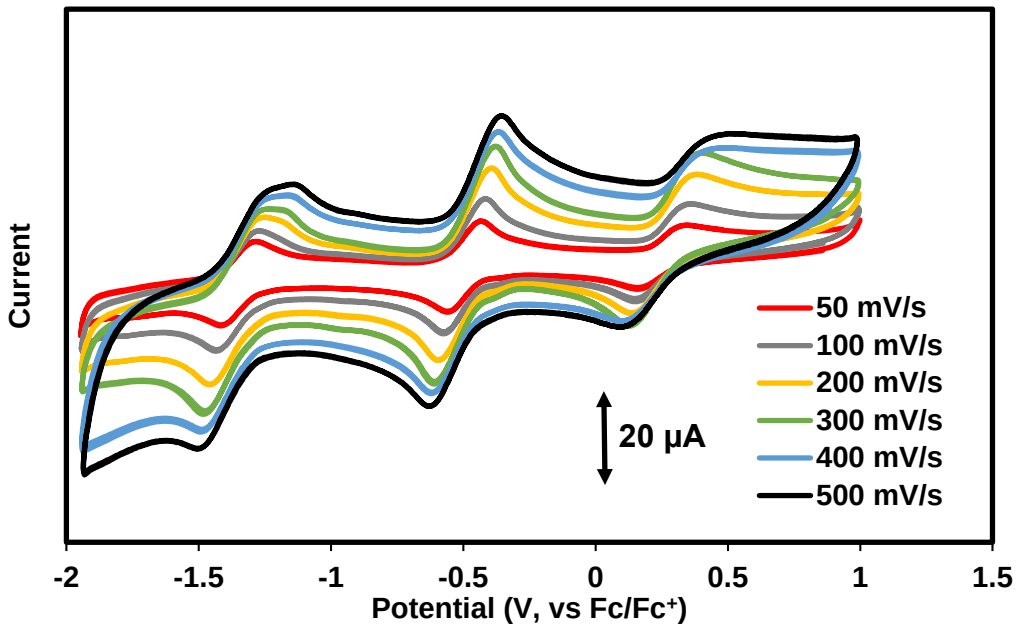

Figure 19. Cyclic voltammograms of $[LFe_3O(Pz)_3Mn(OH)][BAr^F{}_4]$ (**6-[BAr$^F{}_4$]**, 2 mM) in THF [250 mM H_2O] and 100 mM $[^nPr_4N][BAr^F{}_4]$ at various scan rates with glassy carbon, Pt-wire, and Ag-wire as working, counter, and reference electrode, respectively.

Table 3. Peak-to-peak separation (ΔE_p; mV) and peak area ratio ($A_{a/c}$) for the redox couples in 2-[OTf], 2-[BAr$^F{}_4$], and 6-[BAr$^F{}_4$].

Redox Couple Assignment	E_{pa} (mV)	E_{pc}(mV)	ΔE_p(mV)	A_a (µW)	A_c (µW)	A_a/A_p
2-[OTf]						
$[Fe^{II}_2Fe^{III}Mn^{II}] \rightarrow [Fe^{II}Fe^{III}_2Mn^{II}]$	-882	-799	83	22.0	18.5	1.2
$[Fe^{II}Fe^{III}_2Mn^{II}] \rightarrow [Fe^{III}_3Mn^{II}]$	-154	-66	88	11.4	12.2	0.9
2-[BAr$^F{}_4$]						
$[Fe^{II}_2Fe^{III}Mn^{II}] \rightarrow [Fe^{II}Fe^{III}_2Mn^{II}]$	-958	-831	127	7.9	2.8	2.8
$[Fe^{II}Fe^{III}_2Mn^{II}] \rightarrow [Fe^{III}_3Mn^{II}]$	-93	44	137	2.6	2.5	1.0
6-[BAr$^F{}_4$]						
$[Fe^{II}_3Mn^{III}] \rightarrow [Fe^{II}_2Fe^{III}Mn^{III}]$	-1,406	-1,274	132	6.6	2.6	2.5
$[Fe^{II}_2Fe^{III}Mn^{III}] \rightarrow [Fe^{II}Fe^{III}_2Mn^{III}]$	-548	-426	122	4.2	3.6	1.2
$[Fe^{II}Fe^{III}_2Mn^{III}] \rightarrow [Fe^{III}_3Mn^{III}]$	172	354	182	1.6	3.0	0.5

Constructing the Potential – pK_a Diagram of [$LFe_3O(Pz)_3Mn(OH_x)$] Clusters. Cyclic voltammetry was performed on ~2 mM solutions of $[LFe_3O(Pz)_3Mn][BAr^F{}_4]_2$ (**2-[$BAr^F{}_4$]**), or $[LFe_3O(Pz)_3Mn(OH)][BAr^F{}_4]$ (**6-[$BAr^F{}_4$]**) with glassy carbon working, Pt wire counter, and Ag wire reference electrodes in THF [250 mM H_2O] and ca. 100 mM $[^nPr_4N][BAr^F{}_4]$. After collecting a blank CV, and CV of the cluster, one equivalent of a base was added by injecting a concentrated solution of it to the cluster solution and mixing via pipette. It was observed that quasi-reversible waves corresponding to PCET could be observed best at slow scan rates (< 200 mV/s) for all bases tested; faster scan rates led to loss of a return wave for the PCET. We postulate that proton transfer in these experiments is slow relative to the time scale of electrochemistry. With some bases, redox events for the PCET and fully protonated/deprotonated cluster could be observed simultaneously; we propose that this is due to a lower local concentration of base at the electrode surface, or slow proton transfer kinetics. For all measurements reported, it is assumed that half an equivalent of available base is consumed at the electrode at the PCET $E_{½}$ potential; making the observed potential based only on the redox potential of the Mn–OH_x cluster, and the pK_a of the added base.[29] All THF pK_a values used here were obtained from a report by Rosés and co-workers.[22]

Base with **2-[BAr$^F_4$]**	pK_a (THF)	$E_{½}(1)$ (V)	$E_{½}(2)$ (V)	$E_{½}(3)$ (V)
2-methyl-aniline	7.5	-0.885	-0.002 (-0.266)	
2-methyl-pyridine	8.6	-0.891	-0.028	0.327
2,6-dimethyl-pyridine	9.5	-0.894	-0.082	
2,4,6-trimethyl-pyridine	10.4	-0.907	-0.390	
triethylamine	14.9	-0.900	-0.373	
2-phenyl-1,1,3,3-tetramethylguanidine	16.5	-0.956	-0.468	
1,1,3,3-tetramethylguanidine	17.8	-1.034	-0.454	
1,8-diazabicyclo[5.4.0]undec-7-ene	19.1	-1.066	-0.468	
7-methyl-1,5,7-triazabicyclo[4.4.0]dec-5-ene	20.5	-1.148	-0.460	
1,5,7-triazabicyclo[4.4.0]dec-5-ene	22.0	-1.180	-0.451	
tert-butylimino-tri(pyrrolidino)phosphorane	22.8	-1.271	-0.461	
1-ethyl-2,2,4,4,4-pentakis(dimethylamino)2-λ^5,4λ^5-catenadi(phosphazene)	28.1	-1.317	-0.453	
Base with **6-[BAr$^F_4$]**				
tert-butylimino-tri(pyrrolidino)phosphorane	22.8	-1.307	-0.517	0.245
1-ethyl-2,2,4,4,4-pentakis(dimethylamino)2-λ^5,4λ^5-catenadi(phosphazene)	28.1	-1.333	-0.449	0.403

All reported potentials referenced to Fc/Fc$^+$.

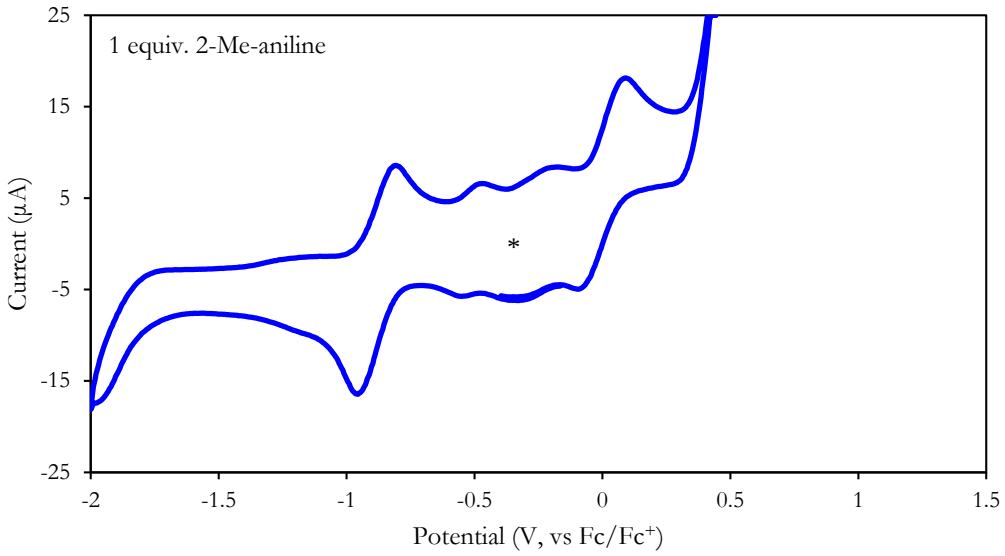

Figure 20. Cyclic voltammogram of [LFe$_3$O(Pz)$_3$Mn][BAr$^F_4$]$_2$ (**2-[BAr$^F_4$]**, 2 mM) in THF [250 mM H_2O] and 100 mM [^{n}Pr$_4$N][BAr$^F_4$] upon addition of 1 equivalent 2-methyl-aniline (pK_a(THF) = 7.5) at a scan rate of 50 mV/s. Asterisk (*) denotes redox couple of the decamethylferrocene internal standard. The open circuit potential was -0.4 V.

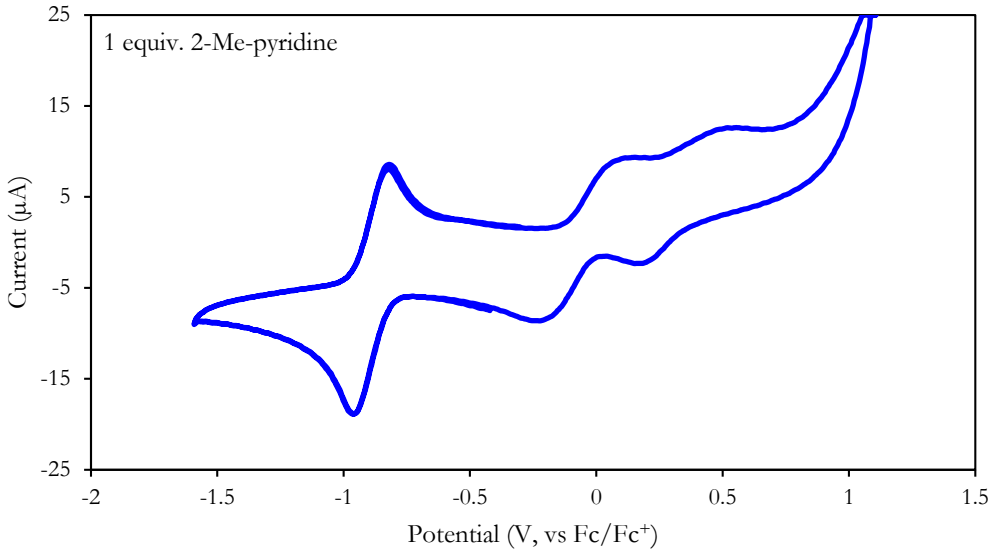

Figure 21. Cyclic voltammogram of $[LFe_3O(Pz)_3Mn][BAr^F{}_4]_2$ (**2-[BAr$^F{}_4$]**, 2 mM) in THF [250 mM H_2O] and 100 mM $[^nPr_4N][BAr^F{}_4]$ upon addition of 1 equivalent 2-methyl-pyridine (pK_a(THF) = 8.6) at a scan rate of 50 mV/s. An independent scan in the presence of a decamethylferrocene internal standard was used as a reference. The open circuit potential was -0.3 V.

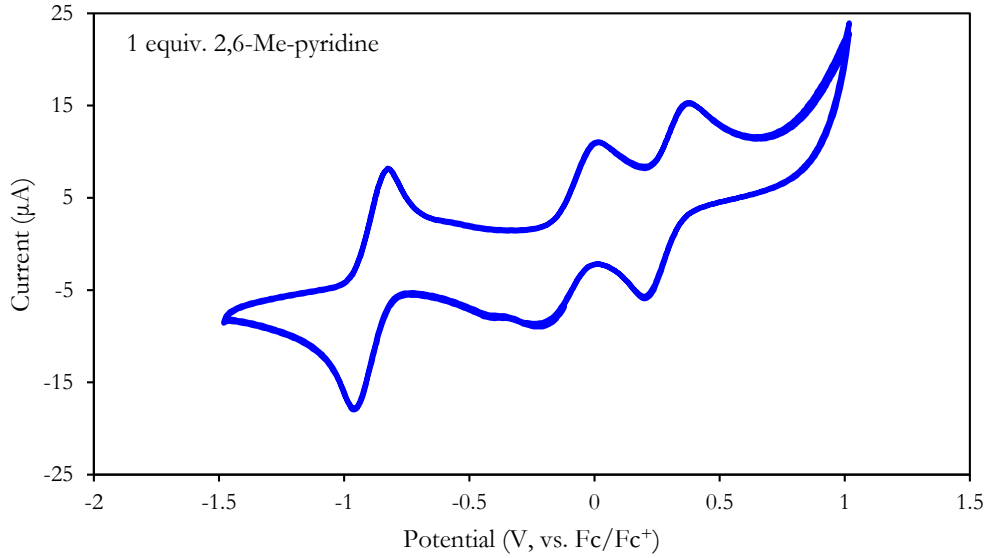

Figure 22. Cyclic voltammogram of $[LFe_3O(Pz)_3Mn][BAr^F{}_4]_2$ (**2-[BAr$^F{}_4$]**, 2 mM) in THF [250 mM H_2O] and 100 mM $[^nPr_4N][BAr^F{}_4]$ upon addition of 1 equivalent 2,6-dimethyl-pyridine

(pK_a(THF) = 9.5) at a scan rate of 50 mV/s. An independent scan in the presence of a decamethylferrocene internal standard was used as a reference. The open circuit potential was -0.3 V.

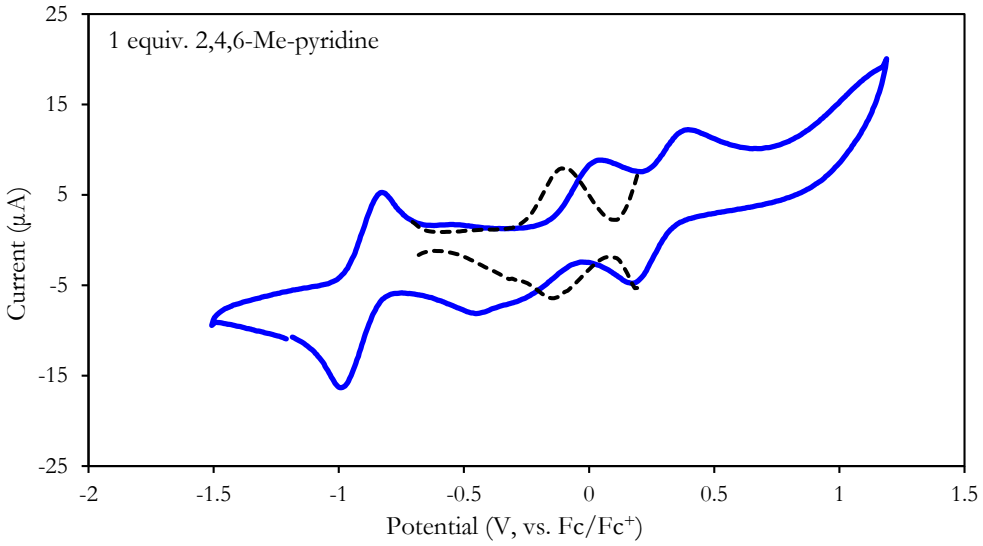

Figure 23. Cyclic voltammogram of $[LFe_3O(Pz)_3Mn][BAr^F{}_4]_2$ (**2-[BAr$^F{}_4$]**, 2 mM) in THF [250 mM H_2O] and 100 mM $[^nPr_4N][BAr^F{}_4]$ upon addition of 1 equivalent 2,4,6-trimethyl-pyridine (pK_a(THF) = 10.4) at a scan rate of 50 mV/s. An independent scan in the presence of a decamethylferrocene internal standard was used as a reference. The open circuit potential was -0.3 V. The $E_{½}$ of middle peak was determined via square wave voltammetry since its return wave was low in current, and overlapping with another peak.

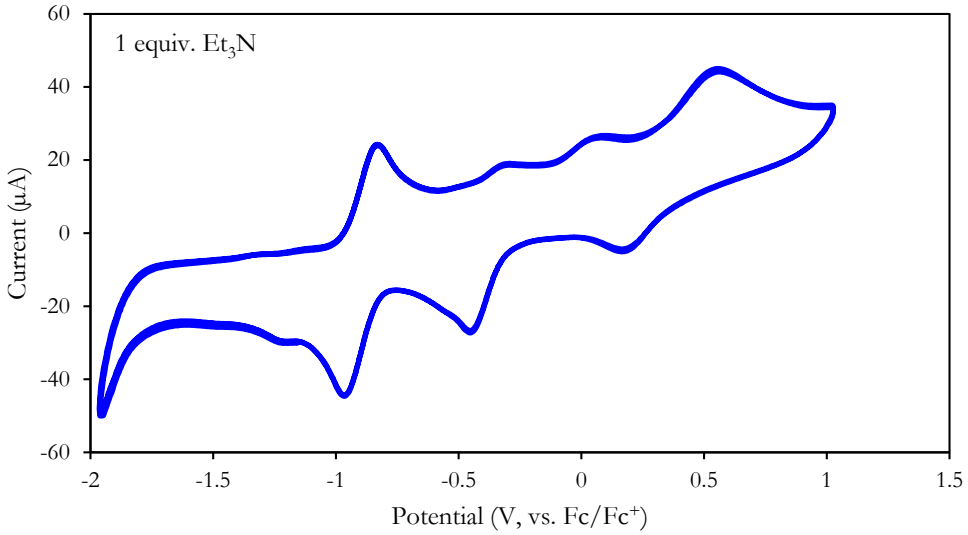

Figure 24. Cyclic voltammogram of $[LFe_3O(Pz)_3Mn][BAr^F{}_4]_2$ (**2-[BAr$^F{}_4$]**, 2 mM) in THF [250 mM H_2O] and 100 mM $[^nPr_4N][BAr^F{}_4]$ upon addition of 1 equivalent triethylamine (pK_a(THF) = 14.9) at a scan rate of 200 mV/s. An independent scan in the presence of a ferrocene internal standard was used as a reference. The open circuit potential was -0.6 V.

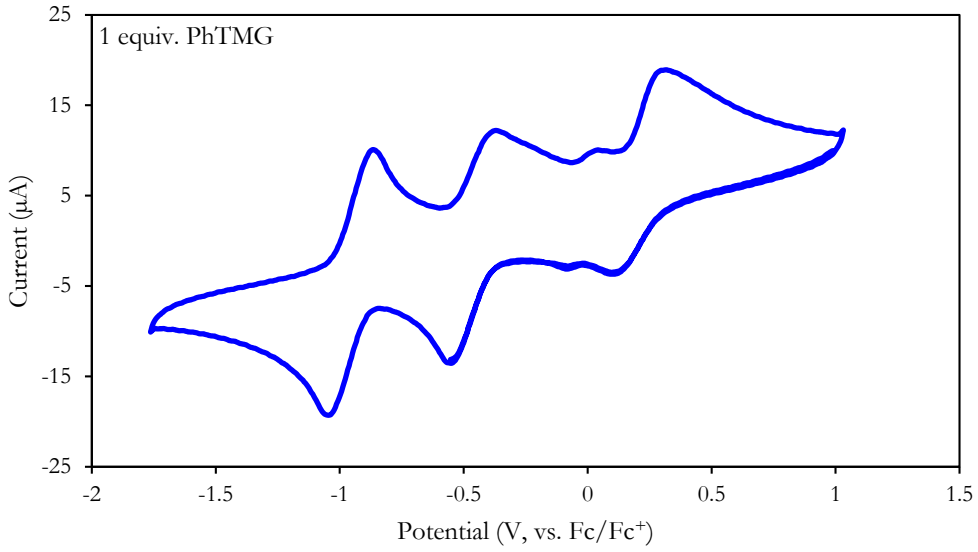

Figure 25. Cyclic voltammogram of $[LFe_3O(Pz)_3Mn][BAr^F{}_4]_2$ (**2-[BAr$^F{}_4$]**, 2 mM) in THF [250 mM H_2O] and 100 mM $[^nPr_4N][BAr^F{}_4]$ upon addition of 1 equivalent 2-phenyl-1,1,3,3-tetramethylguanidine (pK_a(THF) = 16.5) at a scan rate of 50 mV/s. An independent scan in

the presence of a ferrocene internal standard was used as a reference. The open circuit potential was -0.7 V.

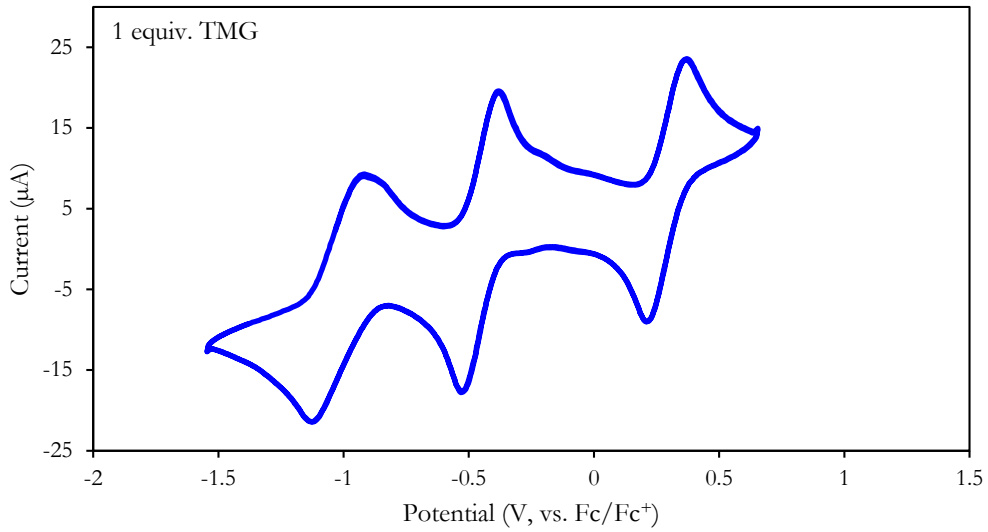

Figure 26. Cyclic voltammogram of $[LFe_3O(Pz)_3Mn][BAr^F{}_4]_2$ (**2-[BAr$^F{}_4$]**, 2 mM) in THF [250 mM H_2O] and 100 mM $[^nPr_4N][BAr^F{}_4]$ upon addition of 1 equivalent 1,1,3,3-tetramethylguanidine (pK_a(THF) = 17.8) at a scan rate of 50 mV/s. An independent scan in the presence of a ferrocene internal standard was used as a reference. The open circuit potential was -0.5 V.

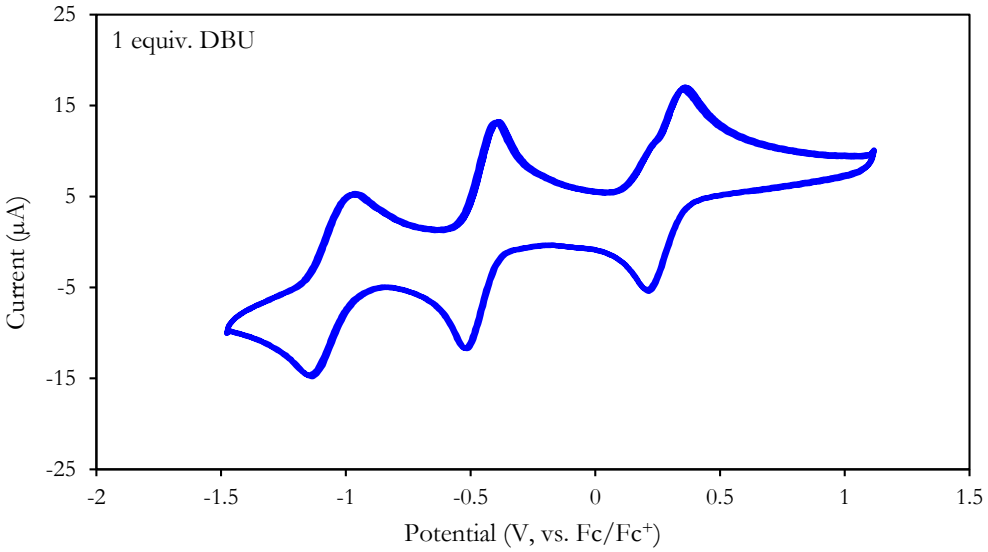

Figure 27. Cyclic voltammogram of $[LFe_3O(Pz)_3Mn][BAr^F{}_4]_2$ (**2-[BAr$^F{}_4$]**, 2 mM) in THF [250 mM H_2O] and 100 mM $[^nPr_4N][BAr^F{}_4]$ upon addition of 1 equivalent 1,8-diazabicyclo[5.4.0]undec-7-ene (pK_a(THF) = 19.1) at a scan rate of 50 mV/s. An independent scan in the presence of a ferrocene internal standard was used as a reference. The open circuit potential was -0.7 V.

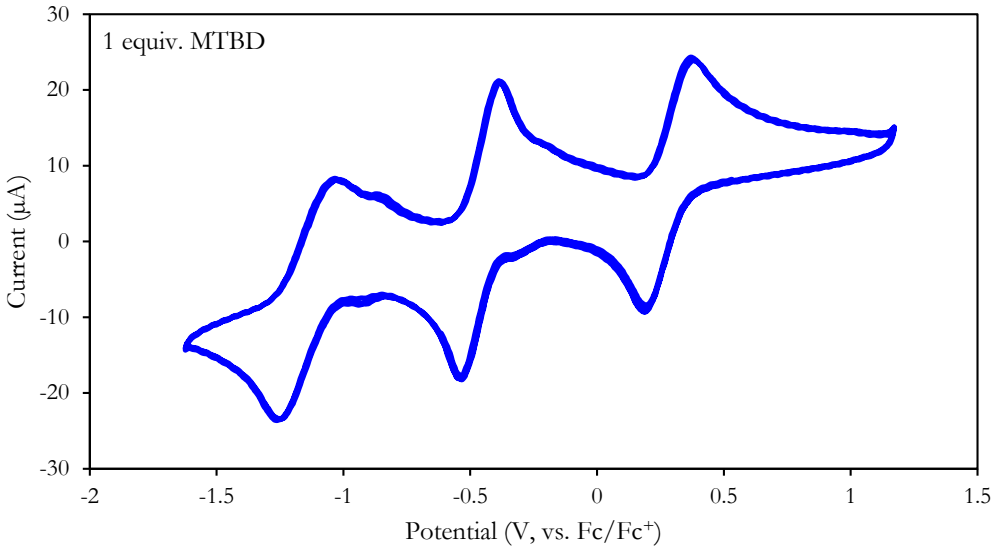

Figure 28. Cyclic voltammogram of $[LFe_3O(Pz)_3Mn][BAr^F{}_4]_2$ (**2-[BAr$^F{}_4$]**, 2 mM) in THF [250 mM H_2O] and 100 mM $[^nPr_4N][BAr^F{}_4]$ upon addition of 1 equivalent 7-methyl-1,5,7-triazabicyclo[4.4.0]dec-5-ene (pK_a(THF) = 20.5) at a scan rate of 50 mV/s. An independent scan in the presence of a ferrocene internal standard was used as a reference. The open circuit potential was -0.7 V.

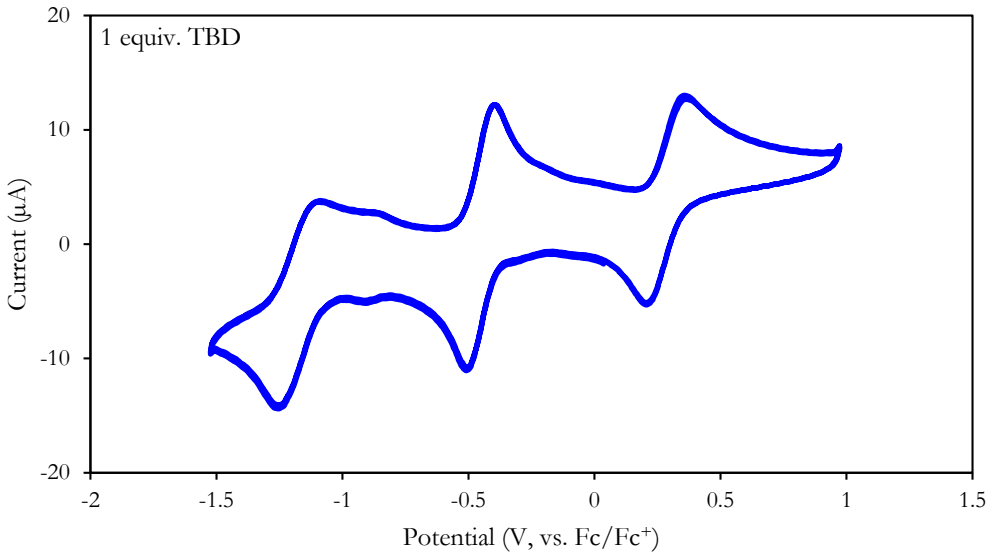

Figure 29. Cyclic voltammogram of $[LFe_3O(Pz)_3Mn][BAr^F{}_4]_2$ (**2-[BAr$^F{}_4$]**, 2 mM) in THF [250 mM H_2O] and 100 mM $[^nPr_4N][BAr^F{}_4]$ upon addition of 1 equivalent 1,5,7-triazabicyclo[4.4.0]dec-5-ene (pK_a(THF) = 22.0) at a scan rate of 50 mV/s. An independent scan in the presence of a ferrocene internal standard was used as a reference. The open circuit potential was -0.7 V.

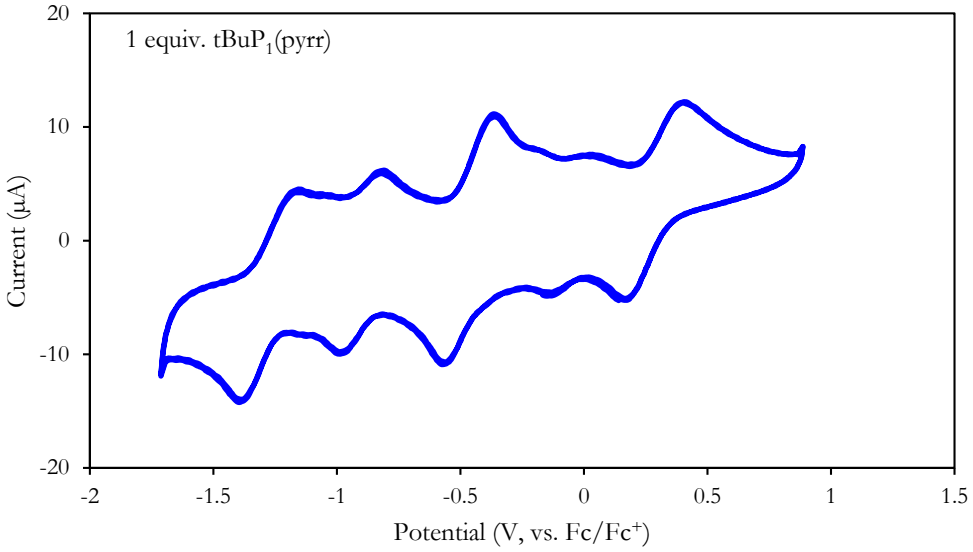

Figure 30. Cyclic voltammogram of $[LFe_3O(Pz)_3Mn][BAr^F{}_4]_2$ (**2-[BAr$^F{}_4$]**, 2 mM) in THF [250 mM H_2O] and 100 mM $[^nPr_4N][BAr^F{}_4]$ upon addition of 1 equivalent *tert*-butylimino-

tri(pyrrolidino)phosphorane (pK_a(THF) = 22.8) at a scan rate of 50 mV/s. An independent scan in the presence of a ferrocene internal standard was used as a reference. The open circuit potential was -0.7 V.

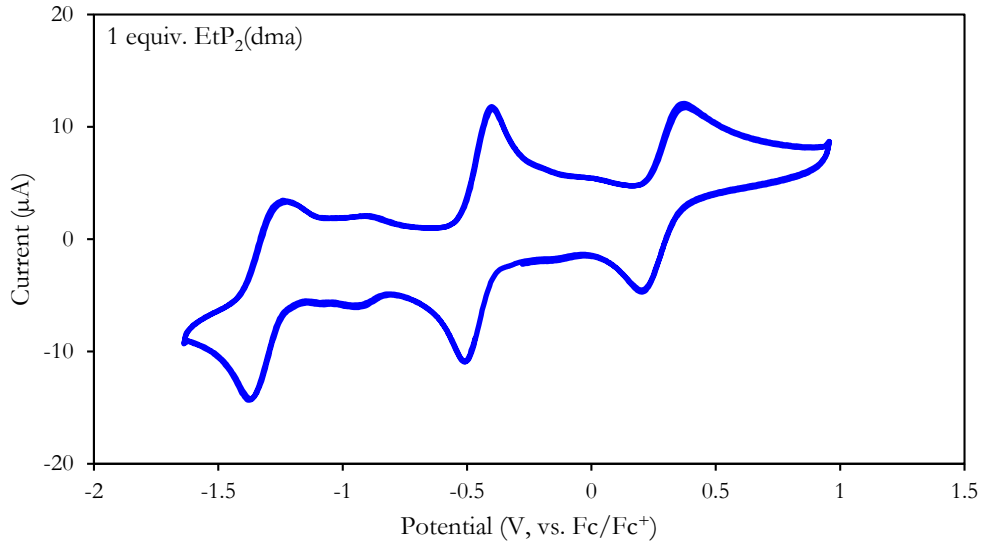

Figure 31. Cyclic voltammogram of [LFe$_3$O(Pz)$_3$Mn][BAr$^F{}_4$]$_2$ (**2-[BAr$^F{}_4$]**, 2 mM) in THF [250 mM H_2O] and 100 mM [^{n}Pr$_4$N][BAr$^F{}_4$] upon addition of 1 equivalent 1-ethyl-2,2,4,4,4-pentakis(dimethylamino)2λ^5,4λ^5-catenadi(phosphazene) (pK_a(THF) = 28.1) at a scan rate of 50 mV/s. An independent scan in the presence of a ferrocene internal standard was used as a reference. The open circuit potential was -0.7 V.

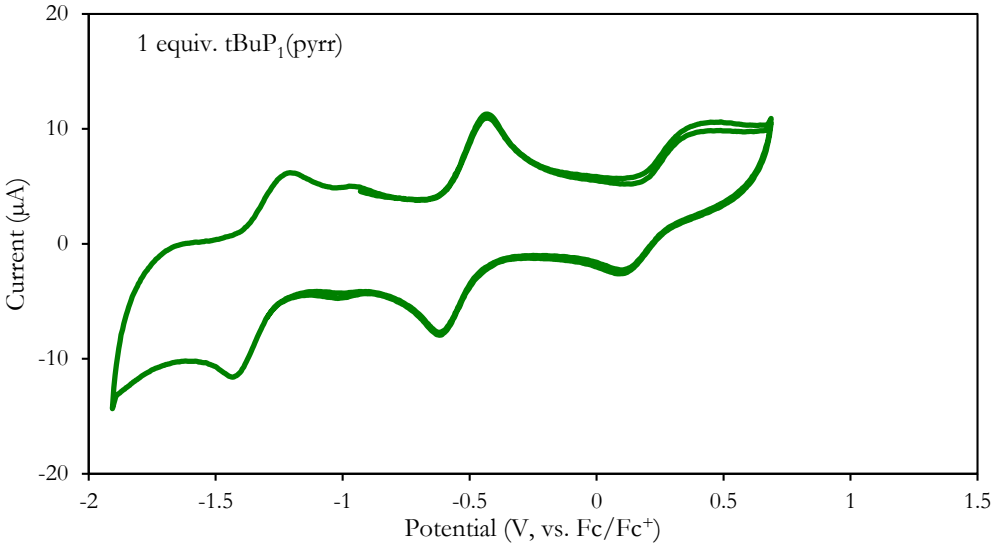

Figure 32. Cyclic voltammogram of $[LFe_3O(Pz)_3Mn(OH)][BAr^F{}_4]$ (**6-[BAr$^F{}_4$]**, 2 mM) in THF [250 mM H_2O] and 100 mM $[^nPr_4N][BAr^F{}_4]$ upon addition of 1 equivalent *tert*-butylimino-tri(pyrrolidino)phosphorane (pK_a(THF) = 22.8) at a scan rate of 50 mV/s. An independent scan in the presence of a ferrocene internal standard was used as a reference. The open circuit potential was -1.3 V.

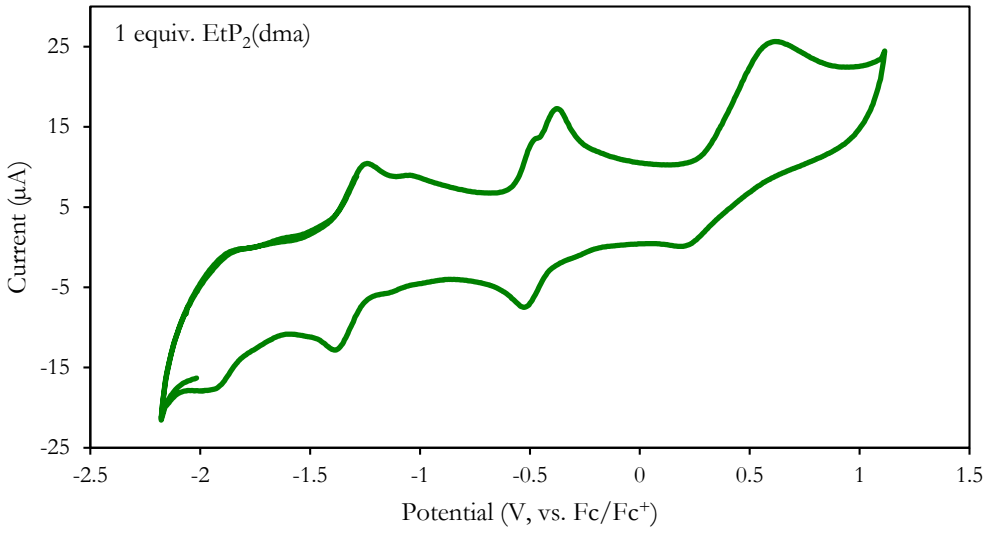

Figure 33. Cyclic voltammogram of $[LFe_3O(Pz)_3Mn(OH)][BAr^F{}_4]$ (**6-[BAr$^F{}_4$]**, 2 mM) in THF [250 mM H_2O] and 100 mM $[^nPr_4N][BAr^F{}_4]$ upon addition of 1 equivalent 1-ethyl-2,2,4,4,4-

pentakis(dimethylamino)2λ^5,4λ^5-catenadi(phosphazene) (pK_a(THF) = 28.1) at a scan rate of 50 mV/s. An independent scan in the presence of a ferrocene internal standard was used as a reference. The open circuit potential was -1.3 V.

CRYSTALOGRAPHIC DETAILS

Crystal and refinement data for complexes 1-[OTf] – 3-[OTf], 6-[OTf] and 2-[OTf] (H_2O).

	1-[OTf]	2-[OTf]	3-[OTf]	6-[OTf]	2-[OTf] (H_2O)
CCDC Number	1848679	1848681	1848680	1848678	1848677
Empirical formula	$C_{77}H_{62}F_3Fe_3MnN_{12}O_8S$	$C_{105.2}H_{81.2}BCl_{0.5}F_3Fe_3MnN_{12}O_{10.5}S$	$C_{76}H_{53.5}F_9Fe_3MnN_{13.4}O_{14.1}S_3$	$C_{67}H_{49}F_3Fe_3MnN_{12}O_8S$	$C_{72}H_{62}F_6Fe_3MnN_{12}O_{13}S_2$
Formula weight (g/mol)	1594.9	2019.8	1869.7	1461.7	1703.9
Radiation	MoKα (λ = 0.71073)	MoKα (λ = 0.71073)	CuKα (λ = 1.54178)	CuKα (λ = 1.54178)	CuKα (λ = 1.54178)
a (Å)	12.2741(5)	14.2908(12)	44.125(2)	14.7283(7)	12.2685(6)
b (Å)	19.4126(8)	15.9691(13)	14.3106(7)	19.3808(10)	29.896(2)
c (Å)	15.5112(6)	24.3709(17)	24.8034(10)	45.518(2)	19.6152(17)
α (°)	90	71.236(4)	90	90	90
β (°)	108.397(2)	75.366(2)	90.402(3)	92.474(3)	92.393(5)
γ (°)	90	70.262(4)	90	90	90
V (Å^3)	3507.0(2)	4891.6(7)	15661.9(13)	12980.9(11)	7188.2(9)
Z	2	2	8	8	4
Cryst. syst.	monoclinic	triclinic	monoclinic	monoclinic	monoclinic
Space group	$P2_1$	P-1	C2/c	C2/c	$P2_1/c$
$\varrho_{calc}g$ (cm^3)	1.510	1.371	1.586	1.496	1.575
2 Θ range (°)	5.028 to 56.648	5.076 to 60.444	6.492 to 145.272	7.544 to 132.498	5.392 to 149.51
μ (mm^{-1})	0.899	0.668	7.226	7.742	7.461
GOF	1.031	1.029	1.037	1.160	1.140
R1, wR2 (I>2σ (I))	0.0244, 0.0583	0.0635, 0.1712	0.0840, 0.2131	0.1305, 0.2771	0.1109, 0.2060

Special refinement details for [LFe$_3$O(Pz)$_3$Mn][OTf] (1-[OTf]). The triflate counterion bound to Mn1 is disordered over two positions with refined occupancies of 12% (S200 through C200) and 88% (S201 through C201).

Special refinement details for [LFe$_3$O(Pz)$_3$Mn][OTf]$_2$ (2-[OTf]). The triflate counterion bound to Mn1 is disordered over two positions with refined occupancies of 51% (S200 through C200) and 49% (S201 through C201). A disordered THF molecule was modeled over two positions with occupancies of 81% (O102 through C107) and 19% (O101 through C111). A different THF molecule was modeled to be only partially occupied (56%; O103 through C115). A co-crystallized solvent site was modeled to contain a mixture of three different molecules: a THF (27% O105 through C123), a DCM (22%; Cl10 through C124), and Et$_2$O (64%; O104 through C119).

Special refinement details for [LFe$_3$O(Pz)$_3$Mn][OTf]$_3$ (3-[OTf]). The triflate counterion bound to Mn1 is disordered over two positions with refined occupancies of 30% (S200 through C200) and 70% (S201 through C201). An outersphere triflate was modeled in two different positions with occupancies of 38% (S203 through C203) and 62% (S204 through C204). For the S203 through C203 triflate, a nearby Et$_2$O molecule was modeled as partially occupied at 62%. For the S204 through C204, a nearby MeCN molecule was modeled as partially occupied at 38%.

Special refinement details for [LFe$_3$O(Pz)$_3$Mn(OH)][OTf] (6-[OTf]).. The outersphere triflate is disordered over two positions, modeled at an occupancy of 50% each. Both triflates are on symmetry elements and positionally disordered. For the S200 through C200 triflate, this was modeled with EXYZ/EADP constraints. For the S201 throughC201 triflate, the C and S atoms were constrained with EXYZ/EACDP, and the O203 through F205 atoms were modeled in alternating positions, at 50% occupancy each. A void in the structure was a mixture

of different solvent molecules that couldn't be adequately modeled, and a solvent mask was used to account for this electron density.

References

1. (a) McEvoy, J. P.; Brudvig, G. W. *Chem. Rev.* **2006,** *106*, 4455-4483; (b) Ferreira, K. N.; Iverson, T. M.; Maghlaoui, K.; Barber, J.; Iwata, S. *Science* **2004,** *303*, 1831-1838; (c) Umena, Y.; Kawakami, K.; Shen, J.-R.; Kamiya, N. *Nature* **2011,** *473*, 55-60; (d) Suga, M.; Akita, F.; Hirata, K.; Ueno, G.; Murakami, H.; Nakajima, Y.; Shimizu, T.; Yamashita, K.; Yamamoto, M.; Ago, H.; Shen, J.-R. *Nature* **2015,** *517*, 99-103.
2. (a) Kok, B.; Forbush, B.; McGloin, M. *Photochem. Photobiol.* **1970,** *11*, 457-475; (b) Yano, J.; Yachandra, V. *Chem. Rev.* **2014,** *114*, 4175-4205; (c) Vinyard, D. J.; Brudvig, G. W. *Annu. Rev. Phys. Chem.* **2017,** *68*, 101-116.
3. Meyer, T. J.; Huynh, M. H. V.; Thorp, H. H. *Angew. Chem. Int. Ed.* **2007,** *46*, 5284-5304.
4. (a) Weinberg, D. R.; Gagliardi, C. J.; Hull, J. F.; Murphy, C. F.; Kent, C. A.; Westlake, B. C.; Paul, A.; Ess, D. H.; McCafferty, D. G.; Meyer, T. J. *Chem. Rev.* **2012,** *112*, 4016-4093; (b) Migliore, A.; Polizzi, N. F.; Therien, M. J.; Beratan, D. N. *Chem. Rev.* **2014,** *114*, 3381-3465; (c) Amin, M.; Vogt, L.; Szejgis, W.; Vassiliev, S.; Brudvig, G. W.; Bruce, D.; Gunner, M. R. *J. Phys. Chem. B* **2015,** *119*, 7366-7377.
5. Suga, M.; Akita, F.; Sugahara, M.; Kubo, M.; Nakajima, Y.; Nakane, T.; Yamashita, K.; Umena, Y.; Nakabayashi, M.; Yamane, T.; Nakano, T.; Suzuki, M.; Masuda, T.; Inoue, S.; Kimura, T.; Nomura, T.; Yonekura, S.; Yu, L.-J.; Sakamoto, T.; Motomura, T.; Chen, J.-H.; Kato, Y.; Noguchi, T.; Tono, K.; Joti, Y.; Kameshima, T.; Hatsui, T.; Nango, E.; Tanaka, R.; Naitow, H.; Matsuura, Y.; Yamashita, A.; Yamamoto, M.; Nureki, O.; Yabashi, M.; Ishikawa, T.; Iwata, S.; Shen, J.-R. *Nature* **2017,** *543*, 131-135.
6. (a) Oyala, P. H.; Stich, T. A.; Stull, J. A.; Yu, F.; Pecoraro, V. L.; Britt, R. D. *Biochemistry* **2014,** *53*, 7914-7928; (b) Sjöholm, J.; Styring, S.; Havelius, K. G. V.; Ho, F. M. *Biochemistry* **2012,** *51*, 2054-2064; (c) Asada, M.; Nagashima, H.; Koua, F. H. M.; Shen, J.-R.; Kawamori, A.; Mino, H. *BBA - Bioenergetics* **2013,** *1827*, 438-445; (d) Krewald, V.; Retegan, M.; Cox, N.; Messinger, J.; Lubitz, W.; DeBeer, S.; Neese, F.; Pantazis, D. A. *Chemical Science* **2015,** *6*, 1676-1695; (e) Pérez Navarro, M.; Ames, W. M.; Nilsson, H.; Lohmiller, T.; Pantazis, D. A.; Rapatskiy, L.; Nowaczyk, M. M.; Neese, F.; Boussac, A.; Messinger, J.; Lubitz, W.; Cox, N. *Proc. Natl. Acad. Sci.* **2013,** *110*, 15561-15566; (f) Lohmiller, T.; Krewald, V.; Sedoud, A.; Rutherford, A. W.; Neese, F.; Lubitz, W.; Pantazis, D. A.; Cox, N. *J. Am. Chem. Soc.* **2017,** *139*, 14412-14424; (g) Lohmiller, T.; Krewald, V.; Navarro, M. P.; Retegan, M.; Rapatskiy, L.; Nowaczyk, M. M.; Boussac, A.; Neese, F.; Lubitz, W.; Pantazis, D. A.; Cox, N. *Phys. Chem. Chem. Phys.* **2014,** *16*, 11877-11892; (h) Peloquin, J. M.; Campbell, K. A.; Randall, D. W.; Evanchik, M. A.; Pecoraro, V. L.; Armstrong, W. H.; Britt, R. D. *J. Am. Chem. Soc.* **2000,** *122*, 10926-10942; (i) Rapatskiy, L.; Cox, N.; Savitsky, A.; Ames, W. M.; Sander, J.; Nowaczyk, M. M.; Rögner, M.; Boussac, A.; Neese, F.; Messinger, J.; Lubitz, W. *J. Am. Chem. Soc.* **2012,** *134*, 16619-16634; (j) Pokhrel, R.; Brudvig, G. W. *Phys. Chem. Chem. Phys.* **2014,** *16*, 11812-11821; (k) Cox, N.; Retegan, M.; Neese, F.; Pantazis, D. A.; Boussac, A.; Lubitz, W. *Science* **2014,** *345*, 804-808.
7. (a) Zaharieva, I.; Chernev, P.; Berggren, G.; Anderlund, M.; Styring, S.; Dau, H.; Haumann, M. *Biochemistry* **2016,** *55*, 4197-4211; (b) Zaharieva, I.; Dau, H.; Haumann, M. *Biochemistry* **2016,** *55*, 6996-7004; (c) Petrie, S.; Stranger, R.; Pace, R. J. *Phys. Chem. Chem. Phys.* **2017,** *19*, 27682-27693; (d) Kubin, M.; Kern, J.; Gul, S.; Kroll, T.; Chatterjee, R.; Löchel, H.; Fuller, F. D.; Sierra, R. G.; Quevedo, W.; Weniger, C.; Rehanek, J.; Firsov, A.; Laksmono, H.; Weninger, C.; Alonso-Mori, R.; Nordlund, D. L.; Lassalle-Kaiser, B.; Glownia, J. M.; Krzywinski, J.; Moeller, S.; Turner, J. J.; Minitti, M. P.; Dakovski, G. L.; Koroidov, S.; Kawde, A.; Kanady, J. S.; Tsui, E. Y.; Suseno, S.; Han, Z.; Hill, E.; Taguchi, T.; Borovik, A. S.; Agapie, T.; Messinger, J.; Erko, A.; Föhlisch, A.; Bergmann, U.; Mitzner, R.; Yachandra, V. K.; Yano, J.; Wernet, P. *Structural Dynamics* **2017,** *4*, 054307.
8. (a) Rossini, E.; Knapp, E.-W. *Coord. Chem. Rev.* **2017,** *345*, 16-30; (b) Siegbahn, P. E. M. *BBA - Bioenergetics* **2013,** *1827*, 1003-1019.
9. (a) Noguchi, T. *BBA - Bioenergetics* **2015,** *1847*, 35-45; (b) Suzuki, H.; Sugiura, M.; Noguchi, T. *J. Am. Chem. Soc.* **2009,** *131*, 7849-7857; (c) Debus, R. J. *BBA - Bioenergetics* **2015,** *1847*, 19-34; (d) Kim, C. J.; Debus, R. J. *Biochemistry* **2017,** *56*, 2558-2570; (e) Polander, B. C.; Barry, B. A. *Proc. Natl. Acad. Sci.* **2012,** *109*, 6112.

10. (a) Siegbahn, P. E. M. *Phys. Chem. Chem. Phys.* **2012,** *14*, 4849-4856; (b) Ichino, T.; Yoshioka, Y. *Chem. Phys. Lett.* **2014,** *595–596*, 237-241; (c) Sproviero, E. M.; Gascón, J. A.; McEvoy, J. P.; Brudvig, G. W.; Batista, V. S. *J. Am. Chem. Soc.* **2008,** *130*, 3428-3442; (d) Yamaguchi, K.; Isobe, H.; Yamanaka, S.; Saito, T.; Kanda, K.; Shoji, M.; Umena, Y.; Kawakami, K.; Shen, J. R.; Kamiya, N.; Okumura, M. *Int. J. Quantum Chem* **2013,** *113*, 525-541.
11. (a) Massie, A. A.; Denler, M. C.; Cardoso, L. T.; Walker, A. N.; Hossain, M. K.; Day, V. W.; Nordlander, E.; Jackson, T. A. *Angew. Chem. Int. Ed.* **2017,** *56*, 4178-4182; (b) Wijeratne, G. B.; Corzine, B.; Day, V. W.; Jackson, T. A. *Inorg. Chem.* **2014,** *53*, 7622-7634; (c) Yin, G.; Danby, A. M.; Kitko, D.; Carter, J. D.; Scheper, W. M.; Busch, D. H. *J. Am. Chem. Soc.* **2008,** *130*, 16245-16253; (d) Kurahashi, T.; Kikuchi, A.; Shiro, Y.; Hada, M.; Fujii, H. *Inorg. Chem.* **2010,** *49*, 6664-6672; (e) Hong, S.; Lee, Y.-M.; Sankaralingam, M.; Vardhaman, A. K.; Park, Y. J.; Cho, K.-B.; Ogura, T.; Sarangi, R.; Fukuzumi, S.; Nam, W. *J. Am. Chem. Soc.* **2016,** *138*, 8523-8532; (f) Chen, J.; Cho, K.-B.; Lee, Y.-M.; Kwon, Y. H.; Nam, W. *Chem. Commun.* **2015,** *51*, 13094-13097; (g) Chen, J.; Lee, Y.-M.; Davis, K. M.; Wu, X.; Seo, M. S.; Cho, K.-B.; Yoon, H.; Park, Y. J.; Fukuzumi, S.; Pushkar, Y. N.; Nam, W. *J. Am. Chem. Soc.* **2013,** *135*, 6388-6391; (h) Chen, J.; Yoon, H.; Lee, Y.-M.; Seo, M. S.; Sarangi, R.; Fukuzumi, S.; Nam, W. *Chemical Science* **2015,** *6*, 3624-3632; (i) Barman, P.; Vardhaman, A. K.; Martin, B.; Wörner, S. J.; Sastri, C. V.; Comba, P. *Angew. Chem. Int. Ed.* **2015,** *54*, 2095-2099; (j) Yin, G. *Acc. Chem. Res.* **2013,** *46*, 483-492.
12. (a) Parsell, T. H.; Yang, M.-Y.; Borovik, A. S. *J. Am. Chem. Soc.* **2009,** *131*, 2762-2763; (b) Gupta, R.; MacBeth, C. E.; Young, V. G.; Borovik, A. S. *J. Am. Chem. Soc.* **2002,** *124*, 1136-1137; (c) Gupta, R.; Borovik, A. S. *J. Am. Chem. Soc.* **2003,** *125*, 13234-13242; (d) Taguchi, T.; Stone, K. L.; Gupta, R.; Kaiser-Lassalle, B.; Yano, J.; Hendrich, M. P.; Borovik, A. S. *Chemical Science* **2014,** *5*, 3064-3071; (e) Goldsmith, C. R.; Cole, A. P.; Stack, T. D. P. *J. Am. Chem. Soc.* **2005,** *127*, 9904-9912; (f) Coggins, M. K.; Brines, L. M.; Kovacs, J. A. *Inorg. Chem.* **2013,** *52*, 12383-12393; (g) Yin, G.; Danby, A. M.; Kitko, D.; Carter, J. D.; Scheper, W. M.; Busch, D. H. *J. Am. Chem. Soc.* **2007,** *129*, 1512-1513; (h) Gardner, K. A.; Kuehnert, L. L.; Mayer, J. M. *Inorg. Chem.* **1997,** *36*, 2069-2078; (i) Lassalle-Kaiser, B.; Hureau, C.; Pantazis, D. A.; Pushkar, Y.; Guillot, R.; Yachandra, V. K.; Yano, J.; Neese, F.; Anxolabehere-Mallart, E. *Energy & Environmental Science* **2010,** *3*, 924-938; (j) Wang, Y.; Sheng, J.; Shi, S.; Zhu, D.; Yin, G. *The Journal of Physical Chemistry C* **2012,** *116*, 13231-13239; (k) Baglia, R. A.; Prokop-Prigge, K. A.; Neu, H. M.; Siegler, M. A.; Goldberg, D. P. *J. Am. Chem. Soc.* **2015,** *137*, 10874-10877.
13. (a) Gupta, R.; Taguchi, T.; Lassalle-Kaiser, B.; Bominaar, E. L.; Yano, J.; Hendrich, M. P.; Borovik, A. S. *Proc. Natl. Acad. Sci.* **2015,** *112*, 5319-5324; (b) Leto, D. F.; Massie, A. A.; Rice, D. B.; Jackson, T. A. *J. Am. Chem. Soc.* **2016,** *138*, 15413-15424; (c) Leto, D. F.; Ingram, R.; Day, V. W.; Jackson, T. A. *Chem. Commun.* **2013,** *49*, 5378-5380; (d) Yin, G.; McCormick, J. M.; Buchalova, M.; Danby, A. M.; Rodgers, K.; Day, V. W.; Smith, K.; Perkins, C. M.; Kitko, D.; Carter, J. D.; Scheper, W. M.; Busch, D. H. *Inorg. Chem.* **2006,** *45*, 8052-8061; (e) Park, Y. J.; Matson, E. M.; Nilges, M. J.; Fout, A. R. *Chem. Commun.* **2015,** *51*, 5310-5313.
14. (a) Wang, K.; Mayer, J. M. *J. Am. Chem. Soc.* **1997,** *119*, 1470-1471; (b) Baldwin, M. J.; Pecoraro, V. L. *J. Am. Chem. Soc.* **1996,** *118*, 11325-11326; (c) Sankaralingam, M.; Jeon, S. H.; Lee, Y.-M.; Seo, M. S.; Ohkubo, K.; Fukuzumi, S.; Nam, W. *Dalton Transactions* **2016,** *45*, 376-383; (d) Carrell, T. G.; Bourles, E.; Lin, M.; Dismukes, G. C. *Inorg. Chem.* **2003,** *42*, 2849-2858; (e) Thorp, H. H.; Sarneski, J. E.; Brudvig, G. W.; Crabtree, R. H. *J. Am. Chem. Soc.* **1989,** *111*, 9249-9250; (f) Amin, M.; Vogt, L.; Vassiliev, S.; Rivalta, I.; Sultan, M. M.; Bruce, D.; Brudvig, G. W.; Batista, V. S.; Gunner, M. R. *J. Phys. Chem. B* **2013,** *117*, 6217-6226.
15. (a) Caudle, M. T.; Pecoraro, V. L. *J. Am. Chem. Soc.* **1997,** *119*, 3415-3416; (b) Cady, C. W.; Shinopoulos, K. E.; Crabtree, R. H.; Brudvig, G. W. *Dalton Transactions* **2010,** *39*, 3985-3989.
16. Tsui, E. Y.; Kanady, J. S.; Agapie, T. *Inorg. Chem.* **2013,** *52*, 13833-13848.
17. (a) Herbert, D. E.; Lionetti, D.; Rittle, J.; Agapie, T. *J. Am. Chem. Soc.* **2013,** *135*, 19075-19078; (b) Tsui, E. Y.; Tran, R.; Yano, J.; Agapie, T. *Nature Chemistry* **2013,** *5*, 293-299; (c) Tsui, E. Y.; Agapie, T. *Proc. Natl. Acad. Sci.* **2013,** *110*, 10084-10088; (d) Kanady, J. S.; Tsui, E. Y.; Day, M. W.; Agapie, T. *Science* **2011,** *333*, 733-736; (e) Lin, P.-H.; Takase, M. K.; Agapie, T. *Inorg. Chem.* **2015,** *54*, 59-64.

18. (a) de Ruiter, G.; Thompson, N. B.; Lionetti, D.; Agapie, T. *J. Am. Chem. Soc.* **2015,** *137*, 14094-14106; (b) Reed, C. J.; Agapie, T. *Inorg. Chem.* **2017,** *56*, 13360-13367; (c) Arnett, C. H.; Chalkley, M. J.; Agapie, T. *J. Am. Chem. Soc.* **2018,** *140*, 5569-5578; (d) de Ruiter, G.; Thompson, N. B.; Takase, M. K.; Agapie, T. *J. Am. Chem. Soc.* **2016,** *138*, 1486-1489; (e) de Ruiter, G.; Carsch, K. M.; Gul, S.; Chatterjee, R.; Thompson, N. B.; Takase, M. K.; Yano, J.; Agapie, T. *Angew. Chem. Int. Ed.* **2017,** *56*, 4772-4776; (f) Carsch, K. M.; de Ruiter, G.; Agapie, T. *Inorg. Chem.* **2017,** *56*, 9044-9054.
19. Han, Z.; Horak, K. T.; Lee, H. B.; Agapie, T. *J. Am. Chem. Soc.* **2017,** *139*, 9108-9111.
20. Lionetti, D. Heterometallic Complexes as Models of Enzymatic Active Sites. PhD dissertation, California Institute of Technology, Pasadena, California, 2015.
21. (a) Sivanesan, D.; Kannan, S.; Thangadurai, T. D.; Jung, K.-D.; Yoon, S. *Dalton Transactions* **2014,** *43*, 11465-11469; (b) Chen, L.-Z.; Huang, D.-D.; Ge, J.-Z.; Pan, Q.-J. *J. Mol. Struct.* **2014,** *1072*, 307-312; (c) Rich, J.; Rodriguez, M.; Romero, I.; Vaquer, L.; Sala, X.; Llobet, A.; Corbella, M.; Collomb, M.-N.; Fontrodona, X. *Dalton Transactions* **2009**, 8117-8126.
22. Garrido, G.; Koort, E.; Ràfols, C.; Bosch, E.; Rodima, T.; Leito, I.; Rosés, M. *The Journal of Organic Chemistry* **2006,** *71*, 9062-9067.
23. (a) MacBeth, C. E.; Gupta, R.; Mitchell-Koch, K. R.; Young, V. G.; Lushington, G. H.; Thompson, W. H.; Hendrich, M. P.; Borovik, A. S. *J. Am. Chem. Soc.* **2004,** *126*, 2556-2567; (b) Shirin, Z.; Hammes, B. S.; Young, V. G.; Borovik, A. S. *J. Am. Chem. Soc.* **2000,** *122*, 1836-1837; (c) Shirin, Z.; S. Borovik, A.; G. Young Jr, V. *Chem. Commun.* **1997**, 1967-1968; (d) Shook, R. L.; Peterson, S. M.; Greaves, J.; Moore, C.; Rheingold, A. L.; Borovik, A. S. *J. Am. Chem. Soc.* **2011,** *133*, 5810-5817; (e) Lacy, D. C.; Mukherjee, J.; Lucas, R. L.; Day, V. W.; Borovik, A. S. *Polyhedron* **2013,** *52*, 261-267.
24. (a) Baglia, R. A.; Krest, C. M.; Yang, T.; Leeladee, P.; Goldberg, D. P. *Inorg. Chem.* **2016,** *55*, 10800-10809; (b) Leeladee, P.; Baglia, R. A.; Prokop, K. A.; Latifi, R.; de Visser, S. P.; Goldberg, D. P. *J. Am. Chem. Soc.* **2012,** *134*, 10397-10400; (c) Bougher, C. J.; Liu, S.; Hicks, S. D.; Abu-Omar, M. M. *J. Am. Chem. Soc.* **2015,** *137*, 14481-14487.
25. (a) Cappellani, E. P.; Drouin, S. D.; Jia, G.; Maltby, P. A.; Morris, R. H.; Schweitzer, C. T. *J. Am. Chem. Soc.* **1994,** *116*, 3375-3388; (b) Tilset, M. The Thermodynamics of Organometallic Systems Involving Electron-Transfer Paths. In *Electron Transfer in Chemistry, 1*, Balzani, V., Ed. Wiley-VCH: Weinheim, Germany, 2001; pp 677-713.
26. (a) Bordwell, F. G.; Satish, A. V.; Zhang, S.; Zhang, X. M. Using thermodynamic cycles to study reactive intermediates. In *Pure Appl. Chem.*, 1995; Vol. 67, p 735; (b) Mayer, J. M. *Acc. Chem. Res.* **1998,** *31*, 441-450; (c) Warren, J. J.; Tronic, T. A.; Mayer, J. M. *Chem. Rev.* **2010,** *110*, 6961-7001.
27. (a) Pourbaix, M. *Atlas of Electrochemical Equilibria in Aqueous Solutions*. 1st English ed.; Pergamon Press: Oxford, New York, 1966; (b) Slattery, S. J.; Blaho, J. K.; Lehnes, J.; Goldsby, K. A. *Coord. Chem. Rev.* **1998,** *174*, 391-416.
28. (a) Bozoglian, F.; Romain, S.; Ertem, M. Z.; Todorova, T. K.; Sens, C.; Mola, J.; Rodríguez, M.; Romero, I.; Benet-Buchholz, J.; Fontrodona, X.; Cramer, C. J.; Gagliardi, L.; Llobet, A. *J. Am. Chem. Soc.* **2009,** *131*, 15176-15187; (b) Nunes, G. S.; Alexiou, A. D. P.; Araki, K.; Formiga, A. L. B.; Rocha, R. C.; Toma, H. E. *Eur. J. Inorg. Chem.* **2006,** *2006*, 1487-1495; (c) Gilbert, J. A.; Eggleston, D. S.; Murphy, W. R.; Geselowitz, D. A.; Gersten, S. W.; Hodgson, D. J.; Meyer, T. J. *J. Am. Chem. Soc.* **1985,** *107*, 3855-3864; (d) Isobe, H.; Tanaka, K.; Shen, J.-R.; Yamaguchi, K. *Inorg. Chem.* **2014,** *53*, 3973-3984.
29. McCarthy, B. D.; Dempsey, J. L. *Inorg. Chem.* **2017,** *56*, 1225-1231.
30. The redox couple that would be assigned to the 7-[BArF] to 8-[BArF] reduction potential unexpectedly increases, inconsistent with PCET to Mn=O and may suggest an undesirable side reaction takes place at these potentials with the base employed.
31. Attempts to obtain supporting data via stoichiometric deprotonation of 7-[BArF4] with various bases led to decomposition via reduction, with no evidence of forming a transient Mn=O moiety. Investigations into the characterization and reactivity of these putative M=O species (M = Fe, Mn) in these and related clusters is ongoing.
32. Riedel, P. J.; Arulsamy, N.; Mehn, M. P. *Inorg. Chem. Commun.* **2011,** *14*, 734-737.
33. Izod, K.; Rayner, D. G.; El-Hamruni, S. M.; Harrington, R. W.; Baisch, U. *Angew. Chem. Int. Ed.* **2014,** *53*, 3636-3640.

34. Huang, C.-Y.; Doyle, A. G. *J. Am. Chem. Soc.* **2012,** *134*, 9541-9544.
35. Zhang, Y.; Santos, A. M.; Herdtweck, E.; Mink, J.; Kuhn, F. E. *New J. Chem.* **2005,** *29*, 366-370.
36. Manner, V. W.; Markle, T. F.; Freudenthal, J. H.; Roth, J. P.; Mayer, J. M. *Chem. Commun.* **2008**, 256-258.
37. Thomson, R. K.; Scott, B. L.; Morris, D. E.; Kiplinger, J. L. *Comptes Rendus Chimie* **2010,** *13*, 790-802.
38. (a) Herold, S.; Lippard, S. J. *Inorg. Chem.* **1997,** *36*, 50-58; (b) Singh, A. K.; Jacob, W.; Boudalis, A. K.; Tuchagues, J.-P.; Mukherjee, R. *Eur. J. Inorg. Chem.* **2008,** *2008*, 2820-2829; (c) Sutradhar, M.; Carrella, L. M.; Rentschler, E. *Eur. J. Inorg. Chem.* **2012,** *2012*, 4273-4278; (d) Schünemann, V.; Hauke, P. Mössbauer Spectroscopy. In *Applications of Physical Methods to Inorganic and Bioinorganic Chemistry*, Scott, R. A.; Lukehart, C. M., Eds. John Wiley & Sons: West Sussex, England, 2007; pp 243-269.

CHAPTER 4

A TERMINAL FE^{III}-OXO IN A TETRANUCLEAR CLUSTER: EFFECTS OF DISTAL METAL CENTERS ON STRUCTURE AND REACTIVITY

The text for this chapter was reproduced in part from:

Reed, C. J.; Agapie, T. *J. Am. Chem. Soc.*., **2019**, *Accepted Manuscript.* doi:10.1021/jacs.9b03157

ABSTRACT

Tetranuclear Fe clusters have been synthesized bearing a terminal Fe^{III}-oxo center stabilized by hydrogen bonding interactions from pendant *tert*-butyl amino pyrazolate ligands. This motif was supported in multiple Fe oxidation states, ranging from $[Fe^{II}_2Fe^{III}_2]$ to $[Fe^{III}_4]$; two oxidation states were structurally characterized by single crystal X-ray diffraction. The reactivity of the Fe^{III}-oxo center in proton coupled electron transfer (PCET) with X–H (X = C, O) bonds of various strengths was studied in conjunction with analysis of thermodynamic square schemes of the cluster oxidation states. These results demonstrate the important role adjacent metal centers have on modulating the reactivity of a terminal metal-oxo.

INTRODUCTION

Terminal metal-oxo moieties are invoked as key intermediates in both natural and synthetic catalysts of mid-first-row transition metal ions (Mn, Fe, and Co).[1] For example in photosynthesis, water is oxidized in photosystem II by a $CaMn_4O_5$ cluster known as the oxygen evolving complex (OEC);[2] numerous computational studies of the catalytic mechanism have proposed a high-valent Mn-oxo playing a key role in O–O bond formation.[3] Similarly, a number of synthetic water oxidation catalysts employing various multinuclear scaffolds have been reported, where a terminal metal-oxo is implicated as a key intermediate (Figure 1).[1e-g, 4]

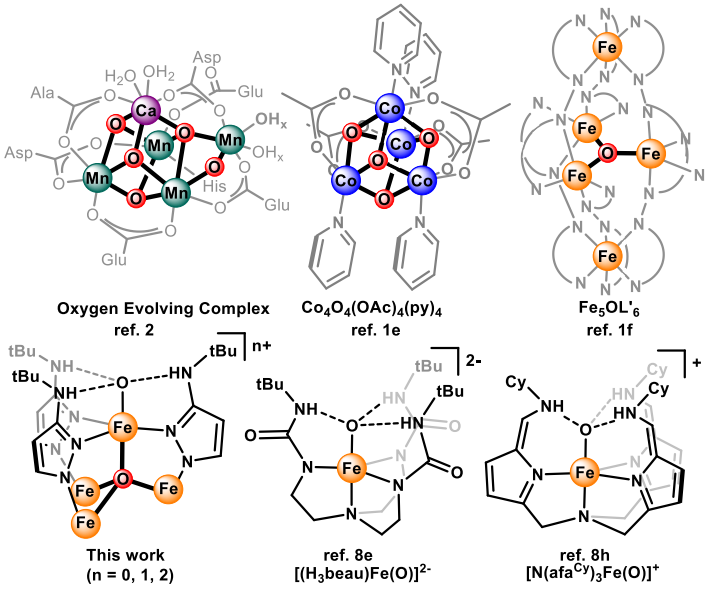

Figure 1. Multinuclear catalysts with proposed terminal metal-oxo intermediates (top), and structurally characterized terminal Fe^{III}-oxo complexes (bottom).

Studies of synthetic transition metal-oxo complexes have been integral for understanding these reactive moieties in catalytic systems.[1a, 5] However, there is a paucity of literature concerning multinuclear complexes bearing well-characterized terminal metal-oxo motifs.[6] In a rare example where the effects of a neighboring metal oxidation state on a terminal metal-oxo could be interrogated, Que and coworkers reported that the spin state of an Fe^{IV}-oxo

center would change depending on the oxidation state of a neighboring Fe in a μ_2-O bridged bimetallic complex ($L'_2OFe_2(OH)(O)^{2+/3+}$).[6c] The authors demonstrated that structural and spin-state changes due to reduction of this secondary Fe leads to a thousand-fold activation of the [Fe_2] complex towards C–H oxidation.

To gain further insight into these multimetallic effects, previous group members, Dr. Graham de Ruiter and Kurtis Carsch, studied the reactivity of Fe_4, Fe_3Mn, and Mn_4 clusters, bearing aryl-substituted pyrazolate ligands, towards oxygen atom transfer reagents; in all cases, intramolecular C–H (or C–F) activation occurs, forming a five-coordinate apical metal with a phenoxypyrazolate donor.[7] Analysis of the reaction mechanism were consistent with rate-limiting iodosylarene activation step, producing a transient reactive moiety (either iodosylarene adduct or terminal-oxo) that could not be directly observed. Inspired by reports of mononuclear terminal metal-oxo motifs stabilized by second coordination sphere hydrogen bonding interactions,[8] our group has previously used this strategy to access a terminal Mn^{III}–OH moiety as part of a [Mn_4] cluster.[9] Dr. Kyle Horak was able to serendipitously isolate the analogous Fe cluster, **[$LFe_3O(PzNHPh)_3Fe(OH)$][OTf]**, however, there were challenges with accessing this cluster in reasonable purity and yield.[10] Due to the observed difficulties in supporting clusters with the amino-phenylpyrazolate ligand, new amino-pyrazolate donors were investigated. Herein, we describe the synthesis, structural characterization, and reactivity studies of clusters bearing a terminal Fe^{III}-oxo motif, stabilized by *tert*-butyl-amino-pyrazolates, to probe the significance of a multinuclear scaffold on structural and reactivity aspects of a terminal metal-oxo.

Scheme 1. Previous Efforts Towards Isolation of a Terminal Metal-Oxo in a Multinuclear System by the Agapie Group

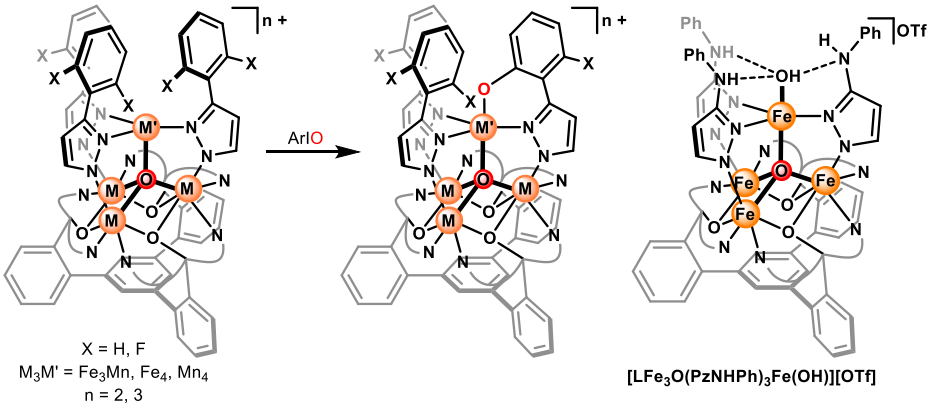

RESULTS AND DISCUSSION

Synthesis of Fe_4-Hyroxide and Fe_4-Oxo Clusters. Treatment of the reported **$LFe_3(OAc)(OTf)_2$** cluster (OTf, triflate = trifluoromethane sulfonate)[11] with three equivalents of potassium *tert*-butyl-amino-pyrazolate (KPzNHtBu) and iodosylbenzene (PhIO), followed by addition of iron (II) triflate bis-acetonitrile ($Fe(OTf)_2$ • 2 MeCN) and excess potassium hydroxide in tetrahydrofuran (THF) produces the neutral [$Fe^{II}_3Fe^{III}$] cluster, **1** (Scheme 2). Single crystal X-ray diffraction (XRD) studies of **1** reveal a structure similar to our previously reported [Mn_4] cluster bearing a terminal hydroxide ligand (Figure 2);[9] the apical metal displays a trigonal bipyramidal geometry, with the terminal hydroxide ligand hydrogen bonded to each amino-pyrazolate (N–O distances of 2.826(1), 2.765(1), 2.789(1) Å for **1**). The relatively short distance between the apical Fe and the interstitial μ_4-O (Fe4–O1), 1.837(1) Å, is consistent with an Fe^{III} in the apical position of the cluster, with the remaining Fe centers being Fe^{II}.[7a, 12]

Scheme 2. Synthesis of [Fe$_4$] clusters. (Inset) 1,3,5-triarylbenzene ligand (L^{3-}) and *tert*-butyl amino pyrazolate ligand (PzNHtBu$^-$).

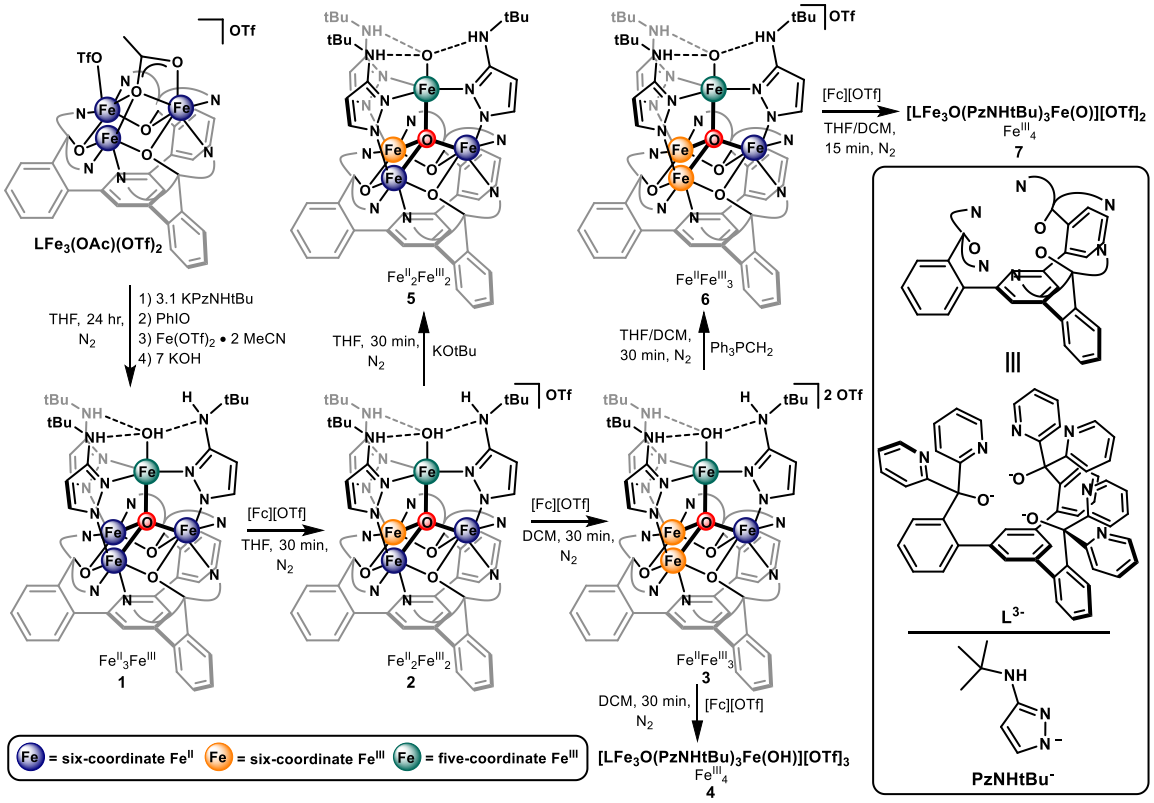

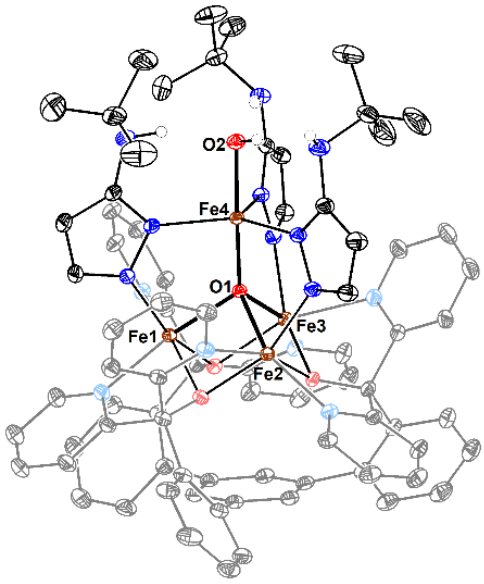

Figure 2. Crystal structure of **1**. Ellipsoids are shown at the 50% probability level. Hydrogen atoms and solvent molecules removed for clarity.

The electrochemistry of the [Fe_4] hydroxide clusters in THF features three quasi-reversible events assigned to the [$Fe^{II}_3Fe^{III}$]→[$Fe^{II}_2Fe^{III}_2$] (-1.53 V; all potentials vs. Fc/Fc^+), [$Fe^{II}_2Fe^{III}_2$]→[$Fe^{II}Fe^{III}_3$] (-0.68 V), and [$Fe^{II}Fe^{III}_3$]→[Fe^{III}_4] (-0.10 V) redox couples (Figure 3). Each of the corresponding oxidation states of the cluster could be isolated (Scheme 1). Mössbauer spectra of the oxidized clusters **2**, **3**, and **4** are consistent with oxidations occurring at the Fe^{II} centers in the tri-iron core and the Fe–OH moiety remaining Fe^{III} (Figure 4 and Table 1).

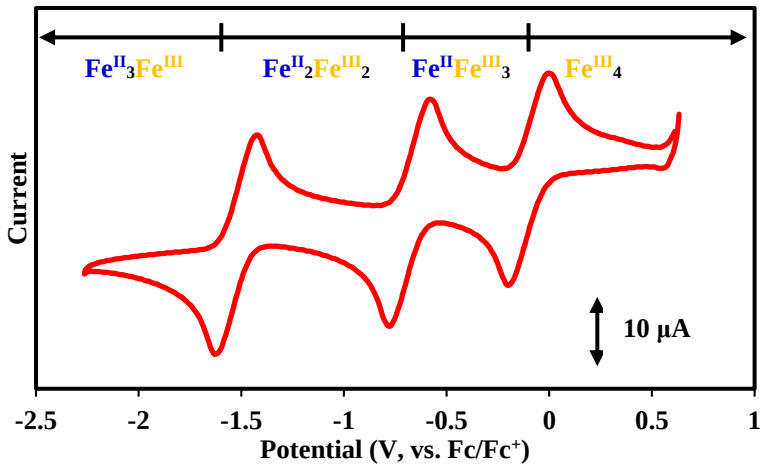

Figure 3. Cyclic voltammetry of **2**, (2.5 mM) at 50 mV/s in THF with a glassy carbon working, platinum counter, and silver wire reference electrodes and ca. 200 mM [Bu_4N][PF_6].

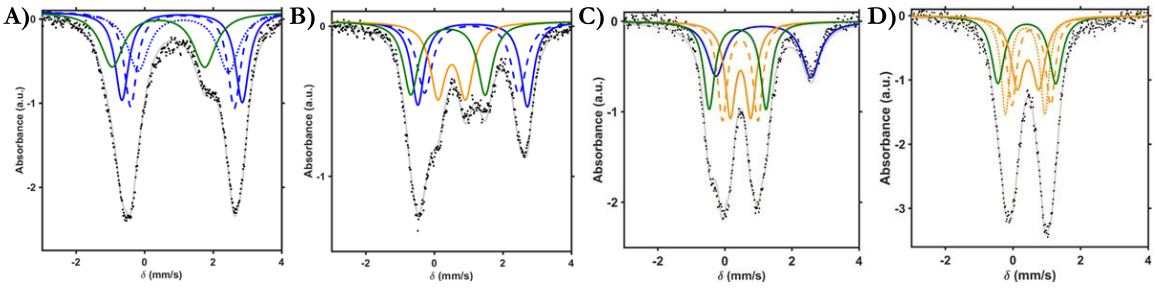

Figure 4. Mössbauer spectra of (A) **1**, (B) **2**, (C) **3**, and (D) **4**; see parameters in Table 1.

Table 1. ^{57}Fe Mössbauer Parameters for Complexes 1 – 4.

	δ (mm/s)	$\|\Delta E_q\|$ (mm/s)	assign-ment
1 ($Fe^{II}_3Fe^{III}$)			
Fe1, Fe2, Fe3	1.10, 1.11, 1.13	3.52, 3.03, 2.64	*h.s.* Fe^{II}
Fe4	0.41	2.71	apical Fe^{III}
2 ($Fe^{II}_2Fe^{III}_2$)			
Fe1, Fe2	1.12, 1.10	3.20, 2.76	*h.s.* Fe^{II}
Fe3	0.52	0.81	*h.s.* Fe^{III}
Fe4	0.41	2.17	apical Fe^{III}
3 ($Fe^{II}Fe^{III}_3$)			
Fe1	1.15	2.83	*h.s.* Fe^{II}
Fe2, Fe3	0.47, 0.46	0.61, 1.06	*h.s.* Fe^{III}
Fe4	0.38	1.69	apical Fe^{III}
4 (Fe^{III}_4)			
Fe1, Fe2, Fe3	0.45, 0.53, 0.36	0.64, 1.15, 1.17	*h.s.* Fe^{III}
Fe4	0.41	1.71	*a*pical Fe^{III}

Access to a terminal Fe^{III}-oxo moiety was achieved by deprotonation of the $[Fe^{II}_2Fe^{III}_2]$ hydroxide cluster, **2**, with potassium *tert*-butoxide (KO*t*Bu; Scheme 1). The resulting compound, **5**, was crystallographically characterized (Figure 5); deprotonation of the hydroxide ligand leads to structural changes to the apical Fe in **5**. The Fe4–O2 distance contracts to 1.817(2) Å, compared to the distances in **1** (1.937(1) Å) and the precursor **2** (1.907(3) Å); this bond length matches closely with the structurally characterized Fe^{III}-oxo complexes reported by Borovik and Fout.[8e, 8h, 8i] Compound **6**, prepared by deprotonating **3**, also displays a short Fe4–O2 distance (1.795(8) Å). Furthermore, the apical Fe-μ_4-O distance (Fe4–O1) elongates to 1.965(2) Å in **5** and 2.049(7) Å in **6**, from 1.890(3) Å in **2** and 1.948(2) Å in **3**, which is consistent with a greater trans influence exerted by the terminal oxo ligand. Terminal Fe^{III}-oxo complexes are rare, and typically stabilized through hydrogen bonding interactions.[8e, 8h, 8i, 13] The structures of **5** and **6** display comparable hydrogen bonding distances

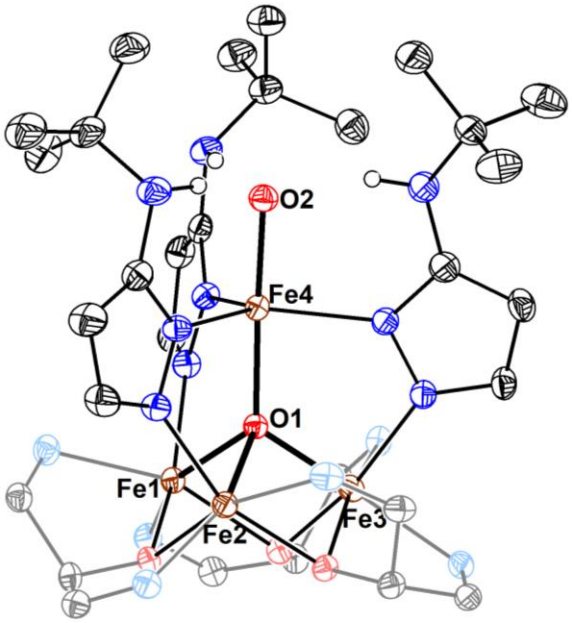

Figure 5. Truncated crystal structure of Fe^{III}-oxo cluster, **5**. Hydrogen atoms and solvent molecules removed for clarity.

Table 2. Selected Bond Distances and Angles, Structural Index Parameter, and Mössbauer Parameters of Reported Fe^{III}-Oxo Complexes

	5	**6**	**$[(H_3beau)Fe(O)]^{2-}$** [8e]	**$[N(afa^{Cy})_3Fe(O)]^{+}$** [8h]
Fe–O (Å)	1.817(2)	1.795(8)	1.813(3)	1.806(1)
$Fe–N_{equatorial}$ (Å)	2.104(2), 2.098(2), 2.093(2)	2.100(8), 2.085(9), 2.087(9)	2.030(4), 2.060(4), 2.082(4)	2.049(1), 2.049(1), 2.052(1)
$Fe–L_{trans}$ (Å)	1.965(2) ($L=O^{2-}$)	2.049(7) ($L=O^{2-}$)	2.271(4) ($L=NR_3$)	2.276(1) ($L=NR_3$)
N–O (H-bond; Å)	2.647, 2.717, 2.685	2.718, 2.790, 2.750	2.732, 2.702, 2.686	2.641, 2.645, 2.673
$\angle N_{equatorial}–Fe–O$ (°)	96.3, 92.8, 92.0	93.6, 97.5, 96.3	103.3, 99.7, 100.8	102.6, 103.1, 103.1
$Fe–N\|N'\|N''_{equatorial}$ (Å)	0.14	0.22	0.42	0.45
Structural Index Parameter (τ)[a]	0.9	0.8	0.5	0.4
Mossbauer parameters (mm/s)	$\delta = 0.43$, $\|\Delta E_q\| = 3.04$	$\delta = 0.47$, $\|\Delta E_q\| = 2.53$	$\delta = 0.30$, $\|\Delta E_q\| = 0.91$	-

[a] $\tau = [\Sigma (\angle N_{equit.}–Fe–N'_{equit.}) - \Sigma (\angle N_{equit.}–Fe–O)]/90$

to other structurally characterized Fe^{III}-oxo complexes, **$[(H_3beau)Fe(O)]^{2-}$** and **$[N(afa^{Cy})_3Fe(O)]^{+}$**, along with similar equatorial Fe–N distances (Table 2). However, the μ_4-O distances in **5** (1.965(2) Å) and **6** (2.049(7) Å) are significantly shorter than the Fe–N

distances for the amine trans to the oxo in the mononuclear systems (~2.27 Å). This is likely a result of greater ligand flexibility in the mononuclear systems; the geometry of these Fe^{III}-oxo complexes display greater deviations from ideal trigonal bipyramidal geometry compared to the apical Fe in **5** and **6**, based on a structural index parameter (τ; ideal trigonal bipyramidal geometry = 1.0). For the clusters reported here, the rigid geometry of the pyrazolate ligands prevents significant distortion of the apical Fe out of the equatorial plane.

Electronic Structure Investigations of Tetranuclear Fe Clusters. The ^{57}Fe Mössbauer spectra of the Fe^{III}-oxo clusters **5** – **7** display relatively unique parameters for the apical Fe, relative to the structurally related Fe^{III}-oxo, where Mössbauer parameters have been reported, **$[(H_3beau)Fe(O)]^{2-}$** (Table 2 and Figure 4).[8e, 14] For example, the Mössbauer parameters assigned to the apical Fe of **5**, δ = 0.43 mm/s and $|\Delta E_Q|$ = 3.04 mm/s, are atypical for high-spin (S= 5/2) Fe^{III} centers, which typically display low quadrupole splitting values. A detailed examination of the electronic structure of the Fe_4 clusters was conducted through magnetic susceptibility measurements and EPR spectroscopy.

Variable temperature, and vaeriable temperature variable field, magnetic susceptibility measusurements were conducted on a series of the thermally stable Fe_4-hydroxide clusters (**2**

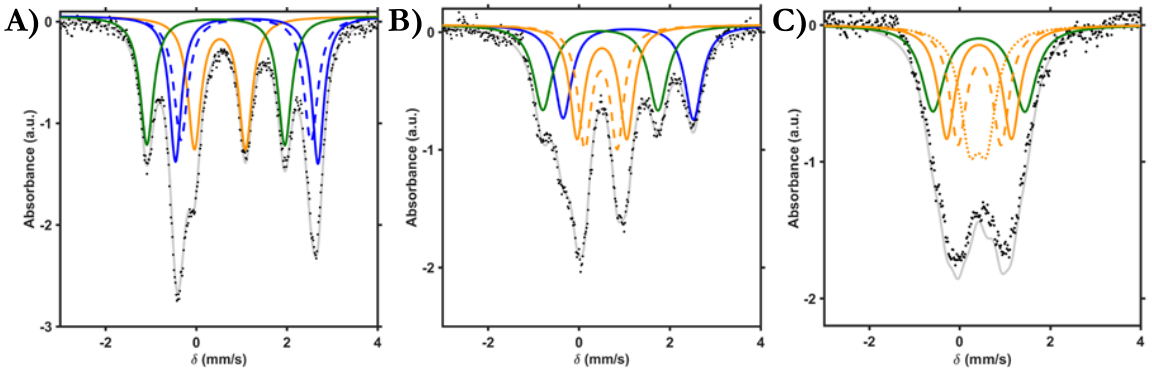

Figure 4. Zero applied-field Mössbauer spectra of (A) **5**, (B) **6**, and (C) **7**. The parameters of each doublet are listed in Table 3.

Table 3. ^{57}Fe Mössbauer Parameters for Complexes 5 – 7.

	δ (mm/s)	$\|\Delta E_q\|$ (mm/s)	assign-ment
5 ($Fe^{II}_3Fe^{III}$)			
Fe1, Fe2	1.12, 1.10	3.14, 2.87	*h.s.* Fe^{II}
Fe3	0.52	1.13	*h.s.* Fe^{III}
Fe4	0.43	3.04	apical Fe^{III}
6 ($Fe^{II}_2Fe^{III}_2$)			
Fe1	1.09	2.87	*h.s.* Fe^{II}
Fe2, Fe3	0.51, 0.49	1.09, 0.72	*h.s.* Fe^{III}
Fe4	0.47	2.53	apical Fe^{III}

	δ (mm/s)	$\|\Delta E_q\|$ (mm/s)	assign-ment
7 (Fe^{III}_4)			
Fe1, Fe2, Fe3	0.43, 0.44, 0.41	1.44, 0.95, 0.38	*h.s.* Fe^{III}
Fe4	0.43	2.03	apical Fe^{III}

– **4**) to establish their electronic ground states (Figure 5) The variable temperature magnetic susceptibility data for these compounds is consistent with high-spin Fe centers composing all cluster redox states for the series; the best fit for each complex is obtained by using exclusively S = 2 Fe^{II} and S = 5/2 Fe^{III}. The spin coupling model for these clusters is similar to that of structurally related high-spin Fe clusters bearing bridging imidazolate ligands, where strong antiferromagnetic coupling between the apical Fe^{III} and the tri-iron core promotes in ferromagnetic alignment of the spins with the remaining three Fe centers (Figure 5B).[12] The variable temperature variable field magnetization data for these compounds can be fit adequately using this coupling scheme, supporting assignments for spin ground states of S = 4, 9/2, and 5 for **2**, **3**, and **4**, respectively (Figure 6). The presence of increasing zero field splitting as **4** is reduced to **3** and **2** is observed in the magnetization data, causing saturation below the expected 2S limit (10 for **4**, 9 for **3**, and 8 for **2**).

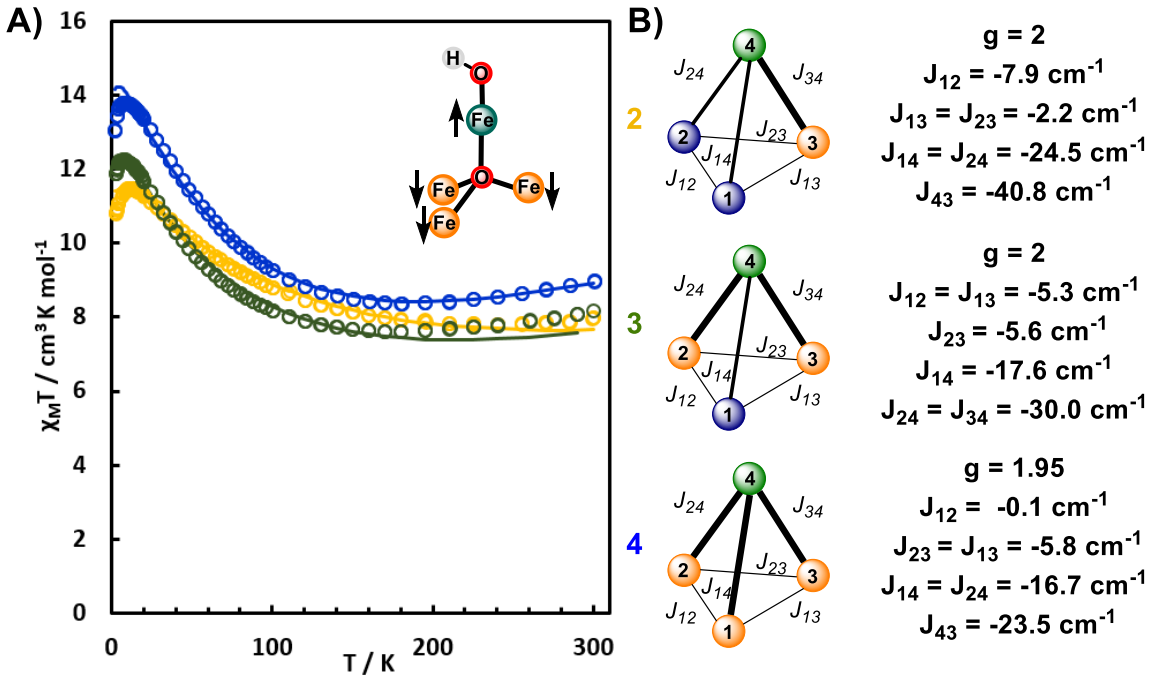

Figure 5. (A) Variable temperature direct current magnetic susceptibility data for Fe4-hydroxide clusters **2** (yellow), **3** (green), and **4** (blue) at 0.1 T. The spin coupling model has strong antiferromagnetic alignment of the apical Fe and the tri-iron core. (B) Simulation of coupling scheme for **2** – **4**, with all metal centers locally high spin.

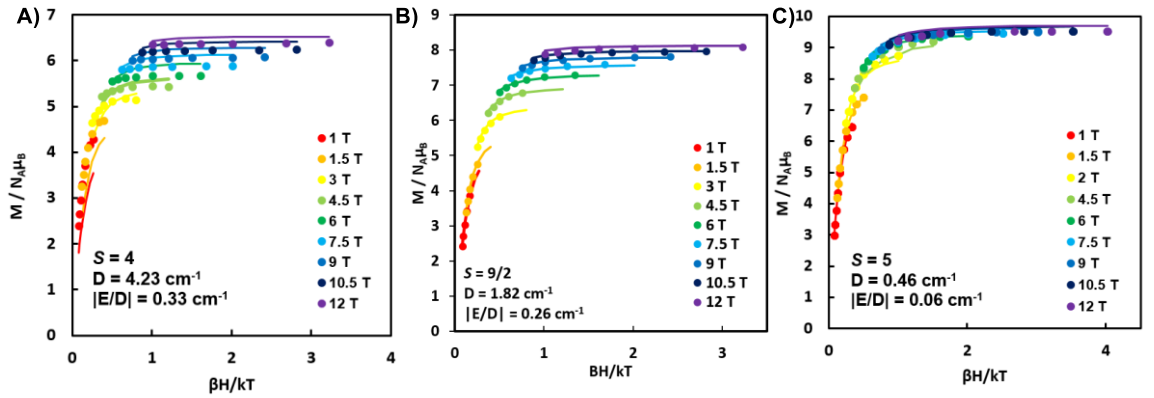

Figure 6. Variable temperature-variable field magnetization data for **2** (A), **3** (B), and **4** (D) from 2.5 K to 8 K. The spin and zero field splitting parameters (S, D, and |E/D|) were used to simulate the data.

Continuous wave EPR spectra of these paramagnetic clusters at low temperature (< 20 K) in frozen solutions display a number of features in regions expected for these high-spin systems (g >16). Figure 7 summarizes the parallel (for integer spin clusters **2**, **4**, **5**, and **7**) and perpendicular (for **3** and **6**) mode data collected. Attempts to simulate these spectra were challenging, even for the complexes where magnetization data was obtained. For example, **2** displays a sharp peak at ca. g = 17 at low temperatures (<15 K), which can be tentatively assigned to the $M_s = \pm 4$ doublet transition (Figure 7A).[12] In contrast, the corresponding $[Fe^{III}_2Fe^{II}_2]$ Fe-oxo cluster, **5**, displays one major transition near g ~ 19, which is consistent with an $S = 4$ or 5 system (Figure 7B). Further studies will examine the field-dependent Mössbauer spectra of these clusters to identify their spin ground states. Even without simulating the EPR data, there are noticable differences for each cluster oxidation state between Fe_4-hydroxide and –oxo, demonstrating the strong influence of the apical ligand on the electronics of the cluster.

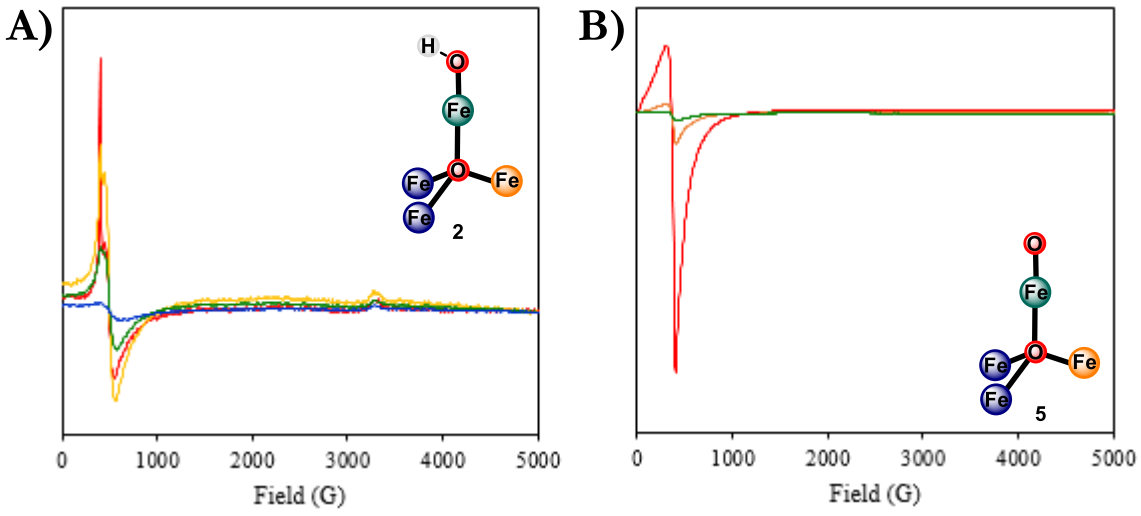

Figure 7. Parallel-mode EPR spectrum in 2-MeTHF of(A) **2** collected at 5 K (red), 10 K (orange), 15 K (green), and 25 K (blue), and (B) **5** at 5 K (red), 10 K (orange), and 15 K (green).

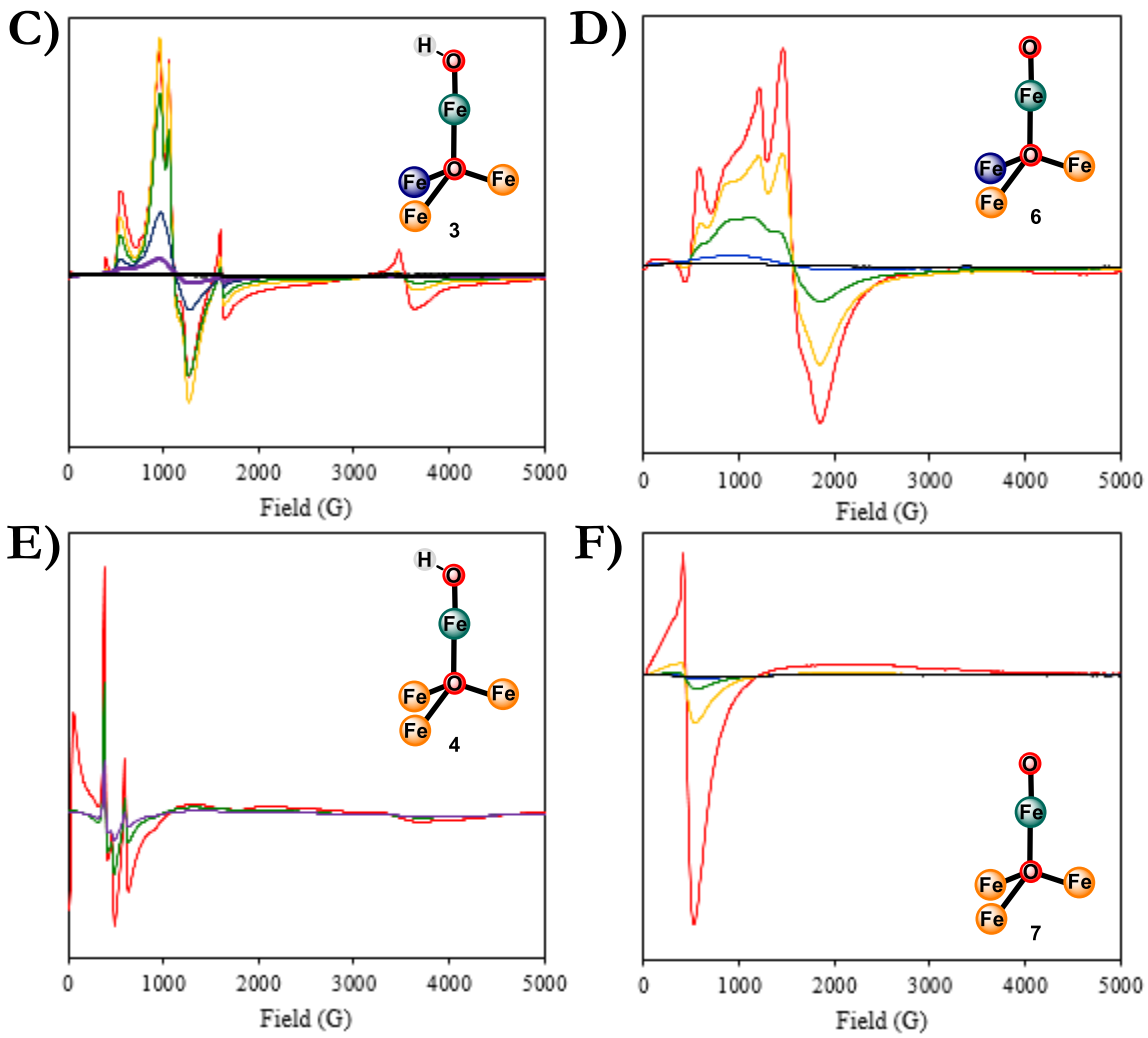

Figure 7 cont. (C) Perpendicular-mode CW-EPR spectrum of **3** collected in EtCN/PrCN at 5 K (red), 7.5 K (orange), 10 K (green), 15 K (blue), 20 K (purple), and 30 K (black). (D) Perpendicular-mode spectrum of **6** collected in EtCN/PrCN at 5 K (red), 7.5 K (orange), 10 K (green), 15 K (blue), and 20 K (black). (E) Parallel-mode spectrum of **4** in EtCN/PrCN at 5 K (red), 10 K (green), and 15 K (purple). (F) Parallel-mode spectrum of **7** in EtCN/PrCN at 5 K (red), 10 K (orange), 15 K (green), and 20 K (black).

---

pK_a and BDE$_{O-H}$ Determination for Fe$_4$-Hydroxide Clusters. The hydroxide ligand in **2** was determined to be very basic in THF (pK_a = 30.1; Table 4). Analogous equilibrium studies were performed on **3** and, as expected, oxidation of the cluster reduces the basicity of the

Fe^{III}-oxo moiety (pK_a = 23.0 for **3**; Table 5). Attempts to deprotonate **4** with various bases, even at low temperatures, only resulted in decomposition, so a pK_a value for this oxidation state was not measured. These data were combined with electrochemical information for clusters **1** (vide supra) and **5** (Figure 8), to produce thermodynamic square schemes according to equation 1 (Figure 9): [15]

$$BDE_{O-H} = 23.06\ E° + 1.37\ pK_a + C \qquad (1)$$

Table 4. pK_a determination of 2 via ^{31}P NMR spectroscopy.[a]

NMR	Equiv. Ph_3PCH_2	Equiv. $[Ph_3PCH_2]^+$	[**5**]/[**2**]	K^b
2 + 1.3 Ph_3PCH_2	~ 1.3	-	n.d.	n.d.
2 + 5 Ph_3PCH_2	4.54	0.46	0.85	0.09
2 + 7 Ph_3PCH_2	6.38	0.62	1.63	0.16
2 + 10 Ph_3PCH_2	9.24	0.76	3.17	0.26
2 + 18 Ph_3PCH_2	16.97	1.03	n.d.	n.d.
			Average *K*	0.17 (±0.09)

[a]The ratio of **2** to **5** was estimated from the relative integrals of the ^{31}P NMR peaks for Ph_3PCH_2 (~15 ppm) and $Ph_3PCH_3^+$ (~18 ppm); it was assumed that the equivalents of $[Ph_3PCH_3]^+$ produced in the NMR were due to partial deprotonation of **2**, and corresponded to equivalents of **5** ([$[Ph_3PCH_3][OTf]$] = [**5**]). [b]An equilibrium constant was determined according to the equation below:

$$K = \frac{[\mathbf{5}][[Ph_3PCH_3][OTf]]}{[\mathbf{2}][Ph_3PCH_2]}$$

where this value, along with the reported pK_a of Ph_3PCH_2 in THF, 29.3, was used to obtain a pK_a value of 30.1 (±1.0) for **2**.[16]

Table 5. pK_a determination of 3 via ^{1}H NMR spectroscopy

NMR	Equiv. **3**[a]	Equiv. **6**[a]	K^b
3 + 1 $tBuP_1$(pyrr)	0.55	0.45	0.70
3 + 5 $tBuP_1$(pyrr)	0.27	0.73	0.46
3 + 10 $tBuP_1$(pyrr)	0.12	0.88	0.71
		Average *K*	0.62 (±0.14)

[a]The ratio of **3** to **6** was based on the relative integrals of the ^{1}H NMR peaks at 17.0 (for **3**) and 14.5 ppm (for **6**); the relative amounts of base and conjugate acid of *tert*-butylimino-tri(pyrrolidino)phosphorene ($tBuP_1$(pyrr)) were assumed based on mass balance. [b]An equilibrium constant was determined according to the equation below:

$$K = \frac{[\mathbf{6}][[H'tBuP_1(pyrr)'][OTf]]}{[\mathbf{3}]['tBuP_1(pyrr)']}$$

where this value, along with the reported pK_a of $tBuP_1$(pyrr) in THF, 22.8, was used to obtain a pK_a value of 23.0 (±1.0) for **3**.[16]

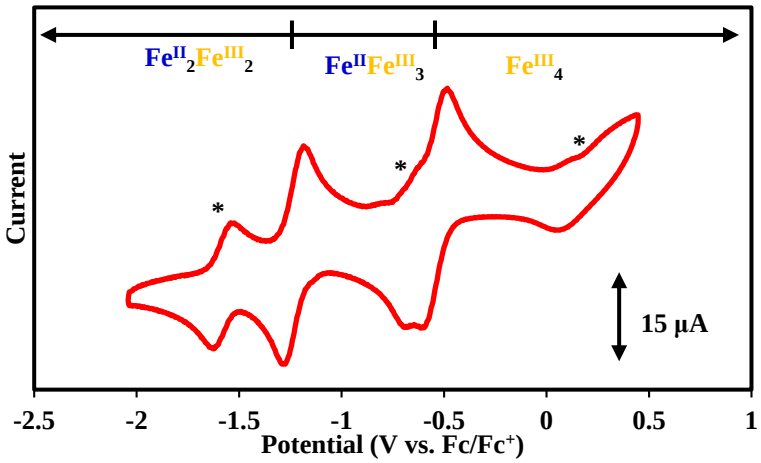

Figure 8. Cyclic voltammetry of **5** (2.3 mM at 200 mV/s scan rate) in THF with a glassy carbon working, platinum counter, and silver wire reference electrodes and ca. 100 mM $[Bu_4N][PF_6]$. Electrochemical events marked with an asterisk (*) are assigned to a small amount of $[LFe_3O(PzNHtBu)_3Fe(OH)]^{n+}$ that formed due to decomposition.

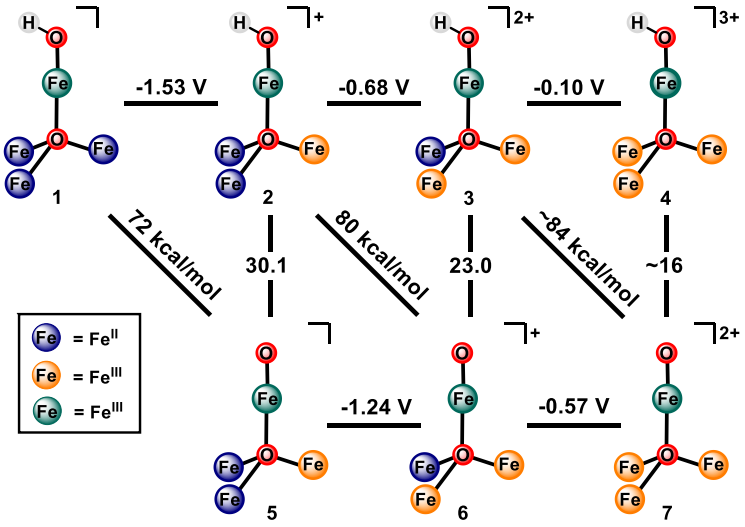

Figure 9. Thermodynamic cycles to evaluate the BDE_{O-H} values of the hydroxide clusters **1** – **3**. Reduction potentials (horizontal lines) are references to Fc/Fc^+. pK_a values (vertical lines) are based on relative pK_a values of cationic acids in THF. Diagonal lines are the BDE_{O-H} values calculated from these parameters according to the Bordwell equation (eq 1). Approximate values (~) have been extrapolated from the Bordwell equation.

Similar to our previously reported studies on [Fe_3Mn] hydroxide and aquo clusters, the bond dissociation enthalpy of the O–H bond ($BDE_{O–H}$) increases upon oxidation of the distal Fe centers, ranging from 72 kcal/mol in **1** to 84 kcal/mol in **3**.[17]

Reactivity Studies of Fe_4-Oxo Clusters. The three distal Fe oxidation states have a dramatic effect on the reactivity of the Fe^{III}-oxo center through modifying the pK_a and $BDE_{O–H}$ values. For example, **5** is incapable of performing proton coupled electron transfer (PCET) reactions[18,19] with substituted phenols over a range of phenol $BDE_{O–H}$ values (79 – 85 kcal/mol); only proton transfer to generate **2** is observed as expected from the combination of low $BDE_{O–H}$ for **1** and high pK_a of **2.** Oxidation of the remote Fe centers in **6** and **7** enables PCET reactivity with these phenols, resulting in the formation of **2** and **3**, respectively (Figure 10).

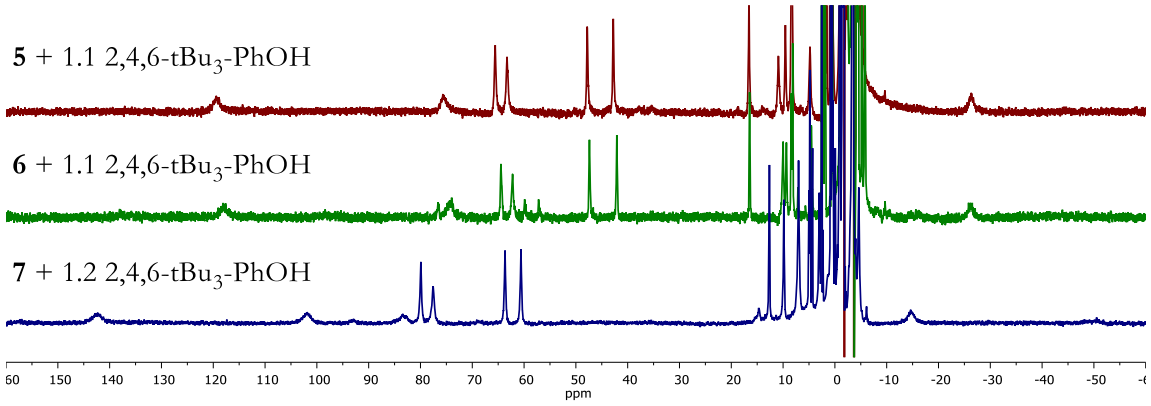

Figure 10. ^{1}H NMR spectra (400 MHz) in THF/C_6D_6 of reaction products with **5** - **7** and 2,4,6-tri-*tert*-butyl phenol (2,4,6-tBu_3-PhOH; BDE = 82 kcal/mol). The major species in the maroon and green spectra corresponds to **2**. The major species in the blue spectrum corresponds to **3**.

---

^{31}P NMR and GC/MS analyses suggest that **7** is capable of transferring an oxygen atom to trimethylphoshine (PMe_3), where the other Fe^{III}-oxo clusters display no reaction towards the phosphine on a similar timescale (Figure 11). The difference in reactivity is likely due to

the low reduction potentials of **5** and **6** precluding efficient oxygen atom transfer reactivity. A more oxidizing cluster, through oxidations of the distal Fe centers, **7** can undergo OAT.

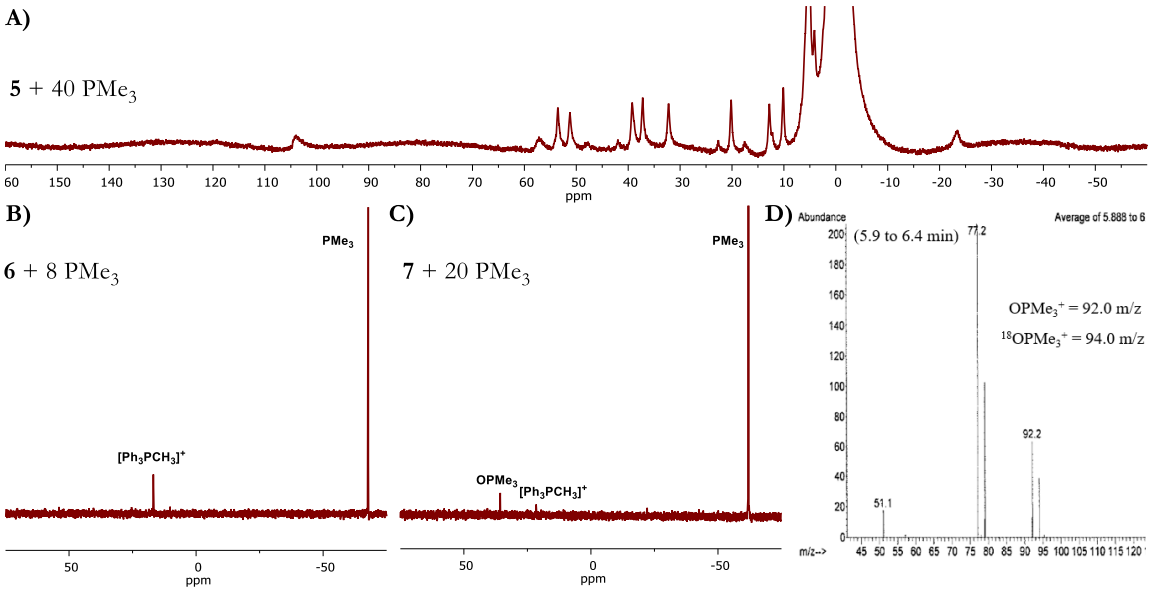

Figure 11. (A) ^{1}H NMR spectrum (400 MHz) in THF/C_6D_6 of **5** with 40 equivalents trimethylphosphine (PMe_3); the resonances are consistent with no reaction occurring. (B) ^{31}P NMR spectrum of **6** and 8 equivalents PMe_3; the only resonances observed on those assigned to unreacted PMe_3 and the conjugate acide of the based used to prepare **6** ($Ph_3PCH_3^+$). (C) ^{31}P NMR spectrum of **7** and 20 equivalents PMe_3, where a resonance assigned to trimethylphosphine oxide ($OPMe_3$) is observed ~ 40 ppm. (D) GC/MS analysis of reaction between **^{18}O-7** and PMe_3 contains mass fragments of $^{18}OPMe_3$ (94 m/z), consistent with oxygen atom transfer from **7** to form the phoshpine oxide.

The kinetics of C–H activation by these clusters was investigated. The reaction between **5** and 9,10-dihydroanthracene (DHA; BDE_{C-H} = 78 kcal/mol)[15c] displays an expected first order dependence on substrate concentration, with an overall second order rate constant of 87 M^{-1} s^{-1}, and a considerable kinetic isotope effect (KIE) of 7 with d_4-DHA. These data are consistent with a rate-limiting C–H bond activation for the PCET process to form **1** and anthracene. The

second-order rate constants between **5** and C–H bonds of varying $BDE_{C–H}$ and pK_a values were measured and display a linear dependence of the PCET reaction rate on the pK_a of the organic substrate (Figure 12), suggesting either a concerted or stepwise pK_a-driven process.[20] Reactions between DHA and **6** or **7** produce the corresponding hydroxide-clusters and anthracene in yields comparable to **5** (Table 6) indicating PCET processes, but complex kinetics precluded the determination of rate constants and further insights into the mechanism of these reactions.

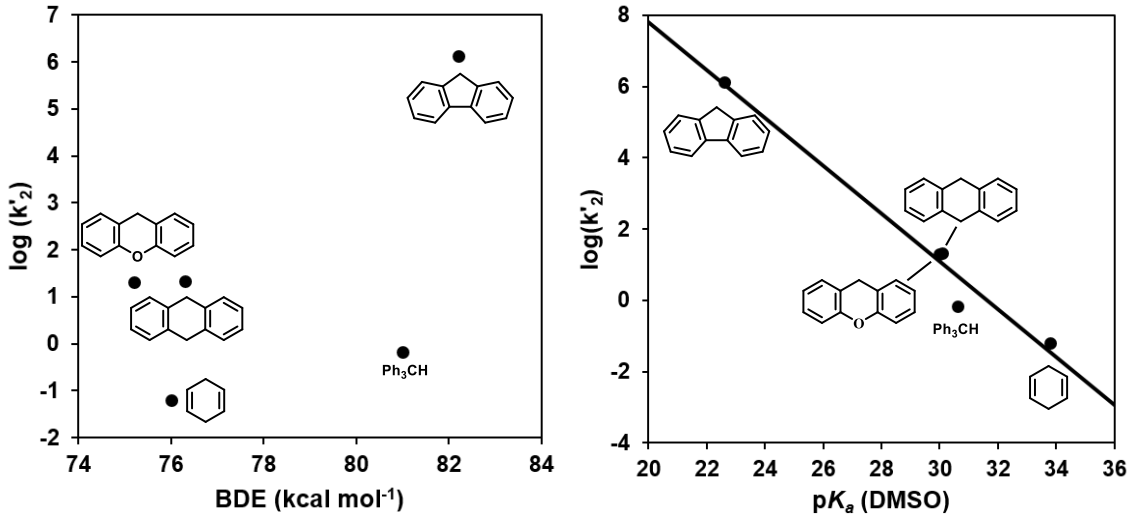

Figure 12. Plots of log (k_2) (normalized to number of reactive C-H bonds) versus BDE (left) and pK_a (in DMSO; right) for **5** with various organic substrates.

Table 6. Product Analysis of PCET and OAT Reactivity of 5 – 7.

	5		**6**		**7**	
Substrate	organic product	cluster product	organic product	cluster product	organic product	cluster product
9,10 -dihydroanthracene	anthracene (53%)[a]	**1** (67%)[b]	anthracene (43%)[a]	**2** (66%)[b]	anthracene (44%)[a]	**3** (110%)[b]
fluorene	n.d.[c]	**1** (83%)[b]	9,9'-bifluorenyl (1%)[a]	**2** (81%)	n.d.[c]	**3** (107%)[b]
2,4,6-tri-tertbutylphenol	-	**2**	phenoxyl radical[d]	**2**	-	**3**
trimethylphosphine	N.R.[e]	N.R.[e]	N.R.[e]	N.R.[e]	$OPMe_3$	**2**

[a]Quanitified by GC/MS versus authentic samples, with triphenylphosphine as an internal standard; percent yield based on a 2:1 cluster/product stoichiometry. [b]Quantified by ^{1}H NMR spectroscopy with 1,3-trimethylsilyl-benzene as an internal standard. [c]Not detected by GC/MS. [d]X-band EPR signal detected at 77 K that matches authentic sample of the corresponding phenoxyl radical.[e] No reaction observed.

CONCLUSIONS

Overall, this report offers a rare systematic study of the effects of neighboring redox active metals on structural and reactivity aspects of a terminal metal-oxo. Because it is part of a cluster, the reactivity of the terminal metal-oxo motif can be tuned without changing the formal redox state of the metal supporting it; however, redox events at distal centers have significant effect on the acidity and BDE of the corresponding O-H bond. Clearly, the cluster as an assembly is essential for reactivity beyond the structural aspects of the isolated metal-oxo motif. Further development of multinuclear model systems is necessary to fully understand the nature and amplitude of these effects.

EXPERIMENTAL DETAILS

General Considerations. All reactions were performed at room temperature in an N_2-filled M. Braun glovebox or using standard Schlenk techniques unless otherwise specified; reactions with KOH were performed in an N_2-filled VAC wetbox. Glassware was oven dried at 140 ºC for at least 2 h prior to use, and allowed to cool under vacuum. **[LFe$_3$(OAc)(OTf)][OTf]**,[11] iodosylbenzene,[21] benzyl potassium,[22] Fe(OTf)$_2$ • 2 MeCN,[23] ferrocenium trifluoromethane sulfonate ([Fc][OTf]),[24] and Ph_3PCH_2[25] were prepared according to literature procedures. *N-tert*-butyl-1*H*-pyrazol-5-amine (HPzNHtBu) was prepared according to a modified literature procedure.[26] 18-oxygen labeled potassium hydroxide ($K^{18}OH$) was prepared by quenching a tetrahydrofuran solution of benzyl potassium (less than 1 mmol) with $H_2{}^{18}O$, and drying the resulting white suspension under vacuum. Tetrahydrofuran, CH_2Cl_2, diethyl ether, benzene, toluene, acetonitrile, hexanes, and pentane were dried by sparging with nitrogen for at least 15 minutes, then passing through a column of activated A2 alumina under positive N_2 pressure. ^{1}H spectra were recorded on a Varian 300 MHz spectrometer; ^{13}C NMR spectra were recorded on a Varian 500 MHz spectrometer. ^{1}H and ^{31}P NMR spectra in THF/C_6D_6 were recorded on a Varian 500 MHz spectrometer using solvent suppression protocols. NMR spectra collected at low temperature were recorded on a Bruker 500 MHz spectrometer. CD_3CN, C_6D_6, and CD_2Cl_2 was purchased from Cambridge Isotope Laboratories, dried over calcium hydride, degassed by three freeze-pump-thaw cycles, and vacuum transferred prior to use.

Physical Methods. *Mössbauer measurements.* Zero applied field ^{57}Fe Mossbauer spectra were recorded at 80 K in constant acceleration mode on a spectrometer from See Co (Edina, MN) equipped with an SVT-400 cryostat (Janis, Wilmington, WA). The isomer shifts are relative to

the centroid of an α-Fe foil signal at room temperature. Samples were prepared by mixing polycrystalline material (20 mg) with boron nitride in a cup fitted with screw cap or freezing a concentrated acetonitrile solution in the cup. The data were fit to Lorentzian lineshapes using WMOSS (www.wmoss.org).

Mössbauer simulation details for all compounds. All spectra were simulated by four pairs of symmetric quadrupole doublets with equal populations and Lorentzian lineshapes. They were refined to a minimum via least squares optimization (13 fitting parameters per spectrum). Signals appearing above 2 mm/s were indicative with the presence of high-spin Fe^{II} centers and correspond to species with isomer shifts of ~ 1 mm/s. The Mössbauer data were fit to be consistent with our previously reported Fe clusters.[7a, 7b, 11, 27] The observed Mossbauer parameters are in agreement with related six-coordinate high-spin Fe^{II}/Fe^{III} centers.[28]

Electrochemical measurements. CVs and SWVs were recorded with a Pine Instrument Company AFCBP1 biopotentiostat with the AfterMath software package. All measurements were performed in a three electrode cell, which consisted of glassy carbon (working; ø = 3.0 mm), silver wire (counter) and bare platinum wire (reference), in a N_2 filled M. Braun glovebox at RT. Dry acetonitrile or tetrahydrofuran that contained ~100 mM $[Bu_4N][PF_6]$ was used as the electrolyte solution. The ferrocene/ferrocinium (Fc/Fc^+) redox wave was used as an internal standard for all measurements.

X-ray crystallography. X-ray diffraction data was collected at 100 K on a Bruker PHOTON100 CMOS based diffractometer (microfocus sealed X-ray tube, Mo Kα (λ) = 0.71073 Å or Cu Kα (λ) = 1.54178 Å). All manipulations, including data collection, integration, and scaling, were carried out using the Bruker APEXII software. Absorption corrections were applied using SADABS. Structures were solved by direct methods using XS (incorporated into SHELXTL) and refined by using ShelXL least squares on Olex2-1.2.7 to convergence. All

non-hydrogen atoms were refined using anisotropic displacement parameters. Hydrogen atoms were placed in idealized positions and refined using a riding model. Due to the size of the compounds (**1** – **3**, **5**, and **6**), most crystals included solvent-accessible voids that contained disordered solvent. In most cases the solvent could be modeled satisfactorily.

Magnetic measurements. Magnetic susceptibility measurements were collected on a Quantum Design DynaCool 14T PPMS instrument at the University of Southern California, Los Angeles. Polycrystalline samples (10 – 20 mg) of **2** – **4** were packed in VSM sample holders. Magnetization data at 100 K from 0 to 4 T were collected to confirm the absence of ferromagnetic impurities. Magnetic susceptibility measurements were collected between 2 and 300 K with a 0.1 T field. Reduced magnetization data was collected between 2 K and 8 K at fields between 1 T and 12 T. Magnetic data was simulated with PHI.[29]

Synthetic Procedures. *Synthesis of 2-tert-butyl-isoxazolium tetrafluoroborate.* 25 mL isoxazole (0.4 mol) was combined with 37 mL *tert*-butanol (0.4 mol) in a 500 mL roundbottom flask. This was cooled to -20 °C with an ice/sodium chloride bath while 160 mL tetrafluoroboric acid diethyl ether complex (1.2 mol) was added dropwise over 1 hour. After the addition was complete, the reaction was warmed to room temperature and stirred for 4 hours. Then, 100 mL Et_2O and 50 mL THF was added to the reaction and cooled to -20 °C; the resulting precipitate was collected on a glass frit, washed three times with 200 mL Et_2O and dried under reduced pressure. 60 g of 2-*tert*-butyl-isoxazolium tetrafluoroborate (72% yield) can be obtained this way; another 6 g can be obtained by cooling the filtrate and Et_2O washings to -20 °C overnight and collecting the resulting crystals (79% overall yield). ^{1}H NMR (300 MHz, $(CD_3)_2CO$): δ 1.90 (s, 9H), 7.46 (s, 1H), 9.55 (s, 1H), 9.77 (s, 1H) ppm.

Synthesis of N-tert-butyl-1H-pyrazol-3-amine (HPzNHtBu). This procedure was adapted from a report describing the synthesis of *tert*-butyl substituted 3-aminopyrazoles.[26] 10.0 g of 2-*tert*-

butyl-isoxazolium tetrafluoroborate (47 mmol) was suspended in 100 mL EtOH in a 250 mL roundbottom flask and cooled with an ice bath to 0 °C. A solution of 4.56 mL hydrazine monohydrate (94 mmol) in 20 mL EtOH was added dropwise to the cooled flask. After complete addition, the reaction was warmed to room temperature and stirred for 30 minutes. EtOH was removed via rotary evaporation and an aqueous work up was performed with 100 mL H_2O and 3 x 100mL CH_2Cl_2, collecting the organic layers. The combined organic fractions were dried with Na_2SO_4, filtered, and dried to yield an orange oil. The crude product was purified via Kugelrohr distillation under dynamic vacuum at 90 °C. The distillate was recrystallized with Et_2O and the resulting white solid was sublimed under vacuum at 60 °C to yield 1.6 g of HPzNHtBu (24% yield). ^{1}H NMR (400 MHz, CD_2Cl_2): δ 1.27 (s, 9H), 3.61 (br), 5.71 (d, 1H), 7.34 (d, 1H), 9.75 (br) ppm. $^{13}C\{^1H\}$ NMR (100 MHz, CD_2Cl_2): 53.28, 75.11, 118.60, 154.26 ppm (a signal for the *tert*-butyl quaternary carbon was likely not observed). Anal. calcd. (%) for $C_7H_{13}N_3$: C, 60.40; H, 9.41; N, 30.19. Found: C, 60.75; H, 9.37; N, 30.20.

Synthesis of potassium N-tert-butyl-1H-pyrazol-3-amine-ate (KPzNHtBu). 1.25 g *N-tert*-butyl-1*H*-pyrazol-3-amine (9 mmol) was dissolved in 5 mL THF. A THF solution of 1.17 g benzyl potassium (9 mmol) was added dropwise, while stirring. After 30 minutes, the reaction was concentrated to 5 mL, and the precipitate was collected via filtration. The precipitate was washed with Et_2O and dried under vacuum to yield 1.2 g KPzNHtBu as a white solid (75% yield). Anal. calcd. (%) for $C_7H_{12}KN_3$: C, 47.42; H, 6.82; N, 23.70. Found: C, 47.50; H, 6.83; N, 23.61.

*Synthesis of $LFe_3O(PzNHtBu)_3Fe(OH)$ (**1**).* 1.287 g (0.93 mmol) $LFe_3(OAc)(OTf)_2$ was suspended in THF and froze in a liquid nitrogen cooled cold well. 502.6 mg (2.83 mmol) KPzNHtBu was added with THF while the suspension was thawing. After stirring at room temperature for 1 hour, 207.0 mg (0.94 mmol) iodosylbenzene was added with THF. After 4

hours, the solvent was removed under reduced pressure. The brown solid was transferred to a coarse porosity glass frit with celite using 50 mL pentane. The desired compound was extracted using toluene until the filtrate appeared colorless. This red-brown solution was dried completely under reduced pressure; the resulting solid (1.207 g obtained) is used in the following steps assuming a molecular formula of $LFe_3O(PzNHtBu)_3$, however this could not be confirmed via X-ray crystallography due to its poor crystallinity.

110.7 mg (0.076 mmol) of the $LFe_3O(PzNHtBu)_3$ solid was dissolved in 5 mL THF. 33.0 mg (0.076 mmol) $Fe(OTf)_2$ • 2 MeCN was added with 1 mL THF. After 45 minutes, 26 mg (0.464 mmol) KOH was added as a THF suspension. After 18 hours, the reaction appeared dark blue; this solution was transferred to a Schlenk tube and dried under vacuum at 100 °C for 1 hour. The reaction mixture is suspended in MeCN and the blue precipitate was collected over a coarse porosity frit with celite. The precipitate was washed with MeCN until the filtrate was colorless, and then dried under vacuum. The dry blue precipitate was extracted with toluene and dried under reduced pressure. This residue was recrystallized via benzene/HMDSO vapor diffusion to yield 25.7 mg (0.017 mmol; 22% yield) of **1** as a blue solid. ^{1}H NMR (300 MHz, C_6D_6): δ 123.0 (br), 64.6 (br), 56.4, 50.1, 44.1, 41.0, 24.6, 19.6, 14.2, 12.2, 4.4, 3.2, 1.7, -40.6 (br) ppm. UV-Vis (THF) [ε (M^{-1} cm^{-1})] 253 nm (5.19×10^4), 494 nm (3.26×10^3), 609 nm (3.81×10^3). Anal. calcd. (%) for $C_{78}H_{76}Fe_4N_{15}O_5$: C, 61.36; H, 5.02; N, 13.76. Found: C, 61.27; H, 5.40; N, 13.12.

The 18-O labeled cluster could be prepared through the analogous protocol, substituting $K^{18}OH$ for KOH. The resulting product has identical spectroscopic features to that of **1**, and was used to prepare the remaining 18-O labeled clusters (via oxidations and/or deprotonation). ESI-MS analysis was consistent with 18-O incorporation of the cluster (Figure S18).

*Synthesis of [LFe$_3$O(PzNHtBu)$_3$Fe(OH)][OTf] (**2**).* 265.2 mg (0.17 mmol) LFe$_3$O(PzNHtBu)$_3$Fe(OH) was dissolved in 5 mL THF. This was transferred to a stirring suspension of 52.3 mg (0.16 mmol) [Fc][OTf] in 3 mL THF. After 1 hour, the reaction was concentrated under vacuum to 1 mL and 15 mL toluene was added. The reaction was stirred for 15 minutes and the resulting red-purple precipitate was collected on a coarse frit with celite and dried completely under vacuum. The red-purple solid was extracted by washing with MeCN until the filtrate appeared colorless; this solution was dried under reduced pressure. The resulting residue was recrystallized via THF/Et$_2$O vapor diffusion to yield 211 mg of red-purple crystals of **2** (0.13 mmol; 82% yield). ^{1}H NMR (300 MHz, CD$_3$CN): δ 127.2 (br), 82.1 (br), 54.4, 49.0, 22.1, 16.5 (br), 14.1, 13.8, 13.3, 10.3 (br), 8.4, 7.8, 7.3, 1.0, -4.9, -5.1, -22.8 (br) ppm. UV-Vis (ACN) [ε (M^{-1} cm^{-1})] 243 nm (5.96 x 10^4), 328 nm (8.83 x 10^3), 503 nm (4.88 x 10^3). Anal. calcd. (%) for $C_{79}H_{76}F_3Fe_4N_{15}O_8S$: C, 56.61; H, 4.57; N, 12.54. Found: C, 56.72; H, 4.70; N, 12.03.

*Synthesis of [LFe$_3$O(PzNHtBu)$_3$Fe(OH)][OTf]$_2$ (**3**).* 102.3 mg (0.06 mmol) [LFe$_3$O(PzNHtBu)$_3$Fe(OH)][OTf] was dissolved in 3 mL DCM and a solution of 20.3 mg (0.06 mmol) [Fc][OTf] in 2 mL DCM was transferred to this stirring solution. After 2 hours, 10 mL pentane was added to the reaction and the blue precipitate was collected on a coarse porosity glass frit with celite. The blue powder was dried under vacuum and extracted with DCM until colorless, and recrystallized from DCM/Et$_2$O to obtain 76.8 mg of **3** as blue crystals (69% yield) ^{1}H NMR (300 MHz, CD_2Cl_2): δ 144.3 (br), 103.7 (br), 82.0, 79.7, 66.0, 63.1, 15.5, 12.8, 9.9, 3.5, 1.2, -0.5, -2.3 (br), -11.6 (br) ppm. [ε (M^{-1} cm^{-1})] 238 nm (5.76 x 10^4), 345 nm (7.74 x 10^3), 634 nm (4.80 x 10^3). Anal. calcd. (%) for $C_{80}H_{76}F_6Fe_4N_{15}O_{11}S_2$: C, 52.65; H, 4.20; N, 11.51. Found: C, 51.70; H, 4.37; N, 11.11.

*Synthesis of [LFe$_3$O(PzNHtBu)$_3$Fe(OH)][OTf]$_3$ (**4**).* 42.9 mg (0.024 mmol) [LFe$_3$O(PzNHtBu)$_3$Fe(OH)][OTf]$_2$ was dissolved in 2 mL DCM and 8.1 mg (0.024 mmol) [Fc][OTf] was added with 2 mL DCM. After 30 minutes, the reaction was concentrated and 10 mL Et_2O was added to produce a green precipitate. This was collected on a frit over celite and rinsed with Et_2O. The precipitate was collected with DCM and recrystallized via vapor diffusion of Et_2O to obtain 39.0 mg (0.020 mmol; 82% yield) **4** as green crystals. ^{1}H NMR (300 MHz, CD_2Cl_2): δ 95.2, 85.0, 14.5, -1.8, -44.9. -48.3 ppm. UV-Vis (ACN) [ε (M^{-1} cm^{-1})] 242 nm (7.11 x 10^4), 355 nm (8.85 x 10^3), 748 nm (7.39 x 10^3). Anal. calcd. (%) for $C_{81}H_{76}F_9Fe_4N_{15}O_{14}S_3$: C, 49.28; H, 3.88; N, 10.64. Found: C, 49.19; H, 4.09; N, 10.02.

*Synthesis of LFe$_3$O(PzNHtBu)$_3$Fe(O) (**5**).* 102.6 mg (0.06 mmol) [LFe$_3$O(PzNHtBu)$_3$Fe(OH)][OTf] was dissolved in 15mL THF and froze in a liquid nitrogen cooled cold well. 7.2 mg (0.06 mmol) KOtBu was added to the thawing solution, and the reaction was stirred at room temperature for 1 hour. The solvent was removed under reduced pressure and the crude product was recrystallized via benzene/HMDSO vapor diffusion to obtain 26.2 mg of **5** as purple crystals (0.02 mmol; 28% yield). ^{1}H NMR (300 MHz, C_6D_6): δ 105.9 (br), 58.5 (br), 55.3, 53.0, 40.9, 38.9, 33.9, 21.8, 14.4, 11.7, 2.4, 1.1, -21.5 (br) ppm. UV-Vis (THF) [ε (M^{-1} cm^{-1})] 248 nm (4.40 x 10^4), 342 nm (6.73 x 10^3), 539 nm (3.41 x 10^3). Anal. calcd. (%) for $C_{78}H_{75}Fe_4N_{15}O_5$: C, 61.40; H, 4.95; N, 13.77. Found: C, 60.04; H, 5.01; N, 13.06 (Calcd. (%) for $C_{78}H_{75}Fe_4N_{15}O_5$ • 0.5 ($C_6H_{18}OSi_2$): C, 60.05; H, 5.27; N, 13.08; compound recrystallized from benzene/HMDSO).

*Synthesis of [LFe$_3$O(PzNHtBu)$_3$Fe(O)][OTf] (**6**).* 50.3 mg (0.03 mmol) [LFe$_3$O(PzNHtBu)$_3$Fe(OH)][OTf]$_2$ was dissolved in 2 mL THF/DCM (1:1) and froze in a liquid nitrogen cooled cold well. 8 mg (0.03 mmol) Ph_3PCH_2 was added to the thawing solution as a THF solution. The reaction turned a deep blue, and at this point care was taken to avoid

warming the mixture to room temperature. The compound was precipitated by addition of cold Et_2O, and the precipitate was dried under vacuum to yield **6** as a blue powder. NMR analysis of this powder revealed the presence of residual $[Ph_3PCH_3][OTf]$, which were difficult to remove with Et_2O washes. This mixture could be recrystallized in THF/Et_2O at -35 °C to obtain X-ray quality crystals of **6**; however, due to the decomposition of this compound, obtaining **6** cleanly as a bulk solid for elemental analysis was unsuccessful. ^{1}H NMR (300 MHz, CD_3CN): δ 122.2 (br), 90.2 (br), 68.5, 66.1, 55.0, 53.2, 14.5, 13.9, 13.0, 10.7, -31.0 (br) ppm.

*Synthesis of [LFe$_3$O(PzNHtBu)$_3$Fe(O)][OTf]$_2$ (**7**).* 43.0 mg $[LFe_3O(PzNHtBu)_3Fe(OH)][OTf]_2$ (**3**; 0.02 mmol) was dissolved in 1:1 DCM/THF and froze in a liquid nitrogen cooled cold well. A THF solution of 6.8 mg Ph_3PCH_2 (0.02 mmol) was added to the thawing solution. The reaction was then combined, while thawing, with a DCM solution of 7.8 mg [Fc][OTf] (0.02 mmol). Keeping this mixture as cold as possible, thawing Et_2O was added to precipitate the oxidized cluster; The blue-green solid was collected on a fine porosity glass frit, and dried under vacuum. The ^{1}H NMR of this solid always contained minor amounts of impurities (<20%, mostly ascribed to **3** and **4**), which **7** could not be isolated from due to its thermal instability. For any subsequent reactions performed on this material, the moles of initial cluster **3** were used to approximate the amount of **7** present. ^{1}H NMR (300 MHz, 1:1 CD_3CN/CD_2Cl_2): δ 145.6 (br), 105.4 (br), 85.2, 81.4, 71.0, 67.2, 19.0, 13.8, 11.1, 8.8, -61.1, -67.3 (br).

Experimental Protocols. *Reactions for product analysis.* 2mM solutions of Fe-oxo clusters **5** – **7** were stirred for 12-24 hours with one equivalent of 9,10-dihydroanthracene (DHA) or fluorene. The solvent was removed under vacuum and the organic products were extracted with Et_2O containing triphenylphosphine as an internal standard. The suspensions were filtered over celite and analyzed via GC-MS. The oxidized products (anthracene and 9,9'-

bifluorene) were quantified based on a calibration curve of authentic samples. Other possible oxidation products, such as fluorenone, or anthraquinone, were not observed.

Oxygen atom transfer studies with ***^{18}O-7*** *and* PMe_3. **^{18}O-7** cluster was prepared in situ by combining a thawing 1:1 THF/DCM solution of 50.3 mg **^{18}O-3** (0.03 mmol) with 7.5 mg Ph_3PCH_2 (0.03 mmol) to prepare a solution of **6-^{18}O**. This solution was combined, while thawing, to a DCM solution of 9.5 mg [Fc][OTf] (0.03 mmol). Keeping this mixture as cold as possible, thawing Et_2O was added to precipitate the oxidized cluster; boron nitride (BN) was added to ease separation of precipitate from the solution. This suspension was filtered to obtain solid **^{18}O-7**, which was eluted from BN with cold 1:1 THF/DCM. 50 μL PMe_3 (0.50 mmol) was added to solution as it thawed, and was gradually warmed to room temperature. ^{31}P NMR analysis of the reaction mixture at this stage showed a peak consistent with trimethylphosphine oxide ($OPMe_3$) formation at ~35 ppm. After 30 minutes, the reaction was pumped down. On the bench, the crude reaction mixture was separated via silica plug; 10% MeOH in DCM was used to elute a dark solution, at which point MeOH was washed through the plug to collect a fraction containing $OPMe_3$. The MeOH fraction was pumped down and analyzed via GC/MS, which displayed a GC peak characteristic of $OPMe_3$, with both $^{16}OPMe_3$ and $^{18}OPMe_3$ based on its mass spectrum.

ELECTROCHEMICAL DETAILS

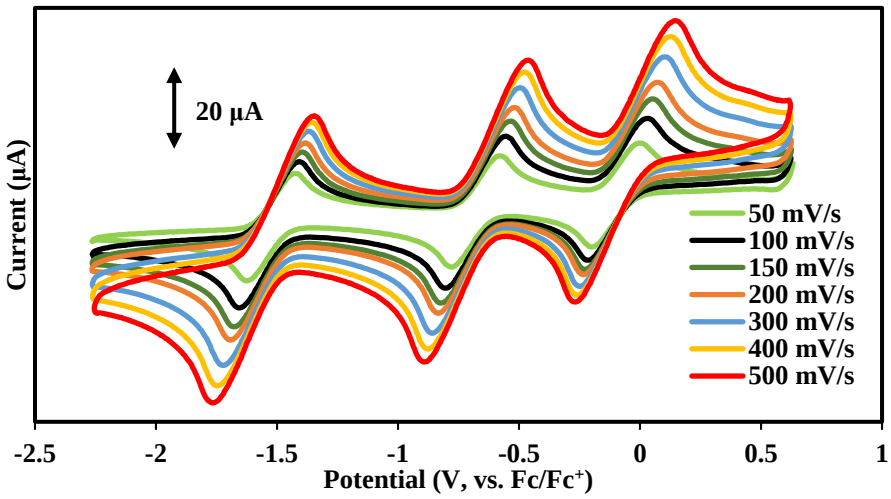

Figure 13. Cyclic voltammetry of $[LFe_3O(PzNHtBu)_3Fe(OH)][OTf]$, **2**, (2.5 mM) in THF with a glassy carbon working, platinum counter, and silver wire reference electrodes and ca. 200 mM $[Bu_4N][PF_6]$ at various scan rates.

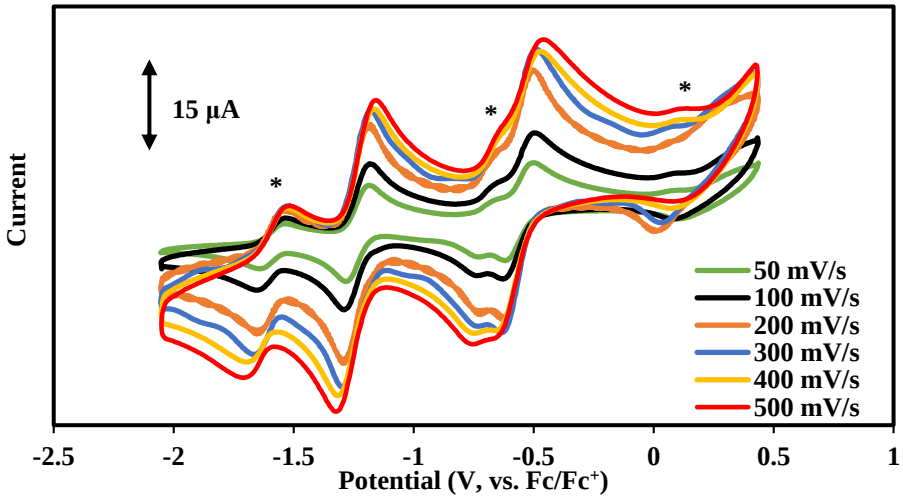

Figure 14. Cyclic voltammetry of $LFe_3O(PzNHtBu)_3Fe(O)$, **5**, (2.3 mM) in THF with a glassy carbon working, platinum counter, and silver wire reference electrodes and ca. 100 mM $[Bu_4N][PF_6]$ at various scan rates. Electrochemical events marked with an asterisk (*) are assigned to a small amount of $[LFe_3O(PzNHtBu)_3Fe(OH)]^{n+}$ that formed due to decomposition.

KINETICS DETAILS

Substrate	BDE (kcal/mol)[30]	pK_a (DMSO)	k_2 (M^{-1} s^{-1}) with **5**
xanthene	75.2	30.0[31]	40
1,4-cyclohexadiene	76.0	~34[a]	~0.3
9,10-dihydroanthracene	76.3	30.1[31]	87
triphenylmethane	81.0	30.6[32]	~0.7
fluorene	82.2	22.6[32]	~3 x 10^6

Reported bond dissociation enthalpies (in kcal mol^{-1}) and pK_a values (in DMSO) of various organic substrates investigated for PCET reactivity with $LFe_3O(PzNHtBu)_3Fe(O)$ (**5**), with their measured second order rate constants. ^{1}H NMR analysis of the reaction mixtures after kinetics measurements show formation of **1** in all cases, consistent with a PCET process.

[a]A reported pK_a value for 1,4-cyclohexadiene could not be obtained, but is approximated based on the reported pK_a value of 1,3-cyclohexadiene in DMSO (pK_a(1,3) = 35.0) and the energy of isomerization between 1,3-cyclohexadiene and 1,4-cyclohexadiene (-1.6 kcal/mol):[33]

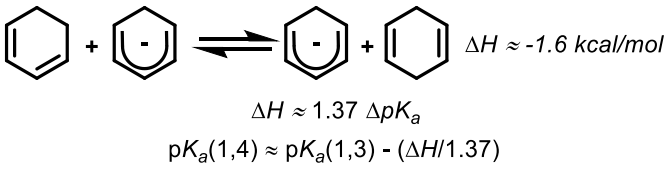

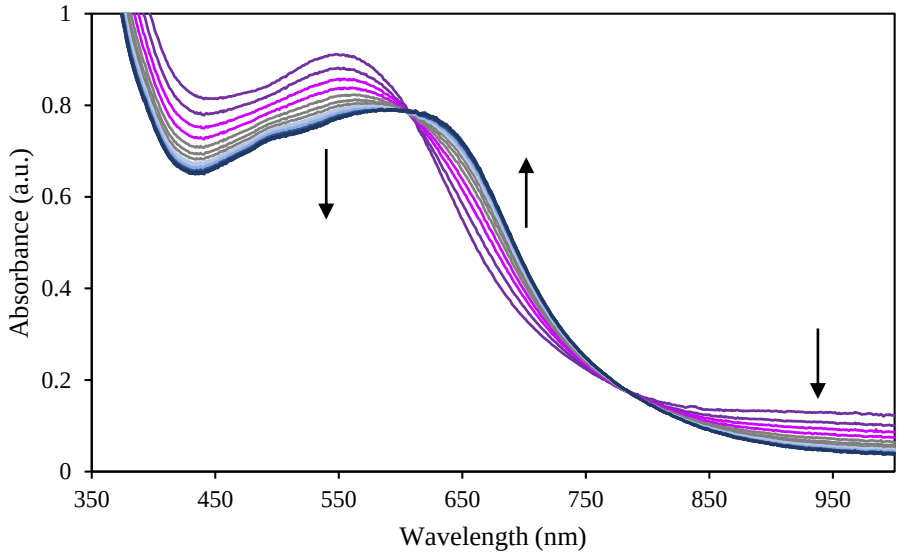

Figure 15. UV-Vis absorbance spectra of $LFe_3O(PzNHtBu)_3Fe(O)$ (**5**; 200 μM) and xanthene (10 mM) at ambient temperature.

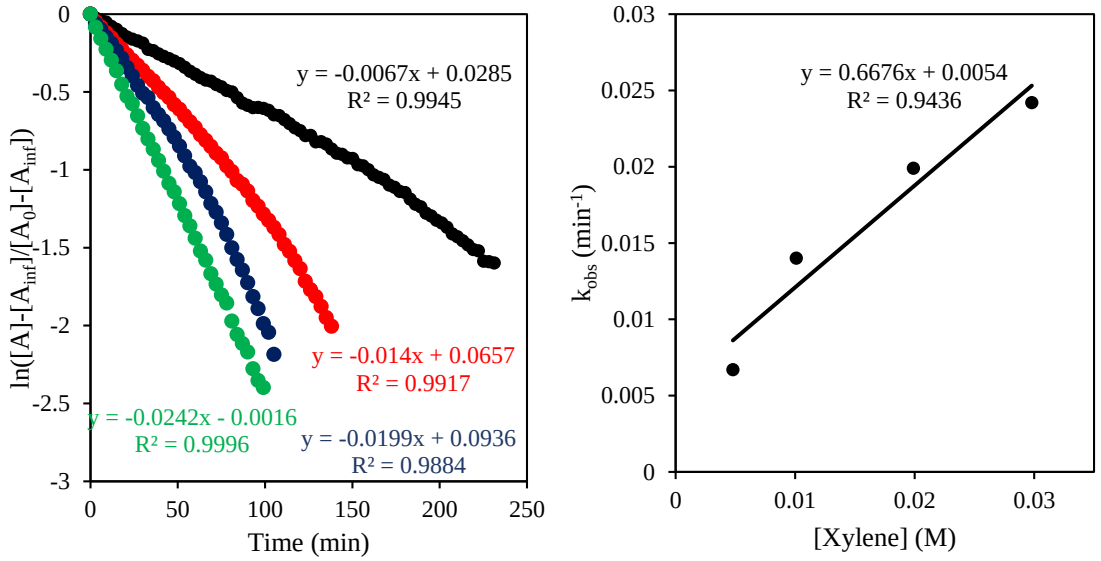

Figure 16. Kinetics data for the reaction between $LFe_3O(PzNHtBu)_3Fe(O)$ (**5**; 200 μM) and xanthene (4.8, 10.1, 19.9, and 29.8 mM) at ambient temperature. The decay of the UV-Vis absorbance feature at 540 nm was used to follow the reaction.

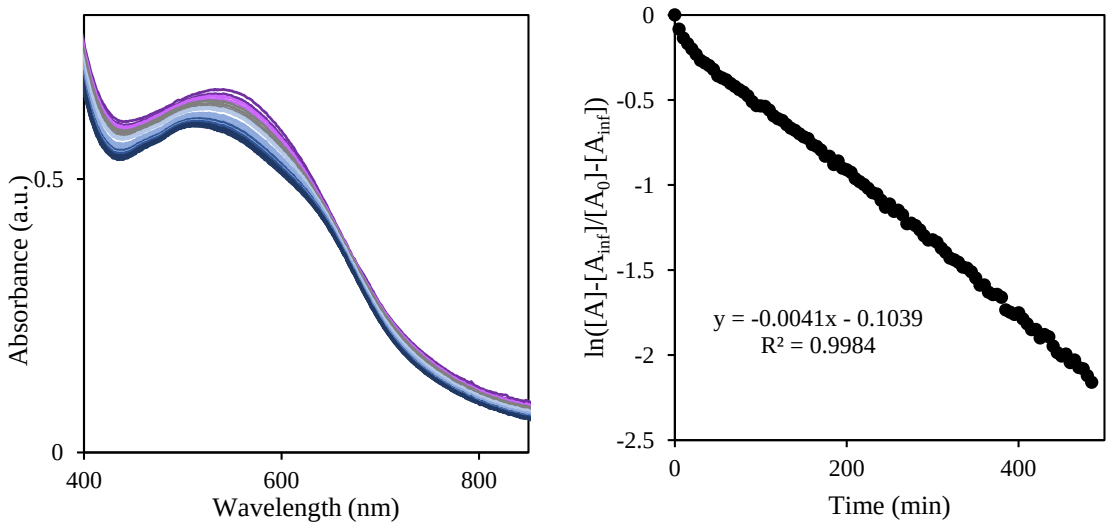

Figure 17. (Left) UV-Vis absorbance spectra of $LFe_3O(PzNHtBu)_3Fe(O)$ (**5**; 200 μM) and 1,4-cyclohexadiene (1 M) at ambient temperature. (Right) Pseudo-first order kinetics plot of the reaction by following the decay of the signal at 516 nm; this wavelength was used since the background decomposition of the compound did not affect this wavelength.

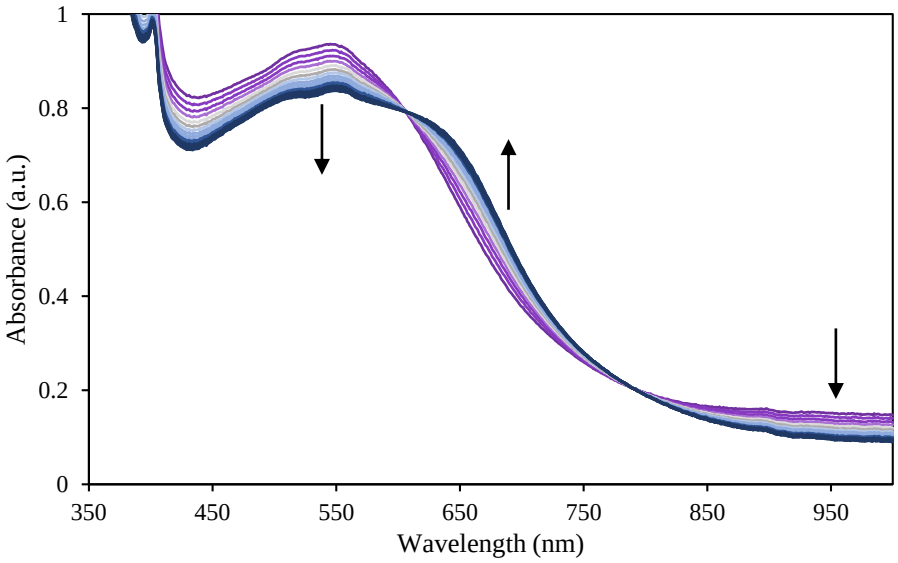

Figure 18. UV-Vis absorbance spectra of $LFe_3O(PzNHtBu)_3Fe(O)$ (**5**; 200 μM) and 9,10-dihydroanthracene (10 mM) at ambient temperature.

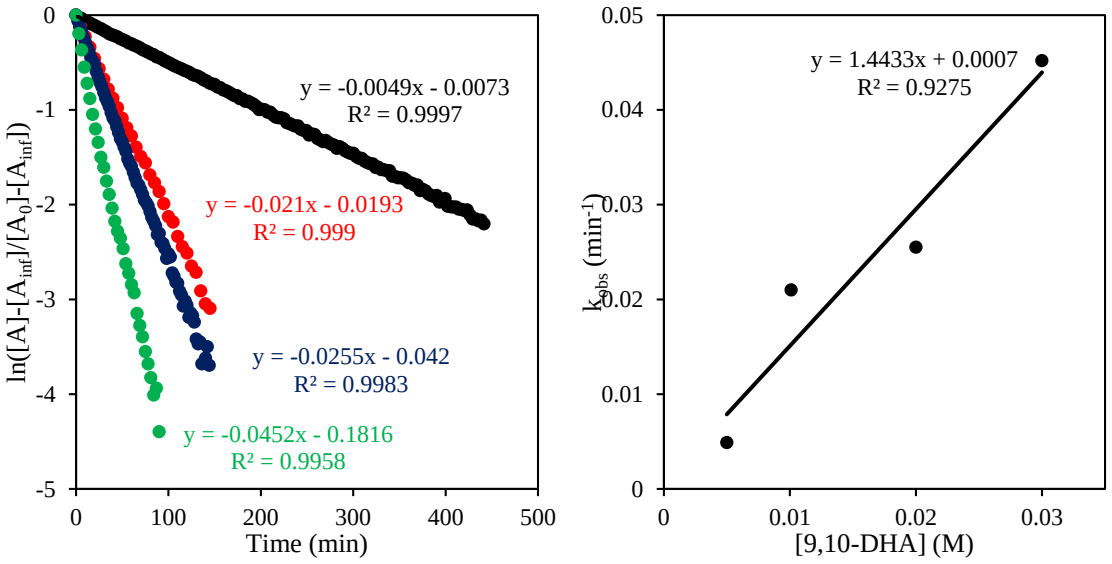

Figure 19. Kinetics data for the reaction between $LFe_3O(PzNHtBu)_3Fe(O)$ (**5**; 200 μM) and 9,10-dihydroanthracene (9,10-DHA; 5, 10, 20, and 30 mM) at ambient temperature. The decay of the UV-Vis absorbance feature at 540 nm was used to follow the reaction.

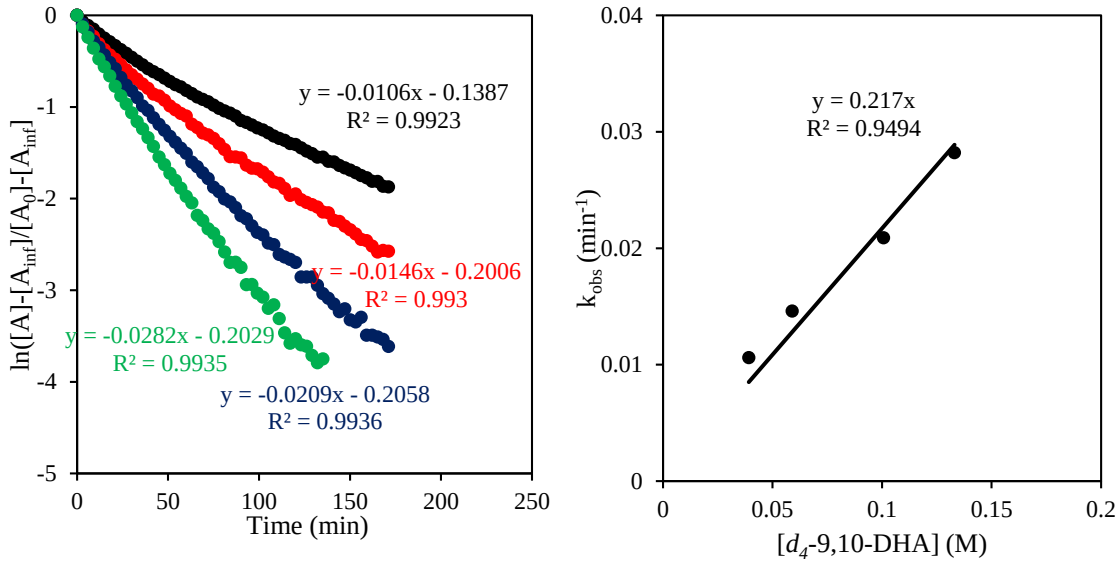

Figure 20. Kinetics data for the reaction between $LFe_3O(PzNHtBu)_3Fe(O)$ (**5**; 200 μM) and *d*$_4$-9,10-dihydroanthracene (*d*$_4$-9,10-DHA; 40, 60, 100, and 130 mM) at ambient temperature. The decay of the UV-Vis absorbance feature at 540 nm was used to follow the reaction.

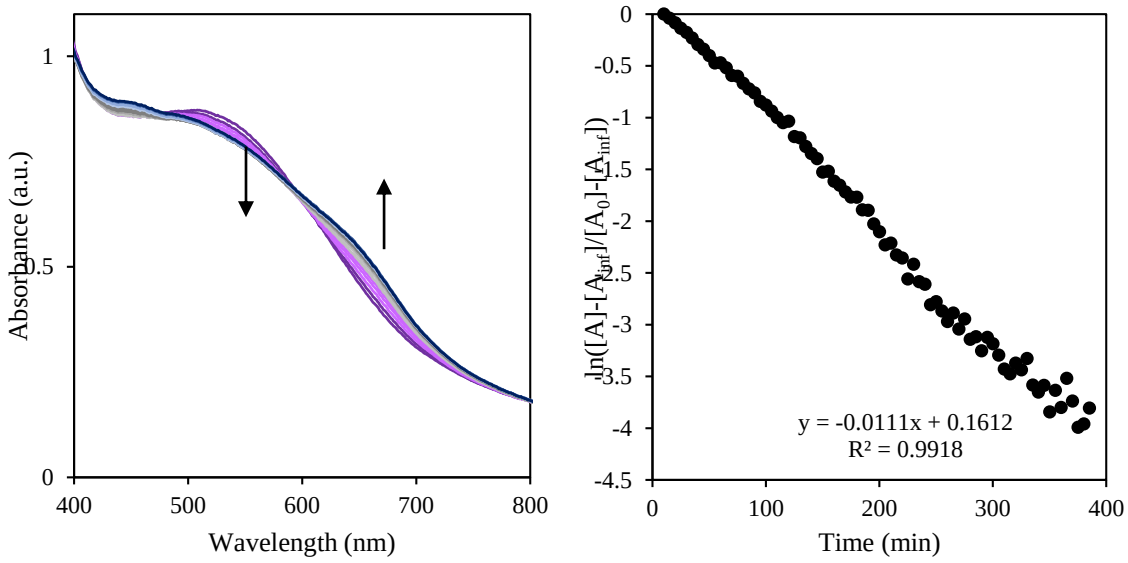

Figure 21. (Left) UV-Vis absorbance spectra of $LFe_3O(PzNHtBu)_3Fe(O)$ (**5**; 200 μM) and triphenylmethane (1 M) at ambient temperature. (Right) Pseudo-first order kinetics plot of the reaction by following the decay of the signal at 516 nm; this wavelength was used since the background decomposition of the compound did not affect this wavelength.

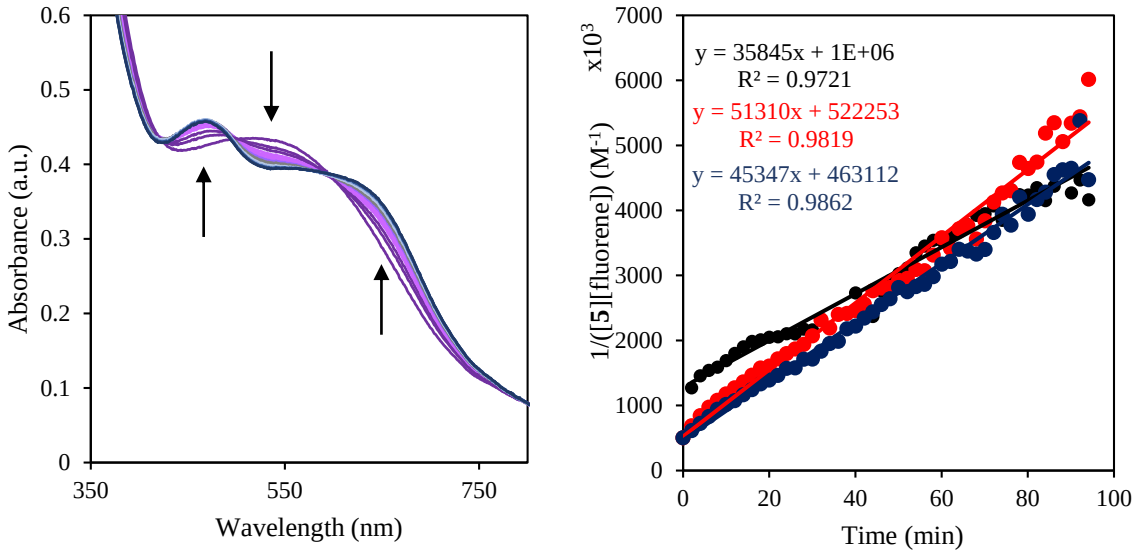

Figure 22. (Left) UV-Vis absorbance spectra of $LFe_3O(PzNHtBu)_3Fe(O)$ (**5**; 1 mM) and fluorene (2 mM) at ambient temperature in a 1 mm cuvette. (Right) Second order kinetics plot of the reaction by following the growth of the signal at 645 nm.

CRYSTALOGRAPHIC DETAILS

Crystal and refinement data for complexes 1 – 3, 5, and 6.

	1	**2-PF_6**	**3**	**5**	**6**
CCDC Number	1903350	1903348	1903352	1903351	1903349
Empirical formula	$C_{90}H_{88}Fe_4N_{15}O_5$	$C_{83}H_{76}F_6Fe_4N_{15}O_{5.5}P$	$C_{80}H_{76}F_6Fe_4N_{15}O_{11}S_2$	$C_{90}H_{87}Fe_4N_{15}O_5$	$C_{91}H_{99}F_3Fe_4N_{15}O_{11}S$
Formula weight (g/mol)	1683.15	1793.95	1825.07	1682.14	1673.00
Radiation	MoKα (λ = 0.71073)	CuKα (λ = 1.54178)	CuKα (λ = 1.54178)	CuKα (λ=1.54178)	CuKα (λ=1.54178)
a (Å)	14.1115(11)	11.9919(11)	12.150(2)	12.3162(13)	19.122(9)
b (Å)	15.0509(11)	13.7630(9)	14.975(5)	15.5743(15)	18.204(5)
c (Å)	21.1556(16)	25.905(2)	23.386(6)	21.6599(15)	24.698(6)
α (°)	70.794(3)	89.286(4)	95.271(14)	102.390(6)	90
β (°)	86.911(3)	87.757(4)	90.124(12)	94.445(4)	90
γ (°)	70.570(3)	79.589(4)	104.172(19)	102.897(9)	90
V (Å^3)	3993.7(5)	4201.8(6)	4106.5(18)	3921.5(7)	8597(5)
Z	2	2	2	2	4
Cryst. syst.	triclinic	triclinic	triclinic	triclinic	orthorhombic
Space group	P-1	P-1	P-1	P-1	$Pna2_1$
ϱ_{calc}g (cm^3)	1.400	1.375	1.476	1.425	1.463
2 Θ range (°)	4.74 to 77.068	6.53 to 149.628	3.796 to 148.742	6.454 to 160.188	6.032 to 130.72
μ (mm^{-1})	0.777	6.219	6.726	6.338	6.172
GOF	1.019	1.044	1.063	1.012	1.064
R1, wR2 (I>2σ (I))	0.0412, 0.0980	0.0710, 0.1919	0.0375, 0.0940	0.0400, 0.0954	0.0732, 0.1352

Special refinement details for [$LFe_3O(PzNHtBu)_3Fe(OH)][PF_6]$. A *tert*-butyl group of one of the pyrazolate ligands is partially disordered over two positions with occupancies of 39% (C93 and C94) and 61% (C97 and C98). There is significant solvent disorder that could not be fully refined, however electron density for a tetrahydrofuran (O100 and C100-C103), and two partial diethyl ether molecules (refined as C104-C109) were refined isotropically with only partial occupancy.

Special refinement details for [$LFe_3O(PzNHtBu)_3Fe(OH)][OTf]_2$. One of the outersphere triflates was modeled as disordered over two nearly identical positions, with occupancies of 75% (S101 through C101) and 25% (S102 through C102). A 'SAME' constraint was used to favor distances and angles of these disordered triflates to the non-disordered one. A partially occupied solvent molecule (likely Et_2O) was present; however, due to its position near a symmetry element, its residual electron density was removed via a solvent mask, as opposed to modeling this disordered solvent.

Special refinement details for [$LFe_3O(PzNHtBu)_3Fe(O)]$. A benzene solvent is positionally disordered over two positions with occupancies of 29% (C106-C111) and 71% (C206-C211).

Special refinement details for [$LFe_3O(PzNHtBu)_3Fe(O)][OTf]$. Generally, these crystals were of relatively poor quality compared to the other structures obtained; the crystal was twinned with a 13% twinned crystal component. While no disorder had to be modeled in the molecule, the outerphere triflate, or the three additional molecules of THF, the low intensity of high angle diffraction data led to low C–C bond precision. Initially, some carbon atoms in the ligand backbone had highly skewed ellipsoids, which were addressed with SIMU/DELU restraints (on O11, C11, C12, C26, C27, and C42 – C45) or, in one case, an ISOR restraint (C44).

Selected bond parameters for structurally characterized compounds 1-3, 5, and 6.

Bond Distance (Å)	1	2-PF_6	3	5	6
Fe1–O1	2.102(1)	2.142(3)	2.148(1)	2.139(1)	2.154(7)
Fe2–O1	2.109(1)	2.101(3)	2.002(2)	2.050(2)	1.927(7)
Fe3–O1	2.089(1)	1.952(3)	1.971(1)	1.967(2)	1.948(7)
Fe4–O1	1.837(1)	1.890(3)	1.948(2)	1.965(2)	2.049(7)
Fe4–O2	1.937(1)	1.907(3)	1.879(2)	1.817(2)	1.795(8)
Fe1–N13	2.129(1)	2.107(4)	2.074(2)	2.124(2)	2.091(9)
Fe2–N23	2.126(1)	2.106(3)	2.057(2)	2.084(2)	2.039(9)
Fe3–N33	2.120(1)	2.071(4)	2.017(2)	2.090(2)	2.015(8)
Fe4–N14	2.097(1)	2.091(4)	2.083(2)	2.093(2)	2.085(9)
Fe4–N24	2.168(1)	2.056(4)	2.047(2)	2.104(2)	2.087(9)
Fe4–N34	2.111(1)	2.105(4)	2.059(2)	2.098(2)	2.100(8)
N13–N14	1.382(1)	1.373(5)	1.377(2)	1.388(2)	1.396(12)
N23–N24	1.368(1)	1.387(5)	1.394(2)	1.387(3)	1.384(11)
N33–N34	1.386(1)	1.389(5)	1.397(2)	1.378(3)	1.387(12)
N15–C72	1.397(2)	1.417(7)	1.422(3)	1.400(3)	1.379(14)
N25–C82	1.422(2)	1.354(7)	1.356(3)	1.366(5)	1.391(14)
(N26–C82)	-	-	-	1.41(2)	-
N35–C92	1.393(2)	1.383(7)	1.350(3)	1.402(3)	1.341(14)
Bond Angles (º)					
N14–Fe4–N24	120.1	119.1	116.6	118.3	113.4
N24–Fe4–N34	122.1	118.8	119.8	123.0	119.6
N34–Fe4–N14	117.8	121.7	122.7	117.5	124.0
N14–Fe4–O2	88.4	91.7	92.6	96.3	97.6
N24–Fe4–O2	91.3	93.5	95.0	92.0	96.3
N34–Fe4–O2	92.2	91.1	92.1	92.8	93.6
O1–Fe4–O2	177.1	177.3	178.7	177.1	176.0
Torsion Angles (º)					
Fe1–N13–N14–Fe4	13.9	2.7	6.2	19.4	21.9
Fe2–N23–N24–Fe4	11.6	9.9	8.2	4.5	17.4
Fe3–N33–N34–Fe4	13.4	12.5	11.1	13.7	2.7
Centroid Distances (Å)					
Fe1|Fe2|Fe3–N14|N24|N34	2.050	1.701	1.643	1.685	1.627
Fe1|Fe2|Fe3–O11|O21|O31	1.121	1.110	1.078	1.120	1.122
Fe1|Fe2|Fe3–O1	1.153	1.105	1.036	1.076	1.012
N14|N24|N34–Fe4	0.025	0.075	0.120	0.138	0.218

References

1. (a) Que Jr, L.; Tolman, W. B. *Nature* **2008,** *455*, 333; (b) Hohenberger, J.; Ray, K.; Meyer, K. *Nature Communications* **2012,** *3*, 720; (c) Costas, M.; Mehn, M. P.; Jensen, M. P.; Que, L. *Chem. Rev.* **2004,** *104*, 939-986; (d) Blakemore, J. D.; Crabtree, R. H.; Brudvig, G. W. *Chem. Rev.* **2015,** *115*, 12974-13005; (e) Nguyen, A. I.; Ziegler, M. S.; Oña-Burgos, P.; Sturzbecher-Hohne, M.; Kim, W.; Bellone, D. E.; Tilley, T. D. *J. Am. Chem. Soc.* **2015,** *137*, 12865-12872; (f) Okamura, M.; Kondo, M.; Kuga, R.; Kurashige, Y.; Yanai, T.; Hayami, S.; Praneeth, V. K. K.; Yoshida, M.; Yoneda, K.; Kawata, S.; Masaoka, S. *Nature* **2016,** *530*, 465-468; (g) Hunter, B. M.; Thompson, N. B.; Müller, A. M.; Rossman, G. R.; Hill, M. G.; Winkler, J. R.; Gray, H. B. *Joule* **2018,** *2*, 747-763.
2. Yano, J.; Yachandra, V. *Chem. Rev.* **2014,** *114*, 4175-4205.
3. (a) Ichino, T.; Yoshioka, Y. *Chem. Phys. Lett.* **2014,** *595–596*, 237-241; (b) Yamaguchi, K.; Isobe, H.; Yamanaka, S.; Saito, T.; Kanda, K.; Shoji, M.; Umena, Y.; Kawakami, K.; Shen, J. R.; Kamiya, N.; Okumura, M. *Int. J. Quantum Chem* **2013,** *113*, 525-541; (c) Sproviero, E. M.; Gascón, J. A.; McEvoy, J. P.; Brudvig, G. W.; Batista, V. S. *J. Am. Chem. Soc.* **2008,** *130*, 3428-3442; (d) Siegbahn, P. E. M. *BBA - Bioenergetics* **2013,** *1827*, 1003-1019.
4. Limburg, J.; Vrettos, J. S.; Liable-Sands, L. M.; Rheingold, A. L.; Crabtree, R. H.; Brudvig, G. W. *Science* **1999,** *283*, 1524-1527.
5. (a) Ozaki, S.-i.; Roach, M. P.; Matsui, T.; Watanabe, Y. *Acc. Chem. Res.* **2001,** *34*, 818-825; (b) Betley, T. A.; Wu, Q.; Van Voorhis, T.; Nocera, D. G. *Inorg. Chem.* **2008,** *47*, 1849-1861; (c) Guo, M.; Corona, T.; Ray, K.; Nam, W. *ACS Cent Sci* **2019,** *5*, 13-28; (d) Sacramento, J. J. D.; Goldberg, D. P. *Acc. Chem. Res.* **2018,** *51*, 2641-2652; (e) Goetz, M. K.; Hill, E. A.; Filatov, A. S.; Anderson, J. S. *J. Am. Chem. Soc.* **2018,** *140*, 13176-13180; (f) Usharani, D.; Janardanan, D.; Li, C.; Shaik, S. *Acc. Chem. Res.* **2013,** *46*, 471-482; (g) Kim, S. H.; Park, H.; Seo, M. S.; Kubo, M.; Ogura, T.; Klajn, J.; Gryko, D. T.; Valentine, J. S.; Nam, W. *J. Am. Chem. Soc.* **2010,** *132*, 14030-14032; (h) Kurahashi, T.; Kikuchi, A.; Shiro, Y.; Hada, M.; Fujii, H. *Inorg. Chem.* **2010,** *49*, 6664-6672; (i) Gunay, A.; Theopold, K. H. *Chem. Rev.* **2010,** *110*, 1060-1081.
6. (a) de Visser, S. P.; Kumar, D.; Neumann, R.; Shaik, S. *Angew. Chem. Int. Ed.* **2004,** *43*, 5661-5665; (b) Khenkin, A. M.; Kumar, D.; Shaik, S.; Neumann, R. *J. Am. Chem. Soc.* **2006,** *128*, 15451-15460; (c) Xue, G.; De Hont, R.; Münck, E.; Que, L., Jr. *Nature Chemistry* **2010,** *2*, 400-405; (d) Vaddypally, S.; Kondaveeti, S. K.; Karki, S.; Van Vliet, M. M.; Levis, R. J.; Zdilla, M. J. *J. Am. Chem. Soc.* **2017,** *139*, 4675-4681; (e) Sarma, R.; Angeles-Boza, A. M.; Brinkley, D. W.; Roth, J. P. *J. Am. Chem. Soc.* **2012,** *134*, 15371-15386.
7. (a) de Ruiter, G.; Thompson, N. B.; Takase, M. K.; Agapie, T. *J. Am. Chem. Soc.* **2016,** *138*, 1486-1489; (b) de Ruiter, G.; Carsch, K. M.; Gul, S.; Chatterjee, R.; Thompson, N. B.; Takase, M. K.; Yano, J.; Agapie, T. *Angew. Chem. Int. Ed.* **2017,** *56*, 4772-4776; (c) Carsch, K. M.; de Ruiter, G.; Agapie, T. *Inorg. Chem.* **2017,** *56*, 9044-9054.
8. (a) Lacy, D. C.; Gupta, R.; Stone, K. L.; Greaves, J.; Ziller, J. W.; Hendrich, M. P.; Borovik, A. S. *J. Am. Chem. Soc.* **2010,** *132*, 12188-12190; (b) Gupta, R.; Taguchi, T.; Lassalle-Kaiser, B.; Bominaar, E. L.; Yano, J.; Hendrich, M. P.; Borovik, A. S. *Proc. Natl. Acad. Sci.* **2015,** *112*, 5319-5324; (c) Gupta, R.; MacBeth, C. E.; Young, V. G.; Borovik, A. S. *J. Am. Chem. Soc.* **2002,** *124*, 1136-1137; (d) Gupta, R.; Borovik, A. S. *J. Am. Chem. Soc.* **2003,** *125*, 13234-13242; (e) MacBeth, C. E.; Golombek, A. P.; Young, V. G.; Yang, C.; Kuczera, K.; Hendrich, M. P.; Borovik, A. S. *Science* **2000,** *289*, 938-941; (f) Ford, C. L.; Park, Y. J.; Matson, E. M.; Gordon, Z.; Fout, A. R. *Science* **2016,** *354*, 741; (g) Park, Y. J.; Matson, E. M.; Nilges, M. J.; Fout, A. R. *Chem. Commun.* **2015,** *51*, 5310-5313; (h) Matson, E. M.; Park, Y. J.; Fout, A. R. *J. Am. Chem. Soc.* **2014,** *136*, 17398-17401; (i) Gordon, Z.; Drummond, M. J.; Matson, E. M.; Bogart, J. A.; Schelter, E. J.; Lord, R. L.; Fout, A. R. *Inorg. Chem.* **2017,** *56*, 4852-4863.
9. Han, Z.; Horak, K. T.; Lee, H. B.; Agapie, T. *J. Am. Chem. Soc.* **2017,** *139*, 9108-9111.
10. Horak, K. T. The Design and Synthesis of Transition Metal Complexes Supported by Non-innocent Ligand Scaffolds for Small Molecule Activation. PhD dissertation, California Institute of Technology, Pasadena, California, 2016.
11. de Ruiter, G.; Thompson, N. B.; Lionetti, D.; Agapie, T. *J. Am. Chem. Soc.* **2015,** *137*, 14094-14106.

12. Arnett, C. H.; Chalkley, M. J.; Agapie, T. *J. Am. Chem. Soc.* **2018,** *140*, 5569-5578.
13. Andris, E.; Navrátil, R.; Jašík, J.; Puri, M.; Costas, M.; Que, L.; Roithová, J. *J. Am. Chem. Soc.* **2018,** *140*, 14391-14400.
14. McDonald, A. R.; Que Jr, L. *Coord. Chem. Rev.* **2013,** *257*, 414-428.
15. (a) Bordwell, F. G.; Satish, A. V.; Zhang, S.; Zhang, X. M. Using thermodynamic cycles to study reactive intermediates. In *Pure Appl. Chem.*, 1995; Vol. 67, p 735; (b) Mayer, J. M. *Acc. Chem. Res.* **1998,** *31*, 441-450; (c) Warren, J. J.; Tronic, T. A.; Mayer, J. M. *Chem. Rev.* **2010,** *110*, 6961-7001.
16. (a) Saame, J.; Rodima, T.; Tshepelevitsh, S.; Kütt, A.; Kaljurand, I.; Haljasorg, T.; Koppel, I. A.; Leito, I. *The Journal of Organic Chemistry* **2016,** *81*, 7349-7361; (b) Garrido, G.; Koort, E.; Ràfols, C.; Bosch, E.; Rodima, T.; Leito, I.; Rosés, M. *The Journal of Organic Chemistry* **2006,** *71*, 9062-9067.
17. Reed, C. J.; Agapie, T. *J. Am. Chem. Soc.* **2018,** *140*, 10900-10908.
18. PCET is broadly referred to here as the transfer of a proton and an electron to different parts of a complex (see ref. 17); the precise mechanism, whether concerted (CPET or EPT) or stepwise (either PTET or ETPT), is left ambiguous, as the present experiments cannot differentiate them.
19. Weinberg, D. R.; Gagliardi, C. J.; Hull, J. F.; Murphy, C. F.; Kent, C. A.; Westlake, B. C.; Paul, A.; Ess, D. H.; McCafferty, D. G.; Meyer, T. J. *Chem. Rev.* **2012,** *112*, 4016-4093.
20. Goetz, M. K.; Anderson, J. S. *J. Am. Chem. Soc.* **2019,** *141*, 4051-4062.
21. Huang, C.-Y.; Doyle, A. G. *J. Am. Chem. Soc.* **2012,** *134*, 9541-9544.
22. Izod, K.; Rayner, D. G.; El-Hamruni, S. M.; Harrington, R. W.; Baisch, U. *Angew. Chem. Int. Ed.* **2014,** *53*, 3636-3640.
23. Hagadorn, J. R.; Que, L.; Tolman, W. B. *Inorg. Chem.* **2000,** *39*, 6086-6090.
24. Adhikari, D.; Mossin, S.; Basuli, F.; Huffman, J. C.; Szilagyi, R. K.; Meyer, K.; Mindiola, D. J. *J. Am. Chem. Soc.* **2008,** *130*, 3676-3682.
25. Ludwiczak, M.; Majchrzak, M.; Marciniec, B.; Kubicki, M. *J. Organomet. Chem.* **2011,** *696*, 1456-1464.
26. Alberola, A.; Antolín, L. F.; Cuadrado, P.; González, A. M.; Laguna, M. A.; Pulido, F. J. *Synthesis* **1988,** *1988*, 203-207.
27. Herbert, D. E.; Lionetti, D.; Rittle, J.; Agapie, T. *J. Am. Chem. Soc.* **2013,** *135*, 19075-19078.
28. (a) Herold, S.; Lippard, S. J. *Inorg. Chem.* **1997,** *36*, 50-58; (b) Singh, A. K.; Jacob, W.; Boudalis, A. K.; Tuchagues, J.-P.; Mukherjee, R. *Eur. J. Inorg. Chem.* **2008,** *2008*, 2820-2829; (c) Sutradhar, M.; Carrella, L. M.; Rentschler, E. *Eur. J. Inorg. Chem.* **2012,** *2012*, 4273-4278; (d) Schünemann, V.; Hauke, P. Mössbauer Spectroscopy. In *Applications of Physical Methods to Inorganic and Bioinorganic Chemistry*, Scott, R. A.; Lukehart, C. M., Eds. John Wiley & Sons: West Sussex, England, 2007; pp 243-269.
29. Chilton, N. F.; Anderson, R. P.; Turner, L. D.; Soncini, A.; Murray, K. S. *J. Comput. Chem.* **2013,** *34*, 1164-1175.
30. Xue, X.-S.; Ji, P.; Zhou, B.; Cheng, J.-P. *Chem. Rev.* **2017,** *117*, 8622-8648.
31. Bordwell, F. G.; Bares, J. E.; Bartmess, J. E.; McCollum, G. J.; Van der Puy, M.; Vanier, N. R.; Matthews, W. S. *The Journal of Organic Chemistry* **1977,** *42*, 321-325.
32. Matthews, W. S.; Bares, J. E.; Bartmess, J. E.; Bordwell, F. G.; Cornforth, F. J.; Drucker, G. E.; Margolin, Z.; McCallum, R. J.; McCollum, G. J.; Vanier, N. R. *J. Am. Chem. Soc.* **1975,** *97*, 7006-7014.
33. Taskinen, E.; Nummelin, K. *The Journal of Organic Chemistry* **1985,** *50*, 4844-4847.

CHAPTER 5

INTERMOLECULAR REACTIVITY OF TETRANUCLEAR FE CLUSTERS VIA PUTATIVE FE–OXO AND –IMIDO INTERMEDIATES

ABSTRACT

Sterically open pyrazolate-bridged tetranuclear Fe clusters were examined for their reactivity towards oxygen and nitrogen transfer reagents. Addition of iodosylarene to a $Fe^{II}_2Fe^{III}_2$ cluster produces a one electron oxidized terminal-hydroxide cluster, which ultimately forms an octanuclear μ_2-O cluster, upon dehydration. Formation of the terminal hydroxide cluster is considered to occur due to formal hydrogen atom abstraction from a reactive intermediate that could not be extensively characterized (either terminal Fe-oxo or iodosylarene adduct). The one electron reduced pyrazolate cluster is capable of activating electron deficient aryl azides, leading to isolation of clusters bearing an NHAr amide ligand, via a putative Fe-imido moiety. Reactivity studies were also performed with an interstitial fluoride containing Fe cluster. Oxygen atom transfer to a μ_4-F containing Fe^{II}_4 cluster leads to formation of analogous octanuclear μ_2-O cluster, or cluster rearrangement to afford a fluoride bound μ_4-O cluster. The intermolecular reactivity of these putative Fe-oxo and –imido moieties were limited to decomposition by formal hydrogen atom transfer in solution, which highlights the high reactivity of these complexes, likely due, in part, to the open coordination environment of the unsubstituted bridging pyrazolates.

INTRODUCTION

Nature utilizes a variety of multinuclear transition metal arrangements to accomplish many catalytic transformations.[1] Three general cases can be considered for the roles these clusters possibly have in metalloenzymes: (i) the transfer of electrons, with no direct substrate-cluster binding or interaction (i.e. [4Fe-4S] clusters); (ii) binding and activation of substrate at a single metal site with the auxiliary metals providing a specific structural or electronic environment for the substrate-binding metal; or (iii) binding and activation of substrate across multiple metal sites within the cluster. Often, the precise role of each metal center within an active site cluster is ambiguous, based on the available biochemical data. Therefore, developing our understanding of the reactivity of transition metal clusters related to these metalloenzymes can help establish the functional purposes of their unique multinuclear architectures.

A number of synthetic mononuclear transition metal complexes have been studied with the goal of providing insight into biological multinuclear active sites that are thought to activate substrates at a single metal site.[2] Due to a number of strategies to tune the reactivity of transition metal complexes through ligand modifications, and the relative ease of structural and spectroscopic characterization of these small molecules, the transition metal chemistry of these systems, which are relevant to biological processes, can be probed in fine detail. However, these studies are not able to establish the possible role of auxiliary metal centers within multinuclear active sites. Examples of multinuclear systems where the reactivity of one metal site can be probed as a function of an auxiliary metal are relatively rare,[3] with most examples limited to binuclear complexes.[4]

A challenge to developing better models of multinuclear active sites, where the level of detail in study can match that of mononuclear systems, lies in the difficulty of producing well-defined multinuclear structures which bear distinct metal coordination environments,

specifically ones where substrate binding and activation is limited to a single metal site within the cluster. These 'site-differentiated' clusters require a fine balance of stability and reactivity to be suitable for detailed studies of their property-reactivity relationships. Along these lines, our group has developed routes to synthesize a family of transition metal clusters supporting various first row transition metal centers (Mn, Fe, Co, Ni, Cu, Zn) in a robust scaffold that arranges the metal in a site-differentiated fashion capable of supporting these property-reactivity studies.[5] These clusters are all based on a common symmetric trinuclear metal precursor, where a fourth (apical) metal site is introduced through the use of bridging pyrazolates (or imidazolates), and anchored into a tetrahedral metal arrangement through a central interstitial μ_4-atom ligand (either O or F).[6] The resulting apical metal center is four coordinate, with a trigonal pyramidal geometry, suitable to study its reactivity as a function of the auxiliary coordinatively saturated metal ions.

The reactivity of these clusters towards accessing M=E (E = O, N) moieties is appealing to study, due to the implication of terminal Mn=O species in the OEC of photosystem II[7] and the possibility of Fe=NR intermediates in nitrogenase FeMo cofactor.[8] Understanding the ways in which neighboring metal centers can affect the nature of these reactive intermediates, therefore, has relevance towards our understanding of multinuclear active sites. Furthermore, interest in the chemistry of these types of reactive intermediates has led to many examples of mononuclear systems capable of supporting these moieties;[9] significantly less developed is the chemistry of these intermediates in complexes with more than two redox active metals.[10]

Previous attempts to examine oxygen- or nitrogen-atom transfer reactivity through terminal M=E intermediates were performed by a number of group members on various pyrazolate-bridged clusters of Fe and Mn. Dr. Graham de Ruiter and Kurtis Carsch studied intramolecular oxygen atom transfer reactions between Fe_4, Mn_4, and Fe_3Mn clusters bearing

arylpyrazolate ligands (Scheme 1);[6b, 11] fast C–H (or C–F) activation of the pendant arene moiety was observed, precluding any reactivity with external substrates, even in large excesses. Attempts to observe intermolecular reactivity led to the development of clusters supported by unsubstituted pyrazolate ligands by Dr. Kyle Horak.[12] Early synthetic routes to these clusters relied on $FeCl_2$ as the source of the apical metal, leading to isolation of **[LFe$_3$O(Pz)$_3$FeCl][OTf]**; removal of the Cl ligand proved challenging, precluding extensive reactivity studies. Exchange of the Cl^- ligand for N_3^- was accomplished, serving as a possible precursor to a reactive Fe-nitride cluster; however, photolysis or thermolysis of this cluster did not lead to activation of the azide ligand.

Scheme 1. Related Studies of Tetranuclear Clusters By Previous Members of the Agapie Group[6b, 11-12]

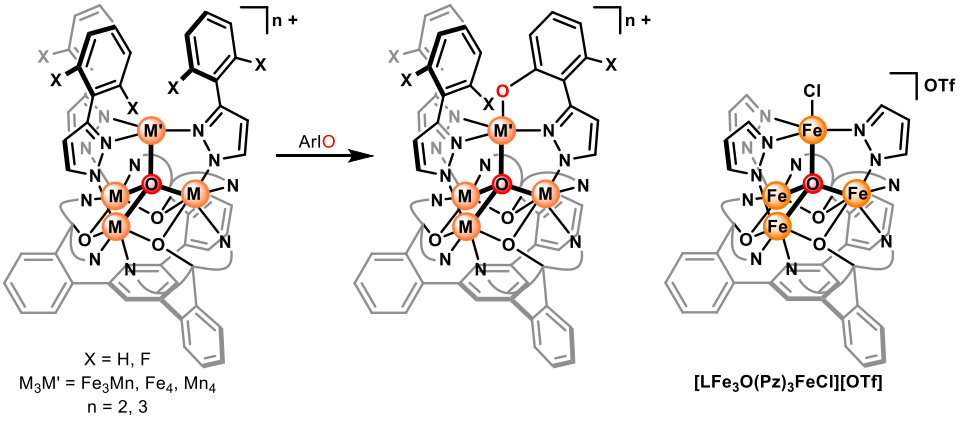

Herein is an extension of the chemistry of the tetranuclear Fe clusters supported by unsubstituted pyrazolate ligands, towards examining intermolecular reactivity via Fe=O or Fe=NR intermediates. Characterization of reaction products demonstrates decomposition by formal hydrogen atom transfer of these putative intermediates to produce the corresponding Fe–OH and Fe–NHR (R = -aryl or –tosyl) species.

RESULTS AND DISCUSSION

Synthesis and Characterization of Fe_4 Clusters Bearing Unsubstituted Pyrazolate Ligands with a Labile Apical Fe Ligand. Tetranuclear Fe clusters with unsubstituted pyrazolates and a labile trifluoromethanesulfonate (triflate, ⁻OTf) ligand bound to the apical Fe can be prepared in two steps starting from the reported tri-iron cluster **$LFe_3(OAc)(OTf)_2$** by stirring this cluster with three equivalents potassium pyrazolate (KPz), iodosylbenzene (PhIO), and Fe(II) acetate (Figure 1A). This produces a tetranuclear Fe cluster bearing unsubstituted pyrazolate ligands and an acetate ligand bound to the apical Fe, **1**. A partial X-ray crystal diffraction dataset was collected to confirm the identity of this cluster; the bond metrics of the Fe–μ_4-O distances were similar to the previously synthesized Fe_4-chloride

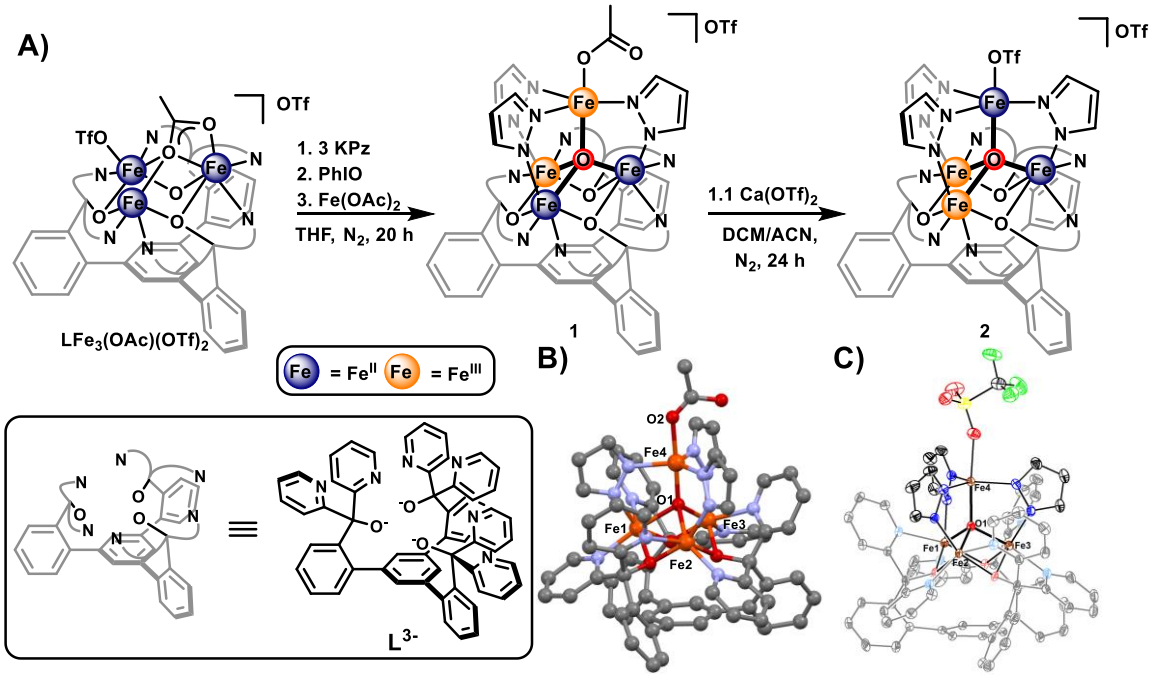

Figure 1. (A) Synthesis of tetranuclear Fe clusters with unsubstituted pyrazolate ligands and labile ligands bound to the apical Fe; inset, 1,3,5-triarylbenzene ligand platform (**L^{3-}**). (B) Preliminary crystal structure of **1** and crystal structure of **2** (C); hydrogen atoms, outersphere anions, and solvent molecules omitted for clarity.

cluster of the same oxidation state, consistent with a redox distribution where the apical Fe is trivalent (Table 1). Addition of calcium triflate to this cluster (to precipitate the less soluble calcium acetate) affords isolation of the tetra-iron dication bis-triflate, **2**. Structural characterization by XRD displays binding of the a triflate counterion to the apical Fe, with changes in the Fe–μ_4-O distances consistent with reduction of the apical Fe to the 2+ oxidation state, and concomitant oxidation of an Fe in the tri-iron core to Fe^{III}. This is supported by the Mössbauer spectrum of **2**, which contains parameters for the apical Fe consistent with a five-coordinate high-spin Fe^{II} (δ = 0.95 mm/s; $|\Delta E_q|$ = 2.22 mm/s; Figure 2 and Table 2).

Table 1. Selected Bond Distances for Structurally Characterized Pz-Fe_4 Clusters

Metric (Å) [b]	$[LFe_3O(Pz)_3Fe(Cl)][OTf]^{12}$	**1**[a]	**3-MeCN**	**2**	**4**
Fe1-O1	2.071(4)	2.17	2.086(9)	2.055(6)	2.143(7)
Fe2-O1	2.145(3)	2.15	2.049(8)	**2.018(5)**	**1.977(7)**
Fe3-O1	**2.024(4)**	**1.91**	**1.926(9)**	**1.949(5)**	**1.989(6)**
Fe4-O1	**1.864(4)**	**1.87**	1.977(8)	1.999(5)	**1.959(6)**
Fe4-L	2.339(2) (Fe4-Cl)	2.04 (Fe4-O2)	2.169(11) (Fe4-N2)	2.155(6) (Fe4-O2)	2.087(8) (Fe4-O2)

[a]Preliminary structure [b]Bold bond distances denote bonds with Fe^{III} centers, the rest are assigned to Fe^{II}.

Cyclic voltammetry of **2** in acetonitrile (MeCN) displays two quasi-reversible peaks, corresponding to the oxidation and reduction of **2**, with reduction potentials of -0.89 V (all potentials vs. Fc/Fc^+) and -0.13 V (Figure 3). A second quasi-reversible oxidation is observed at 0.57 V, however the return reductive scan produces new electrochemical events, suggesting a putative Fe^{III}_4 cluster is accessible, but unstable under the electrochemical conditions. The reduced and oxidized clusters **3** and **4** were accessed through treatment of **2** with cobaltocene ($CoCp_2$) and silver triflate (AgOTf), respectively (Figure 2). Mössbauer spectra of these clusters was consistent with reduction of **2** occurring at an Fe within the tri-iron core, but oxidation

occurring at the apical Fe, as opposed to the Fe^{II} in the core. This is an unusual observation for these types of tetranuclear clusters, where redox changes are typically restricted to the six-coordinate metal centers (only when there are changes to are ligand bound to the apical metal are redox changes for that metal observed). The redox distribution of **4** can be reversibly perturbed by displacement of triflate bound to the apical Fe; the solution state Mossbauer spectrum of **4** in MeCN (**4-MeCN**) displays notable changes to the parameters for the Fe centers, consistent with the loss of high-spin Fe^{II} in the tri-iron core and reduction of the apical Fe.

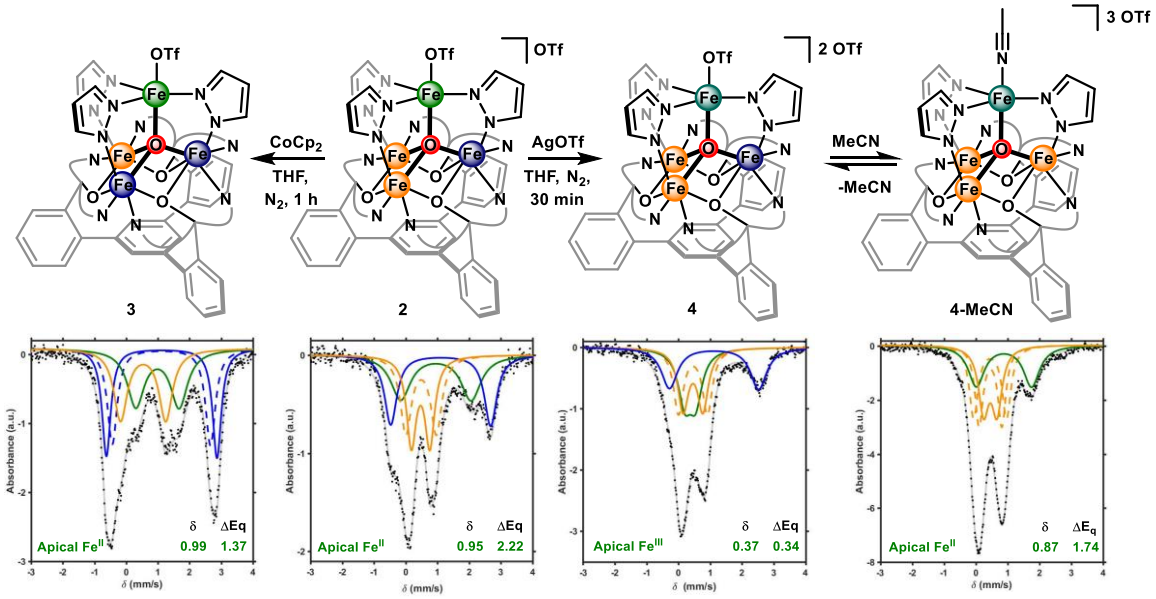

Figure 2. Chemical reduction and oxidation of **2** to afford **3** and **4**, respectively. Zero applied-field ^{57}Fe Mössbauer spectra of these clusters in the solid state, and **4** in a solution of MeCN (**4-MeCN**).

Table 2. ^{57}Fe Mössbauer Parameters for Pz-Fe$_4$ Clusters 2 – 4, and 4-MeCN

	δ (mm/s)	$\|\Delta E_q\|$ (mm/s)	assign-ment
3 ($Fe^{II}_3Fe^{III}$)			
Fe1, Fe2	1.12, 1.11	3.49, 3.10	*h.s.* Fe^{II}
Fe3	0.53	1.43	*h.s.* Fe^{III}
Fe4	0.99	1.37	*h.s.* apical Fe^{II}
2 ($Fe^{II}_2Fe^{III}_2$)			
Fe1	1.10	3.15	*h.s.* Fe^{II}
Fe2, Fe3	0.47, 0.48	0.58, 0.96	*h.s.* Fe^{III}
Fe4	0.95	2.22	*h.s.* apical Fe^{II}

	δ (mm/s)	$\|\Delta E_q\|$ (mm/s)	assign-ment
4 ($Fe^{II}Fe^{III}_3$)			
Fe1	1.12	2.81	*h.s.* Fe^{II}
Fe2, Fe3	0.46, 0.48	0.62, 0.91	*h.s.* Fe^{III}
Fe4	0.37	0.34	*h.s.* apical Fe^{III}
4-MeCN ($Fe^{II}Fe^{III}_3$)			
Fe1, Fe2, Fe3	0.45, 0.46, 0.46	1.03, 0.72, 0.42	*h.s.* Fe^{III}
Fe4	0.89	1.74	*h.s.* apical Fe^{II}

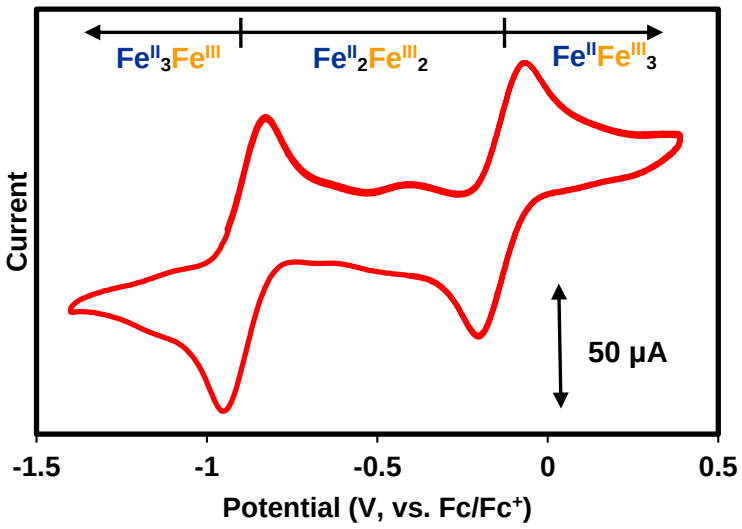

Figure 3. Cyclic voltammetry of **2** in MeCN (2 mM) with $[Bu_4N][PF_6]$ electrolyte (100 mM) at a scan rate of 200 mV/s with glassy carbon, Pt-wire, and Ag-wire as working, counter, and reference electrode, respectively. The open circuit potential was -0.4 V.

Investigations of Pz-Fe$_4$ Clusters with Oxygen Atom Transfer Reagents. With access to these pyrazolate-bridged Fe clusters with a relatively labile ligand (OTf) bound to the site-differentiated Fe, their reactivity towards oxygen atom transfer (OAT) agents were investigated towards performing reactivity studies through a terminal Fe-oxo moiety. Treatment of the [$Fe^{II}_2Fe^{III}_2$] cluster, **2**, with 2-*tert*-butyl-sulfonyl iodosylbenzene (sPhIO) produces a [$Fe^{II}Fe^{III}_3$] cluster with a terminal hydroxide ligand bound to the apical Fe, **5**, based on TOF-MS, ^{1}H NMR spectroscopy, and Mössbauer spectroscopy (Figure 4). This cluster decomposes upon standing, or if concentrated under vacuum, to produce an octanuclear Fe

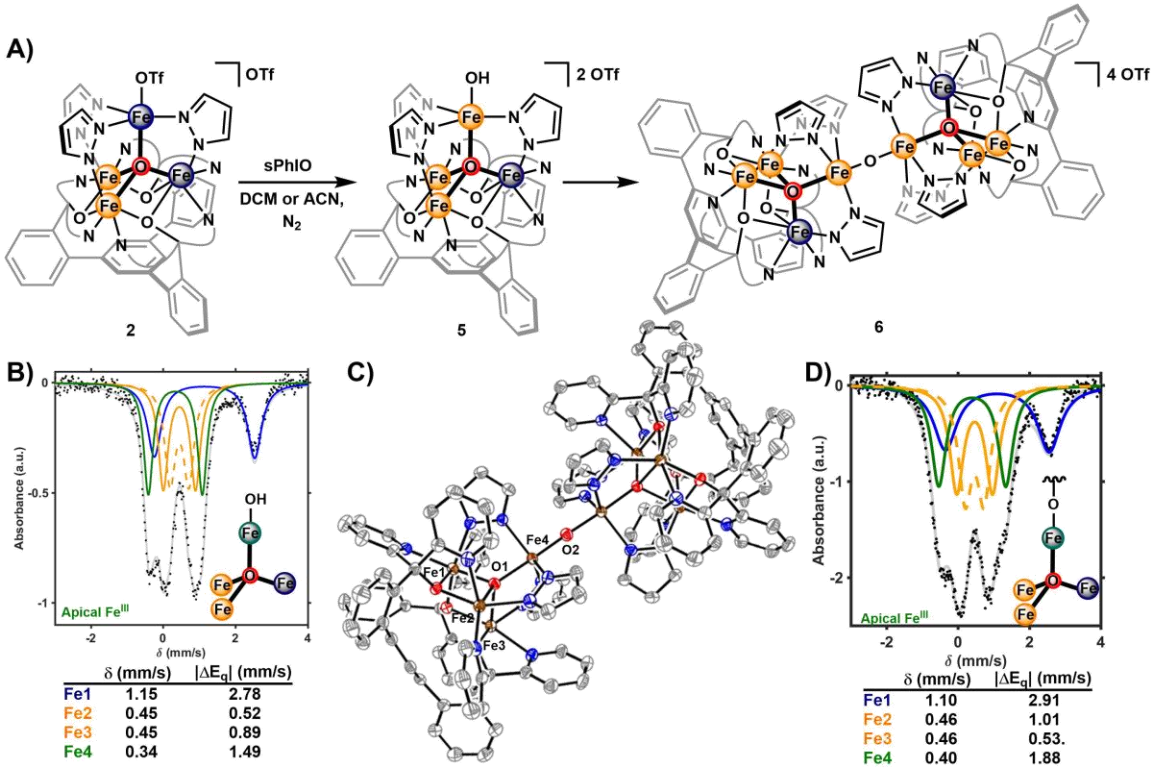

Figure 4. (A) Reactivity of **2** towards OAT reagent sPhIO. (B) Zero applied-field Mössbauer spectrum of **5** in MeCN with parameters for each unique quadrupole doublet. (C) Structure of **6**, with hydrogen atoms, outersphere counterions, and solvent molecules omitted for clarity. (D) Zero applied-field Mössbauer spectrum of **6** in MeCN with parameters for each unique quadrupole doublet.

cluster with a μ_2-O ligand bound to two pyrazolate-bridged [$Fe^{II}Fe^{III}_3$] cluster subunits, **6**; this compound was structurally characterized via XRD. Similar results are obtained with different OAT reagents, such as *tert*-butyl hydroperoxide and tetrabutylammonium *meta*-periodate.

Observation of **5** in solution, likely followed by dehydration to form **6**, supports the conclusion that, under the experimental conditions employed here, a 1:1 cluster to sPhIO stoichiometry is dominant, as opposed to consuming half an equivalent of sPhIO to afford **6** directly. Producing **5** from **2** and sPhIO is consistent with formation of a reactive species which undergoes formal hydrogen atom transfer; both terminal metal-oxo and iodosylarene adduct complexes are known to undergo this type of chemistry.[13]

In an attempt to distinguish between these two possible reactive intermediates, variable temperature ^{1}H NMR experiments were performed. In deuterated solvents (CD_2Cl_2 or CD_3CN) at low temperatures (below -20 °C), mixtures of **5** and a putative intermediate were

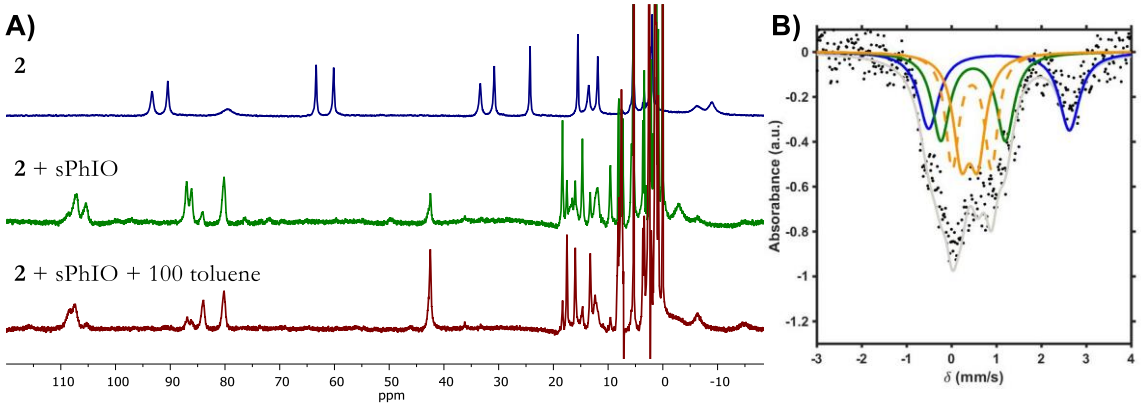

Figure 5. (A) ^{1}H NMR (400 MHz, CD_2Cl_2, -40 °C) spectra of **2** (blue), intermediate of **2** and sPhIO before formation of **5** (green), and **5** formed by addition of excess toluene to this intermediate (red). (B) Mössbauer spectrum of the putative intermediate, collected by cold pentane precipitation, with parameters: (i) δ = 1.06 mm/s, $|\Delta E_q|$ = 3.13 mm/s (blue trace), (ii) δ = 0.40 mm/s, $|\Delta E_q|$ = 0.36 mm/s (solid orange trace), and (iii) δ = 0.46 mm/s, $|\Delta E_q|$ = 0.87 mm/s (dashed orange trace), (iv) δ = 0.49 mm/s, $|\Delta E_q|$ = 1.44 mm/s (green trace).

observed (Figure 5). A Mössbauer spectrum of this mixture was obtained, and it ruled out the presence of an Fe^{IV}-oxo moiety, with parameters that were best fit with **5** and another [$Fe^{II}Fe^{III}_3$] cluster. However, assigning this species to either possible oxidizing intermediate (Fe^{III}-oxo or -iodosylarene adduct) was inconclusive. Analogous experiments were performed on the other oxidation states of the Pz-Fe_4 clusters, **3** and **4**. In neither case could a reactive intermediate be observed by NMR at an appreciable concentration; **3** would react completely, even at -40 °C, while **4** would remain mostly unreacted towards sPhIO at low temperatures.

The electrochemical and spectroscopic properties of **6** were investigated; however, it was later determined that isolation and recrystallization of samples of **6** contained two species by ^{1}H NMR with nearly identical resonances (Figure 6). These species could be separated from each other through extraction of **6** (as confirmed by XRD) in MeCN. Attempts to structurally characterize the remaining MeCN precipitate were unsuccessful.

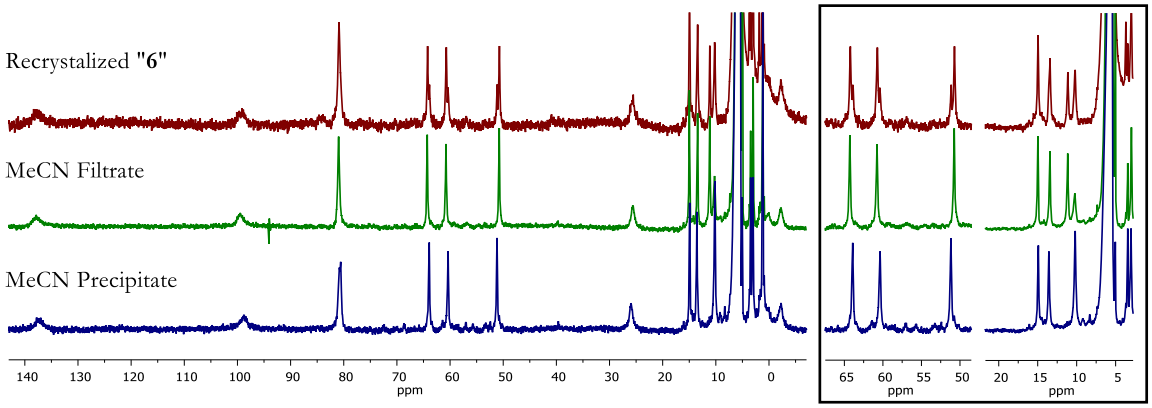

Figure 6. ^{1}H NMR (300 MHz, CD_2Cl_2) of as-isolated and recrystallized **6** (red) and the species separated by trituration in MeCN (green and blue). (Inset) Paramagnetic regions highlighting the differences in peak positions of these two species.

Cyclic voltammetry of **6** in CH_2Cl_2 displays five quasi-reversible redox events separated into closely spaced pairs, attributable to redox changes occurring within each of the tetra-iron

subunits (Figure 7). The reduction potentials of these processes, where the charge of the cluster is used to abbreviate oxidation state (0 = $[Fe^{II}_3Fe^{III}]_2O$, 1+ = $[Fe^{II}_3Fe^{III}]O[Fe^{III}_2Fe^{II}_2]$, etc.): 0 → 1+, -1.98 V (all potentials vs Fc/Fc^+); 1+ → 2+, -1.64 V; 2+ → 3+, -0.75 V; 3+ → 4+, -0.56 V; 4+ → 5+, 0.10 V. The small separation between the pairs of redox events is consistent with relatively little electronic interaction between the individual Pz-Fe_4 subunits. The redox event to form the 6+ cluster ($[Fe^{III}_4]_2O$) was not observed in the CV, or via square-wave voltammetry.

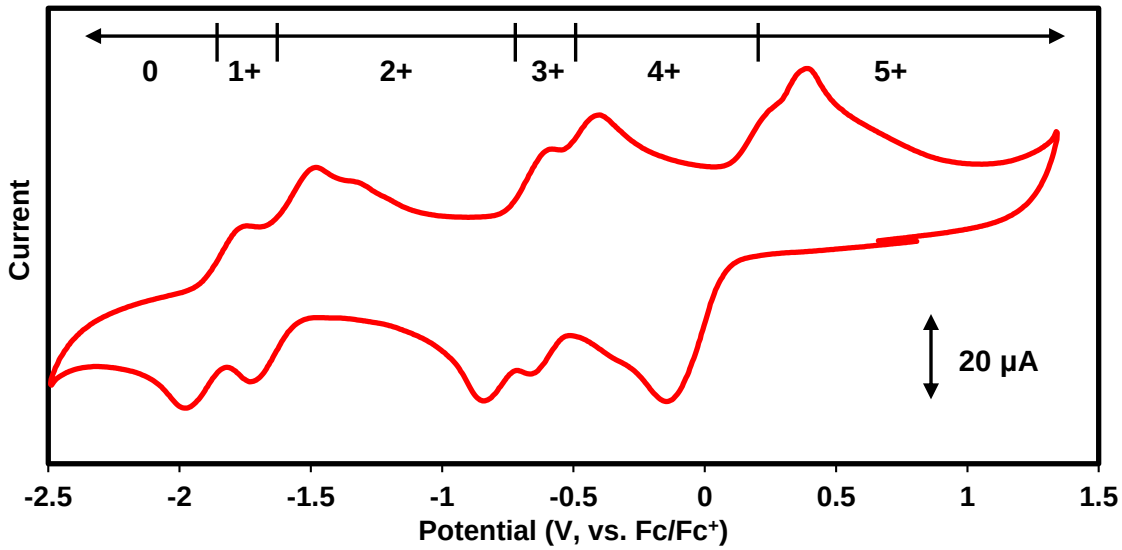

Figure 7. Cyclic voltammetry of **6** in CH_2Cl_2 (2 mM) with $[Bu_4N][PF_6]$ electrolyte (100 mM) at a scan rate of 200 mV/s with glassy carbon, Pt-wire, and Ag-wire as working, counter, and reference electrode, respectively. The open circuit potential was 0 V.

Reactivity of Pz-Fe_4 Clusters with Organic Azides and *N*-Tosylimino-Transfer Reagent. Due to the challenges in observing evidence for formation of, and reactivity from, a terminal Fe-oxo with **2** and OAT reagents, reactions targeting an Fe-imido species were attempted; it was hypothesized that substituents on the nitrogen atom could be selected to stabilize the Fe-bound intermediate, i.e. having a bulky, electron withdrawing group would

slow down decomposition by formal hydrogen atom transfer, and disfavor formation of μ_2-NR clusters (analogous to **6**). **2** proved to be unreactive towards aryl- or alkyl-azides, but the one electron reduced cluster, **3**, was competent for activation of relatively electron poor aryl azides. These reactions were typically complete upon warming to room temperature; preliminary structural characterization of reactions between **3** and 2-azideobiphenyl and 3,5-trifluoromethyl-phenylazide displayed apical Fe centers with a coordinated aryl amide (–NHAr), as evidenced by the relatively long apical Fe–N distance of ~2.0 Å and small Fe–N–C angle of ~130°, consistent with reported structures of Fe^{III}–NHAr complexes.[14]

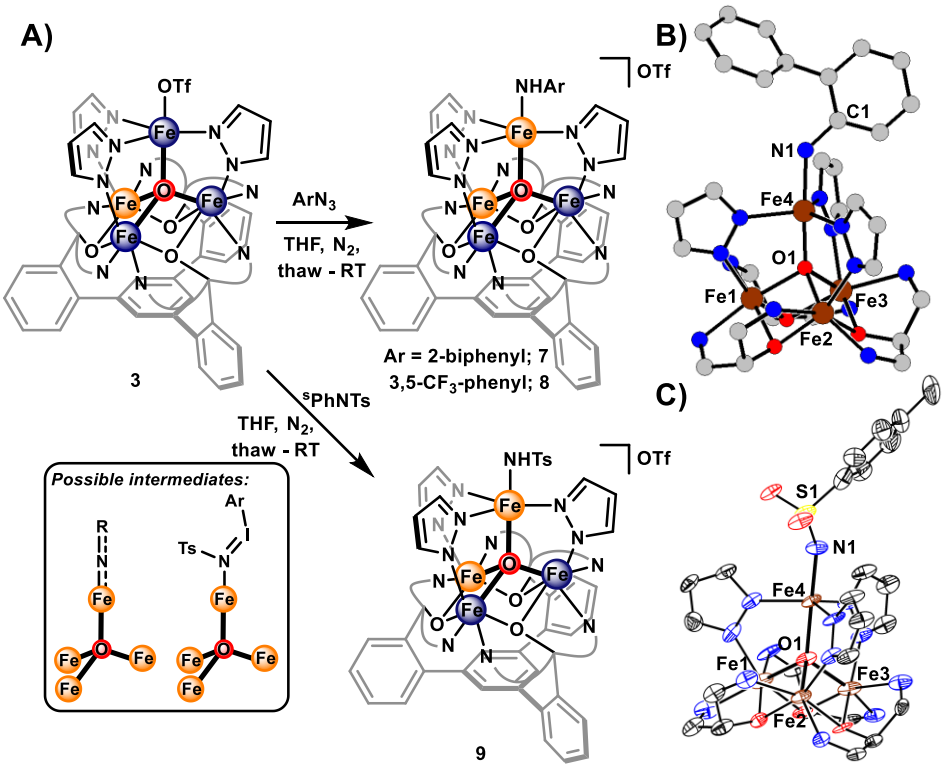

Figure 8. (A) Synthesis of aryl- and tosyl-amide clusters **7** – **9** from **3**; (inset) possible Fe-bound intermediates include a terminal Fe-imido or iodo-tosylimino adduct. (B) Truncated preliminary crystal structure of **7**. (C) Truncated crystal structure of **8**; hydrogen atoms, counterions, and solvent molecules omitted for clarity.

Table 3. Selected Bond Distances and Angles for Complexes 7 – 9.

Metric (Å)[b]	**7**[a]	**8**[a]	**9**
Fe1-O1	2.10	2.16	2.047(8)
Fe2-O1	2.08	2.09	2.044(9)
Fe3-O1	**2.04**	**1.99**	**1.993(7)**
Fe4-O1	**1.87**	**1.90**	**2.035(8)**
Fe4-N1	2.01	1.99	1.856(10)
∠Fe4–N1–C1	131	131	146.8 (∠Fe4–N1–S1)

[a] Preliminary structure. [b]Bold bond distances denote bonds with Fe^{III} centers, the rest are assigned to Fe^{II}.

Similarly, treatment of **3** with an iodoimino transfer agent, 2-*tert*-butyl-sulfonyl-*N*-para-toluenesulfonyl-iminoiodobenzene (sPhNTs), leads to isolation of the tosylamide-bound cluster, **9**.

Overall, attempts to stabilize Fe-imido clusters with electron withdrawing or sterically bulky aryl groups were unable to lead to observation of this intermediate before formal hydrogen atom transfer to produce the corresponding amide. For reactions with aryl azides, it is possible that azide activation leads to a short-lived aryl-imido cluster, although off-metal reactive species cannot be ruled out, i.e. outersphere electron transfer producing reactive nitrene. Application of these reactions towards amination of cyclohexene were attempted, however no N-transfer product was observed.

Reactivity of μ_4-F Pz-Fe_4 Clusters Towards Oxygen Atom Transfer Reagents and Azide. Due to the challenge of observing evidence of a terminal Fe-oxo or –imido moiety within these clusters, investigations on related clusters bearing a different electronic environment were pursued. Previous investigations on μ_4-F bridged clusters demonstrated a significant effect the interstitial ligand has on the properties and reactivity of the Fe_4 cluster (see Chapter 2).[6d] A μ_4-F ligand could make the apical Fe more electron deficient, and any resulting terminal Fe-oxo less basic; furthermore, weaker the bonding to the μ_4-F may promote

multiple bonding to a terminal-oxo by facilitating pseudo-tetrahedral geometry at the apical Fe.

Unsubstituted pyrazolate-bridged clusters bearing an interstitial F^- ligand were prepared through addition of tetrabutylammonium fluoride to **$LFe_3(OAc)(OTf)_2$** with a combination of potassium pyrazolate and two equivalents of pyrazole (HPz). The apical Fe is introduced with $Fe(N(SiMe_3)_2)_2$ and calcium triflate was added to sequester acetate from the initial trinuclear cluster, to afford isolation of a fluoride-bridged Fe^{II}_4 cluster, **10** (Scheme 2).

Scheme 2. Synthesis and Reactivity of Pz-Fe_4 Clusters Bearing μ_4-F Ligand.

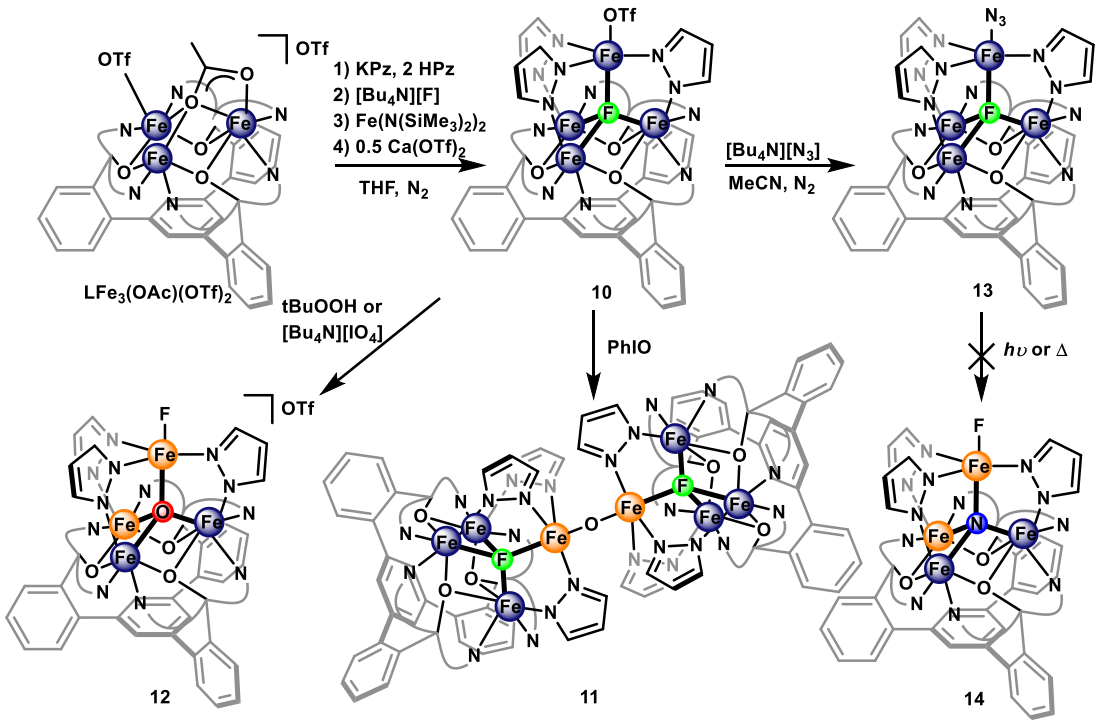

Structural characterization of **10** confirms a cluster geometry analogous to the μ_4-O versions (Figure 9A). The electrochemistry of this cluster is more complex than **2**. In MeCN, only one quasi-reversible feature is observed, corresponding to a reduction potential for the oxidation of **10** at -0.52 V (vs. Fc/Fc^+), followed by two irreversible oxidations, which change

over multiple CV scans (Figure 10), likely due to decomposition of the $Fe^{II}Fe^{III}_3$ cluster oxidation state.

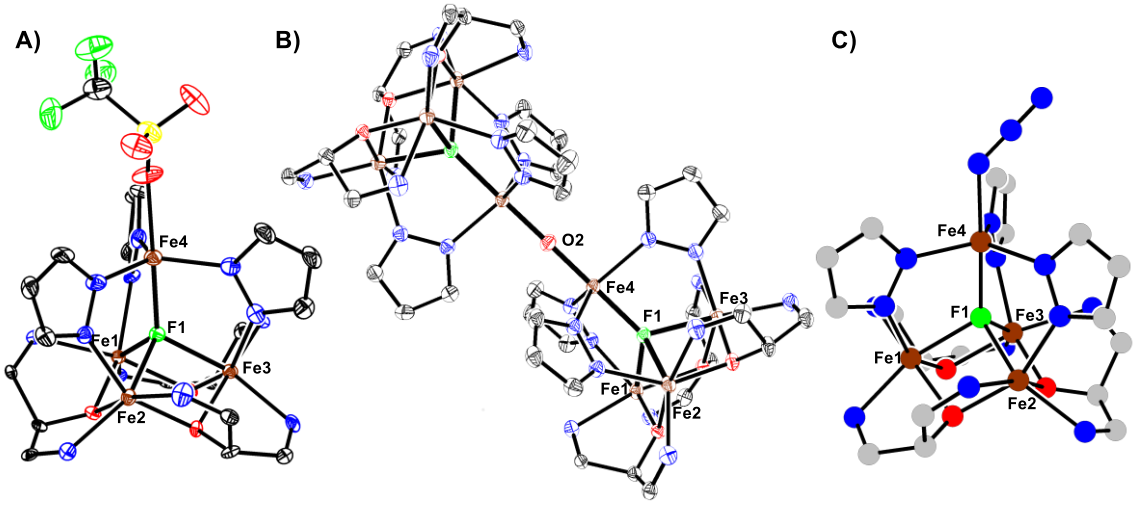

Figure 9. Truncated crystal structures of **10** (A), **11** (B), and **13** (C; preliminary).

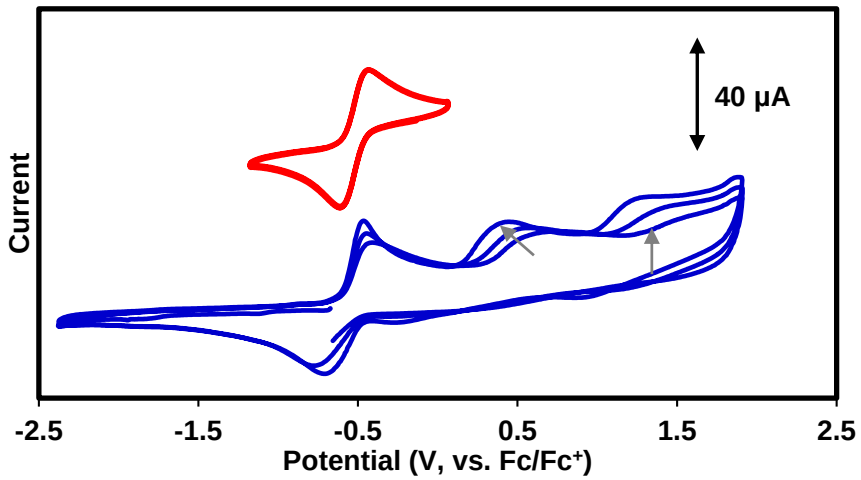

Figure 10. Cyclic voltammetry of **10** in MeCN (2 mM) with $[Bu_4N][PF_6]$ electrolyte (100 mM) at a scan rate of 200 mV/s with glassy carbon, Pt-wire, and Ag-wire as working, counter, and reference electrode, respectively. The open circuit potential was -0.7 V. The full CV scan (blue) displays two irreversible oxidations, which shift over multiple CV scans.

Treatment of **10** with different OAT reagents results in multiple reaction products, with product distributions that depends on the nature of the OAT reagent. Reactions with

iodosylbenzene (PhIO), which is polymeric and insoluble, leads to isolation of a μ_2-O cluster (**11**), with a structure analogous to **6** (Figure 9B). Analysis of bond metrics of **6** and **11** display shorter bonds to the μ_2-O in **11** (1.7853(6) vs. 1.8079(7) Å), with a shift of the apical Fe out of the equatorial plane (Table 4).

Table 4. Selected Bond Distances in Complexes 6 and 11.

Metric (Å)	**6** ($[Fe^{II}Fe^{III}_3]_2O$)	**11** ($[Fe^{II}_3Fe^{III}]_2O$)
Fe1-O1/F1	**1.942(3)**	2.191(2)
Fe2-O1/F1	**2.096(3)**	2.205(2)
Fe3-O1/F1	2.176(3)	2.235(2)
Fe4-O1/F1	**1.925(3)**	**1.991(2)**
Fe4-O2	1.8079(7)	1.7853(6)
Fe4-N14|N24|N34	0.099	0.174

Alternatively, *tert*-butyl hydroperoxide (tBuOOH) or tetrabutylammonium periodate ($[Bu_4N][IO_4]$) react very quickly with **10** to produce a species which is assigned to an interstitial O cluster with a terminal F ligand, **12**. This is supported by independent synthesis of **12** from **1** and tetrabutylammonium fluoride, as evidenced by ^{1}H NMR spectroscopy. A possible intermediate to **12** could be a terminal Fe-oxo, followed by internal ligand rearrangement to form the more stable interstitial oxo cluster, although direct substitution of the μ_4-F by the OAT reagent is also a possible route to this complex.

Observation of substitution of the μ_4-F in **10** suggested a potential route to tetranuclear clusters with a bridging nitride ligand, via formation of a terminal nitride that undergoes cluster rearrangement. The azide-bound Pz-Fe_4 cluster, **13**, can be prepared through addition of tetrabutylammonium azide to **10** (Figure 9C). Attempts to thermalyze or photolyze this moiety, however, led to no reaction being observed (Scheme 1).

CONCLUSIONS

A series of tetranuclear Fe clusters bearing a sterically open coordination environment at the apical Fe could be prepared with a coordinated labile triflate ligand, suitable for reactivity studies towards oxygen and nitrogen atom transfer reagents. For **2**, and its one electron reduced form, **3**, fast intermolecular decomposition of putative Fe-oxo and Fe-imido moieties (or iodosylarene adducts) occur by formal hydrogen atom transfer, likely from organic solvent. A cluster bearing an interstitial F ligand, **10**, demonstrated similar reactivity, forming an octanuclear μ_2-O cluster containing fluoride, but was also capable undergoing substitution of this interstitial fluoride ligand with oxygen.

Overall, it is challenging to reach a suitable balance between stability and reactivity for these Pz-Fe_4 clusters to prepare terminal-oxo or -imido moieties. Subsequent studies demonstrated the necessity of pendant hydrogen bonding donors on the pyrazolate ligands to stabilize an Fe-oxo (Chapter 4). Further investigations could examine strategies to tune these secondary coordination sphere interactions to access a suitably reactive, but still well-defined, Fe-oxo cluster.

EXPERIMENTAL DETAILS

General Considerations. All reactions were performed at room temperature in an N_2-filled M. Braun glovebox or using standard Schlenk techniques unless otherwise specified. Glassware was oven dried at 140 ºC for at least 2 h prior to use, and allowed to cool under vacuum. **$LFe_3(OAc)(OTf)_2$**,[6a] potassium pyrazolate (KPz),[6e] iodosobenzene (PhIO),[15], tetrabutylammonium fluoride ($[Bu_4N][F]$),[16], iron(II) bis-hexamethyldisilylamide ($Fe(N(SiMe_3)_2)_2$),[17] 2-*tert*-butyl-sulfonyl-iodosylbenzene (sPhIO),[18] 2-*tert*-butyl-sulfonyl-*N*-para-toluenesulfonyl-iminoiodobenzene (sPhINTs),[18] and 3.5-trifluoromethyl-phenylazide,[19] were prepared according to literature procedures. All organic solvents were dried by sparging with nitrogen for at least 15 minutes, then passing through a column of activated A2 alumina under positive N_2 pressure. ^1H spectra were recorded on a Varian 300 MHz spectrometer; variable temperature spectra were recorded on a Varian 400 MHz spectrometer. CD_3CN and CD_2Cl_2 were purchased from Cambridge Isotope Laboratories, dried over calcium hydride, degassed by three freeze-pump-thaw cycles, and vacuum transferred prior to use.

Physical Methods. *Mössbauer measurements.* Zero field ^{57}Fe Mossbauer spectra were recorded at 80 K in constant acceleration mode on a spectrometer from See Co (Edina, MN) equipped with an SVT-400 cryostat (Janis, Wilmington, WA). The isomer shifts are relative to the centroid of an α-Fe foil signal at room temperature. Samples were prepared by mixing polycrystalline material (20 mg) with boron nitride in a cup fitted with screw cap or freezing a concentrated solution in MeCN. The data were fit to Lorentzian lineshapes using WMOSS (www.wmoss.org).

Mössbauer simulation details for all compounds. All spectra were simulated as four pairs of symmetric quadrupole doubles with equal populations and Lorentzian lineshipes. They were refined to a minimum via least squares optimization (13 fitting parameters per spectrum).

Signals appearing above 2 mm/s were indicative with the presence of high-spin Fe^{II} centers and correspond to species with isomer shifts ~ 1 mm/s. The Mössbauer data were fit to be consistent with our previously reported iron clusters.[6a, 11b, 20] The observed Mossbauer parameters are in agreement with related six-coordinate high-spin Fe^{II}/Fe^{III} centers.[21]

Electrochemical measurements. CVs and SWVs were recorded with a Pine Instrument Company AFCBP1 biopotentiostat with the AfterMath software package. All measurements were performed in a three electrode cell, which consisted of glassy carbon (working; ø = 3.0 mm), silver wire (reference) and bare platinum wire (counter), in a N_2 filled M. Braun glovebox at RT. The ferrocene/ferrocinium (Fc/Fc^+) redox wave were used as an internal standard for all measurements.

X-ray crystallography. X-ray diffraction data was collected at 100 K on a Bruker PHOTON100 CMOS based diffractometer (microfocus sealed X-ray tube, Mo Kα (λ) = 0.71073 Å or Cu Kα (λ) = 1.54178 Å). All manipulations, including data collection, integration, and scaling, were carried out using the Bruker APEXII software. Absorption corrections were applied using SADABS. Structures were solved by direct methods using XS (incorporated into SHELXTL) and refined by using ShelXL least squares on Olex2-1.2.7 to convergence. All non-hydrogen atoms were refined using anisotropic displacement parameters. Hydrogen atoms were placed in idealized positions and were refined using a riding model. Due to the size of the compounds most crystals included solvent-accessible voids that contained disordered solvent. In most cases the solvent could be modeled satisfactorily.

Synthetic Procedures. *Synthesis of [LFe₃O(Pz)₃Fe(OAc)][OTf]* ***(1).*** 627 mg (0.45 mmol) **$LFe_3(OAc)(OTf)_2$** was suspended in 8 mL THF in a 20 mL scintillation vial. This suspension was frozen in a liquid N_2-cooled cold-well. In a separate vial, a suspension of 152 mg (1.43 mmol) potassium pyrazolate in 2 mL was also frozen. The suspensions were combined, while

thawing, and stirred for 10 minutes. Then, 2 mL THF was used to transfer 101 mg (0.46 mmol) iodosylbenzene to the stirring suspension; after 60 minutes, a brown suspension forms. 80 mg (0.465 mmol) $Fe(OAc)_2$ was added to the reaction with 3 mL THF and stirred for 20 hours. The precipitate was collected over a bed of celite on a glass frit, washed with 3 mL THF, and dried under vacuum. A brown solution was collected by washing this solid with CH_2Cl_2 and filtering it through the frit. Recrystallization via CH_2Cl2/Et_2O vapor diffusion affords 375 mg (55% yield) **1** as brown crystals. ^{1}H NMR (300 MHz, CD_2Cl_2) δ 131.9 (br), 83.9 (br), 75.9, 56.6, 50.9, 37.6, 26.2, 22.9, 14.4, 13.6, 11.0, 2.6), 1.3, -2.3 (br), -12.3, -17.8 (br) ppm.

Synthesis of [LFe$_3$O(Pz)$_3$Fe][OTf]$_2$ ***(2).*** 124 mg $Ca(OTf)_2$ (0.37 mmol) was dissolved in 10 mL MeCN and 290 mg (0.19 mmol) **1** was added as a 10 mL DCM solution. This was stirred for 24 – 48 hours, until the ^{1}H NMR showed complete conversion to $[LFe_3O(Pz)_3Fe][OTf]_2$. The reaction was dried completely under vacuum, and a green-brown compound was dissolved in 15 mL DCM, filtered over celite, and recrystallized via vapor diffusion of Et_2O. 293 mg (0.184 mmol; 96% yield) of **2** were obtained after drying the resulting crystals under vacuum. X-ray quality crystals were obtained by oxidizing **3** with 1 equivalent $AgBPh_4$ in THF. Crystallization via diffusion of pentane into a CH_2Cl_2 solution of this compound affords crystals of $[LFe_3O(Pz)_3Fe][OTf][BPh_4]$ (^{1}H NMR identical to $[LFe_3O(Pz)_3Fe][OTf]_2$). ^{1}H NMR (300 MHz, CD_3CN) δ 122.0 (br), 71.1, 69.0, 53.3, 50.9, 42.4, 38.4, 16.7, 14.2, 13.9 (br), 12.5, 8.4 (br), 7.2, 3.9, 3.4, -5.5 (br) ppm. ^{19}F NMR (300 MHz, CD_3CN) δ -76 ppm. UV-Vis (CH_3CN) [ε (M^{-1} cm^{-1})]: 246 nm (6.4 x 10^4), 369 nm (6.7 x 10^3). Anal. Calcd. (%) for $C_{68}H_{48}F_6Fe_4N_{12}O_{10}S_2$: C, 51.77; H, 3.03; N, 10.54. Found: C, 51.17; H, 3.11; N, 10.46.

Synthesis of [LFe$_3$O(Pz)$_3$Fe][OTf] ***(3).*** A suspension of $[LFe_3O(Pz)_3Fe][OTf]_2$ (**2**; 43.8 mg, 0.027 mmol) in 2 mL THF was stirred as a THF solution of 5.9 mg $CoCp_2$ (0.031 mmol) was added. After 1 hour, the reaction was dried under vacuum. 4 mL DME was added to the purple

solid and stirred for 12 hours. The resulting purple precipitate was collected on a bed of celite, washed with 2 mL DME, dried, and eluted with 2:1 THF/MeCN; crystals of $[LFe_3O(Pz)_3Fe][OTf]$ (**3**) were obtained by vapor diffusion of Et_2O into this solution. ^1H NMR (300 MHz, CD_3CN): 101.8 (br), 59.4, 57.4, 35.8, 30.0, 29.5, 19.5, 15.9, 13.3, 7.2, 4.5, 3.9, -1.6 (br), -5.9 (br) ppm.

*Synthesis of $[LFe_3O(Pz)_3Fe][OTf]_3$ (**4**).* 45 mg (0.03 mmol) of $[LFe_3O(Pz)_3Fe][OTf]_2$ (**2**) was stirred as a suspension in THF. A THF solution of AgOTf (7 mg; 0.03 mmol) was added. After 30 minutes the reaction was dried under vacuum. The resulting solid was filtered over celite with DCM and the filtrate was dried under vacuum. This brown solid was crystallized via vapor diffusion of Et_2O into a DCM/MeCN solution to obtain 47 mg $[LFe_3O(Pz)_3Fe][OTf]_3$ (95% yield). ^1H NMR (300 MHz, CD_3CN) δ 169.0 (br), 94.7 (br), 81.8, 78.9, 72.9, 64.5, 45.0, 17.3, 10.4, 8.5, 7.9, 5.2, -0.8 (br) ppm. ^{19}F NMR (300 MHz, CD_3CN) δ -76 ppm.

*Synthesis of $[LFe_3O(Pz)_3Fe(OH)][OTf]_2$ (**5**). Method A.* 10.8 mg (0.007 mmol) **1** was layered in an NMR tube in MeCN with 100 μL of a 0.11 M MeCN solution of tBuOOH (0.011 mmol; prepared by diluting a 3.3 M stock in toluene) in a liquid N_2-cooled cold well. The layers were mixed upon thawing. **5** decomposes upon pumping down, or standing for long periods of time. In some experiments, excess (~2 equiv.) DABCO was added, but this had no noticeable effect on the production **5**. ^1H NMR (300 MHz, CD_3CN) δ 145.0 (br), 103.7 (br), 85.6, 66.6, 63.9, 45.5, 30.0 (br), 15.3, 13.6, 11.1, 7.2, -3.0 (br) ppm.

Method B. 54 mg (0.034 mmol) **2** was dissolved in 10 mL MeCN and froze in a liquid N_2-cooled cold well. This was combined with 12 mg (0.035 mmol) sPhIO upon thawing and mixed for 30 minutes. This produces an NMR identical to Method A, with a minor amount of **6**, due to decomposition.

*Synthesis of [(LFe$_3$O(Pz)$_3$Fe)$_2$O][OTf]$_4$ (**6**) Method A.* Concentration of a solution of **5** under vacuum produces a change in the NMR consistent with formation of **6**. ^{1}H NMR (300 MHz, CD_2Cl_2) δ 137.4 (br), 98.9 (br), 80.3, 63.7, 60.2, 50.3, 25.3 (br), 14.6, 13.1, 10.8, 9.9, 2.7, 1.7, -2.6 (br) ppm.

Method B. A MeCN solution of **2** was mixed with 0.6 equivalents PhIO for 5 hours at room temperature. The reaction was dried under vacuum and filtered with CH_2Cl_2. This crude product was recrystallized via CH_2Cl2/Et_2O vapor diffusion to obtain mostly **6** (with an unidentified impurity, vide infra), with an NMR identical to Method A.

Regardless of preparation method, a side product (ca. 30% relative to **6**) would be present with nearly identical NMR shifts: ^{1}H NMR (300 MHz, CD_2Cl_2) δ 137.5 (br), 98.7 (br), 80.6, 63.6, 60.1, 50.9, 25.7 (br), 14.6, 13.2, 9.9, 2.7, 0.84, -2.6 (br) ppm. This could be separated from **6** by stirring a solution of the mixture for 18 hours in MeCN and collecting the filtrate, or via MeCN/Et_2O vapor diffusion, where the mother liquor is collected upon precipitation of the side product. Attempts to identify this side product by XRD were unsuccessful.

*Synthesis of [LFe$_3$O(Pz)$_3$Fe(2-phenyl-anilide)][OTf] (**7**).* 22.3 mg (0.014 mmol) **2** was combined with 2.6 mg (0.013 mmol) 2-azidobiphenyl in thawing THF. After 24 hours, no reaction had been observed and 3.8 mg (0.02 mmol) $CoCp_2$ was added to the reaction; the solution turned purple, signifying the formation of **3**, and over multiple hours became blue. After stirring 20 hours, the reaction was recrystallized via THF/pentane vapor diffusion to afford crystals of **7**. ^{1}H NMR (500 MHz, THF/C_6D_6) δ 122.2 (br), 78.5 (br), 71.7, 71.1, 53.2, 47.5, 37.7, 33.4, 21.2, 14.0, 13.5, 11.4, 9.4, -16.8 ppm.

*Synthesis of [LFe$_3$O(Pz)$_3$Fe(3,5-trifluoromethyl-anilide)][OTf] (**8**).* 11.2 mg (0.008 mmol) **3** was dissolved in 3 mL THF and froze in a liquid N_2-cooled cold well. This was combined with a 1 mL solution of 2 mg (0.008 mmol) 3,5-trifluoromethyl phenylazide in THF, while thawing.

The solution turned blue as it warmed to room temperature, producing a mixture of **8** and side products. This was recrystallized via THF/pentane vapor diffusion. ^{1}H NMR (500 MHz, THF/C_6D_6) δ 123.4 (br), 78.9 (br), 70.4, 69.5, 50.7, 44.8, 25.7, 17.1, 8.9, 8.5, -6.8, -25.3 (br) ppm.

*Synthesis of [LFe$_3$O(Pz)$_3$Fe(p-toluenesulfonimide)][OTf] (**9**).* 11.3 mg (0.008 mmol) **3** was dissolved in THF and froze in a liquid N_2-cooled cold well. This was combined with 4.5 mg (0.009 mmol) sPhINTs in THF while thawing. The solution turns orange-red upon warming to room temperature to produce **9**. This was recrystallized via MeCN/Et_2O. ^{1}H NMR (300 MHz, CD_3CN) δ 125.7 (br), 91.6 (br), 73.7, 58.0, 55.1, 51.1, 14.0, 13.4, 534, 3.4, -1.1 (br) ppm.

*Synthesis of [LFe$_3$F(Pz)$_3$Fe][OTf] (**10**).* 763 mg (0.55 mmol) **LFe$_3$(OAc)(OTf)$_2$** was suspended in 5 mL THF in a 20 mL scintillation vial. This suspension was frozen in a liquid N_2-cooled cold-well. In a separate vial, a suspension of 64 mg (0.60 mmol) potassium pyrazolate and 88 mg (1.30 mmol) pyrazole in 2 mL THF was also frozen. These were combined while thawing, followed by addition of a THF suspension of [Bu_4N][F], 156 mg (0.60 mmol). After stirring for 30 minutes, a solution of 210 mg (0.56 mmol) Fe(N($SiMe_3$)$_2$)$_2$ was added. The solvent was removed under vacuum upon stirring for 20 hours. The solid was washed with Et_2O and toluene on a course porosity glass frit with celite; The remaining precipitate was eluted with a 1:1 mixture of THF/MeCN, until the washings from the frit were colorless. The filtrate was dried completely under vacuum, then suspended in 10 mL MeCN. 120 mg (0.34 mmol) Ca(OTf)$_2$ was added to the suspension and stirred for 24 hours. The red orange precipitate was collected over celite, dried under vacuum, then eluted with CH_2Cl_2 and recrystallized via CH_2Cl_2/Et_2O vapor diffusion to yield 450 mg of **10** as red-orange crystals (56% yield). ^{1}H NMR (300 MHz, CD_2Cl_2) δ 110.3 (br), 77.2, 72.5, 40.4, 30.0, 27.1, 23.3, 16.7, 11.9, 11.4, 4.5, 4.1, 1.2, -1.3 (br), -30.1 (br) ppm

*Synthesis of [(LFe$_3$F(Pz)$_3$Fe)$_2$O][OTf]$_2$ (**11**). Method A.* 102 mg (0.07 mmol) **10** was dissolved in CH_2Cl_2 a connected to the Schlenk line in a Schlenk tube. The reaction was degassed with three freeze-pump-thaw cycles and froze with liquid N_2. On the Schlenk line, 10.5 cmHg of O_2 was collected in a volumetric gas bulb (36.7 mL; 0.21 mmol O_2), which was connected between the Schlenk line and the reaction vessel. This was introduced to the frozen solution for 5 minutes, then thawed -78 °C and stirred briefly before warming to -30 °C. The reaction was left open to the partial atmosphere of O_2 for 30 minutes and stirred. Then, the solvent was removed under vacuum and the solid was recrystallized via CH_2Cl_2/Et_2O vapor diffusion to afford crude **11** (with an unidentified side product, vide infra). ^{1}H NMR (300 MHz, CD_2Cl_2) δ 92.1 (br), 77.3, 76.3, 43.2, 42.7 (br), 38.3, 26.7, 25.2, 24.3, 22.1,16.0, 9.2, 0.9, -1.1, -10.5 (br), -11.9 (br) ppm

Method B. 48 mg (0.033 mmol) **10** was dissolved in MeCN and combined with 4.6 mg (0.021 mmol) PhIO; **11** with its side product was produced as the major species after 5 minutes, with a ^{1}H NMR identical to Method A.

Similar to **6**, regardless of preparation method, a side product would be present with nearly identical NMR shifts: ^{1}H NMR (300 MHz, CD_2Cl_2) δ 77.9, 77.1, 43.1, 38.6, 27.4, 23.7, 22.7, 16.1 (br), 9.2, 0.89, -1.3, -10.8 (br) ppm. This could be separated from **11** by stirring a solution of the mixture for 18 hours in MeCN and collecting the filtrate, or via MeCN/Et_2O vapor diffusion, where the mother liquor is collected upon precipitation of the side product. Attempts to identify this side product by XRD were unsuccessful.

*Synthesis of [LFe$_3$O(Pz)$_3$Fe(F)][OTf] (**12**). Method A.* 20.2 mg (0.014 mmol) **10** was dissolved in MeCN and froze in a liquid N_2-cooled cold well. This was combined with 6.8 mg (0.016 mmol) [Bu_4N][IO_4] in MeCN while thawing. The reaction became a brown suspension. After 16 hours, the solvents were removed under vacuum and the residue was washed with Et_2O,

toluene, THF, and eluted with MeCN to obtain 14.2 mg of a brown solid, corresponding to mostly clean (>90%) **12** (~70% yield). ^{1}H NMR (300 MHz, CD_2Cl_2) δ 127.7 (br), 77.3 (br), 74.5, 73.9, 59.9, 49.0, 31.1, 28.6, 23.4, 14.4,13.3, 11.4, 3.6 (br), -10.7 (br) ppm

Method B. 83.3 mg (0.058 mmol) **10** was dissolved in MeCN and froze in a liquid N_2-cooled cold well. This was combined with 370 μL of a tBuOOH solution (3.3 M in toluene diluted to 5% in MeCN; 0.061 mmol) and 7.1 mg (0.063 mmol) DABCO while thawing. The reaction became a brown suspension. After 12 hours, reaction was filtered.

Method C. 36.4 mg (0.024 mmol) of a suspension of **1** in MeCN was combined with 8.7 mg (0.033 mmol) $[Bu_4N][F]$ in MeCN to produce **12**.

*Synthesis of $LFe_3F(Pz)_3Fe(N_3)$ (**13**).* 20.9 mg (0.014 mmol) **10** in MeCN was mixed with 4.3 mg (0.015 mmol) $[Bu_4N][N_3]$ to produce an orange precipitate. After 2 hours, the precipitate was collected over a frit with celite, washed with minimal MeCN, eluted with CH_2Cl_2, and dried under vacuum to obtain 14.1 mg **13** as a red orange solid (75% yield). ^{1}H NMR (300 MHz, CD_2Cl_2) δ 111.2 (br), 75.9, 71.5, 41.1, 31.5, 30.8, 29.3, 15.0, 14.2, 11.1, 3.6, -2.5 (br), -18.9 (br) ppm

ELECTROCHEMICAL DETAILS

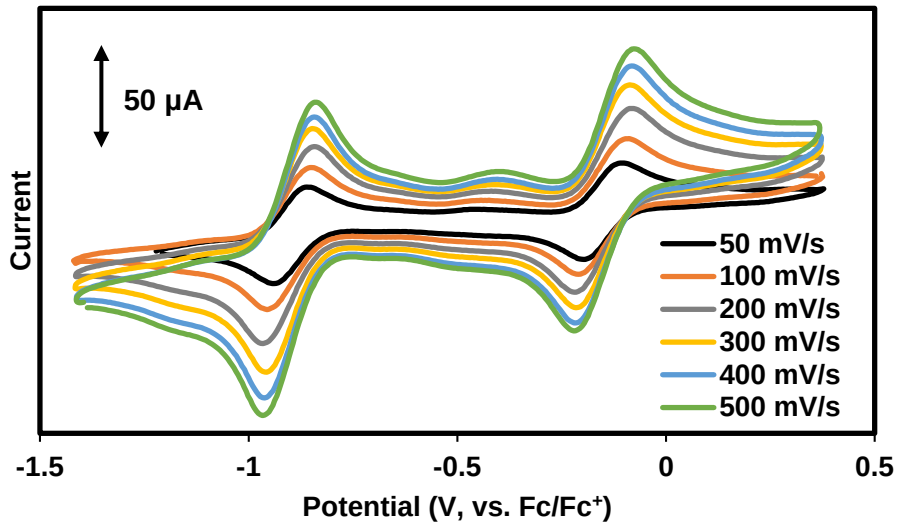

Figure 11. Cyclic voltammograms of $[LFe_3O(Pz)_3Fe][OTf]_2$ (**2**, 2 mM) in MeCN with 100 mM $[Bu_4N][PF_6]$ at various scan rates with glassy carbon, Pt-wire, and Ag-wire as working, counter, and reference electrode, respectively.

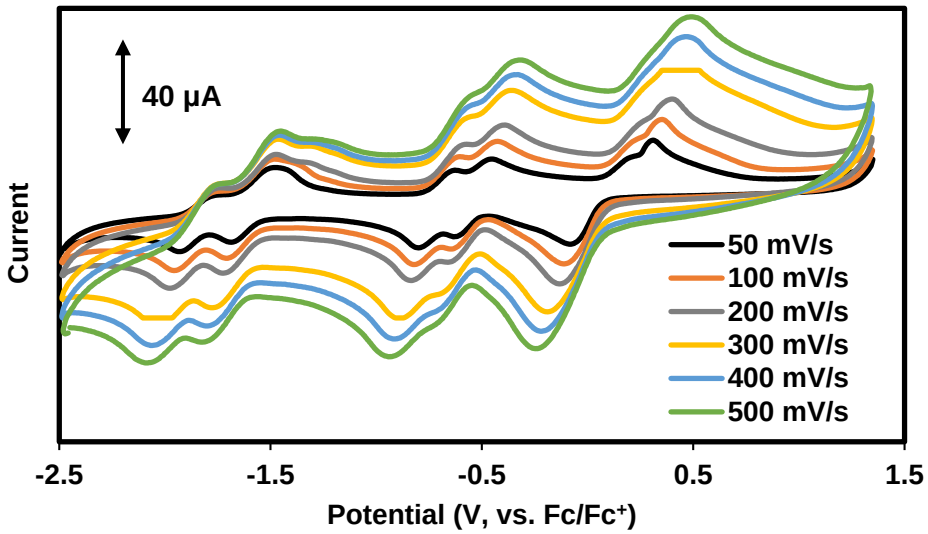

Figure 12. Cyclic voltammograms of $[(LFe_3O(Pz)_3Fe)_2O][OTf]_4$ (**6**, 2 mM) in CH_2Cl_2 with 100 mM $[Bu_4N][PF_6]$ at various scan rates with glassy carbon, Pt-wire, and Ag-wire as working, counter, and reference electrode, respectively.

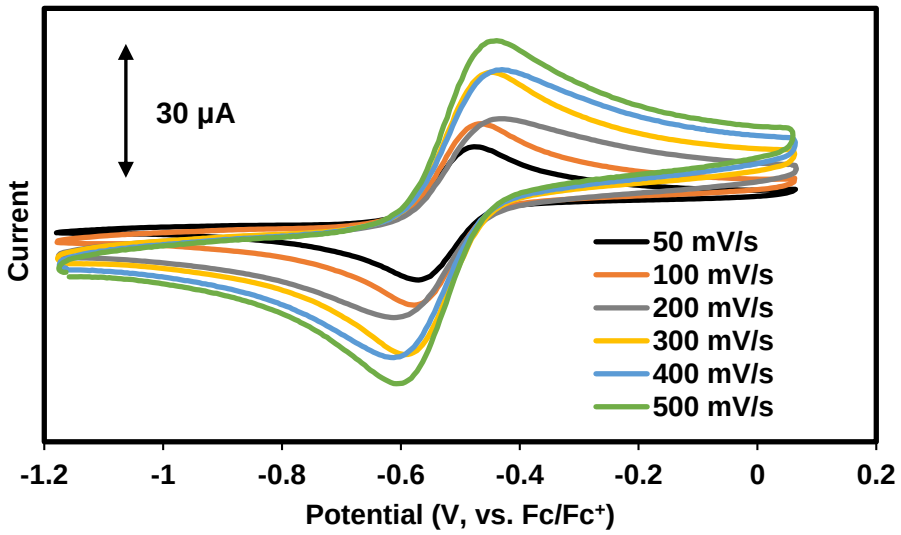

Figure 13. Cyclic voltammograms of $[LFe_3F(Pz)_3Fe][OTf]$ (**10**, 2 mM) in MeCN with 100 mM $[Bu_4N][PF_6]$ at various scan rates with glassy carbon, Pt-wire, and Ag-wire as working, counter, and reference electrode, respectively.

CRYSTALOGRAPHIC DETAILS

Crystal and refinement data for complexes 1 – 3-MeCN, 4, 6 – 11, and 13

	1[a]	2	3-MeCN	4	6
Empirical formula	$C_{78}F_2Fe_4N_{13}O_8$	$C_{95.28}H_{74.56}BCl_{8.56}F_3Fe_4N_{12}O_7S$	$C_{73}H_{52}F_3Fe_4N_{15}O_7S$	$C_{71.75}H_{49.5}ClF_{8.34}Fe_4N_{10.5}O_{12.61}S_3$	$C_{141.57}H_{102.25}Cl_{1.79}F_{12}Fe_8N_{24}O_{28.11}S_4$
Formula weight (g/mol)	1594.6	2124.57	1445.63	1717.62	3273.34
Radiation	CuKα (λ = 1.54178)	MoKα (λ = 0.71073)	CuKα (λ = 1.54178)	CuKα (λ = 1.54178)	CuKα (λ = 1.54178)
a (Å)	14.5023(10)	13.5663(9)	14.6522(6)	15.0846(9)	27.057(2)
b (Å)	19.6777(15)	17.3765(12)	19.7336(8)	15.0846(9)	14.2472(9)
c (Å)	47.912(4)	20.9073(14)	47.0533(17)	57.491(4)	40.302(3)
α (°)	90	84.592(3)	90	90	90
β (°)	93.256(3)	71.407(3)	91.934(2)	90	105.371(3)
γ (°)	90	80.890(2)	90	120	90
V (Å^3)	13650.8(18)	4607.4(5)	13597.3(9)	11329.2(15)	14980.0(18)
Z	8	2	8	6	4
Cryst. syst.	monoclinic	triclinic	monoclinic	trigonal	monoclinic
Space group	C2/c	P-1	C2/c	$P3_1$	C2/c
ϱ_{calc}g (cm^3)	1.552	1.531	1.412	1.511	1.451
2 Θ range (°)	7.392 to 69.236	4.656 to 56.496	7.518 to 158.694	4.61 to 158.116	6.776 to 149.24
μ (mm^{-1})	4.997	0.937	7.573	7.400	7.521
GOF	1.673	1.066	1.151	1.010	1.050
R1, wR2 (I>2σ (I))	R1 = 0.1227, wR2 = 0.3416	R_1 = 0.0694, wR_2 = 0.1905	R_1 = 0.1808, wR_2 = 0.3527	R_1 = 0.0674, wR_2 = 0.1620	R_1 = 0.1030, wR_2 = 0.2767

[a]Preliminary structure

	7[a]	**8**[a]	**9**	**10**	**11**	**13**[a]
Empirical formula	$C_{91}F_3Fe_4N_{13}O_9S$	$C_{80}Cl_{0.14}F_7Fe_4N_{12.36}O_7$	$C_{81}H_{55}Fe_4N_{13}O_9S_2$	$C_{68}H_{51}Cl_{1.91}F_4Fe_4N_{12}O_6S$	$C_{134}H_{94}F_8Fe_8N_{24}O_{13}S_2$	$C_{74.5}H_{47}FFe_4N_{18.39}O_3$
Formula weight (g/mol)	1873.11	1598.15	1641.90	1531.3	2884.12	1315.48
Radiation	MoKα (λ = 0.71073)	CuKα (λ = 1.54178)	CuKα (λ = 1.54178)	CuKα (λ = 1.54178)	MoKα (λ = 0.71073)	CuKα (λ = 1.54178)
a (Å)	18.1272(9)	19.0607(9)	55.590(10)	12.1433(15)	23.1614(12)	45.024(3)
b (Å)	16.5232(7)	15.6115(10)	12.4282(12)	23.562(4)	16.6931(8)	12.4123(7)
c (Å)	30.3724(15)	47.591(3)	22.632(2)	23.005(3)	33.0662(17)	51.116(3)
α (°)	90	90	90	90	90	90
β (°)	103.749(2)	91.952(2)	98.040(7)	99.807(5)	94.436(3)	109.157(5)
γ (°)	90	90	90	90	90	90
V (Å^3)	8836.5(7)	14153.3(14)	15482(3)	6485.8(16)	12746.3(11)	26984(3)
Z	4	8	8	4	4	16
Cryst. syst.	monoclinic	monoclinic	monoclinic	monoclinic	monoclinic	monoclinic
Space group	$P2_1/n$	C2/c	C2/c	$P2_1/C$	C2/c	C2/c
ϱ_{calc}g (cm^3)	1.408	1.500	1.409	1.568	1.503	1.295
2 Θ range (°)	4.7 to 60.842	7.32 to 127.554	7.292 to 116.164	5.41 to 130.452	3.306 to 60.97	4.156 to 129.078
μ (mm^{-1})	0.739	7.504	6.937	8.690	1.003	7.231
GOF	1.517	1.620	1.115	1.042	1.119	1.032
R1, wR2 (I>2σ (I))	R_1 = 0.1346, wR_2 = 0.3671	R1 = 0.1532, wR2 = 0.4118	R_1 = 0.1353, wR_2 = 0.3364	R_1 = 0.0801, wR_2 = 0.163	R_1 = 0.0891, wR_2 = 0.2464	R_1 = 0.0945, wR_2 = 0.2274

[a]Preliminary structure

Special refinement details for [$LFe_3O(Pz)_3Fe(OAc)$][OTf] (1). This is a preliminary structure; 80% complete dataset. The counterions and solvent molecules were not modeled beyond the XT structure solution. The cluster was kept isotropic.

Special refinement details for [$LFe_3O(Pz)_3Fe$][OTf][BPh_4] (2). This structure contains five co-crystalized CH_2Cl_2 molecules. One was modeled as partially occupied (28%; C014 and Cl1 and Cl12). Another was positionally disordered, with a common carbon atom (Cl4 and Cl5, 21%, and Cl2 and Cl3, 79%). Relatively high residual Q peak density near the bound triflate, corresponding to a small amount of disorder for this ligand, was present, but could not be modeled adequately.

Special refinement details for [$LFe_3O(Pz)_3Fe(MeCN)$][OTf] (3-MeCN). The outersphere triflate is disordered over two positions, which is on a symmetry element. Each half triflate was modeled as partially occupied (fixed to 50%) with the CF_3 and SO_3 groups refined via EXYZ constraints. There were 1 or 2 co-crystalized solvent molecules, which could not be adequately modeled, and were left as isotropic C atoms.

Special refinement details for [$LFe_3O(Pz)_3Fe$][$OTf]_3$ (4). There are two clusters in the asymmetric unit. All but two of the six triflates are disordered; the disordered triflates bound to the clusters could not be completely modeled, but the sulfur and carbon of the minor component were modeled isotropically. The two outersphere triflates are positionally disordered with occupancies of 64% (S11 through O141) and 36% (S3CA through O142), and 60% (S0AA through O2AA) and 40% (S7CA through O21).

Special refinement details for [$(LFe_3O(Pz)_3Fe)_2O$][$OTf]_4$ (6). There was a significant amount of solvent disorder in the crystal. It could be adequately modeled with CH_2Cl_2, Et_2O, and H_2O molecules. They were all modeled as partially occupied: Et_2O, 45%; CH_2Cl_2, 45%; H_2O, 55% (O18, O3AA) and 87% (O15).

Special refinement details for [$LFe_3O(Pz)_3Fe$(2-phenyl-anilide)][OTf] (7). This is a preliminary structure with a 37% complete dataset. The outersphere triflate was modeled, along with two co-crystalized THF molecules. There was some remaining solvent that could not be adequately modeled. Everything was modeled isotropically.

Special refinement details for [$LFe_3O(Pz)_3Fe$(3,5-trifluoromethyl-anilide)][OTf] (8). This is a preliminary structure with a 77% complete dataset. Everything was modeled isotropically. A complete triflate counterion and the trifluoromethyl groups could not be modeled adequately.

Special refinement details for [$LFe_3O(Pz)_3Fe$(para-toluenesulfonamide)][OTf] (9). Everything but the cluster was modeled isotropically, where no complete solvent molecule or counterion could be modeled.

Special refinement details for [$LFe_3F(Pz)_3Fe$][OTf] (10). The crystal contained a disordered co-crystalized CH_2Cl_2 molecule, with partial occupancies of 48% (C3, Cl2, and Cl6) and 52% (C3A, Cl1, and Cl3). 89% complete dataset.

Special refinement details for [$(LFe_3F(Pz)_3Fe)_2O$][OTf]$_2$ (11). The outersphere triflate was disordered over two positions in a ~50/50 ratio; however, each molecule could not be modeled completely. The presence of co-crystalized solvent molecules was suggested by large residual Q peaks, but nothing could be modeled adequately.

Special refinement details for $LFe_3F(Pz)_3Fe(N_3)$ (13). This is a preliminary structure with a 71% complete dataset. Everything was left isotropic. A number of co-crystallized MeCN molecules could be modeled.

References

1. Bertini, I.; Gray, H. B.; Stiefel, E. I.; Valentine, J. S. *Biological Inorganic Chemistry: Structure and Reactivity*. 1st ed.; University Science Books: Sausolito, California, 2007.
2. (a) Rittle, J.; Peters, J. C. *Proc. Natl. Acad. Sci.* **2013,** *110*, 15898-15903; (b) Taguchi, T.; Stone, K. L.; Gupta, R.; Kaiser-Lassalle, B.; Yano, J.; Hendrich, M. P.; Borovik, A. S. *Chemical Science* **2014,** *5*, 3064-3071; (c) Čorić, I.; Mercado, B. Q.; Bill, E.; Vinyard, D. J.; Holland, P. L. *Nature* **2015,** *526*, 96.
3. Li, F.; Meyer, R. L.; Carpenter, S. H.; VanGelder, L. E.; Nichols, A. W.; Machan, C. W.; Neidig, M. L.; Matson, E. M. *Chemical Science* **2018,** *9*, 6379-6389.
4. (a) Yu, F.; Pecoraro, V. L. *Polyhedron* **2013,** *64*, 99-105; (b) Xue, G.; De Hont, R.; Münck, E.; Que, L., Jr. *Nature Chemistry* **2010,** *2*, 400-405; (c) Caudle, M. T.; Pecoraro, V. L. *J. Am. Chem. Soc.* **1997,** *119*, 3415-3416; (d) Creutz, S. E.; Peters, J. C. *J. Am. Chem. Soc.* **2015,** *137*, 7310-7313; (e) Rittle, J.; McCrory, C. C. L.; Peters, J. C. *J. Am. Chem. Soc.* **2014,** *136*, 13853-13862.
5. Tsui, E. Y.; Kanady, J. S.; Day, M. W.; Agapie, T. *Chem. Commun.* **2011,** *47*, 4189-4191.
6. (a) de Ruiter, G.; Thompson, N. B.; Lionetti, D.; Agapie, T. *J. Am. Chem. Soc.* **2015,** *137*, 14094-14106; (b) Carsch, K. M.; de Ruiter, G.; Agapie, T. *Inorg. Chem.* **2017,** *56*, 9044-9054; (c) Arnett, C. H.; Chalkley, M. J.; Agapie, T. *J. Am. Chem. Soc.* **2018,** *140*, 5569-5578; (d) Reed, C. J.; Agapie, T. *Inorg. Chem.* **2017,** *56*, 13360-13367; (e) Reed, C. J.; Agapie, T. *J. Am. Chem. Soc.* **2018,** *140*, 10900-10908.
7. (a) Siegbahn, P. E. M. *BBA - Bioenergetics* **2013,** *1827*, 1003-1019; (b) Vinyard, D. J.; Brudvig, G. W. *Annu. Rev. Phys. Chem.* **2017,** *68*, 101-116; (c) Sproviero, E. M.; Gascón, J. A.; McEvoy, J. P.; Brudvig, G. W.; Batista, V. S. *J. Am. Chem. Soc.* **2008,** *130*, 3428-3442.
8. Hoffman, B. M.; Lukoyanov, D.; Yang, Z.-Y.; Dean, D. R.; Seefeldt, L. C. *Chem. Rev.* **2014,** *114*, 4041-4062.
9. (a) McDonald, A. R.; Que Jr, L. *Coord. Chem. Rev.* **2013,** *257*, 414-428; (b) Berry, J. F. *Comments Inorg. Chem.* **2009,** *30*, 28-66; (c) Lu, X.; Li, X.-X.; Seo, M. S.; Lee, Y.-M.; Clémancey, M.; Maldivi, P.; Latour, J.-M.; Sarangi, R.; Fukuzumi, S.; Nam, W. *J. Am. Chem. Soc.* **2019,** *141*, 80-83; (d) Wilding, M. J. T.; Iovan, D. A.; Wrobel, A. T.; Lukens, J. T.; MacMillan, S. N.; Lancaster, K. M.; Betley, T. A. *J. Am. Chem. Soc.* **2017,** *139*, 14757-14766.
10. (a) Vaddypally, S.; Kondaveeti, S. K.; Karki, S.; Van Vliet, M. M.; Levis, R. J.; Zdilla, M. J. *J. Am. Chem. Soc.* **2017,** *139*, 4675-4681; (b) de Visser, S. P.; Kumar, D.; Neumann, R.; Shaik, S. *Angew. Chem. Int. Ed.* **2004,** *43*, 5661-5665; (c) Khenkin, A. M.; Kumar, D.; Shaik, S.; Neumann, R. *J. Am. Chem. Soc.* **2006,** *128*, 15451-15460.
11. (a) Ruiter, G. d.; Carsch, K. M.; Takase, M. K.; Agapie, T. *Chemistry – A European Journal* **2017,** *23*, 10744-10748; (b) de Ruiter, G.; Thompson, N. B.; Takase, M. K.; Agapie, T. *J. Am. Chem. Soc.* **2016,** *138*, 1486-1489; (c) de Ruiter, G.; Carsch, K. M.; Gul, S.; Chatterjee, R.; Thompson, N. B.; Takase, M. K.; Yano, J.; Agapie, T. *Angew. Chem. Int. Ed.* **2017,** *56*, 4772-4776.
12. Horak, K. T. The Design and Synthesis of Transition Metal Complexes Supported by Non-innocent Ligand Scaffolds for Small Molecule Activation. PhD dissertation, California Institute of Technology, Pasadena, California, 2016.
13. (a) Nam, W.; Choi, S. K.; Lim, M. H.; Rohde, J.-U.; Kim, I.; Kim, J.; Kim, C.; Que, J. L. *Angew. Chem. Int. Ed.* **2003,** *42*, 109-111; (b) Wang, B.; Lee, Y.-M.; Seo, M. S.; Nam, W. *Angew. Chem. Int. Ed.* **2015,** *54*, 11740-11744; (c) MacBeth, C. E.; Golombek, A. P.; Young, V. G.; Yang, C.; Kuczera, K.; Hendrich, M. P.; Borovik, A. S. *Science* **2000,** *289*, 938-941; (d) Wijeratne, G. B.; Corzine, B.; Day, V. W.; Jackson, T. A. *Inorg. Chem.* **2014,** *53*, 7622-7634.
14. (a) Mankad, N. P.; Müller, P.; Peters, J. C. *J. Am. Chem. Soc.* **2010,** *132*, 4083-4085; (b) Iovan, D. A.; Betley, T. A. *J. Am. Chem. Soc.* **2016,** *138*, 1983-1993; (c) Spasyuk, D. M.; Carpenter, S. H.; Kefalidis, C. E.; Piers, W. E.; Neidig, M. L.; Maron, L. *Chemical Science* **2016,** *7*, 5939-5944; (d) Sazama, G. T.; Betley, T. A. *Inorg. Chem.* **2014,** *53*, 269-281.
15. Huang, C.-Y.; Doyle, A. G. *J. Am. Chem. Soc.* **2012,** *134*, 9541-9544.
16. Sun, H.; DiMagno, S. G. *J. Am. Chem. Soc.* **2005,** *127*, 2050-2051.
17. Rauchfuss, T. B. Bio-Inspired Iron and Nickel Complexes. In *Inorg. Synth.*, John Wiley & Sons, Inc.: 2010; pp 129-147.

18. Macikenas, D.; Skrzypczak-Jankun, E.; Protasiewicz, J. D. *J. Am. Chem. Soc.* **1999,** *121*, 7164-7165.
19. Altimari, J. M.; Niranjan, B.; Risbridger, G. P.; Schweiker, S. S.; Lohning, A. E.; Henderson, L. C. *Biorg. Med. Chem.* **2014,** *22*, 2692-2706.
20. Herbert, D. E.; Lionetti, D.; Rittle, J.; Agapie, T. *J. Am. Chem. Soc.* **2013,** *135*, 19075-19078.
21. (a) Herold, S.; Lippard, S. J. *Inorg. Chem.* **1997,** *36*, 50-58; (b) Singh, A. K.; Jacob, W.; Boudalis, A. K.; Tuchagues, J.-P.; Mukherjee, R. *Eur. J. Inorg. Chem.* **2008,** *2008*, 2820-2829; (c) Sutradhar, M.; Carrella, L. M.; Rentschler, E. *Eur. J. Inorg. Chem.* **2012,** *2012*, 4273-4278; (d) Schünemann, V.; Hauke, P. Mössbauer Spectroscopy. In *Applications of Physical Methods to Inorganic and Bioinorganic Chemistry*, Scott, R. A.; Lukehart, C. M., Eds. John Wiley & Sons: West Sussex, England, 2007; pp 243-269.

NMR DATA

CHAPTER 2

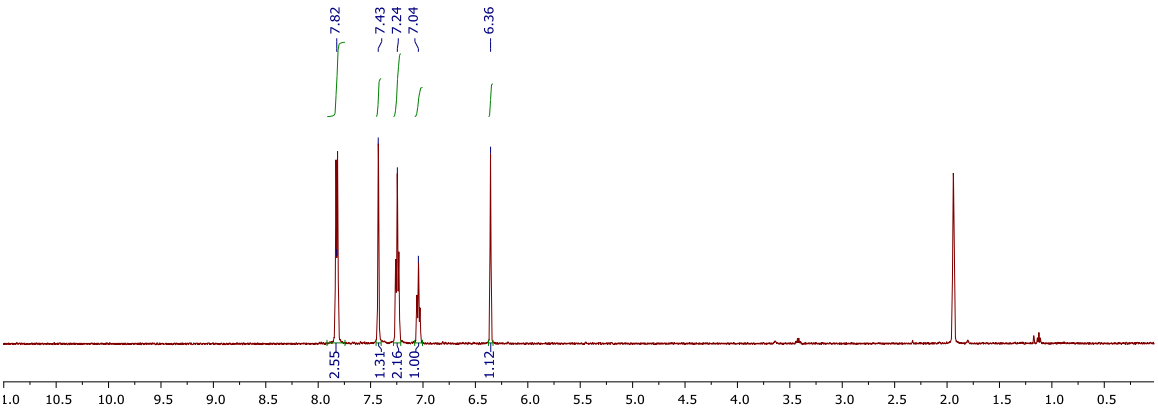

Figure 1. ^{1}H NMR spectrum (300 MHz) of potassium 3-phenyl pyrazolate in CD_3CN.

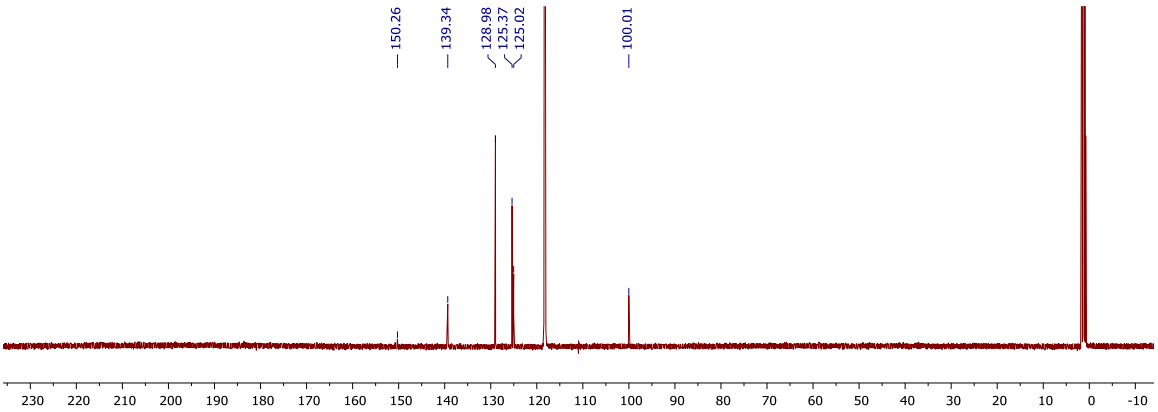

Figure 2. ^{13}C {^{1}H} NMR spectrum (300 MHz) of potassium 3-phenyl pyrazolate in CD_3CN.

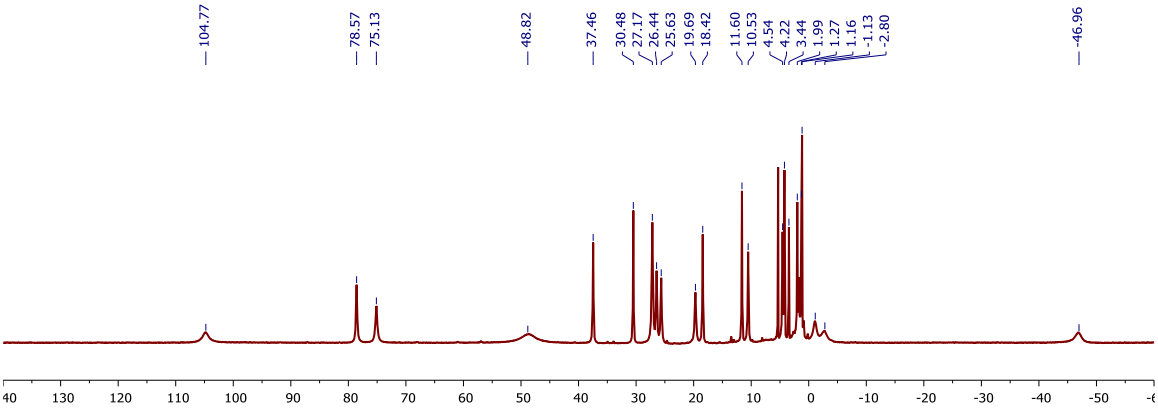

Figure 3. ^{1}H NMR spectrum (300 MHz) of $[LFe_3F(PhPz)_3Fe][OTf]$ (**1**) in CD_2Cl_2.

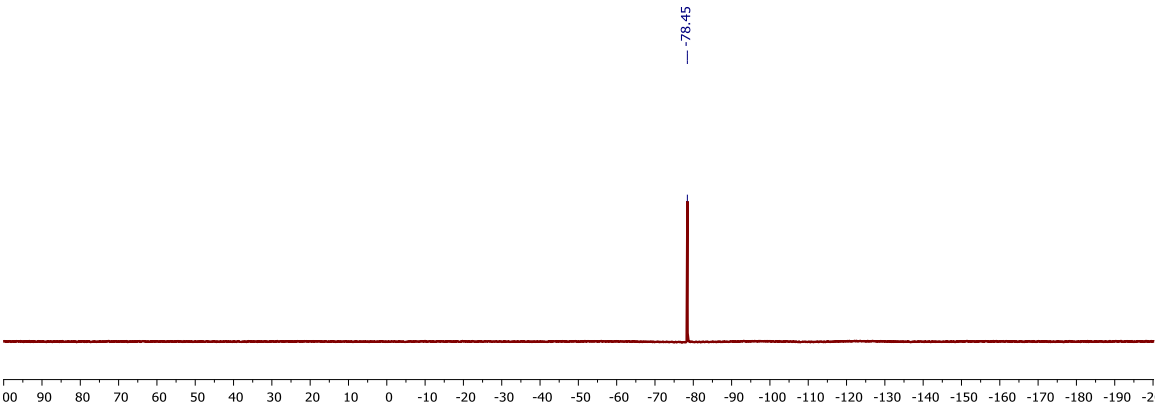

Figure 4. ^{19}F NMR spectrum (300 MHz) of $[LFe_3F(PhPz)_3Fe][OTf]$ (**1**) in CD_2Cl_2.

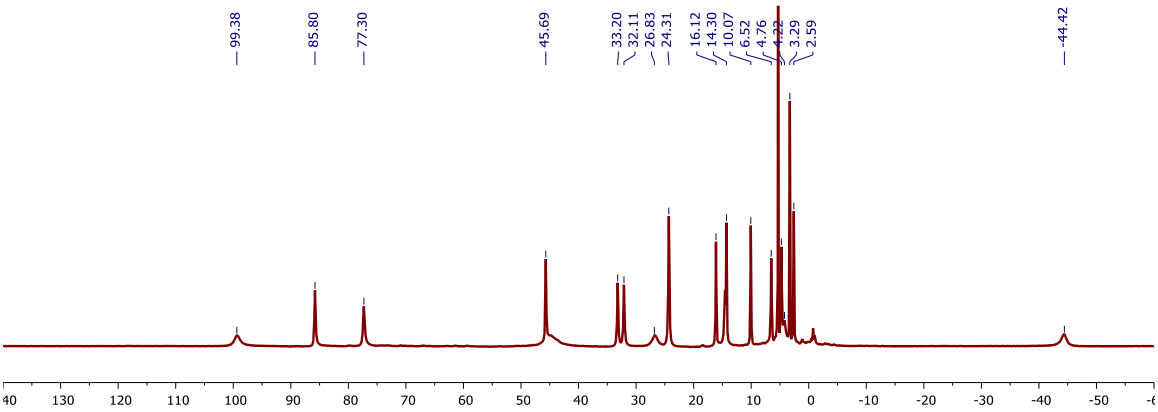

Figure 5. ^{1}H NMR spectrum (300 MHz) of $[LFe_3F(PhPz)_3Fe][OTf]_2$ (**2**) in CD_2Cl_2.

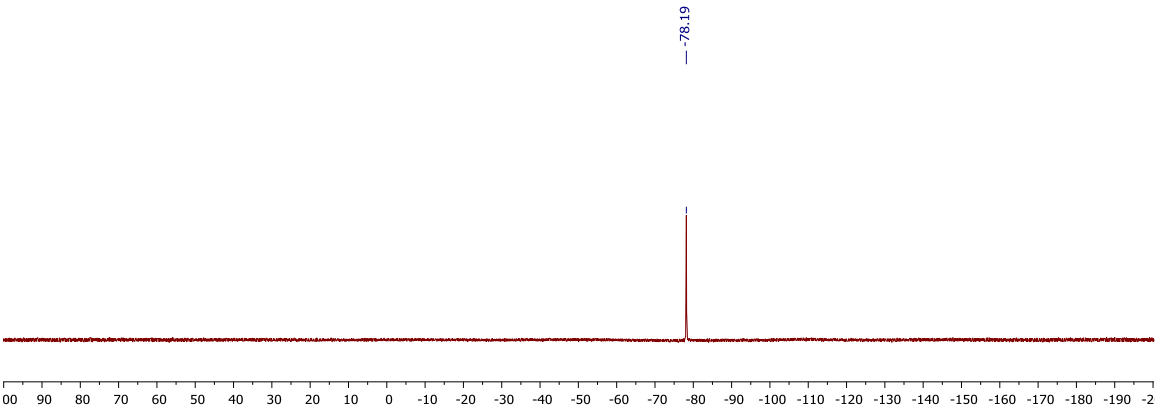

Figure 6. ^{19}F NMR spectrum (300 MHz) of $[LFe_3F(PhPz)_3Fe][OTf]_2$ (**2**) in CD_2Cl_2.

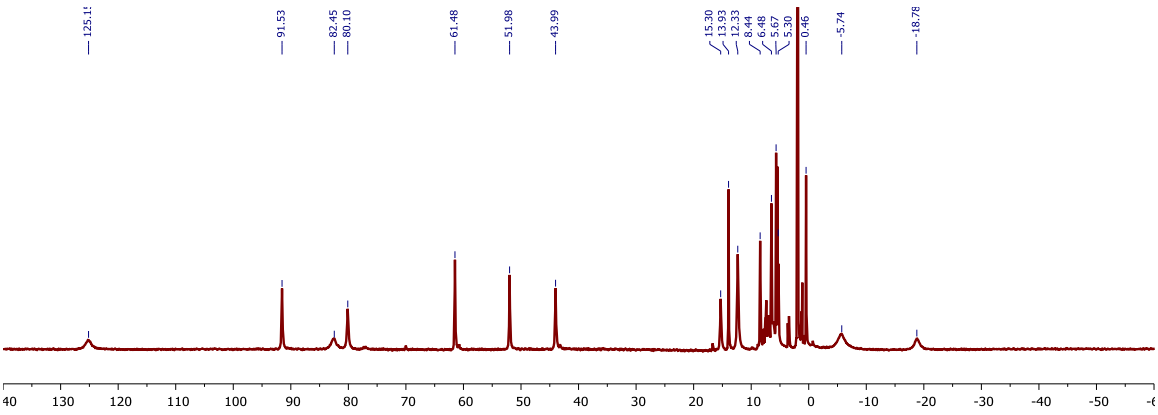

Figure 7. ^{1}H NMR spectrum (300 MHz) of $[LFe_3F(PhPz)_3Fe(CH_3CN)][OTf]_3$ (**3**) in CD_3CN.

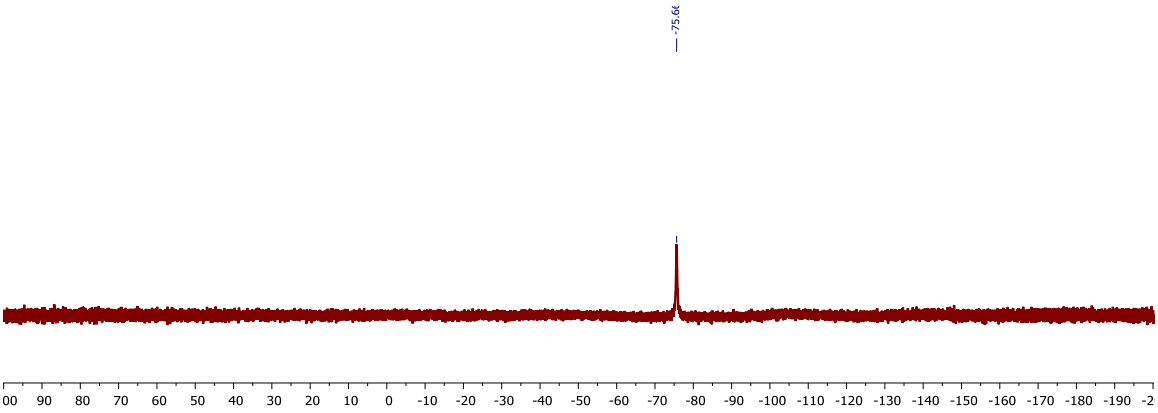

Figure 8. ^{19}F NMR spectrum (300 MHz) of $[LFe_3F(PhPz)_3Fe(CH_3CN)][OTf]_3$ (**3**) in CD_3CN.

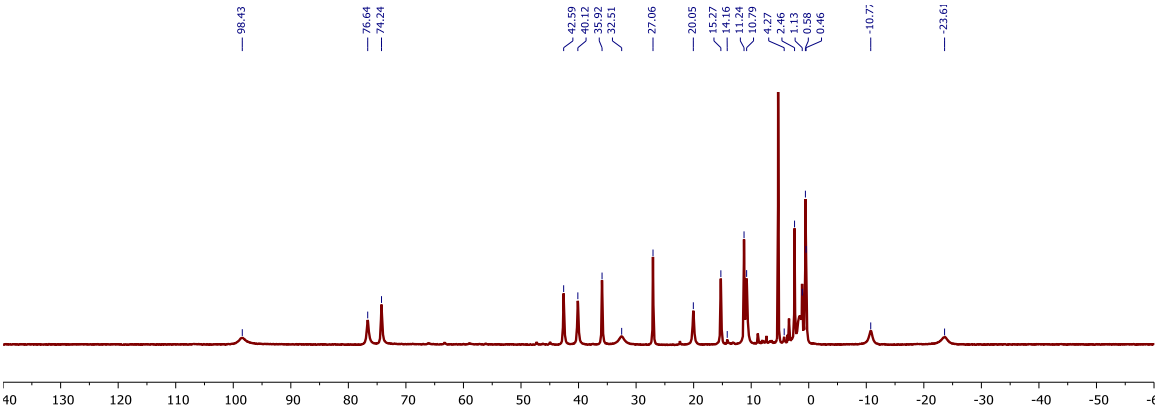

Figure 9. ^{1}H NMR spectrum (300 MHz) of $[LFe_3F(PhPz)_3Fe(NO)][OTf]$ (**1-NO**) in CD_2Cl_2.

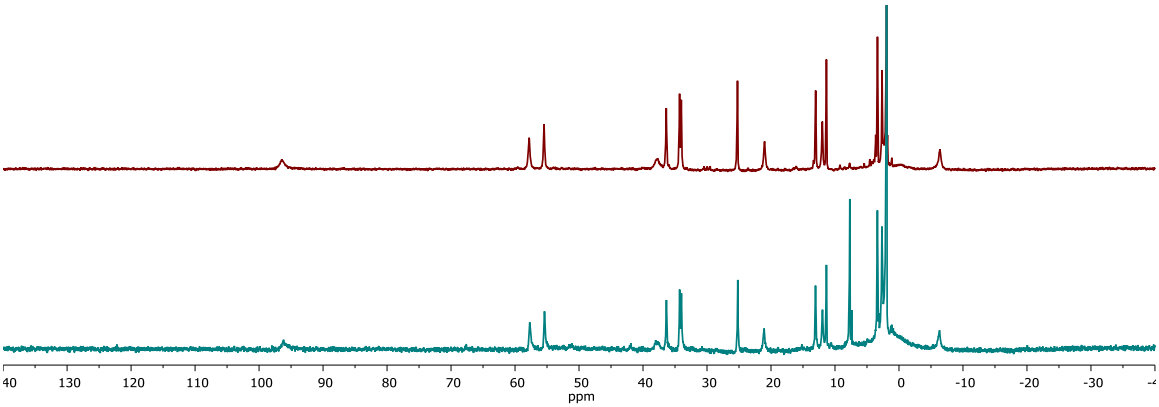

Figure 10. ^{1}H NMR spectrum (300 MHz) of [$LFe_3O(Pz)_3Mn$][OTf] (**1-[OTf]**) (top) and [$LFe_3O(Pz)_3Mn$][[BArF4]] (**1-[$BAr^F{}_4$]**; bottom) in CD_3CN.

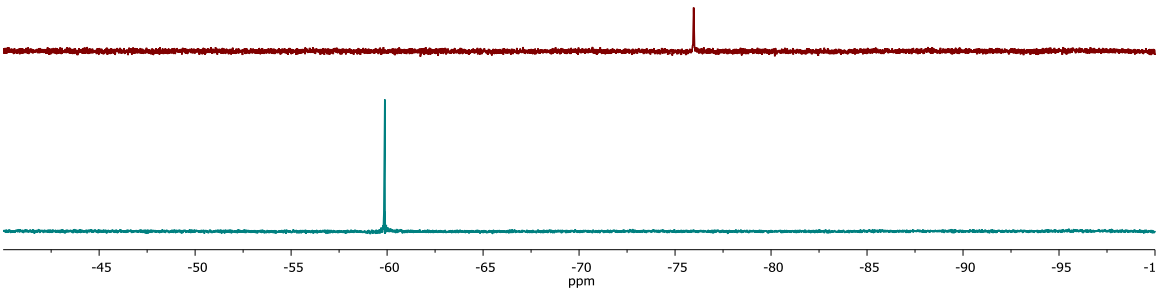

Figure 11. ^{19}F NMR spectrum (300 MHz) of [$LFe_3O(Pz)_3Mn$][OTf] (**1-[OTf]**; top) and [$LFe_3O(Pz)_3Mn$][$BAr^F{}_4$] (**1-[$BAr^F{}_4$]**; bottom) in CD_3CN.

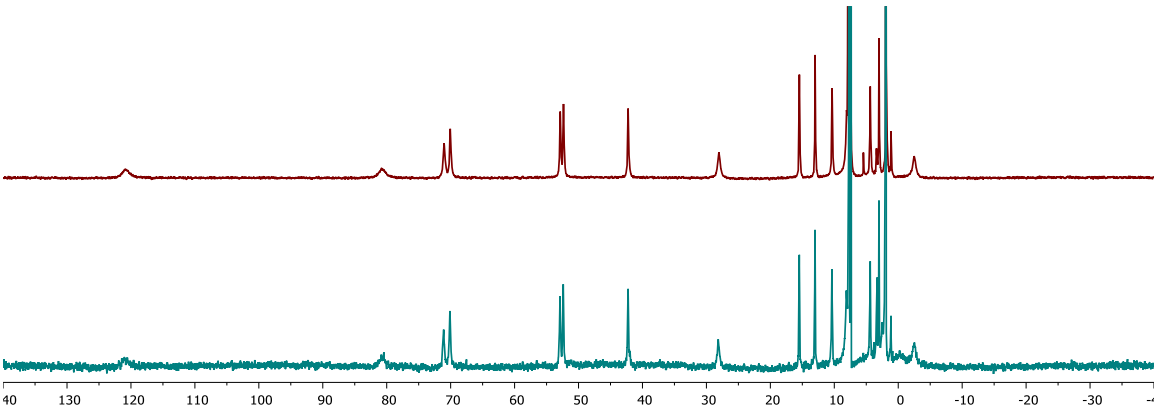

Figure 12. ^{1}H NMR spectrum (300 MHz) of [$LFe_3O(Pz)_3Mn$][$OTf]_2$ (**2-[OTf]**; top) and [$LFe_3O(Pz)_3Mn$][$BAr^F{}_4]_2$ (**2-[$BAr^F{}_4$]**; bottom) in CD_3CN.

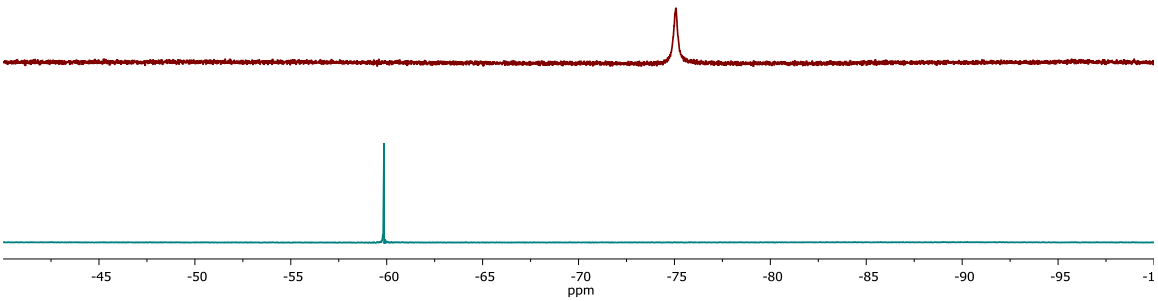

Figure 13. ^{19}F NMR spectrum (300 MHz) of $[LFe_3O(Pz)_3Mn][OTf]_2$ (**2-[OTf]**; top) and $[LFe_3O(Pz)_3Mn][BAr^F{}_4]_2$ (**2-[BAr$^F{}_4$]**; bottom) in CD_3CN.

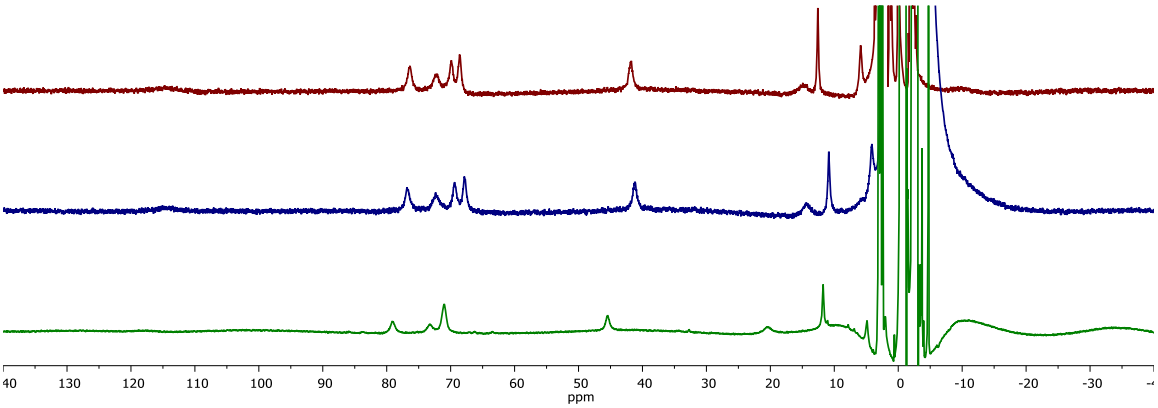

Figure 14. ^1H NMR spectrum (300 MHz) of $[LFe_3O(Pz)_3Mn][OTf]_3$ in CD_2Cl_2 (**3-[OTf]**; top), $[LFe_3O(Pz)_3Mn][BAr^F{}_4]_3$ in THF/C_6D_6 with three equivalents tetrabutylammonium trifluoromethanesulfonate (400 MHz, middle), and $[LFe_3O(Pz)_3Mn][BAr^F{}_4]_3$ in THF/C_6D_6 (500 MHz) (**3-[BAr$^F{}_4$]**; bottom).

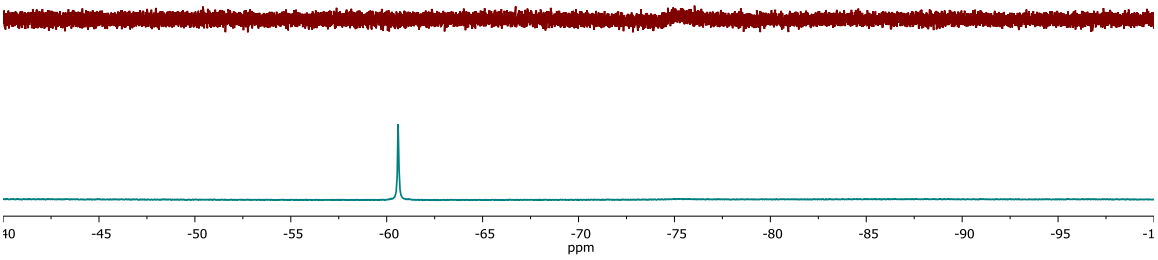

Figure 15. ^{19}F NMR spectrum (300 MHz) of $[LFe_3O(Pz)_3Mn][OTf]_3$ (**3-[OTf]**) in CD_2Cl_2 (top) and $[LFe_3O(Pz)_3Mn][BAr^F{}_4]_3$ (**3-[BAr$^F{}_4$]**; bottom) in THF/C_6D_6 (400 MHz).

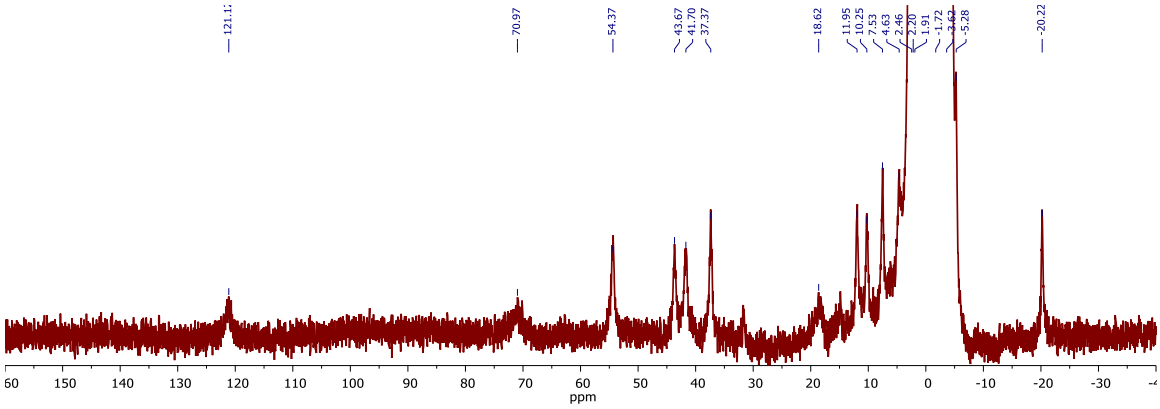

Figure 16. ^{1}H NMR spectra (400 MHz) of [$LFe_3O(Pz)_3Mn(OH)$] (**5**) in THF/C_6D_6 [250 mM H_2O].

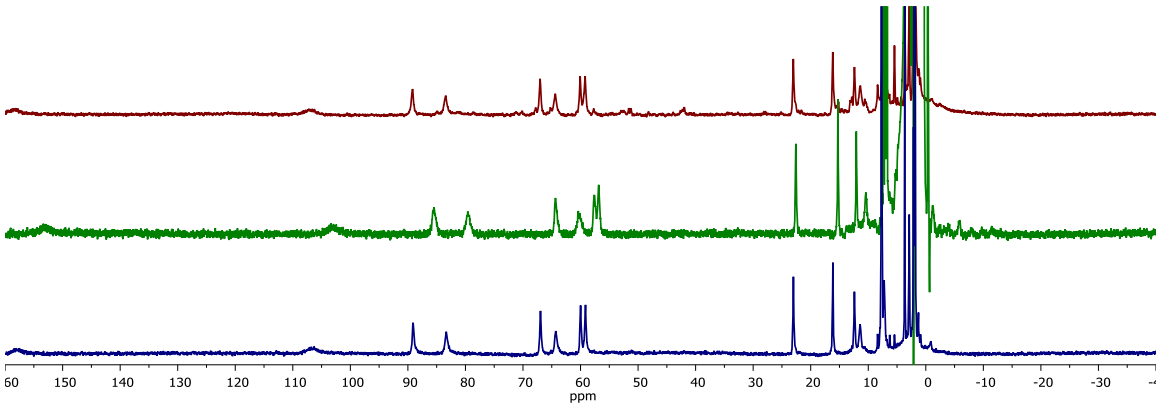

Figure 17. ^{1}H NMR spectrum (300 MHz) of [$LFe_3O(Pz)_3Mn(OH)$][OTf] (**6-[OTf]**; top) and [$LFe_3O(Pz)_3Mn(OH)$][$BAr^F{}_4$] (**6-[$BAr^F{}_4$]**; middle) in CD3CN. ^{1}H NMR spectrum (400 MHz) of [$LFe_3O(Pz)_3Mn(OH)$][$BAr^F{}_4$] (**6-[$BAr^F{}_4$]**; bottom) in THF/C_6D_6 [250 mM H_2O].

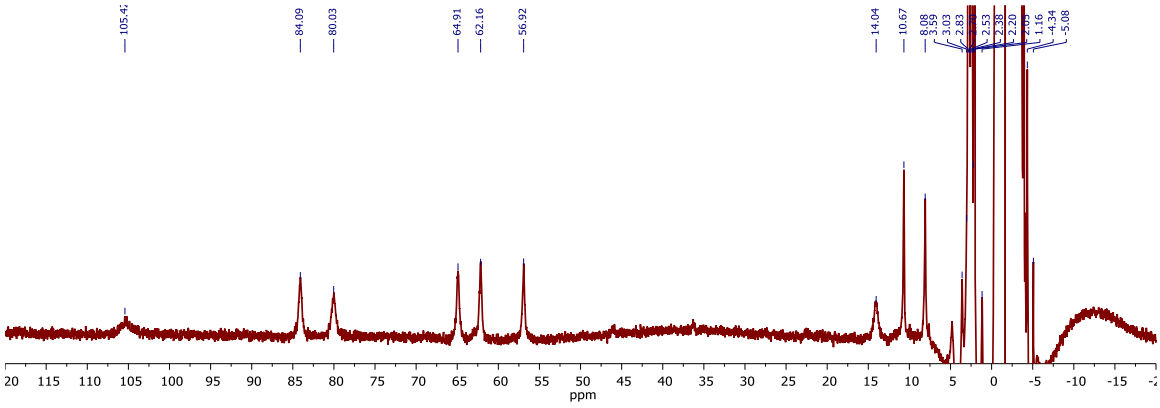

Figure 18. ^{1}H NMR spectrum (400 MHz) of [$LFe_3O(Pz)_3Mn(OH)$][$BAr^F{}_4$]$_2$ (**7-[$BAr^F{}_4$]**) in THF/C_6D_6 [250 mM H_2O].

CHAPTER 4

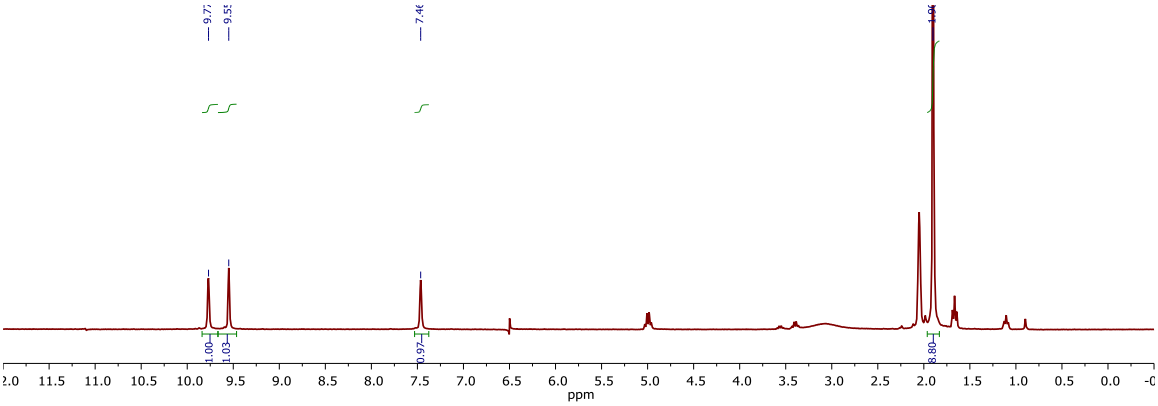

Figure 19. ^{1}H NMR spectrum (300 MHz) of 2-*tert*-butyl-isoxazolium tetrafluoroborate in $(CD_3)_2CO$.

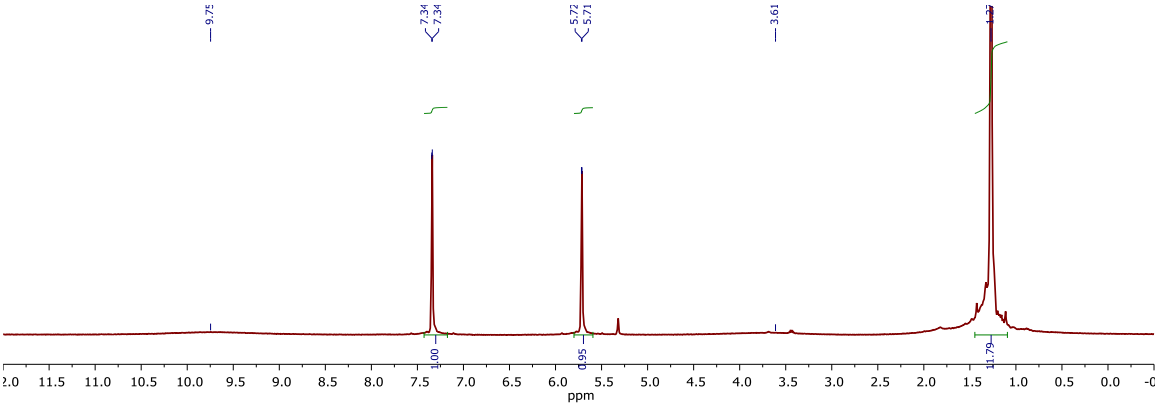

Figure 20. ^{1}H NMR spectrum (400 MHz) of *N*-*tert*-butyl-1*H*-pyrazol-3-amine in CD_2Cl_2.

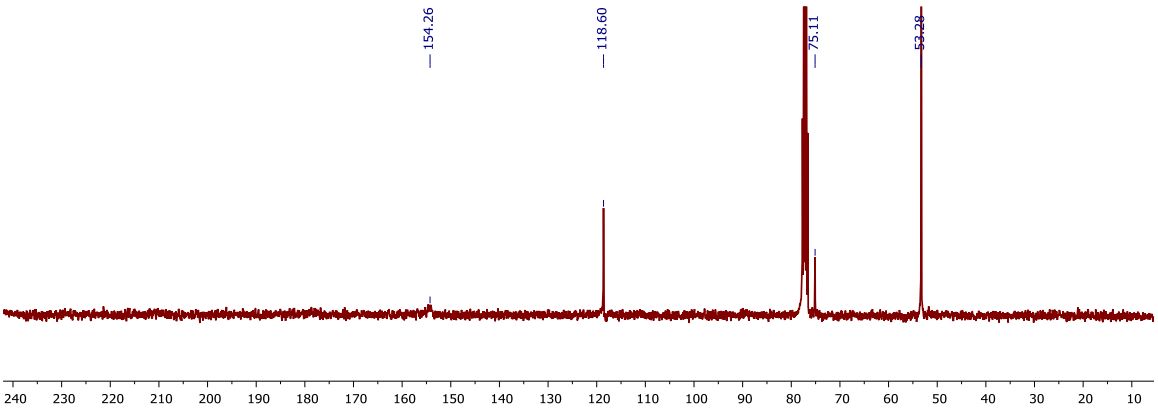

Figure 21. ^{13}C{^{1}H} NMR spectrum (100 MHz) of *N*-*tert*-butyl-1*H*-pyrazol-3-amine in CD_2Cl_2.

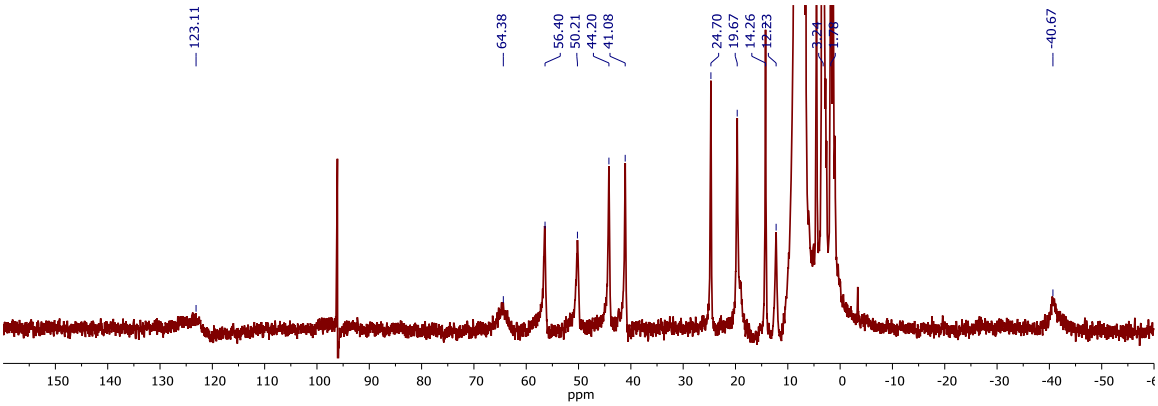

Figure 22. ^{1}H NMR spectrum (300 MHz) of $LFe_3O(PzNHtBu)_3Fe(OH)$ (**1**) in C_6D_6. The sharp signal ~ 95 ppm is a spectral artifact.

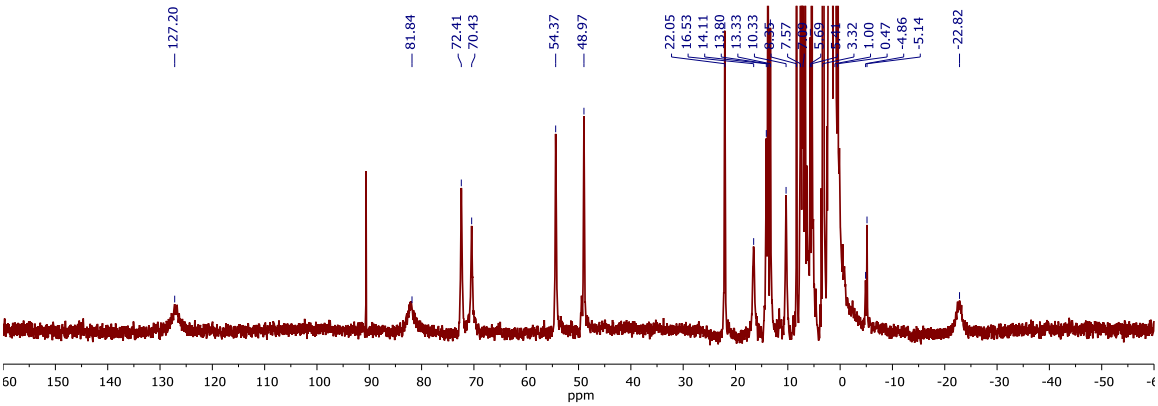

Figure 23. ^{1}H NMR spectrum (300 MHz) of $[LFe_3O(PzNHtBu)_3Fe(OH)][OTf]$ (**2**) in CD_3CN. The sharp signal ~ 90 ppm is a spectral artifact.

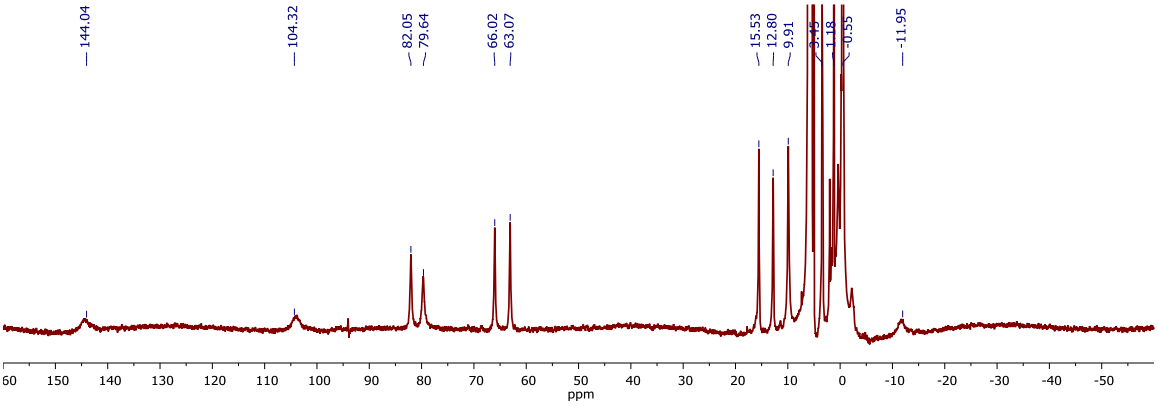

Figure 24. ^{1}H NMR spectrum (300 MHz) of $[LFe_3O(PzNHtBu)_3Fe(OH)][OTf]_2$ (**3**) in CD_2Cl_2.

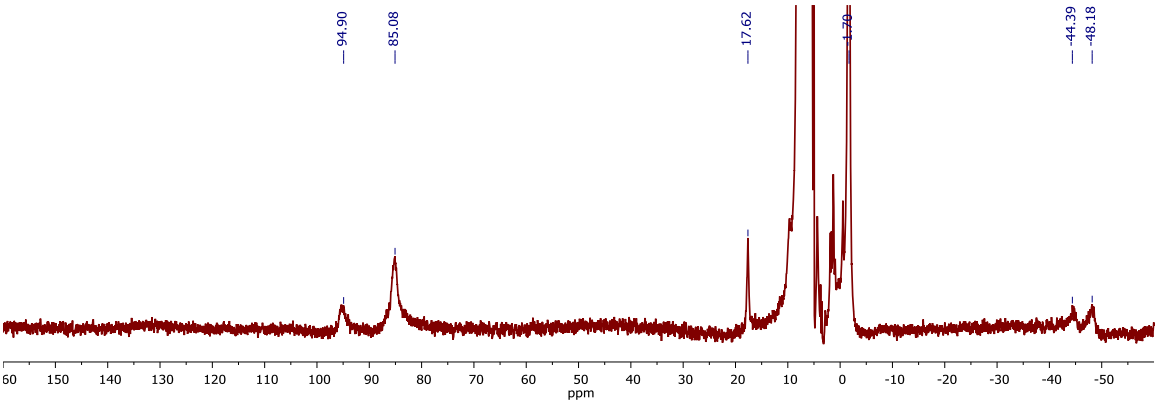

Figure 25. ^{1}H NMR spectrum (300 MHz) of [LFe$_3$O(PzNHtBu)$_3$Fe(OH)][OTf]$_3$ (**4**) in CD_2Cl_2.

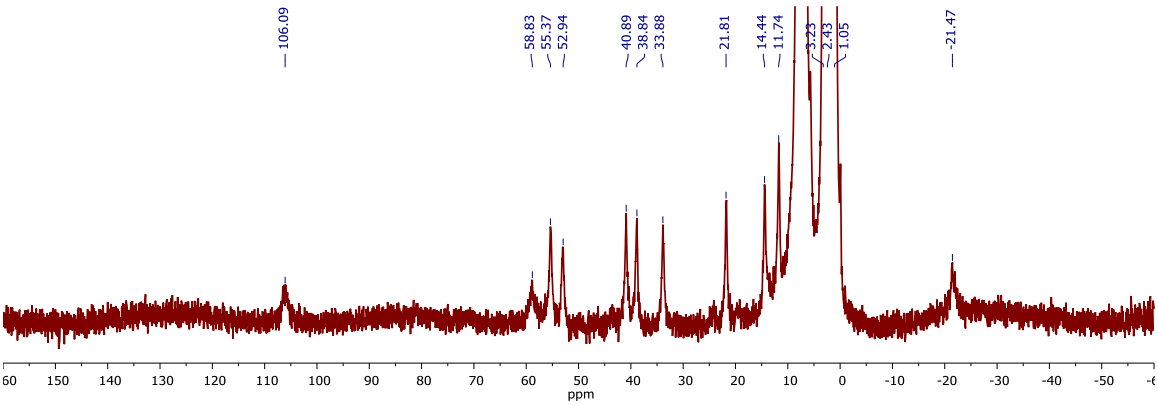

Figure 26. ^{1}H NMR spectrum (300 MHz) of LFe$_3$O(PzNHtBu)$_3$Fe(O) (**5**) in C_6D_6.

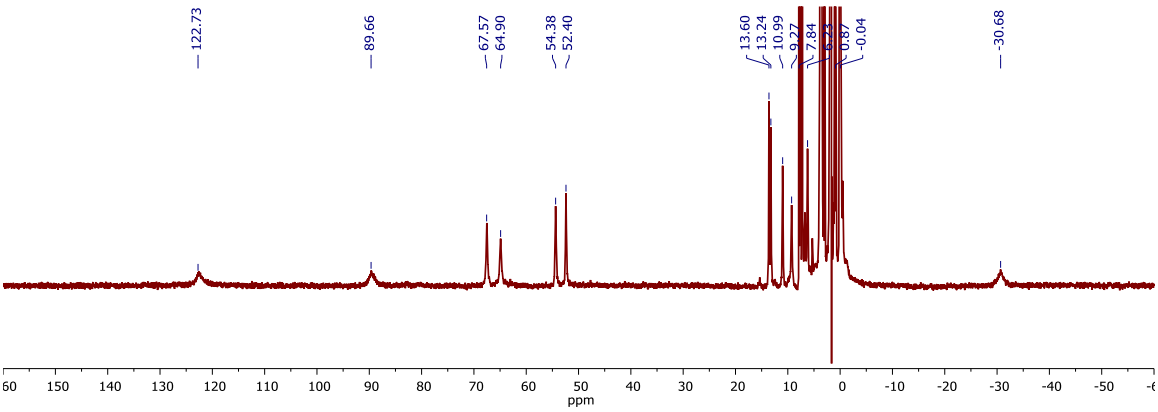

Figure 27. ^{1}H NMR spectrum (400 MHz) of [LFe$_3$O(PzNHtBu)$_3$Fe(O)][OTf] (**6**) in THF/C_6D_6.

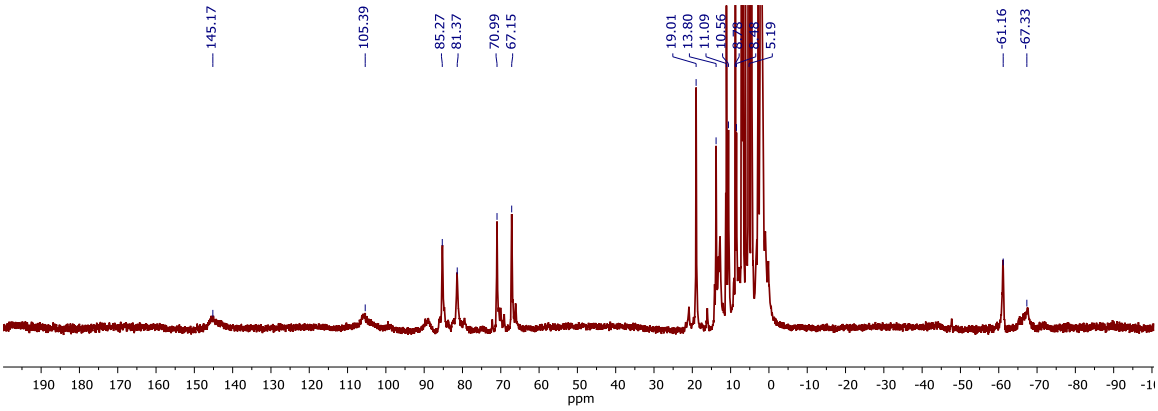

Figure 28. ^{1}H NMR spectrum (300 MHz) of [LFe$_3$O(PzNHtBu)$_3$Fe(O)][OTf]$_2$ (**7**) in 1:1 CD$_3$CN/CD$_2$Cl$_2$.

CHAPTER 5

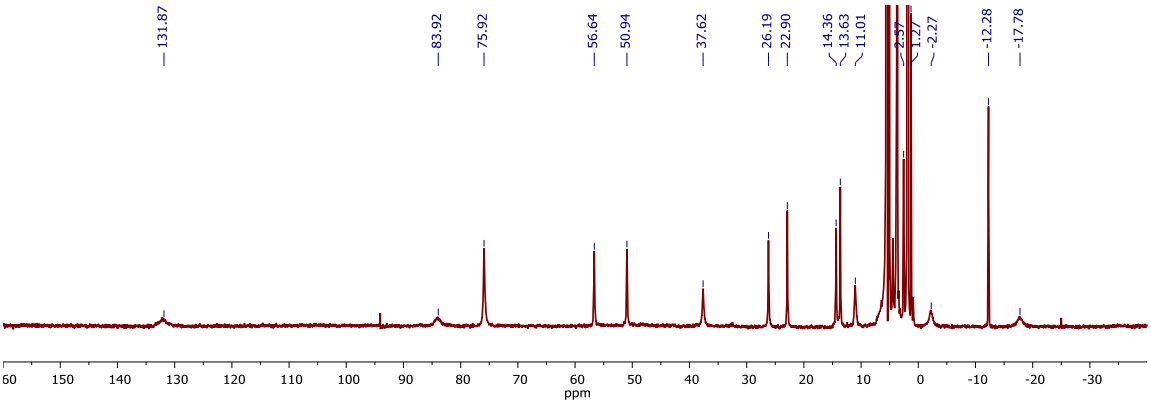

Figure 29. ^{1}H NMR spectrum (300 MHz) of [$LFe_3O(Pz)_3Fe(OAc)$][OTf] (**1**) in CD_2Cl_2.

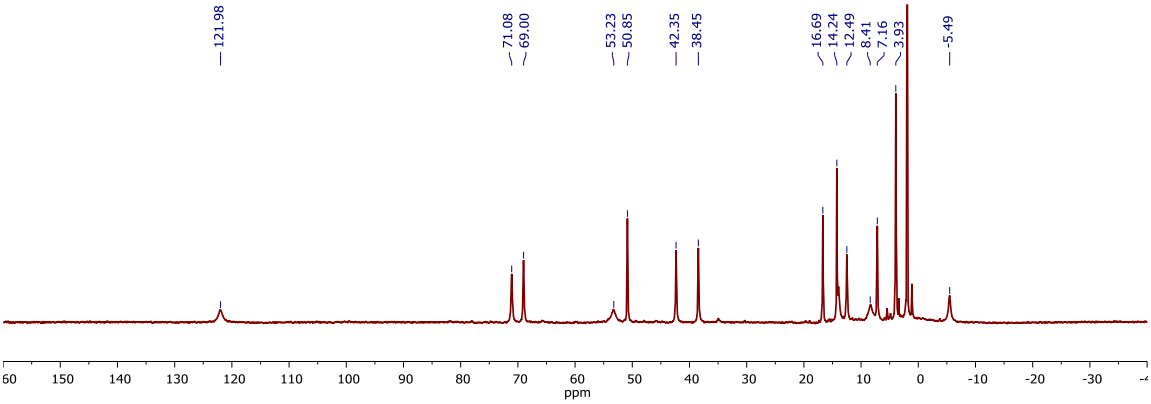

Figure 30. ^{1}H NMR spectrum (300 MHz) of [$LFe_3O(Pz)_3Fe$][OTf]$_2$ (**2**) in CD_3CN.

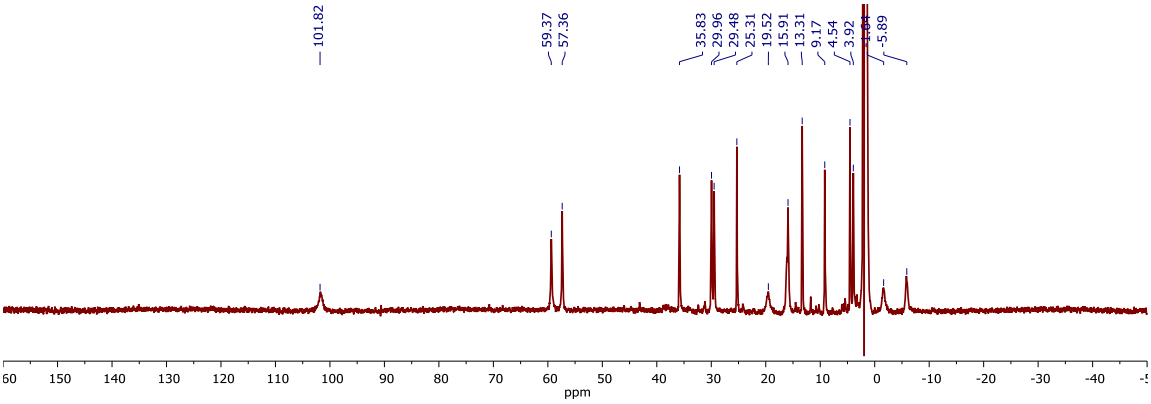

Figure 31. ^{1}H NMR spectrum (300 MHz) of [$LFe_3O(Pz)_3Fe$][OTf] (**3**) in CD_3CN.

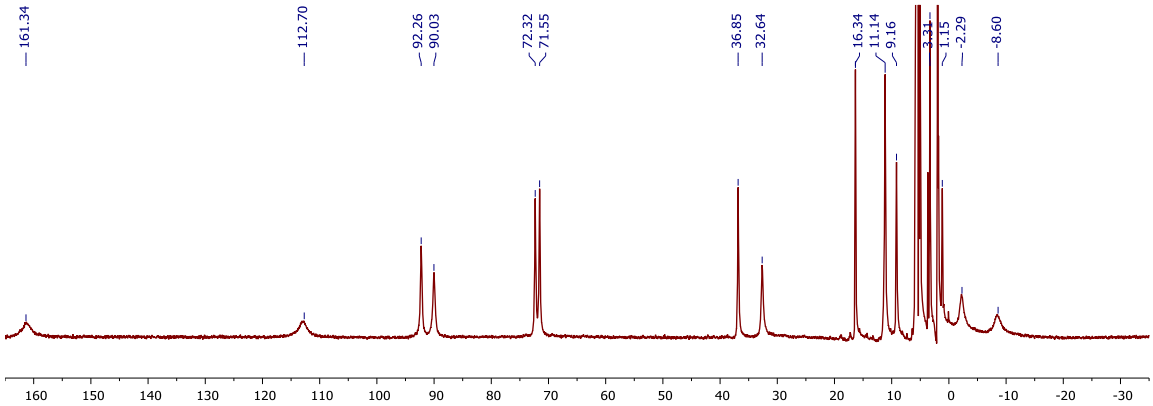

Figure 32. ^{1}H NMR spectrum (300 MHz) of $[LFe_3O(Pz)_3Fe][OTf]_3$ (**4**) in CD_2Cl_2.

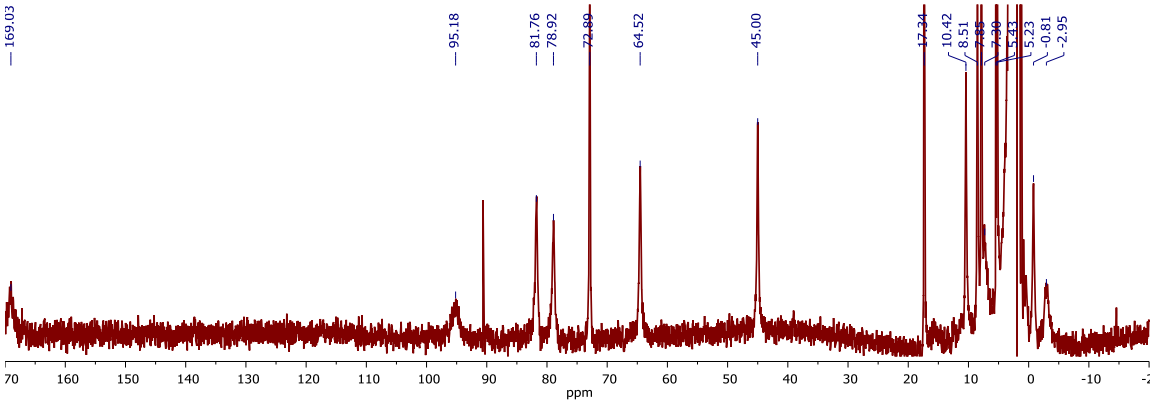

Figure 33. ^{1}H NMR spectrum (300 MHz) of $[LFe_3O(Pz)_3Fe(MeCN)][OTf]_3$ (**4-MeCN**) in CD_3CN.

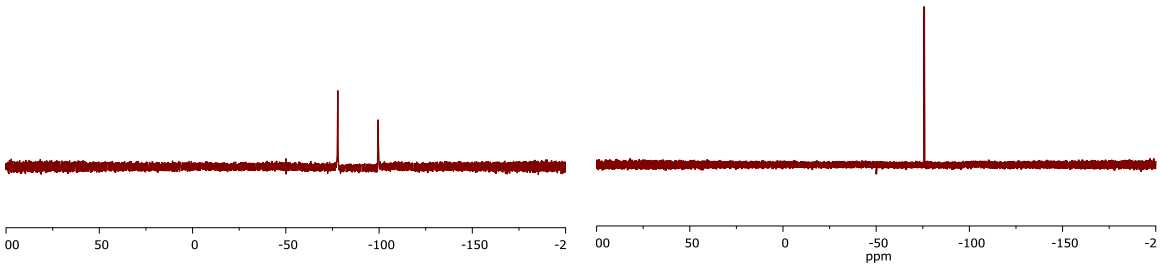

Figure 34. ^{19}F NMR spectra (300 MHz) of $[LFe_3O(Pz)_3Fe][OTf]_3$ (**4**) in CD_2Cl_2 (left) and $[LFe_3O(Pz)_3Fe(MeCN)][OTf]_3$ (**4-MeCN**) in CD_3CN (right).

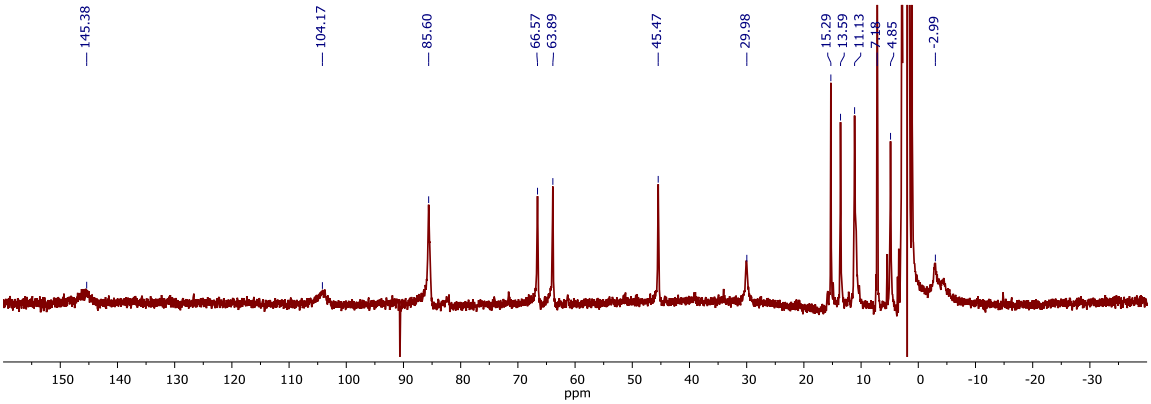

Figure 35. ^{1}H NMR spectrum (300 MHz) of $[LFe_3O(Pz)_3Fe(OH)][OTf]_2$ (**5**) in CD_3CN.

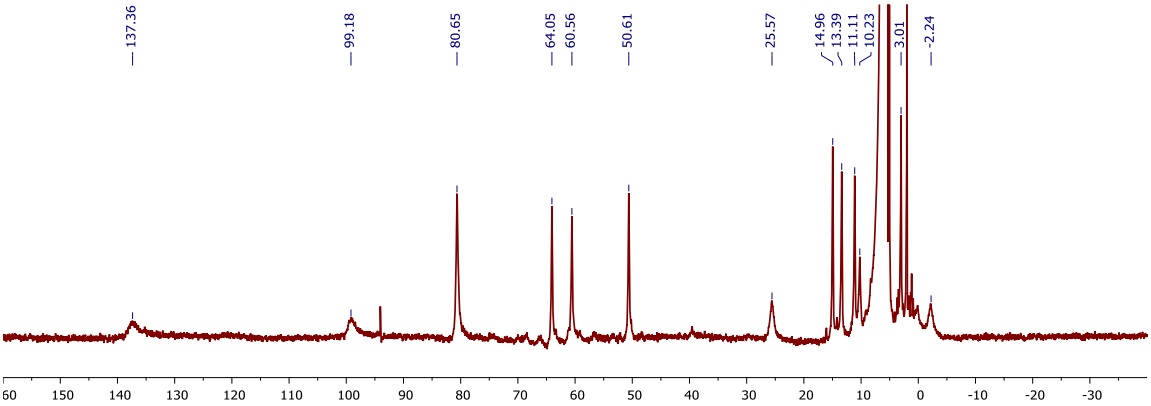

Figure 36. ^{1}H NMR spectrum (300 MHz) of $[(LFe_3O(Pz)_3Fe)_2O][OTf]_4$ (**6**) in CD_2Cl_2.

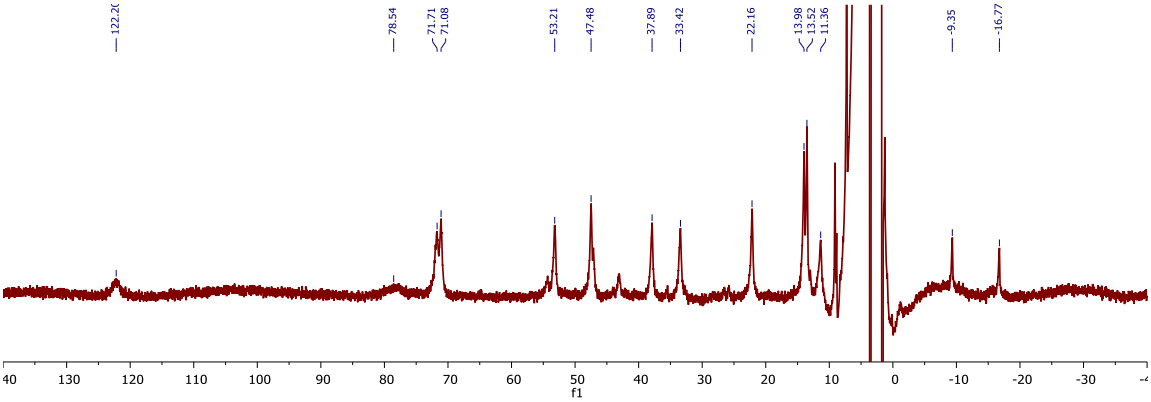

Figure 37. ^{1}H NMR spectrum (500 MHz) of $[LFe_3O(Pz)_3Fe(2\text{-phenyl-anilide})][OTf]$ (**7**) in THF/C_6D_6.

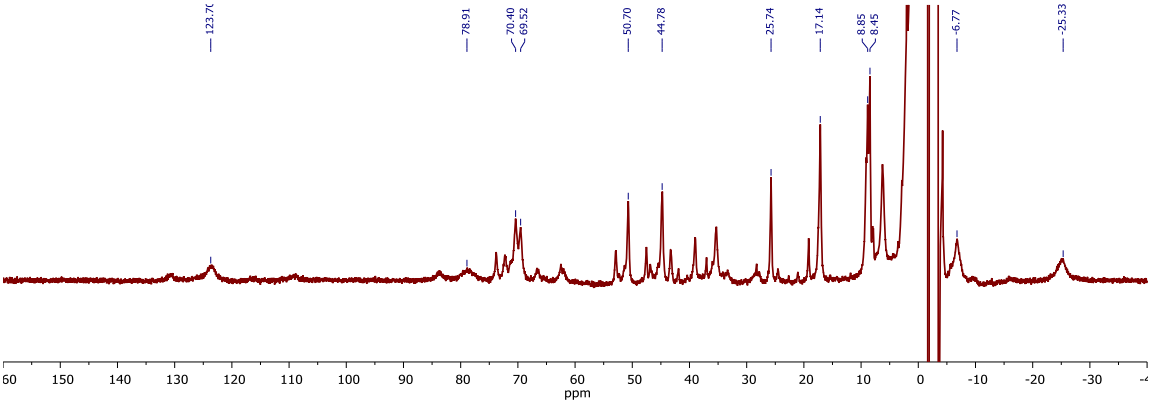

Figure 38. ^{1}H NMR spectrum (500 MHz) of reaction mixture containing [$LFe_3O(Pz)_3Fe$(3,5-trifluoromethyl-anilide)][OTf] (**8**) in THF/C_6D_6.

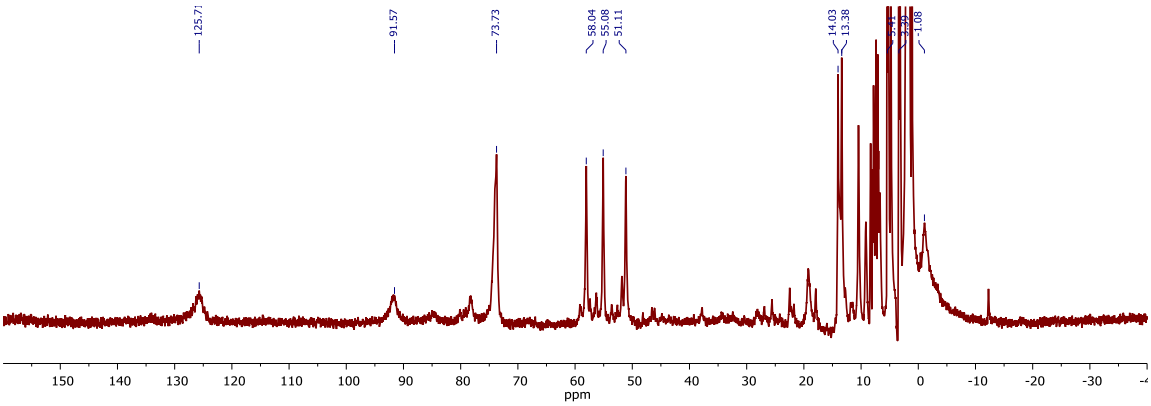

Figure 39. ^{1}H NMR spectrum (300 MHz) of [$LFe_3O(Pz)_3Fe$(para-tolylsulfonamide)][OTf] (**9**) in CD_3CN.

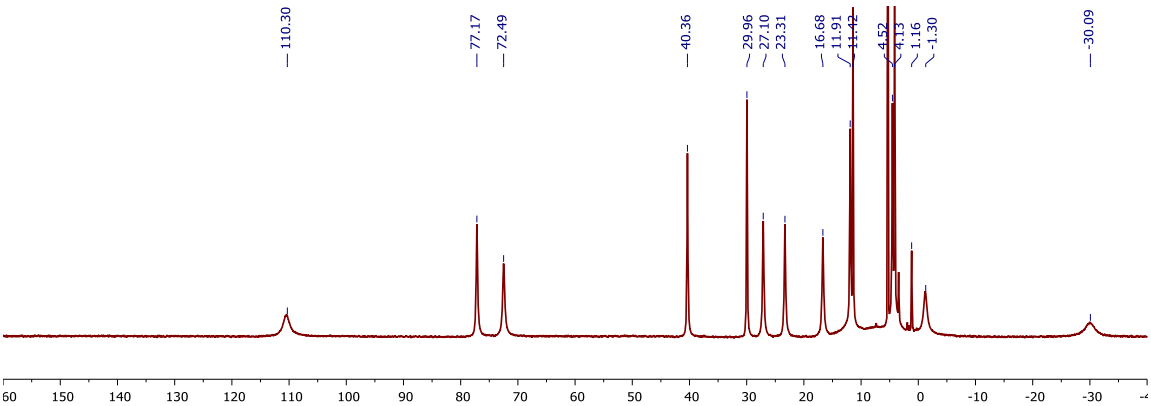

Figure 40. ^{1}H NMR spectrum (300 MHz) of [$LFe_3F(Pz)_3Fe$][OTf] (**10**) in CD_2Cl_2.

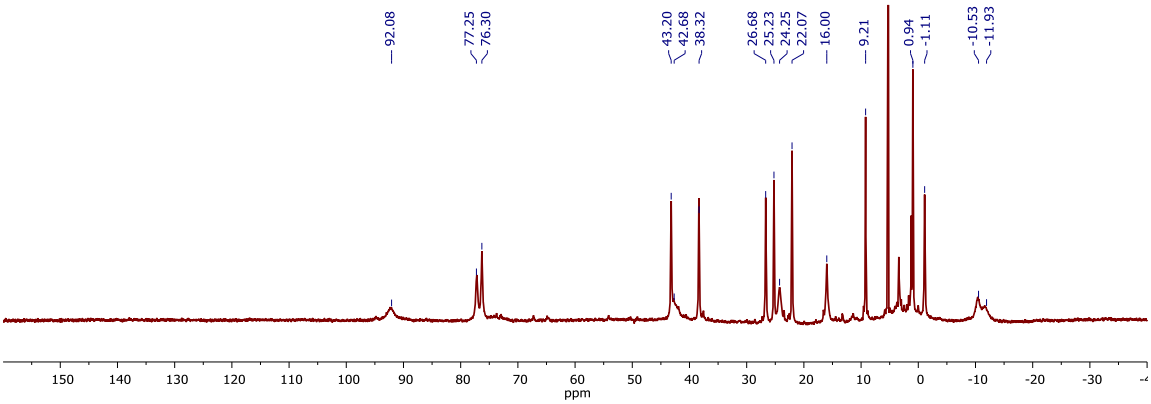

Figure 41. ^{1}H NMR spectrum (300 MHz) of $[(LFe_3F(Pz)_3Fe)_2O][OTf]_2$ (**11**) in CD_2Cl_2.

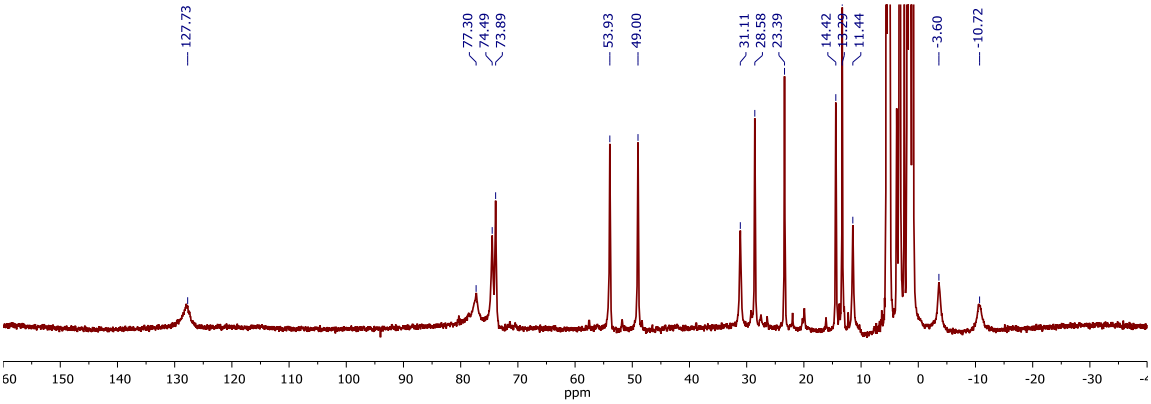

Figure 42. ^{1}H NMR spectrum (300 MHz) of $[LFe_3O(Pz)_3Fe(F)][OTf]$ (**12**) in CD_2Cl_2.

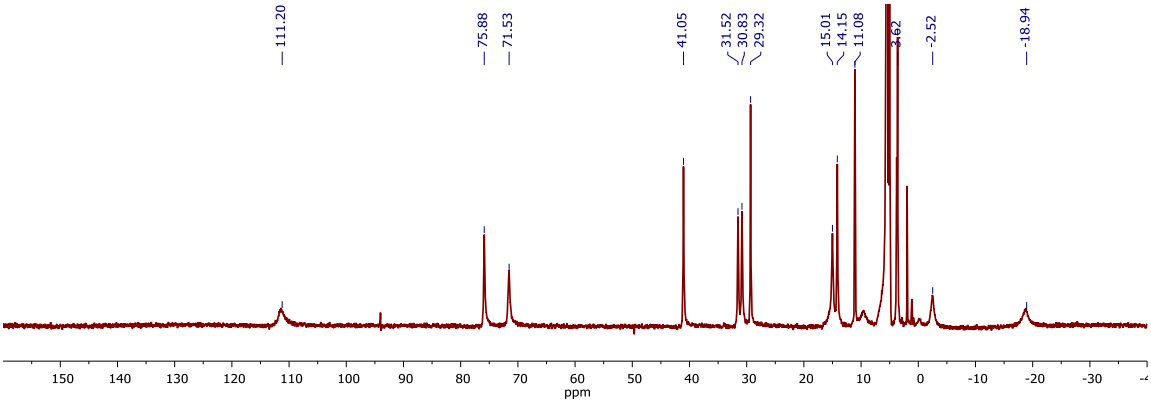

Figure 43. ^{1}H NMR spectrum (300 MHz) of $LFe_3N(Pz)_3Fe(N_3)$ (**13**) in CD_2Cl_2.

^{57}FE MÖSSBAUER DATA

Simulation details for [LFe$_3$(PhPz)$_3$FFe][OTf] (1): The Mössbauer spectrum of **1** features an intense signal around 3 mm/s characteristic of a high-spin Fe(II) center. Fitting a quadrupole doublet for this peak led to a model that accounted for ~75% of the overall signal, with a second doublet satisfactorily accounting for the rest of the signal (Figure 1). The final refinement spli t the 75%-abundant high-spin Fe(II) signal into three equally populated doublets (Figure 2).

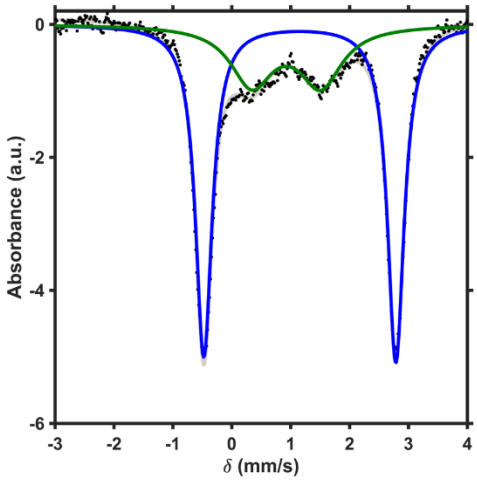

Figure 1. Mössbauer spectrum of **1** (black dots) fit with two doublets in ~3:1 ratio refined with parameters: δ = 1.156 mm/s; ΔE_q = 3.260 mm/s (blue trace) and δ = 0.925 mm/s; ΔE_q = 1.171 mm/s (green trace). The overall fit is the gray trace.

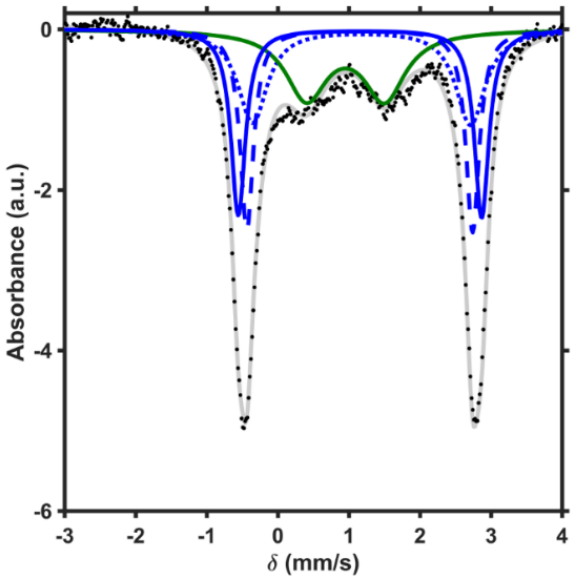

	δ (mm/s)	$\lvert\Delta E_q\rvert$ (mm/s)	Γ	Rel. %
———	1.156	3.424	0.25	25
– – –	1.152	3.176	0.23	25
·····	1.178	3.065	0.50	25
———	0.951	1.099	0.70	25

Figure 2. Zero applied field ^{57}Fe Mössbauer spectrum of [LFe$_3$F(PhPz)$_3$Fe][OTf] (**1**). The data (black dots) was fit to four Fe quadrupole doublets (gray trace). The blue traces represent signals assigned to the high-spin Fe^{II} of the tri-iron core and the green trace is assigned to the apical high-spin Fe^{II}.

Simulation details for [LFe$_3$(PhPz)$_3$FFe][OTf]$_2$ (2): The Mössbauer spectrum of **2** was fit by first fitting the signal at 3 mm/s to high-spin Fe(II) (Figure 3A); this fit accounted for ~50% the total spectrum. The remaining spectrum was fit with two nearly equal doublets (Figure 3B); other combinations of this signal to arrive at alternative parameters for these two signals could not be satisfactorily modeled, so these are not included. The final fit split the 50%-abundant Fe(II) signal into two equal doublets (Figure 4).

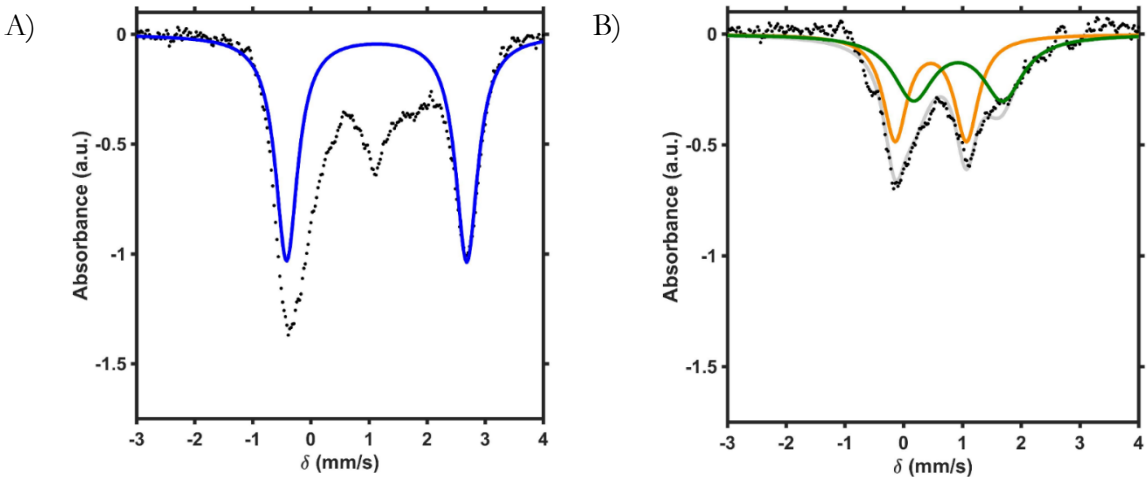

Figure 3. Mössbauer spectrum of **2** (black dots) (A) fit with a single doublet refined with parameters consistent with high-spin Fe(II): δ = 1.132 mm/s; ΔE_q = 3.101 mm/s (blue trace). (B) Mössbauer spectrum of **2** with this Fe(II) doublet subtracted (black dots) and two equally abundant signals fit (gray trace): δ = 0.462 mm/s; ΔE_q = 1.213 mm/s (orange trace), and δ = 0.928 mm/s; ΔE_q = 1.522 mm/s (green trace).

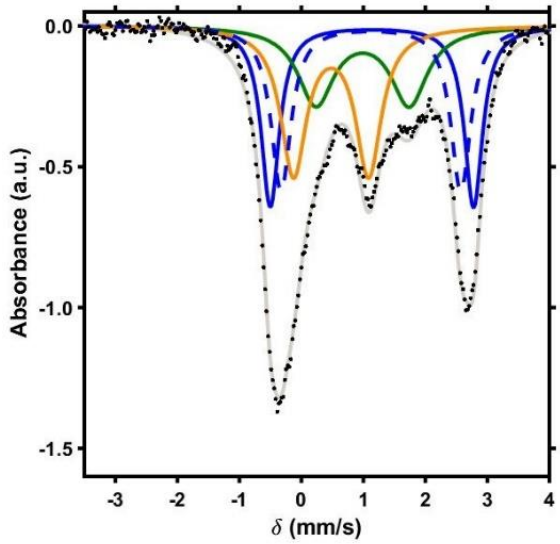

	δ (mm/s)	$\lvert\Delta E_q\rvert$ (mm/s)	Γ	Rel. %
	1.138	3.297	0.35	25
	1.122	2.899	0.39	25
	0.479	1.211	0.50	29
	0.987	1.504	0.70	21

Figure 4. Zero applied field ^{57}Fe Mössbauer spectrum of [LFe$_3$F(PhPz)$_3$Fe][OTf]$_2$ (**2**). The data (black dots) was fit to four Fe quadrupole doublets (gray trace). The blue traces represent signals assigned to the high-spin Fe^{II} of the tri-iron core, the orange trace is assigned to high-

spin Fe^{III} in the tri-iron core, and the green trace is assigned to the apical high-spin Fe^{II}. The best fit was obtained by having a slight deviation from four equally abundant Fe centers.

Simulation details for $[LFe_3(PhPz)_3FFe(CH_3CN)][OTf]_3$ (3): The Mössbauer spectrum of **3** contains three easily observable features, which was first approximated by fitting two doublets (Figure 5A). This fit shows inadequate modeling for the signal around 2 mm/s, so a third doubled was modeled in (Figure 5B-D). This fit led to three signals in an approximately 1:1:2 ratios. Of the possible distribution of these three signals, the fit in Figure 5D is favored, because it has isomer shifts self-consistent for the two Fe(III) centers (0.4 – 0.5 mm/s) and the Fe(II) center (1.00 – 1.15 mm/s) of the 'tri-iron' core of our related iron clusters presented here and previously reported. Furthermore, the third signal is most consistent with a high-spin five-coordinate Fe(II) (~0.1 mm/s lower than the corresponding six-coordinate Fe(II) signal), which is in agreement of the coordination of the apical Fe(II) in the crystal structure of **3**. The final fit was refined by splitting the 50%-abundant Fe(III) signal into two equal signals (Figure 6).

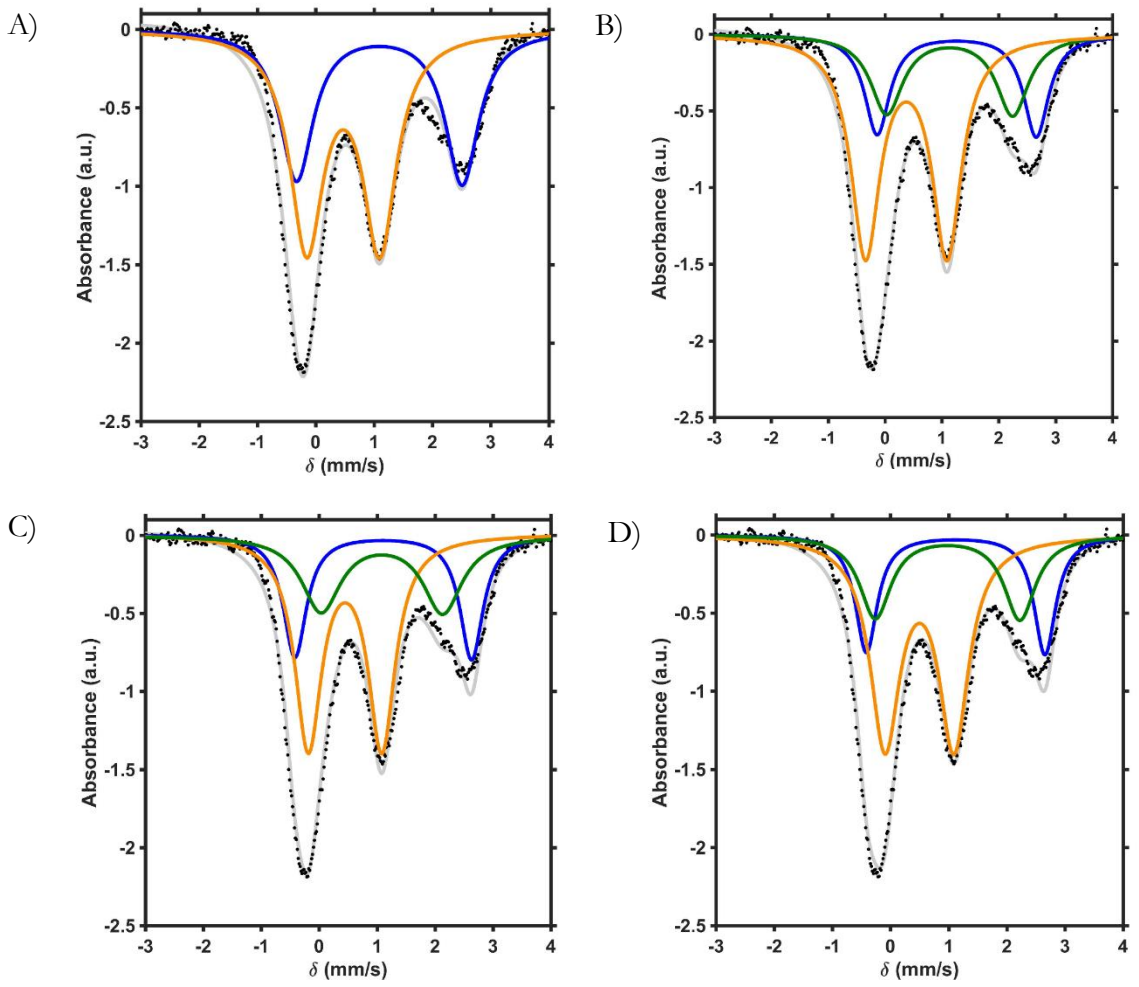

Figure 5. Mössbauer spectrum of **3** (black dots) (A) fit with two signals (gray trace) refined with parameters: δ = 1.091 mm/s; ΔE_q = 2.841 mm/s (blue trace), and δ = 0.471 mm/s; ΔE_q = 1.253 mm/s (orange trace). (B) Mössbauer spectrum of **3** fit with three signals in a 1:1:2

ratio (gray trace) with the parameters: δ = 1.261 mm/s; ΔE_q = 2.797 mm/s (blue trace), δ = 1.137 mm/s; ΔE_q = 2.216 mm/s (green trace), and δ = 0.374 mm/s; ΔE_q = 1.433 mm/s (orange trace). (C) Mössbauer spectrum of **3** fit with three signals in a 1:1:2 ratio (gray trace) with the parameters: δ = 1.106 mm/s; ΔE_q = 3.050mm/s (blue trace), δ = 1.083 mm/s; ΔE_q = 2.098 mm/s (green trace), and δ = 0.447 mm/s; ΔE_q = 1.269 mm/s (orange trace). (D) Mössbauer spectrum of **3** fit with three signals in a 1:1:2 ratio (gray trace) with the parameters: δ = 1.120 mm/s; ΔE_q = 3.071 mm/s (blue trace), δ = 0.981 mm/s; ΔE_q = 2.486 mm/s (green trace), and δ = 0.498 mm/s; ΔE_q = 1.186 mm/s (orange trace).

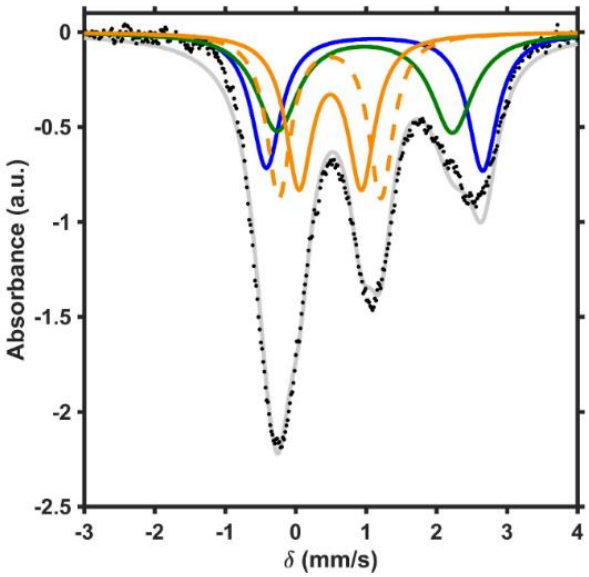

	δ (mm/s)	$\lvert\Delta E_q\rvert$ (mm/s)	Γ	Rel. %
	1.120	3.071	0.51	25
	0.492	0.889	0.46	25
	0.487	1.449	0.42	25
	0.981	2.486	0.72	25

Figure 6. Zero applied field ^{57}Fe Mössbauer spectrum of $[LFe_3F(PhPz)_3Fe(CH_3CN)][OTf]_3$ (**3**). The data (black dots) was fit to four Fe quadrupole doublets (gray trace). The blue trace represents the signal assigned to the high-spin Fe^{II} of the tri-iron core, the orange traces are assigned to high-spin Fe^{III} in the tri-iron core, and the green trace is assigned to the apical high-spin Fe^{II}.

Simulation details for $LFe_3(PhPz)_3FFe(NO)$ (5-NO): The Mössbauer spectrum of **5-NO** displays three readily distinguished signals. The major two were initially fit with a single doublet, which had parameters consistent with high-spin Fe(II) (Figure 7); the remaining signal was fit in a 3:1 ratio relative to the first signal. The final fit split the high-spin Fe(II) doublet into three equal doublets (Figure 8).

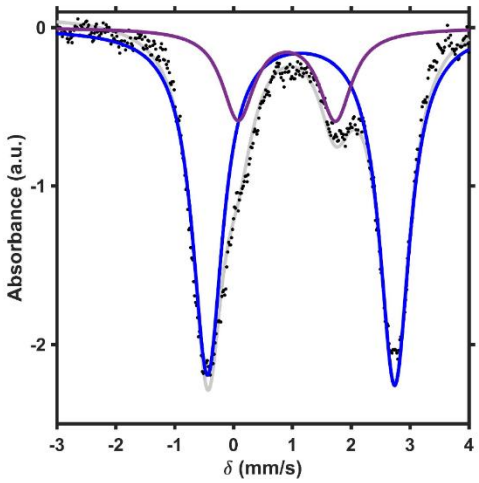

Figure 7. Mössbauer spectrum of **5-NO** (black dots) fit with two doublets in a ~3:1 ratio (gray trace) with the parameters: δ = 1.149 mm/s; ΔE_q = 3.177 mm/s (blue trace), and δ = 0.906 mm/s; ΔE_q = 1.651 mm/s (purple trace).

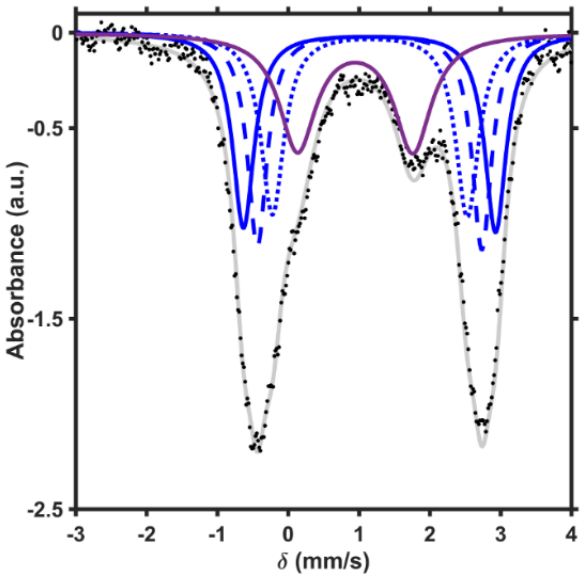

	δ (mm/s)	$\lvert\Delta E_q\rvert$ (mm/s)	Γ	Rel. %
———	1.148	3.561	0.37	25
– – –	1.150	3.172	0.33	25
·····	1.153	2.753	0.39	25
———	0.947	1.629	0.63	25

Figure 8. Zero applied field ^{57}Fe Mössbauer spectrum of $LFe_3F(PhPz)_3Fe(NO)$ (**5-NO**). The data (black dots) was fit to four Fe quadrupole doublets (gray trace). The blue traces represent the signal assigned to the high-spin Fe^{II} of the tri-iron core and the purple trace is assigned to the apical $\{FeNO\}^8$.

Simulation details for [LFe$_3$(PhPz)$_3$FFe(NO)][OTf] (1-NO): The Mössbauer spectrum of **1-NO** contains four distinguishable signals (one being a shoulder on the peak below 0 mm/s). These four signals were fit to two doublets based on their relative intensities and had an approximate 3:1 ratio (Figure 9). The final fit refined the intense Fe(II) doublet into three equal signals (Figure 10).

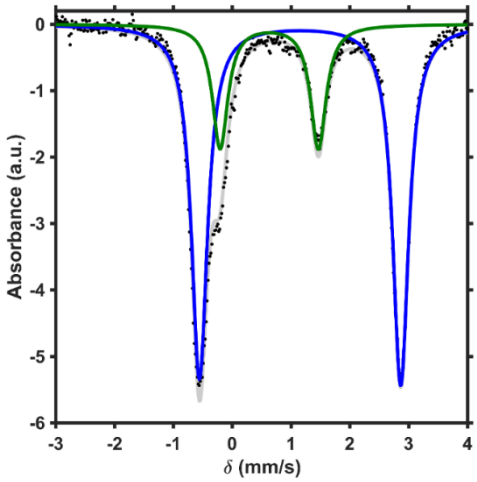

Figure 9. Mössbauer spectrum of **1-NO** (black dots) fit with two doublets in a ~3:1 ratio (gray trace) with the parameters: δ = 1.139 mm/s; ΔE_q = 3.308 mm/s (blue trace), and δ = 0.609 mm/s; ΔE_q = 1.631 mm/s (green trace).

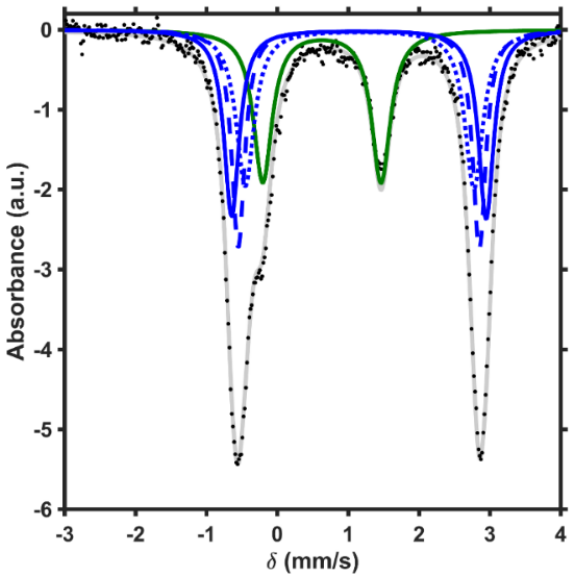

	δ (mm/s)	$\lvert\Delta E_q\rvert$ (mm/s)	Γ	Rel. %
———	1.152	3.592	0.26	25
– – –	1.150	3.403	0.22	25
·····	1.162	3.229	0.31	25
———	0.630	1.669	0.32	25

Figure 10. Zero applied field ^{57}Fe Mössbauer spectrum of [LFe$_3$F(PhPz)$_3$Fe(NO)][OTf] (**1-NO**). The data (black dots) was fit to four Fe quadrupole doublets (gray trace). The blue traces represent the signal assigned to the high-spin Fe^{II} of the tri-iron core and the green trace is assigned to the apical {FeNO}^{7}.

Simulation details for [LFe$_3$(PhPz)$_3$FFe(NO)][OTf]$_2$ (2-NO): The Mössbauer spectrum of **2-NO** displays four readily-distinguished signals. The signal above 3 mm/s was initially fit as high-spin Fe(II), and this doublet accounts for 50% of the overall spectrum (Figure 11A). The remaining signal was fit as two equally abundant doublets in three different ways (Figures 11B-D). The fit in Figure S39B gives unreasonable isomer shifts of -0.1 and 0.2 mm/s (orange and green traces, respectively). The fits in Figures 11C and 11D are only slightly different, but the fit in Figure 11D gives parameters that are more self-consistent with isomer shift values for the Fe(III) center of the 'tri-iron core' (0.4 mm/s; orange trace) and the {FeNO}^{7} center of the fluoride-bridged tetranuclear iron clusters (0.6 mm/s; green trace; see parameter refinement for **1-NO**). The final fit split the 50%-abundant Fe(II) signal into two doublets (Figure 12).

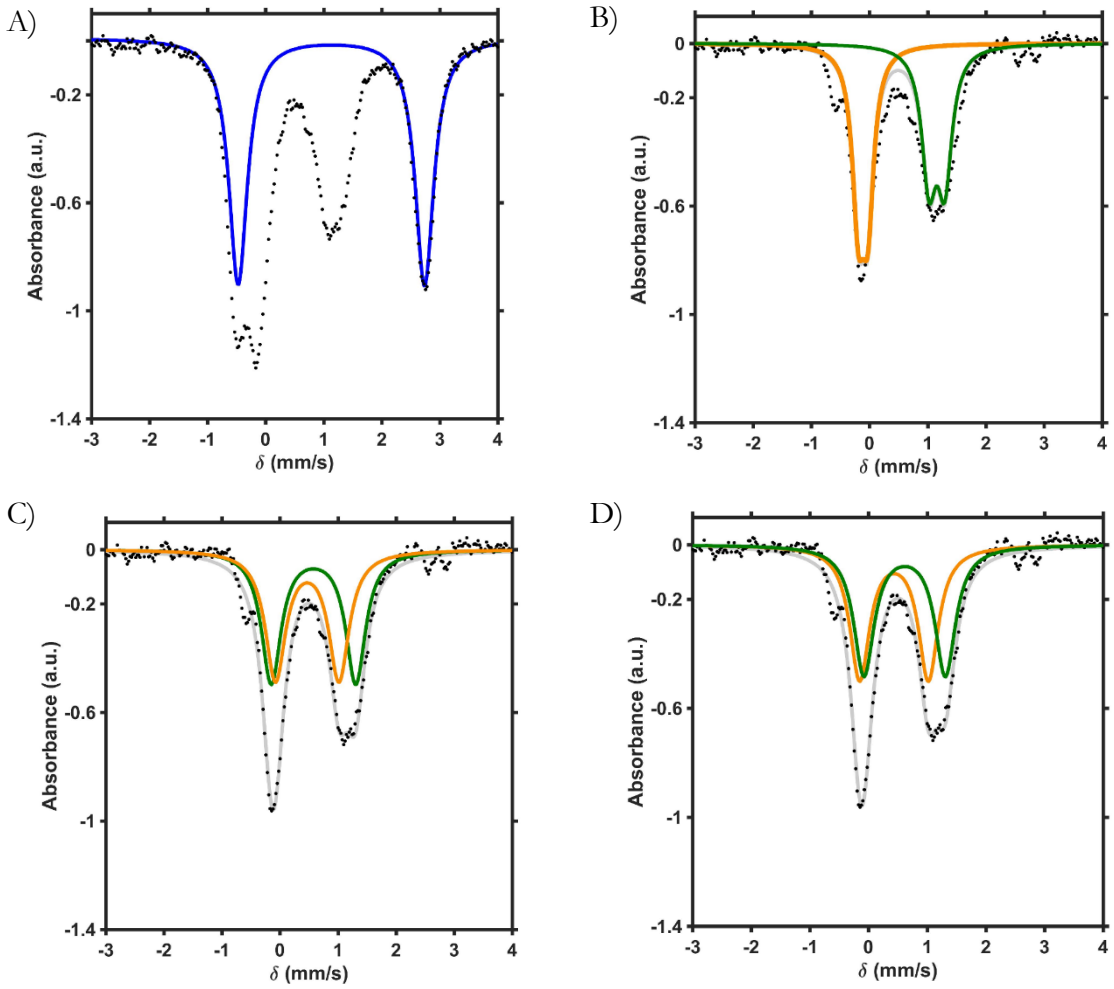

Figure 11. Mössbauer spectrum of **2-NO** (black dots) (A) fit with a single doublet refined with parameters consistent with high-spin Fe(II): δ = 1.132 mm/s; ΔE_q = 3.211 mm/s (blue trace). (B) Mössbauer spectrum of **2-NO** with this Fe(II) doublet subtracted (black dots) and two equally abundant signals fit (gray trace): δ = -0.111 mm/s; ΔE_q = 0.165 mm/s (orange trace), and δ = 1.158 mm/s; ΔE_q = 0.270 mm/s (green trace). (C) Mössbauer spectrum of **2-NO** with this Fe(II) doublet subtracted (black dots) and two equally abundant signals fit (gray trace): δ = 0.577 mm/s; ΔE_q = 1.456 mm/s (green trace), and δ = 0.469 mm/s; ΔE_q = 1.094

mm/s (orange trace). (D) Mössbauer spectrum of **2-NO** with this Fe(II) doublet subtracted (black dots) and two equally abundant signals fit (gray trace): δ = 0.616 mm/s; ΔE_q = 1.387 mm/s (green trace), and δ = 0.435 mm/s; ΔE_q = 1.171 mm/s (orange trace).

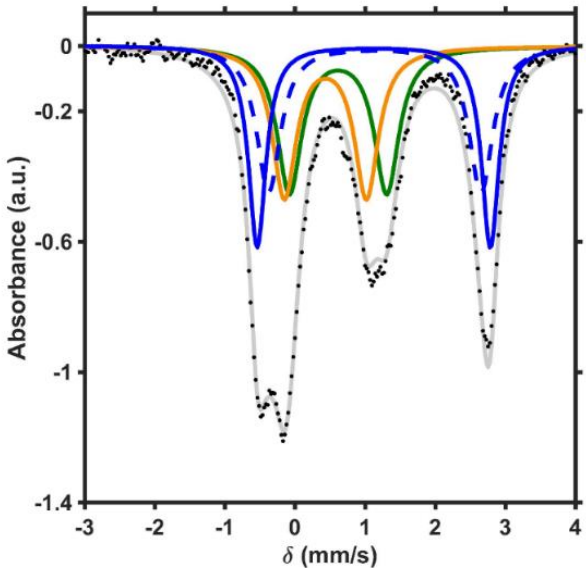

	δ (mm/s)	$\lvert\Delta E_q\rvert$ (mm/s)	Γ	Rel. %
	1.121	3.309	0.30	25
	1.150	3.026	0.46	25
	0.435	1.171	0.41	25
	0.616	1.387	0.42	25

Figure 12. Zero applied field ^{57}Fe Mössbauer spectrum of $[LFe_3F(PhPz)_3Fe(NO)][OTf]_2$ (**2-NO**). The data (black dots) was fit to four Fe quadrupole doublets (gray trace). The blue traces represent the signal assigned to the high-spin Fe^{II} of the tri-iron core, the orange trace is assigned to the high-spin Fe^{III} in the tri-iron core, and the green trace is assigned to the apical $\{FeNO\}^7$.

Simulation details for $[LFe_3(PhPz)_3FFe(NO)][OTf]_3$ (3-NO): The Mössbauer spectrum of **3-NO** displays three major features (instead of the expected eight for four Fe centers). The peak around 3 mm/s was modeled as a high-spin Fe(II) with parameters consistent with other Fe(II) centers in the 'tri-iron core' of the tetranuclear clusters; this fit accounted for 25% of the total signal (Figure 13A). Subtracting this doublet from the data, the remaining signal could be fit reasonably well with either one or two equally abundant quadrupole doublets (Figures 13B and 13C), however these fits were ruled out since they were inconsistent with our crystallographic analysis of **3-NO**. There are many possible ways to fit 3 doublets in this residual signal; below are shown three fits that give reasonable fit parameters for two high-spin Fe(III) centers and a high-spin five-coordinate $\{FeNO\}^7$ (Figure 13D-F). The fit in Figure 13F gave parameters the most self-consistent within this series of clusters, and was used for the final refinement (Figure 14).

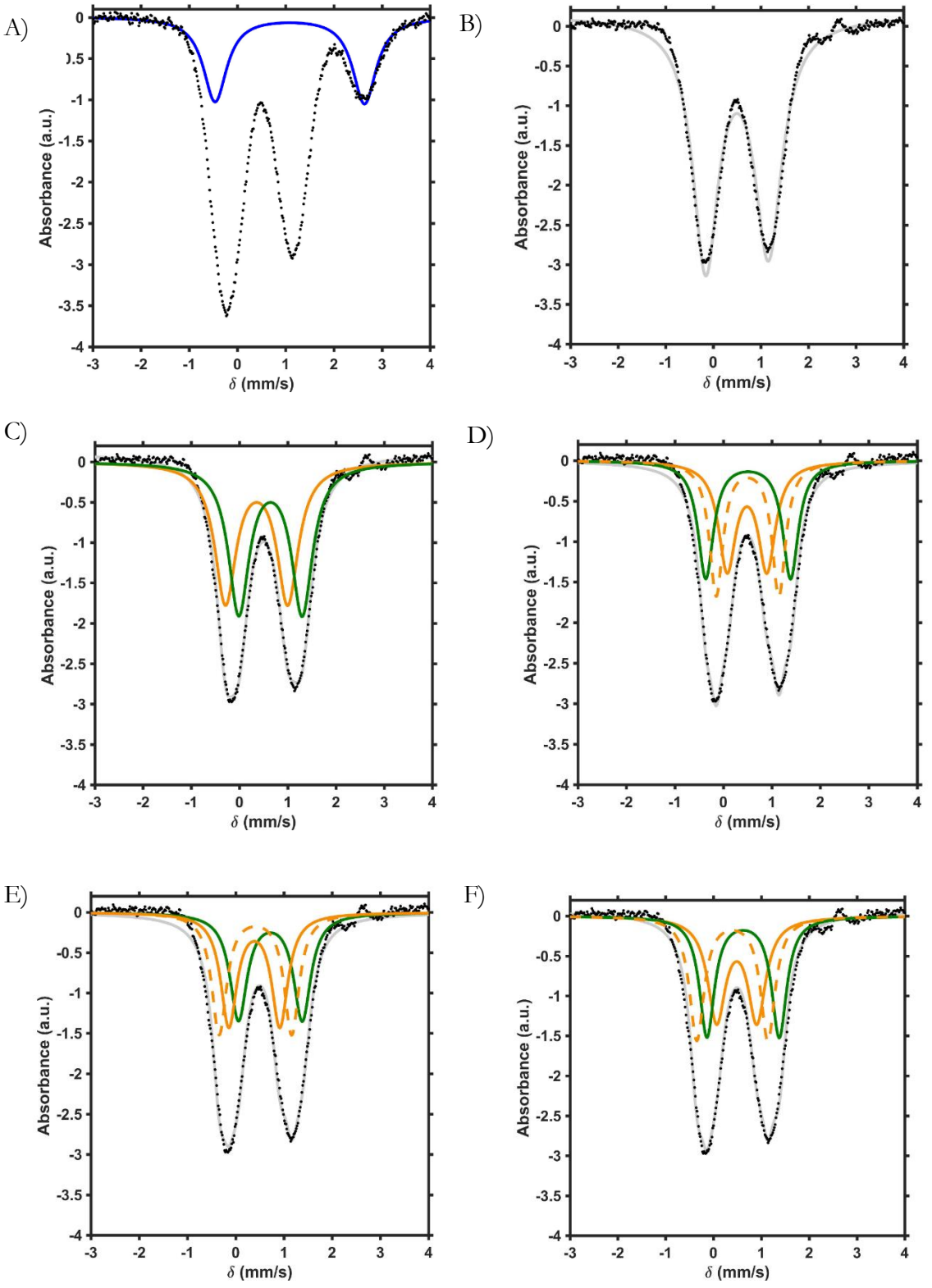

Figure 13. Mössbauer spectrum of **3-NO** (black dots) (A) fit with a single doublet refined with parameters consistent with high-spin Fe(II): δ = 1.087 mm/s; ΔE_q = 3.100 mm/s (blue trace). (B) Mössbauer spectrum of **3-NO** with this Fe(II) doublet subtracted (black dots) and

fit with a single quadrupole doublet (gray trace): δ = 0.501 mm/s; ΔE_q = 1.319 mm/s. (C) Mössbauer spectrum of **3-NO** with this Fe(II) doublet subtracted (black dots) and two equally abundant signals fit (gray trace): δ = 0.354 mm/s; ΔE_q = 1.291 mm/s (orange trace), and δ = 0.643 mm/s; ΔE_q = 1.314 mm/s (green trace). (D) Mössbauer spectrum of **3-NO** with this Fe(II) doublet subtracted (black dots) and three equally abundant signals fit (gray trace): δ = 0.488 mm/s; ΔE_q = 0.819 mm/s (solid orange trace), and δ = 0.499 mm/s; ΔE_q = 1.292 mm/s (dashed orange trace), and δ = 0.512 mm/s; ΔE_q = 1.750 mm/s (green trace). (E) Mössbauer spectrum of **3-NO** with this Fe(II) doublet subtracted (black dots) and three equally abundant signals fit (gray trace): δ = 0.387 mm/s; ΔE_q = 1.058 mm/s (solid orange trace), and δ = 0.409 mm/s; ΔE_q = 1.503 mm/s (dashed orange trace), and δ = 0.719 mm/s; ΔE_q = 1.321 mm/s (green trace). (F) Mössbauer spectrum of **3-NO** with this Fe(II) doublet subtracted (black dots) and three equally abundant signals fit (gray trace): δ = 0.486 mm/s; ΔE_q = 0.840 mm/s (solid orange trace), and δ = 0.395 mm/s; ΔE_q = 1.486 mm/s (dashed orange trace), and δ = 0.620 mm/s; ΔE_q = 1.512 mm/s (green trace).

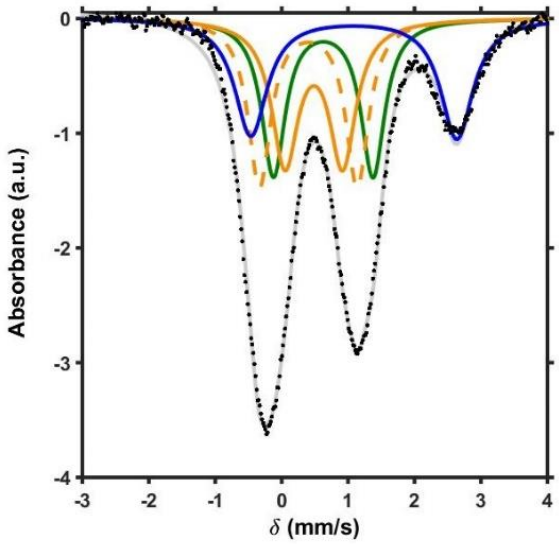

	δ (mm/s)	$\lvert\Delta E_q\rvert$ (mm/s)	Γ	Rel. %
	1.087	3.100	0.59	25
	0.484	0.868	0.49	25
	0.402	1.471	0.41	25
	0.615	1.507	0.44	25

Figure 14. Zero applied field ^{57}Fe Mössbauer spectrum of $[LFe_3F(PhPz)_3Fe(NO)][OTf]_3$ (**3-NO**). The data (black dots) was fit to four Fe quadrupole doublets (gray trace). The blue trace represents the signal assigned to the high-spin Fe^{II} of the tri-iron core, the orange traces are assigned to the high-spin Fe^{III} in the tri-iron core, and the green trace is assigned to the apical $\{FeNO\}^7$.

Simulation details for $[LFe_3(PhPz)_3FFe(NO)][OTf]_3[SbCl_6]$ (4-NO): The Mössbauer spectrum of **4-NO** displays two broad features, which were adequately fit as a single quadrupole doublet (Figure 15). Since it is likely that the Fe(III) signals are overlapping with the $\{FeNO\}^7$ signal (see Mössbauer spectra of **2-NO** and **3-NO**), modeling the four separate Fe centers is not included. This spectrum is consistent, however, with our assignment of **4-NO** as a cluster containing no Fe(II) centers, since there the characteristic signal around 3 mm/s is absent.

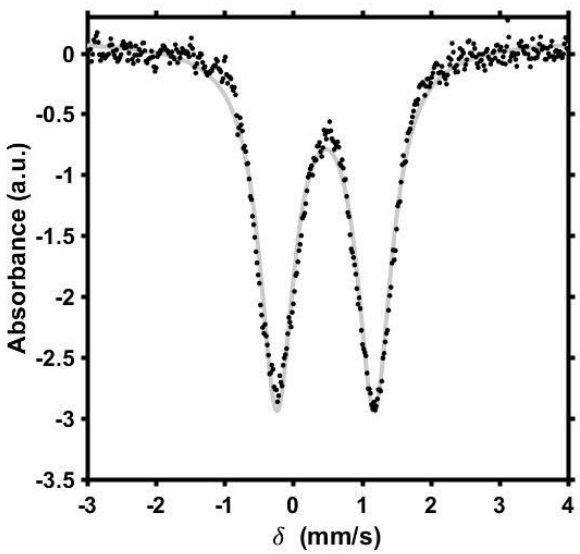

	δ (mm/s)	$\lvert\Delta E_q\rvert$ (mm/s)	Γ	Rel. %
	0.471	1.420	0.61	100

Figure 15. Zero applied field ^{57}Fe Mössbauer spectrum of $[LFe_3F(PhPz)_3Fe(NO)][OTf]_3[SbCl_6]$ (**4-NO**). The data (black dots) was fit to a single Fe quadrupole doublet (gray trace). We postulate that the signal for the apical $\{FeNO\}^7$ is overlapping with the doublet(s) for the high-spin Fe(III) in the 'tri-iron core'.

Simulation details for 1-[OTf]: The spectrum displays three discernable peaks corresponding to two quadrupole doublets in ~ 1:2 ratio (Figure 16). The parameters of the more intense peak are consistent with a high-spin Fe(II) assignment, while the smaller doublet displays parameters consistent with high-spin Fe(III). The final fit split the large doublet into two equal signals (Figure 17).

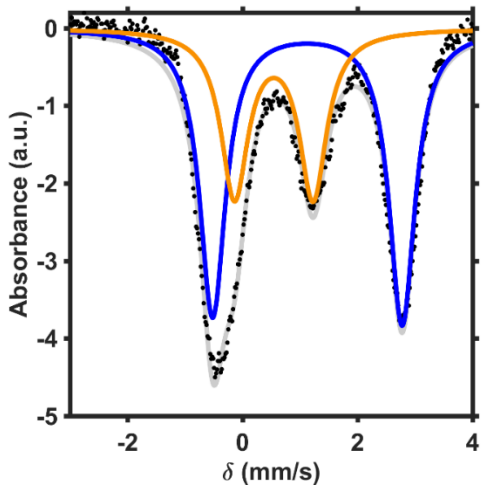

Figure 16. Mössbauer spectrum of **1-[OTf]** (black dots) fit with two doublets in a ~1:2 ratio (gray trace) with parameters $\delta = 0.543$ mm/s; $\Delta E_q = 1.366$ mm/s (orange trace) and $\delta = 1.126$ mm/s; $\Delta E_q = 3.294$ mm/s (blue trace).

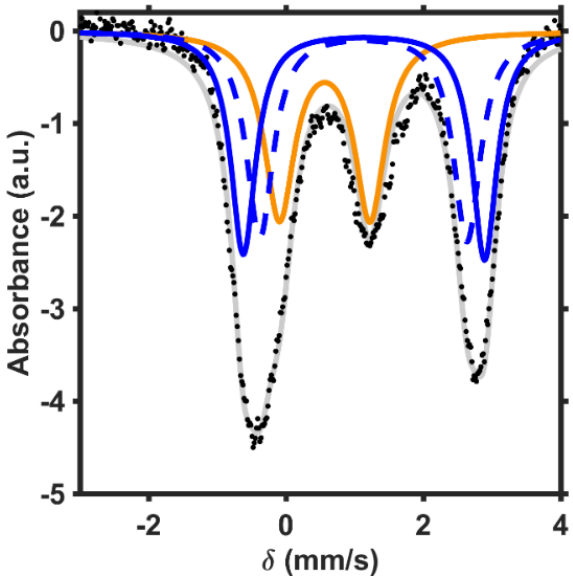

	δ (mm/s)	$\lvert\Delta E_q\rvert$ (mm/s)	Rel. %
———	1.135	3.513	33
– – –	1.127	3.016	33
———	0.563	1.318	33

Figure 17. Zero applied field Mössbauer spectrum of **1-[OTf]** (black dots) fit with three quadrupole doublets. The blue traces are assigned to high-spin Fe(II) and the orange trace is assigned as high-spin Fe(III).

Simulation details for 2-[OTf]: The spectrum displays four discernable peaks corresponding to two quadrupole doublets in ~ 1:2 ratio (Figure 18). The parameters of the more intense peak are consistent with a high-spin Fe(III) assignment, while the smaller doublet displays parameters consistent with high-spin Fe(II). The final fit split the large doublet into two equal signals (Figure 19).

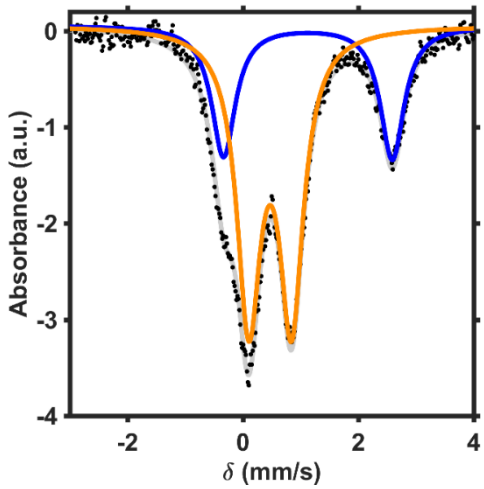

Figure 18. Mössbauer spectrum of **2-[OTf]** (black dots) fit with two doublets in a ~1:2 ratio (gray trace) with parameters $\delta = 0.469$ mm/s; $\Delta E_q = 0.740$ mm/s (orange trace) and $\delta = 1.124$ mm/s; $\Delta E_q = 2.926$ mm/s (blue trace).

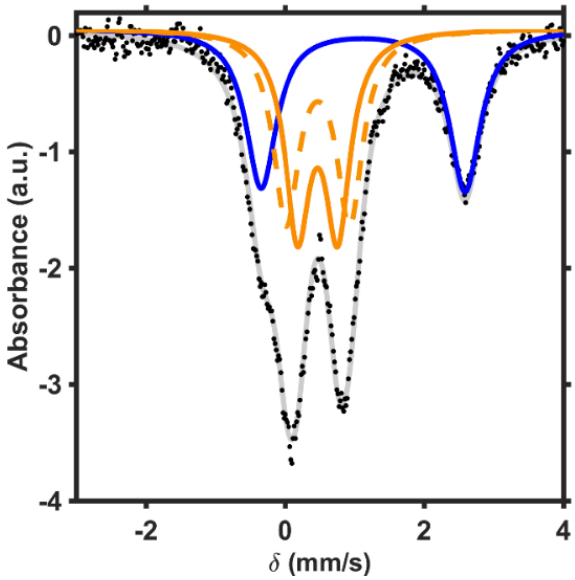

	δ (mm/s)	$\lvert\Delta E_q\rvert$ (mm/s)	Rel. %
———	1.119	2.931	33
———	0.468	0.578	33
- - -	0.423	0.913	33

Figure 19. Zero applied field Mössbauer spectrum of **2-[OTf]** (black dots) fit with three quadrupole doublets. The blue trace is assigned to high-spin Fe(II) and the orange traces are assigned to high-spin Fe(III).

Simulation details for 3-[OTf]: The spectrum displays a single quadrupole doublet signal. Although three Fe(III) signals are expected, the best fit was obtained with only one set of parameters (Figure 20).

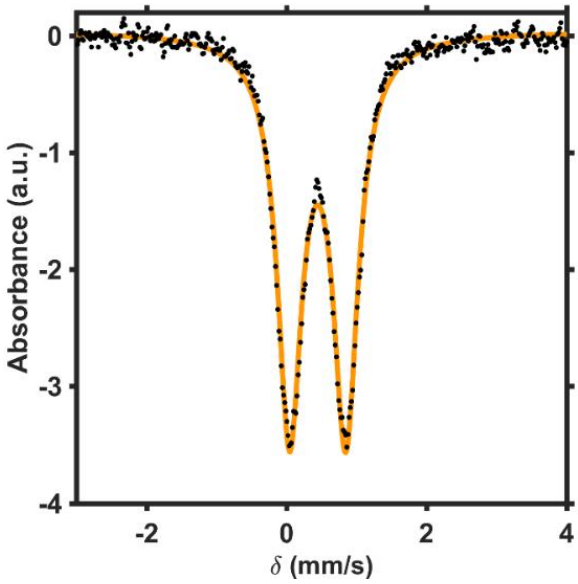

	δ (mm/s)	$\lvert\Delta E_q\rvert$ (mm/s)	Rel. %
	0.443	0.804	100

Figure 20. Zero applied field Mössbauer spectrum of **3-[OTf]** (black dots) fit to a single quadrupole doublet (orange trace); this signal is assigned to the high-spin Fe(III) centers in the cluster.

Simulation details for 1-[BAr$^F_4$]: The spectrum displays three discernable peaks corresponding to two quadrupole doublets in ~ 1:2 ratio (Figure 21). The parameters of the more intense peak are consistent with a high-spin Fe(II) assignment, while the smaller doublet displays parameters consistent with high-spin Fe(III). The final fit split the large doublet into two equal signals (Figure 22).

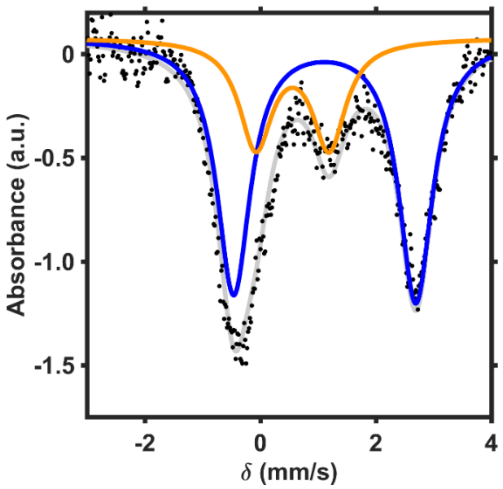

Figure 21. Mössbauer spectrum of **1-[BAr$^F_4$]** (black dots) fit with two doublets in a ~1:2 ratio (gray trace) with parameters δ = 0.556 mm/s; ΔE_q = 1.267 mm/s (orange trace) and δ = 1.115 mm/s; ΔE_q = 3.153 mm/s (blue trace).

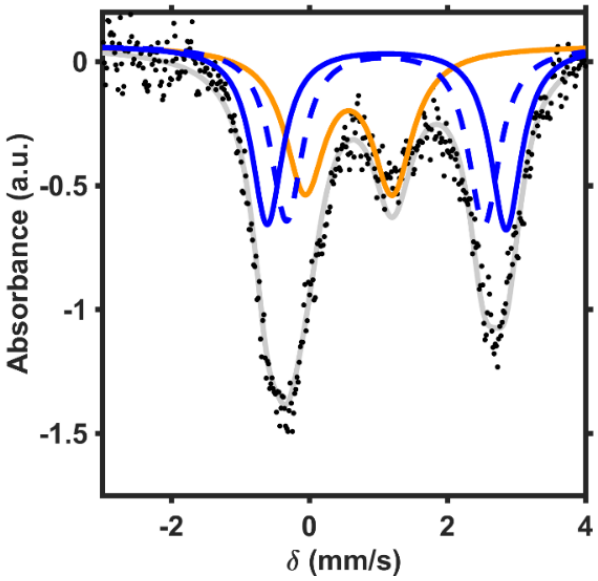

	δ (mm/s)	$\lvert\Delta E_q\rvert$ (mm/s)	Rel. %
———	1.119	3.460	33
– – –	1.099	2.860	33
———	0.570	1.266	33

Figure 22. Zero applied field Mössbauer spectrum of **1-[BAr$^{F}_{4}$]** (THF solution [250 mM H_2O]; black dots) fit with three quadrupole doublets. The blue traces are assigned to high-spin Fe(II) and the orange trace is assigned to high-spin Fe(III).

Simulation details for 2-[BAr$^{F}_{4}$]: The spectrum displays four discernable peaks corresponding to two quadrupole doublets in ~ 1:2 ratio (Figure 23). The parameters of the more intense peak are consistent with a high-spin Fe(III) assignment, while the smaller doublet displays parameters consistent with high-spin Fe(II). The final fit split the large doublet into two equal signals (Figure 24).

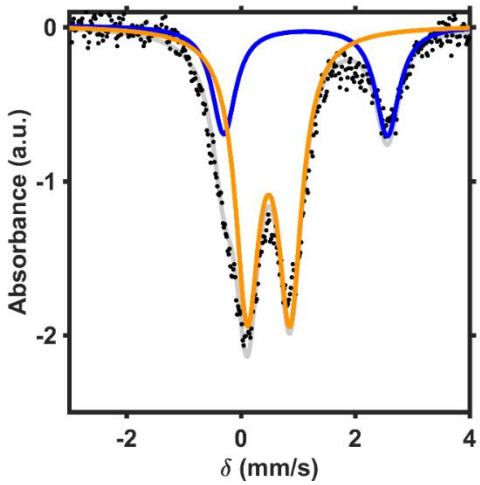

Figure 23. Mössbauer spectrum of **2-[BAr$^{F}_{4}$]** (black dots) fit with two doublets in a ~1:2 ratio (gray trace) with parameters δ = 0.485 mm/s; ΔE_q = 0.746 mm/s (orange trace) and δ = 1.132 mm/s; ΔE_q = 2.858 mm/s (blue trace).

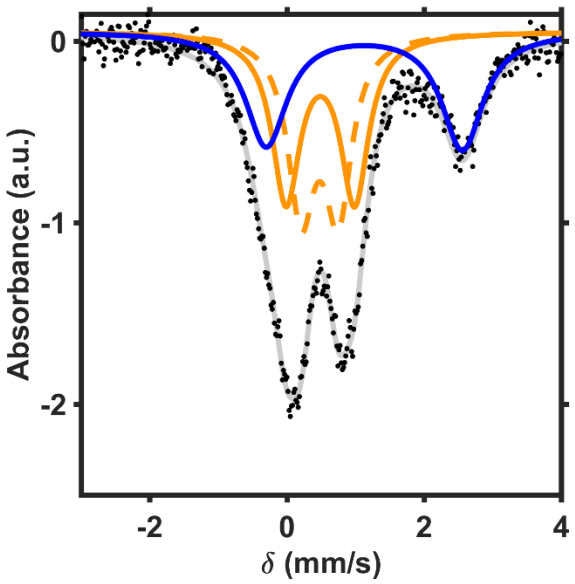

	δ (mm/s)	$\lvert\Delta E_q\rvert$ (mm/s)	Rel. %
———	1.128	2.858	33
———	0.487	0.999	33
- - -	0.478	0.540	33

Figure 24. Zero applied field Mössbauer spectrum of **2-[BAr$^{F}_{4}$]** (THF solution [250 mM H_2O]; black dots) fit with three quadrupole doublets. The blue trace is assigned to high-spin Fe(II) and the orange traces are assigned to high-spin Fe(III).

Simulation details for 3-[BAr$^{F}_{4}$]: The spectrum displays a single quadrupole doublet signal. Although three Fe(III) signals are expected, the best fit was obtained with only one set of parameters (Figure 25).

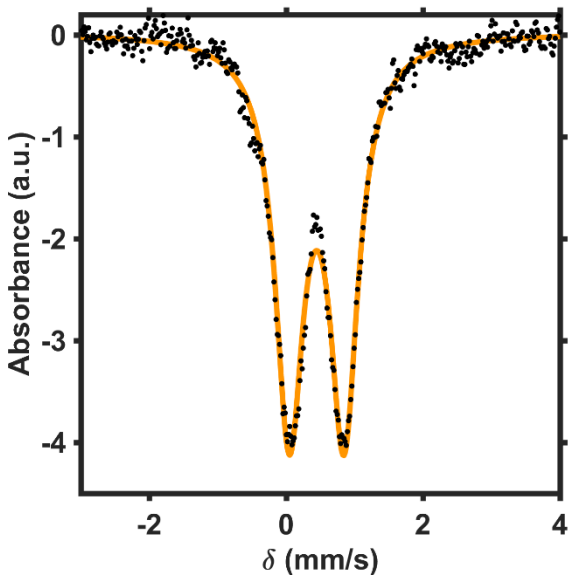

	δ (mm/s)	$\lvert\Delta E_q\rvert$ (mm/s)	Rel. %
———	0.444	0.800	100

Figure 25. Zero applied field Mössbauer spectrum of **3-[BAr$^{F}_{4}$]** (THF solution [250 mM H_2O]; black dots) fit with a single quadrupole doublet assigned to high-spin Fe(III) centers.

Simulation details for 5: The spectrum displays an apparently asymmetric quadrupole doublet signal. The data could be fit to a single quadrupole doublet (Figure 26). The final fit split this signal into three equally abundant Fe(II) centers, to account for the asymmetry of the doublet (Figure 27).

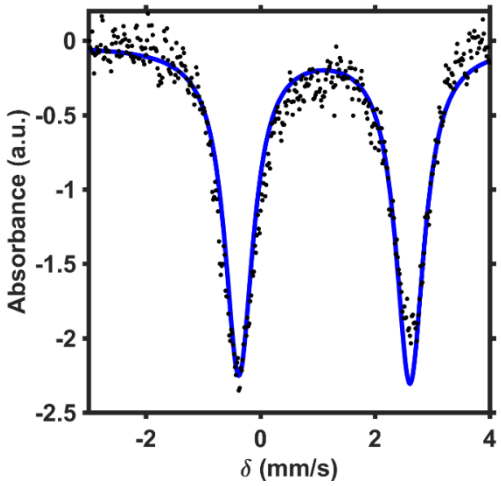

Figure 26. Mössbauer spectrum of **5** (black dots) fit with a single quadrupole doublet with parameters δ = 1.113 mm/s; ΔE_q = 2.985 mm/s (blue trace).

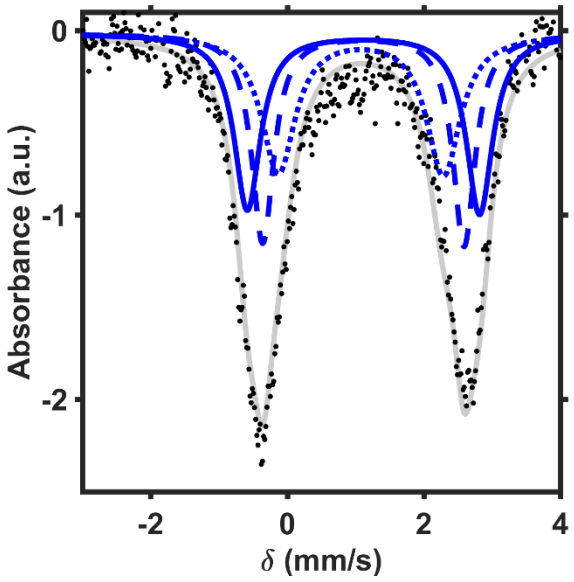

	δ (mm/s)	$\lvert\Delta E_q\rvert$ (mm/s)	Rel. %
———	1.115	3.399	33
– – –	1.115	2.947	33
·····	1.078	2.417	33

Figure 27. Zero applied field Mössbauer spectrum of **5** (black dots) fit with three quadrupole doublets. The blue traces are assigned to high-spin Fe(II).

Simulation details for 6-[BAr$^{F}_{4}$]: The spectrum displays four discernable peaks corresponding to two quadrupole doublets in ~ 1:2 ratio (Figure 28). The parameters of the more intense peak are consistent with a high-spin Fe(II) assignment, while the smaller doublet displays parameters consistent with high-spin Fe(III). The final fit split the large doublet into two equal signals (Figure 29).

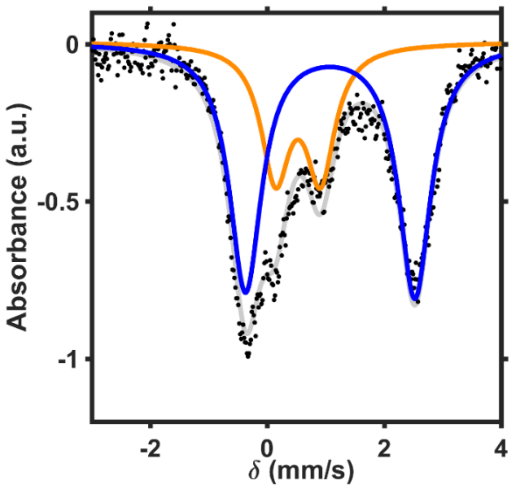

Figure 28. Mössbauer spectrum of **6-[BAr$^{F}_{4}$]** (black dots) fit with two doublets in a ~1:2 ratio (gray trace) with parameters δ = 0.525 mm/s; ΔE_q = 0.769 mm/s (orange trace) and δ = 1.075 mm/s; ΔE_q = 2.893 mm/s (blue trace).

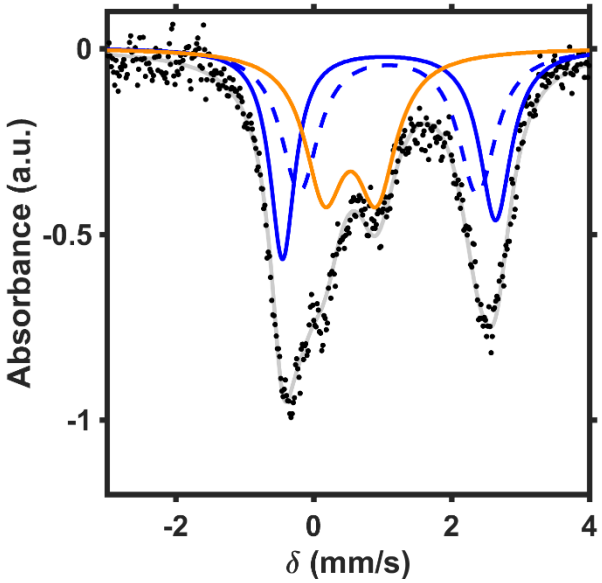

	δ (mm/s)	$\lvert\Delta E_q\rvert$ (mm/s)	Rel. %
———	1.093	3.091	33
– – –	1.083	2.576	33
———	0.534	0.756	33

Figure 29. Zero applied field Mössbauer spectrum of **6-[BAr$^{F}_{4}$]** (THF solution [250 mM H_2O]; black dots) fit with three quadrupole doublets. The blue traces are assigned to high-spin Fe(II) and the orange trace is assigned to high-spin Fe(III).

Simulation details for 7-[BAr$^{F}_{4}$]: The spectrum displays three discernable peaks, with a shoulder on the lowest peak, corresponding to two quadrupole doublets in ~ 1:2 ratio (Figure 30). The parameters of the more intense peak are consistent with a high-spin Fe(III) assignment, while the smaller doublet displays parameters consistent with high-spin Fe(III). The final fit split the large doublet into two equal signals (Figure 31).

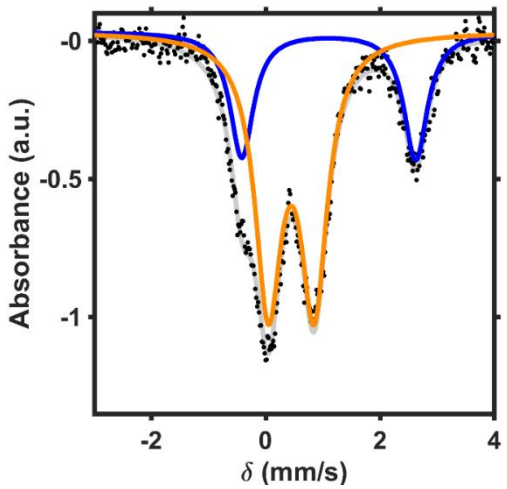

Figure 30. Mössbauer spectrum of **7-[BAr$^{F}_{4}$]** (black dots) fit with two doublets in a ~1:2 ratio (gray trace) with parameters δ = 0.447 mm/s; ΔE_q = 0.790 mm/s (orange trace) and δ = 1.109 mm/s; ΔE_q = 3.018 mm/s (blue trace).

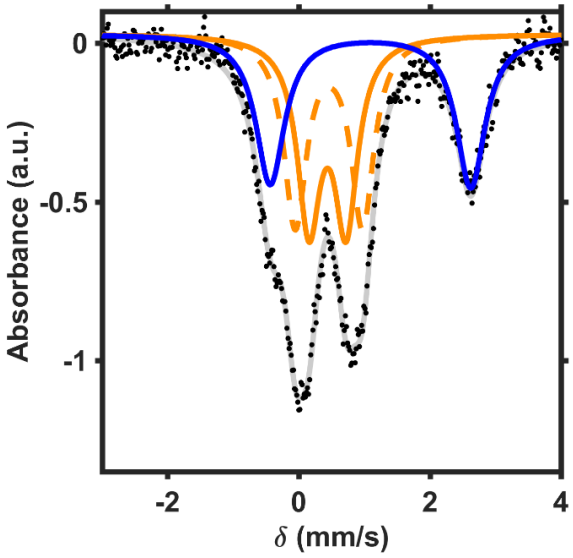

	δ (mm/s)	$\lvert\Delta E_q\rvert$ (mm/s)	Rel. %
	1.096	3.033	33
	0.434	0.547	33
	0.462	1.019	33

Figure 31. Zero applied field Mössbauer spectrum of **7-[BAr$^{F}_{4}$]** (THF solution [250 mM H_2O]; black dots) fit with three quadrupole doublets. The blue trace is assigned to high-spin Fe(II) and the orange traces are assigned to high-spin Fe(III).

Simulation details for $LFe_3O(PzNHtBu)_3Fe(OH)$ (1): The spectrum displays three discernable peaks corresponding to two quadrupole doublets in ~ 1:3 ratio. The parameters of the more intense peak are consistent with a high-spin Fe(II) assignment, while the smaller doublet could be fit a number of ways, two of which are shown here (Figure 32). Figure 32B gives parameters most consistent with an apical Fe(III). The final fit split the large doublet into three equal signals (Figure 33).

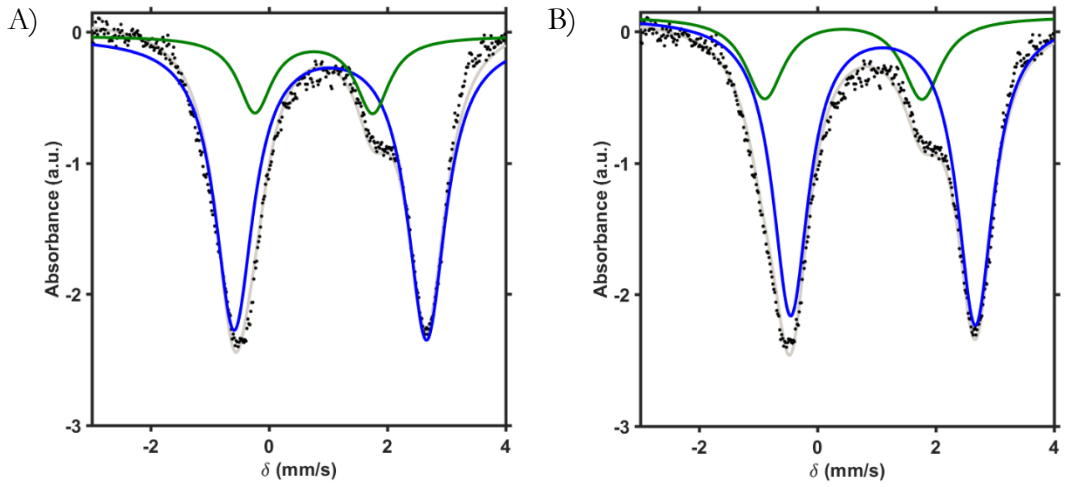

Figure 32. Mössbauer spectrum of **1** (black dots) fit with two doublets in a ~1:3 ratio (gray trace) with parameters (A) δ = 1.035 mm/s; ΔE_q = 3.255 mm/s (blue trace) and δ = 0.756 mm/s; ΔE_q = 1.993 mm/s (green trace) and (B) δ = 1.107 mm/s; ΔE_q = 3.126 mm/s (blue trace) and δ = 0.436 mm/s; ΔE_q = 2.663 mm/s (green trace).

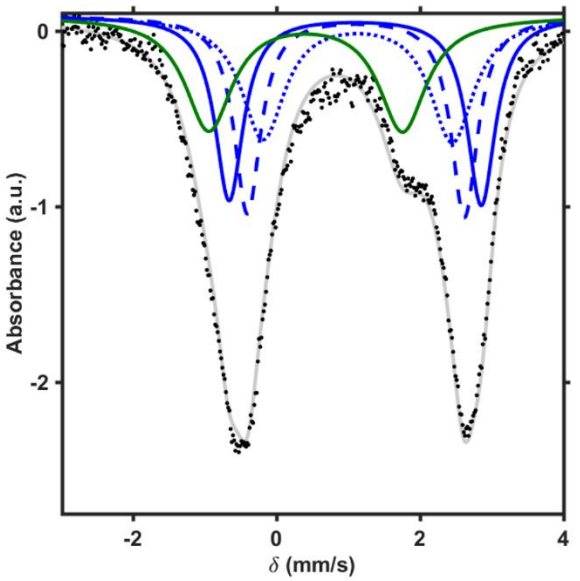

	δ (mm/s)	$\lvert\Delta E_q\rvert$ (mm/s)	Rel. %
———	1.099	3.519	25
– – –	1.109	3.029	25
– – – –	1.134	2.640	25
———	0.407	2.706	25

Figure 33. Zero applied field Mössbauer spectrum of **1** (black dots) fit with four quadrupole doublets. The blue traces are assigned to high-spin Fe(II) and the green trace is assigned as Fe(III).

Simulation details for [LFe$_3$O(PzNHtBu)$_3$Fe(OH)][OTf] (2): The spectrum displays five discernable peaks corresponding to three quadrupole doublets in ~ 1:1:2 ratio. The parameters of the most intense peak are consistent with a high-spin Fe(II) assignment, and the remainder of the signal can be fit a number of ways (Figures 34). Figure 34B gives parameters most consistent with an apical Fe(III). The final fit split the large doublet into two equal signals (Figure 35).

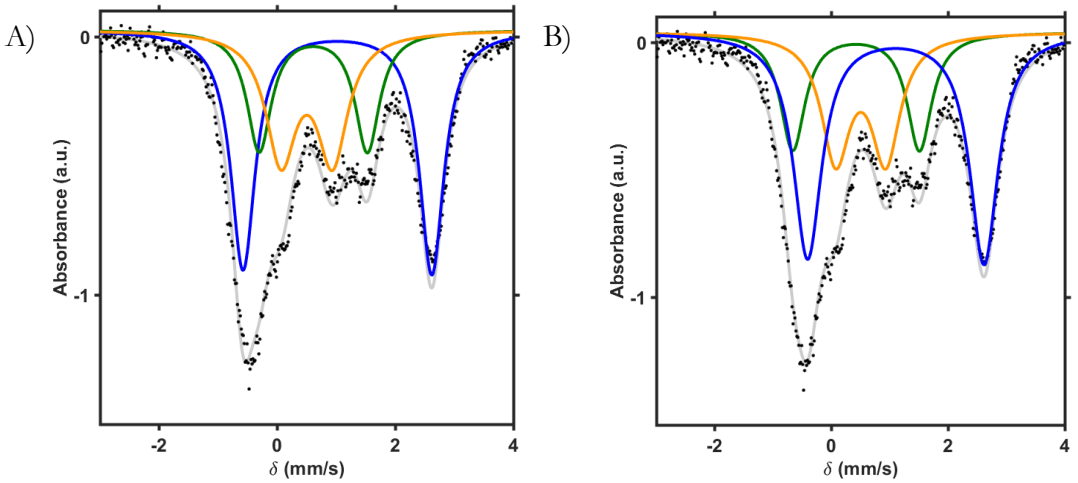

Figure 34. Mössbauer spectrum of **2** (black dots) fit with three doublets in a ~1:1:2 ratio (gray trace) with parameters (A) δ = 1.020 mm/s; ΔE_q = 3.197 mm/s (blue trace), δ = 0.502 mm/s; ΔE_q = 0.871 mm/s (orange trace) and δ = 0.612 mm/s; ΔE_q = 1.832 mm/s (green trace) and (B) δ = 1.107 mm/s; ΔE_q = 3.126 mm/s (blue trace), δ = 0.504 mm/s; ΔE_q = 0.857 mm/s (orange trace) and δ = 0.425 mm/s; ΔE_q = 2.172 mm/s (green trace).

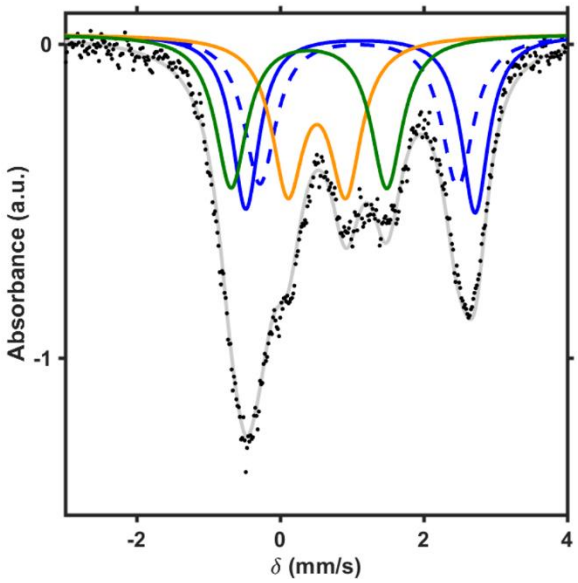

	δ (mm/s)	$\lvert\Delta E_q\rvert$ (mm/s)	Rel. %
———	1.123	3.197	25
- - -	1.100	2.757	25
———	0.515	0.809	25
———	0.406	2.171	25

Figure 35. Zero applied field Mössbauer spectrum of **2** (black dots) fit with four quadrupole doublets. The blue traces are assigned to high-spin Fe(II), the orange trace is assigned to high-spin Fe(III), and the green trace is assigned as Fe(III).

Simulation details for $[LFe_3O(PzNHtBu)_3Fe(OH)][OTf]_2$ (3): The spectrum displays three discernable peaks corresponding to two quadrupole doublets in ~ 1:3 ratio. The parameters of the less intense peak are consistent with a high-spin Fe(II) assignment, and the remainder of the signal can be fit a number of ways. Based on the Mossbauer parameters for the other cluster oxidation states (Figures 33 and 35), a fit was performed to obtain self-consistent parameters (i.e. making apical Fe(III) doublet with second largest quadrupole splitting). This fit led to parameters that are in good agreement for a high-spin Fe(II), two high-spin Fe(III), and the unique apical Fe(III) environment (Figure 36).

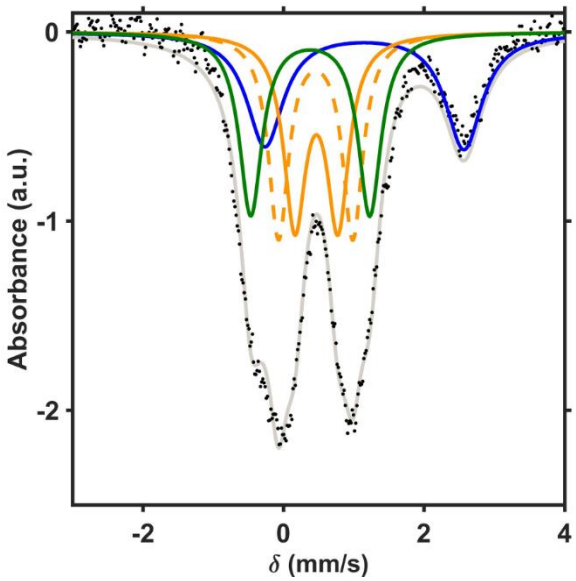

	δ (mm/s)	$\lvert\Delta E_q\rvert$ (mm/s)	Rel. %
	1.153	2.829	25
	0.469	0.613	25
	0.459	1.056	25
	0.381	1.693	25

Figure 36. Zero applied field Mössbauer spectrum of **3** (black dots) fit with four quadrupole doublets. The blue trace is assigned to high-spin Fe(II), the orange traces are assigned to high-spin Fe(III), and the green trace is assigned as Fe(III).

Simulation details for $[LFe_3O(PzNHtBu)_3Fe(OH)][OTf]_3$ (4): The spectrum displays two peaks of different intensities and shapes, consistent with multiple overlapping quadrupole doublets. In order to obtain self-consistent parameters, the spectrum was fit to four quadrupole doublets, with the doublet with the highest quadrupole splitting assigned to the apical Fe(III) (Figure 37).

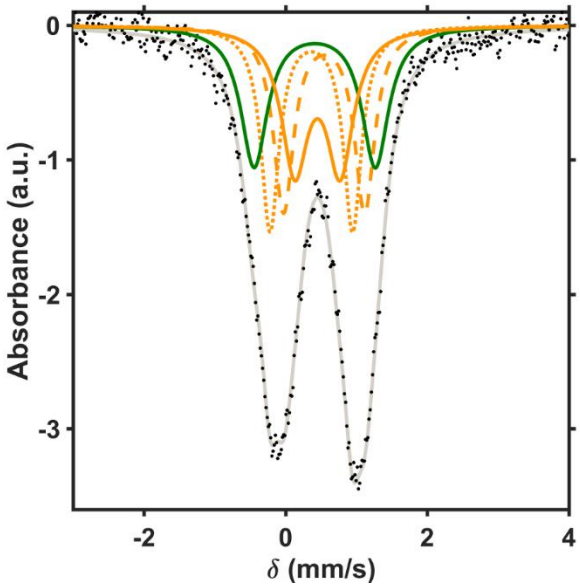

	δ (mm/s)	$\|\Delta E_q\|$ (mm/s)	Rel. %
———	0.449	0.641	25
– – –	0.543	1.145	25
– – – ·	0.363	1.166	25
———	0.411	1.712	25

Figure 37. Zero applied field Mössbauer spectrum of **4** (black dots) fit with four quadrupole doublets. The orange traces are assigned to high-spin Fe(III) and the green trace is assigned as Fe(III).

Simulation details for $LFe_3O(PzNHtBu)_3Fe(O)$ (5): The spectrum displays six discernable peaks corresponding to three quadrupole doublets in ~ 1:1:2 ratio. The parameters of the most intense peak are consistent with a high-spin Fe(II) assignment, and the remainder of the signal can be fit a number of ways (Figure 38). Figure 38C gives parameters most consistent with an apical Fe(III) and high-spin Fe(III) in the tri-iron core. The final fit split the large doublet into two equal signals (Figure 39).

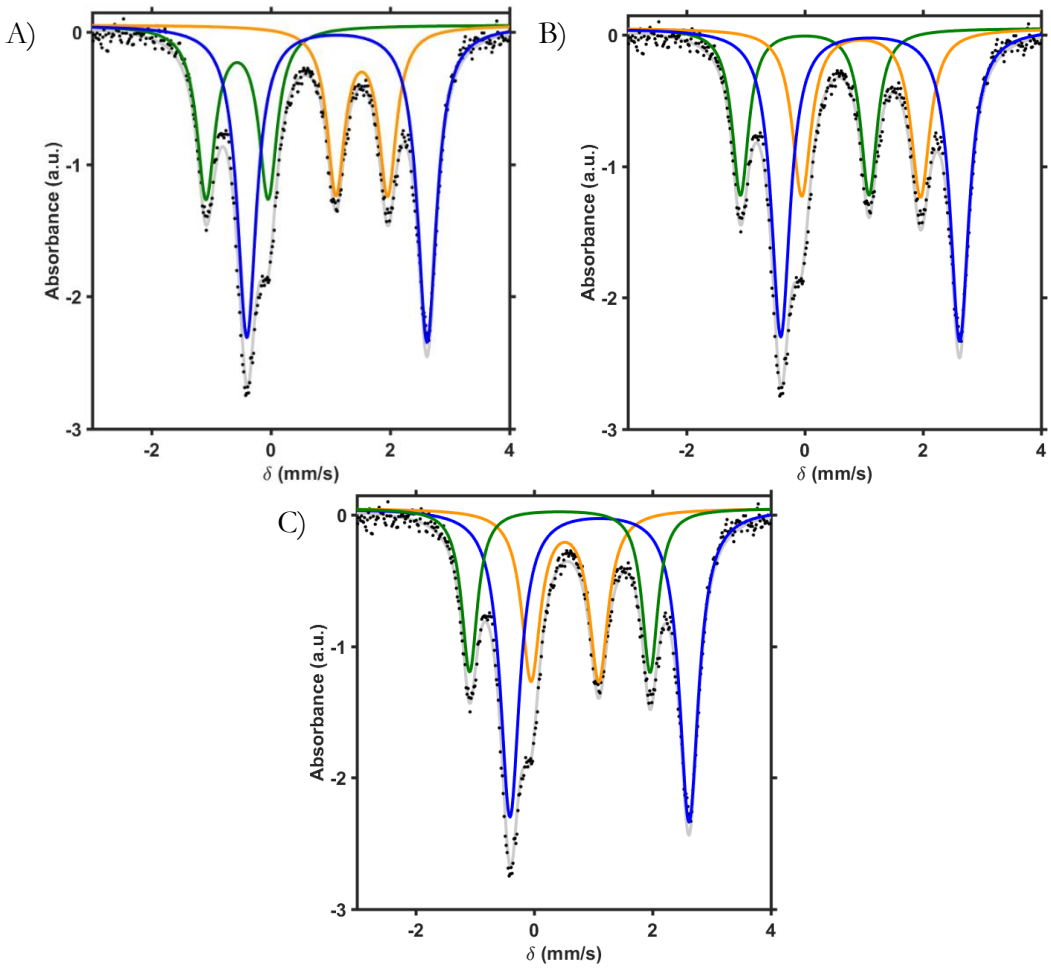

Figure 38. Mössbauer spectrum of **5** (black dots) fit with three doublets in a ~1:1:2 ratio (gray trace) with parameters (A) δ = 1.106 mm/s; ΔE_q = 3.023 mm/s (blue trace), δ = 1.522 mm/s; ΔE_q = 0.868 mm/s (orange trace) and δ = -0.569 mm/s; ΔE_q = 1.042 mm/s (green trace)., (B) δ = 1.106 mm/s; ΔE_q = 3.029 mm/s (blue trace), δ = 0.952 mm/s; ΔE_q = 2.010 mm/s (orange trace) and δ = -0.003 mm/s; ΔE_q = 2.178 mm/s (green trace), and (C) δ = 1.103 mm/s; ΔE_q = 3.027 mm/s (blue trace), δ = 0.518 mm/s; ΔE_q = 1.146 mm/s (orange trace) and δ = 0.432 mm/s; ΔE_q = 3.051 mm/s (green trace).

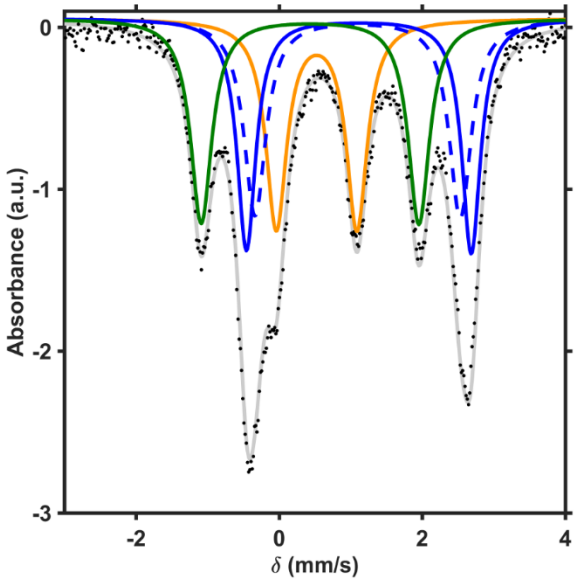

	δ (mm/s)	$\lvert\Delta E_q\rvert$ (mm/s)	Rel. %
———	1.115	3.141	25
– – –	1.097	2.869	25
———	0.524	1.126	25
———	0.433	3.042	25

Figure 39. Zero applied field Mössbauer spectrum of **5** (black dots) fit with four quadrupole doublets. The blue traces are assigned to high-spin Fe(II), the orange trace is assigned to high-spin Fe(III), and the green trace is assigned to Fe(III).

Simulation details for [LFe$_3$O(PzNHtBu)$_3$Fe(O)][OTf] (6): The spectrum displays five discernable peaks corresponding to three quadrupole doublets in ~ 1:1:2 ratio. The parameters of the most intense peak are consistent with a high-spin Fe(III) assignment, and the remainder of the signal can be fit a number of ways (Figures 40). Figure 40B gives parameters most consistent with an apical Fe(III). The final fit split the large doublet into two equal signals (Figure 41).

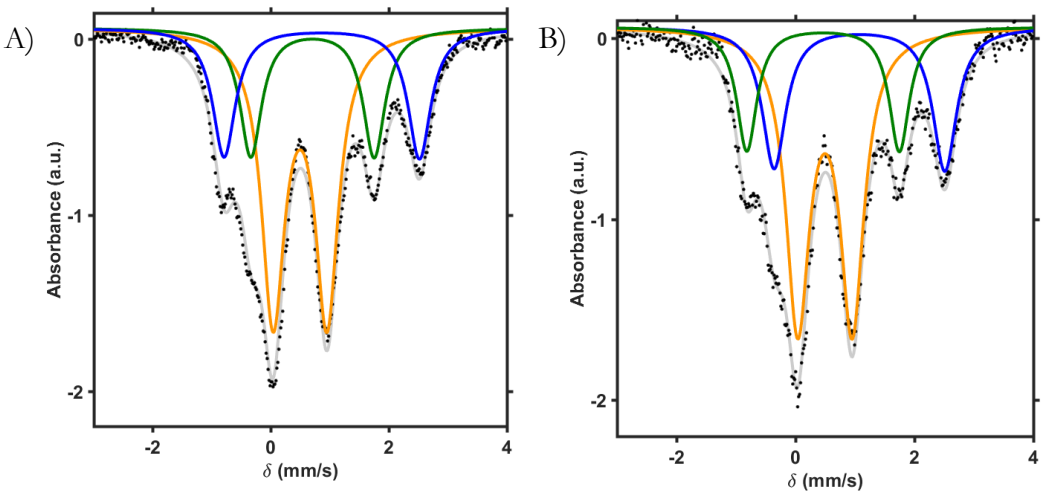

Figure 40. Mössbauer spectrum of **6** (black dots) fit with three doublets in a ~1:1:2 ratio (gray trace) with parameters (A) δ = 0.864 mm/s; ΔE_q = 3.311 mm/s (blue trace), δ = 0.495 mm/s; ΔE_q = 0.912 mm/s (orange trace) and δ = 0.706 mm/s; ΔE_q = 2.089 mm/s (green trace), and (B) δ = 1.077 mm/s; ΔE_q = 2.870 mm/s (blue trace), δ = 0.496 mm/s; ΔE_q = 0.916 mm/s (orange trace) and δ = 0.465 mm/s; ΔE_q = 2.565 mm/s (green trace).

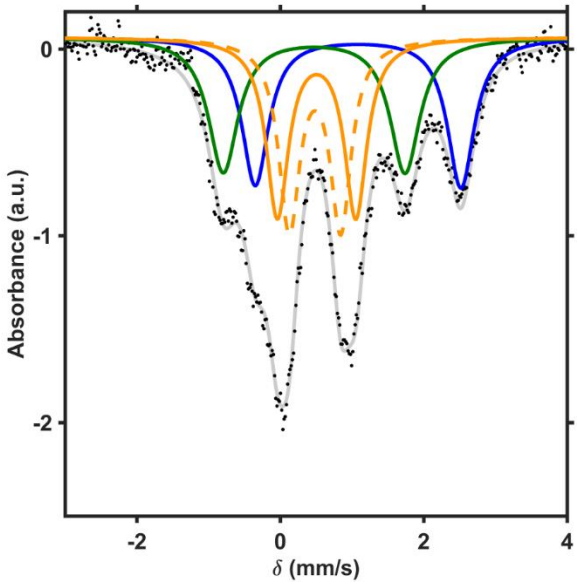

	δ (mm/s)	$\lvert\Delta E_q\rvert$ (mm/s)	Rel. %
	1.085	2.867	25
	0.507	1.093	25
	0.485	0.717	25
	0.473	2.532	25

Figure 41. Zero applied field Mössbauer spectrum of **6** (black dots) fit with four quadrupole doublets. The blue trace is assigned to high-spin Fe(II), the orange traces are assigned to high-spin Fe(III), and the green trace is assigned to Fe(III).

Simulation details for $[LFe_3O(PzNHtBu)_3Fe(O)][OTf]_2$ (7): The small peak at >2 mm/s indicated the presence of a FeII-containing impurity; NMRs of this cluster typically contained $[LFe_3O(PzNHtBu)_3Fe(OH)][OTf]_2$ (**3**) as an impurity (Figures 36 and 42). Using the parameters for **3** above, the Fe^{II} doublet was used to estimate the amount of this impurity (30 – 40% of the spectrum). This was subtracted from the data, and the remaining data appeared to be one broad doublet, similar to the $[Fe^{III}_4]$ spectrum of **4**. It was fit as four equal doublets, with the apical Fe(III) tentatively assigned to the doublet with the highest quadrupole splitting, to represent the highest value possible for this parameter (Figure 43).

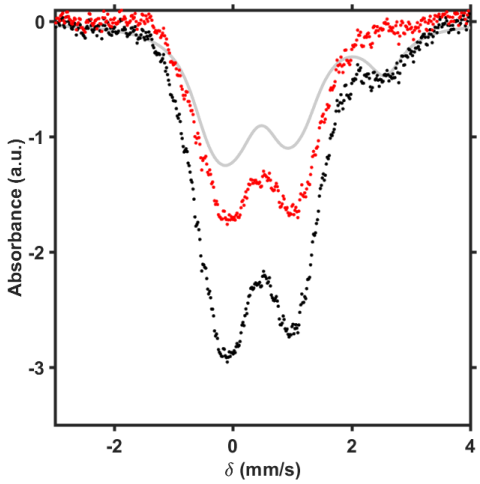

Figure 42. Mössbauer spectrum of reaction mixture containing **7** and **3** (black dots) fit with parameters to account for **3** (gray trace). The remaining signal (red dots) is assigned to the Mossbauer signal of **7**.

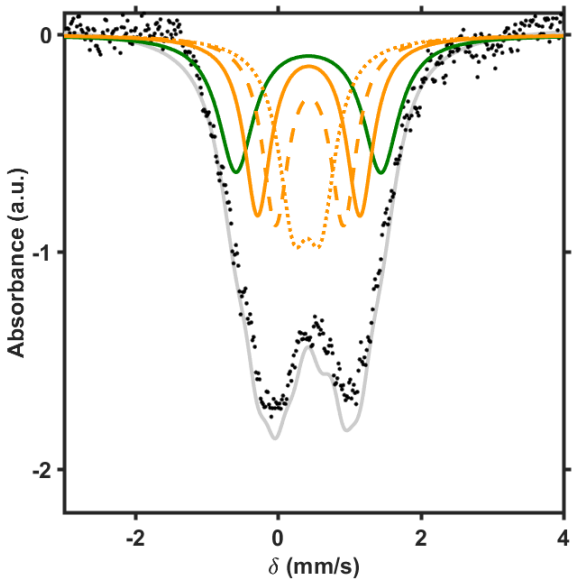

	δ (mm/s)	$\lvert\Delta E_q\rvert$ (mm/s)	Rel. %
———	0.430	1.435	25
– – –	0.440	0.953	25
·····	0.407	0.379	25
———	0.426	2.033	25

Figure 43. Zero applied field Mössbauer spectrum of **7** (black dots) fit with four quadrupole doublets. The orange traces are assigned to high-spin Fe(III), and the green trace is assigned to the unique Fe(III).

Simulation details for $[LFe_3O(Pz)_3Fe][OTf]_2$ (2): The spectrum displays five discernable peaks corresponding to three quadrupole doublets in ~ 1:1:2 ratio. The parameters of the most intense peak are consistent with a high-spin Fe(III) assignment, and the remainder of the signal can be fit a number of ways (Figure 44). Figure 44B gives parameters most consistent with an apical Fe(II). The final fit split the large doublet into two equal signals (Figure 45).

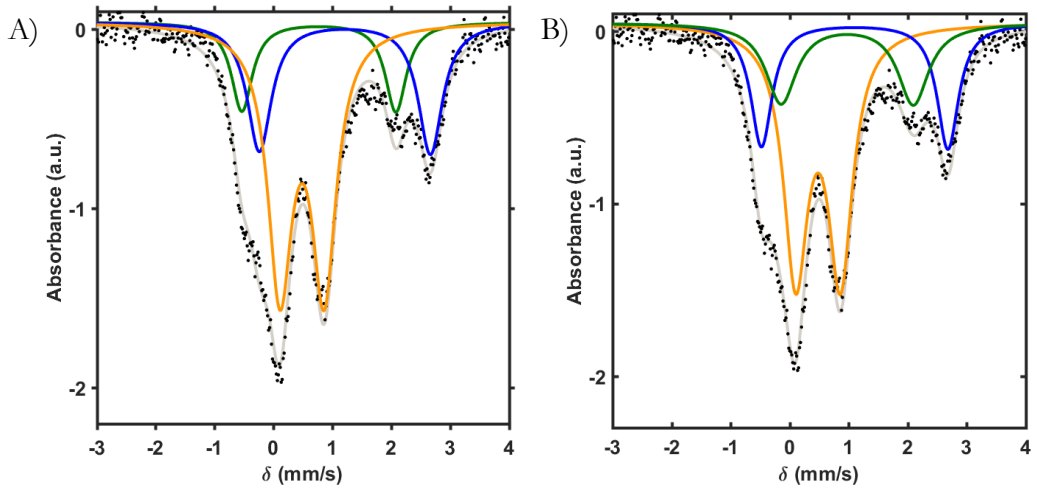

Figure 44. Mössbauer spectrum of **2** (black dots) fit with three doublets in a ~1:1:2 ratio (gray trace) with parameters (A) δ = 1.215 mm/s; ΔE_q = 2.905 mm/s (blue trace), δ = 0.487 mm/s; ΔE_q = 0.750 mm/s (orange trace) and δ = 0.773 mm/s; ΔE_q = 2.615 mm/s (green trace) and (B) δ = 1.101 mm/s; ΔE_q = 3.158 mm/s (blue trace), δ = 0.481 mm/s; ΔE_q = 0.757 mm/s (orange trace) and δ = 0.975 mm/s; ΔE_q = 2.239 mm/s (green trace).

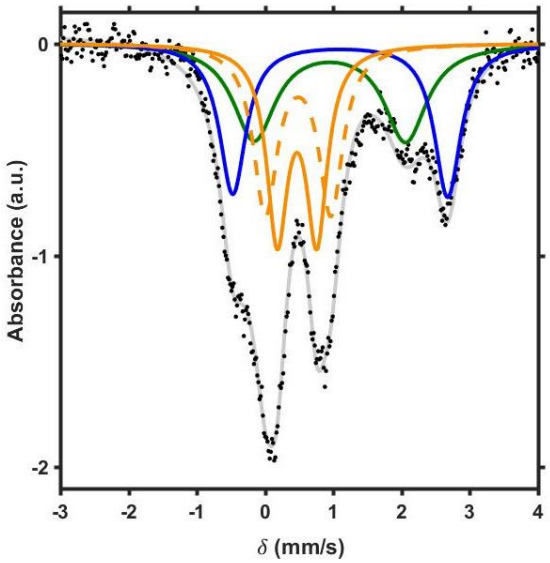

	δ (mm/s)	$\lvert\Delta E_q\rvert$ (mm/s)	Rel. %
	1.101	3.148	25
	0.469	0.580	25
	0.485	0.959	25
	0.950	2.218	25

Figure 45. Zero applied field Mössbauer spectrum of **2** (black dots) fit with four quadrupole doublets. The blue trace is assigned to high-spin Fe(II), the orange traces are assigned to high-spin Fe(III), and the green trace is assigned to Fe(II).

Simulation details for [LFe$_3$O(Pz)$_3$Fe][OTf] (3): The spectrum displays ca. four discernable peaks corresponding to three quadrupole doublets in ~ 1:1:2 ratio. The parameters of the most intense peak are consistent with a high-spin Fe(II) assignment (Figure 46A), and the remainder of the signal can be fit a number of ways (Figures 45B - D). Figure 45D gives parameters most consistent with an apical Fe(II) and high-spin Fe(III) in the tri-iron core. The final fit split the large doublet into two equal signals (Figure 46).

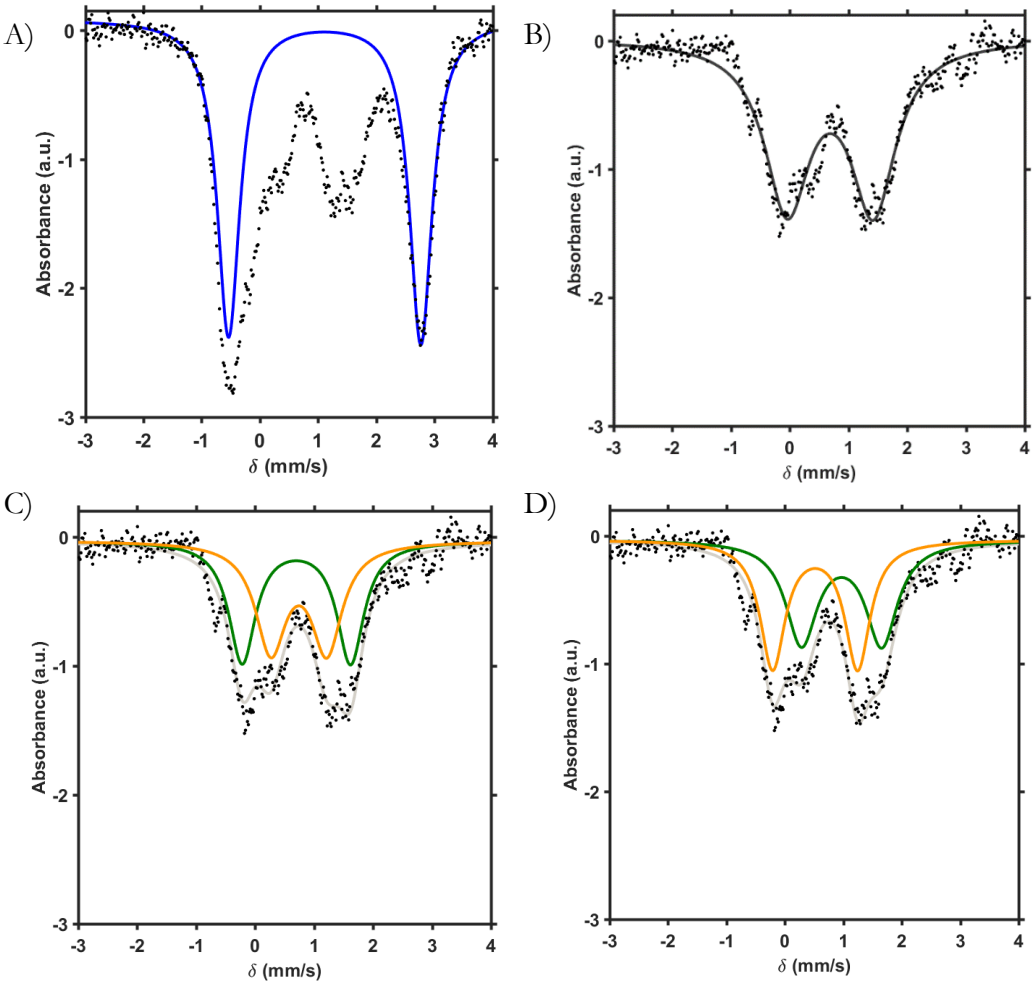

Figure 45. (A) Mössbauer spectrum of **3** (black dots) fit with a single doublet (blue trace) with parameters δ = 1.116 mm/s; ΔE_q = 3.304 mm/s, consistent with high-spin Fe^{II}. (B) Mössbauer spectrum of **3** minus the quadrupole doublet for the high-spin Fe(II) (black dots) fit with a single doublet (gray trace) with parameters δ = 0.689 mm/s; ΔE_q = 1.467 mm/s. (C) Mössbauer spectrum of **3** minus the quadrupole doublet for the high-spin Fe(II) (black dots) fit with two doublets (gray trace) with parameters δ = 0.742 mm/s; ΔE_q = 0.950 mm/s (orange trace), and δ = 0.700 mm/s; ΔE_q = 1.837 mm/s (green trace).(D) Mössbauer spectrum of **3** minus the quadrupole doublet for the high-spin Fe(II) (black dots) fit with two doublets (gray trace) with parameters δ = 0.517 mm/s; ΔE_q = 1.455 mm/s (orange trace), and δ = 0.970 mm/s; ΔE_q = 1.373 mm/s (green trace).

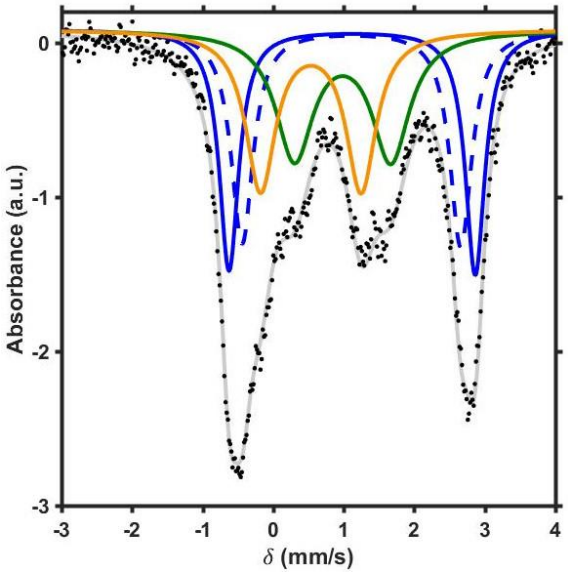

	δ (mm/s)	$\lvert\Delta E_q\rvert$ (mm/s)	Rel. %
———	1.119	3.489	25
– – –	1.110	3.099	25
———	0.534	1.425	25
———	0.985	1.366	25

Figure 46. Zero applied field Mössbauer spectrum of **3** (black dots) fit with four quadrupole doublets. The blue traces are assigned to high-spin Fe(II), the orange trace is assigned to high-spin Fe(III), and the green trace is assigned to Fe(II).

Simulation details for $[LFe_3O(Pz)_3Fe][OTf]_3$ (4): The spectrum displays three discernable peaks, corresponding to two quadrupole doublets in ~ 1:3 ratio. The parameters of the most intense peak are consistent with a high-spin Fe(III) assignment, and the remainder of the signal is consistent with high-spin Fe(II) (Figure 47). The final fit split the large doublet into three equal signals, one of which was assigned to the apical Fe(III) (Figure 48).

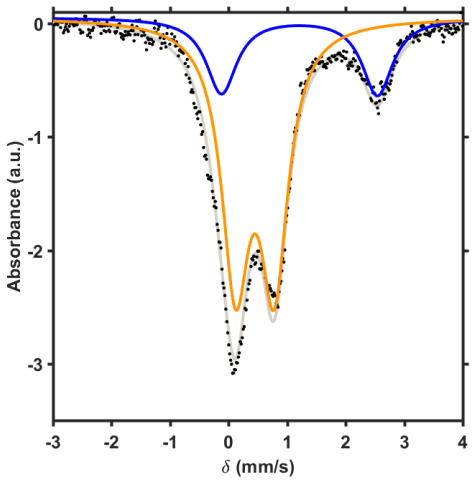

Figure 47. Mössbauer spectrum of **4** (black dots) fit with two doublets in ~ 1:3 ratio (gray trace) with parameters δ = 1.211 mm/s; ΔE_q = 2.664 mm/s (blue trace), and δ = 0.448 mm/s; ΔE_q = 0.662 mm/s (orange trace).

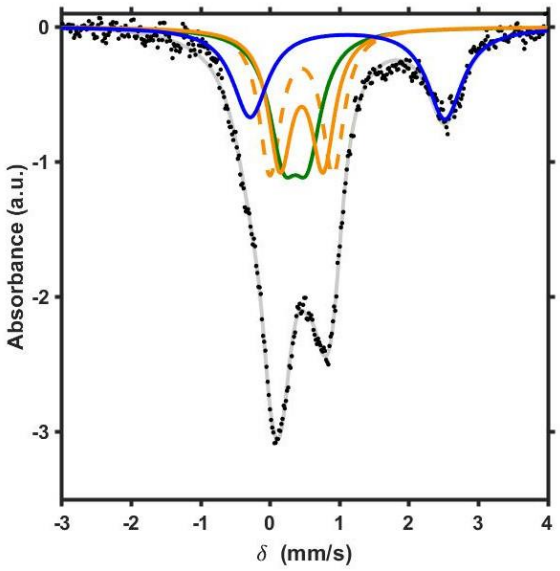

	δ (mm/s)	$\lvert\Delta E_q\rvert$ (mm/s)	Rel. %
	1.120	2.807	25
	0.458	0.621	25
	0.457	0.910	25
	0.368	0.343	25

Figure 48. Zero applied field Mössbauer spectrum of **4** (black dots) fit with four quadrupole doublets. The blue trace is assigned to high-spin Fe(II), the orange traces are assigned to high-spin Fe(III), and the green trace is assigned to the apical Fe(III).

Simulation details for [LFe$_3$O(Pz)$_3$Fe(MeCN)][OTf]$_3$ (4-MeCN): The spectrum displays three discernable peaks, corresponding to two quadrupole doublets in ~ 1:3 ratio. The parameters of the most intense peak are consistent with a high-spin Fe(III) assignment, and the remainder of the signal is consistent with five-coordinate high-spin Fe(II) (Figure 49). The final fit split the large doublet into three equal signals, one of which was assigned to the apical Fe(II) (Figure 50).

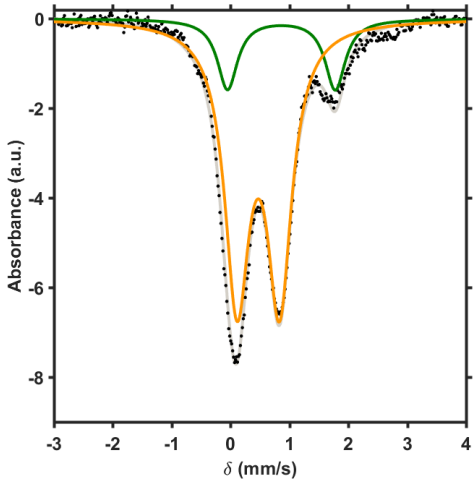

Figure 49. Mössbauer spectrum of **4-MeCN** (black dots) fit with two doublets in ~ 1:3 ratio (gray trace) with parameters δ = 0.863 mm/s; ΔE_q = 1.830 mm/s (green trace), and δ = 0.470 mm/s; ΔE_q = 0.722 mm/s (orange trace).

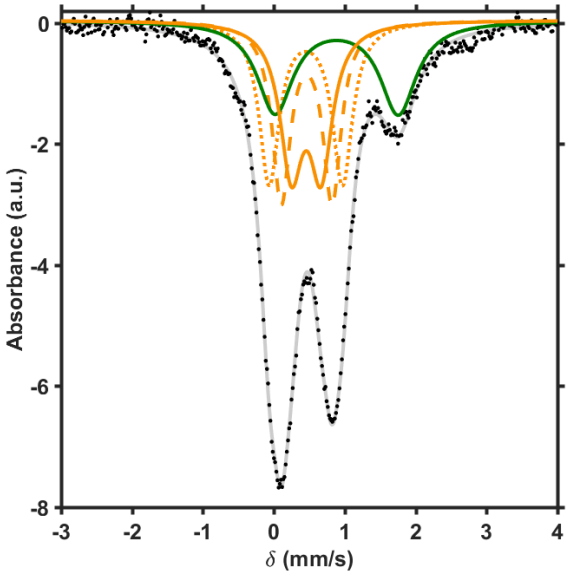

	δ (mm/s)	$\lvert\Delta E_q\rvert$ (mm/s)	Rel. %
	0.457	0.420	25
	0.464	0.716	25
	0.452	1.033	25
	0.886	1.738	25

Figure 50. Zero applied field Mössbauer spectrum of **4-MeCN** (black dots) fit with four quadrupole doublets. The orange traces are assigned to high-spin Fe(III), and the green trace is assigned to the apical Fe(II).

Simulation details for $[LFe_3O(Pz)_3Fe(OH)][OTf]_2$ (5): The spectrum displays four discernable peaks corresponding to three quadrupole doublets in ~ 1:1:2 ratio. The parameters of the most intense peak are consistent with a high-spin Fe(III) assignment, and the remainder of the signal can be fit a number of ways (Figure 51). Figure 51C gives parameters most consistent with an apical Fe(III) and high-spin Fe(II) in the tri-iron core. The final fit split the large doublet into two equal signals (Figure 52).

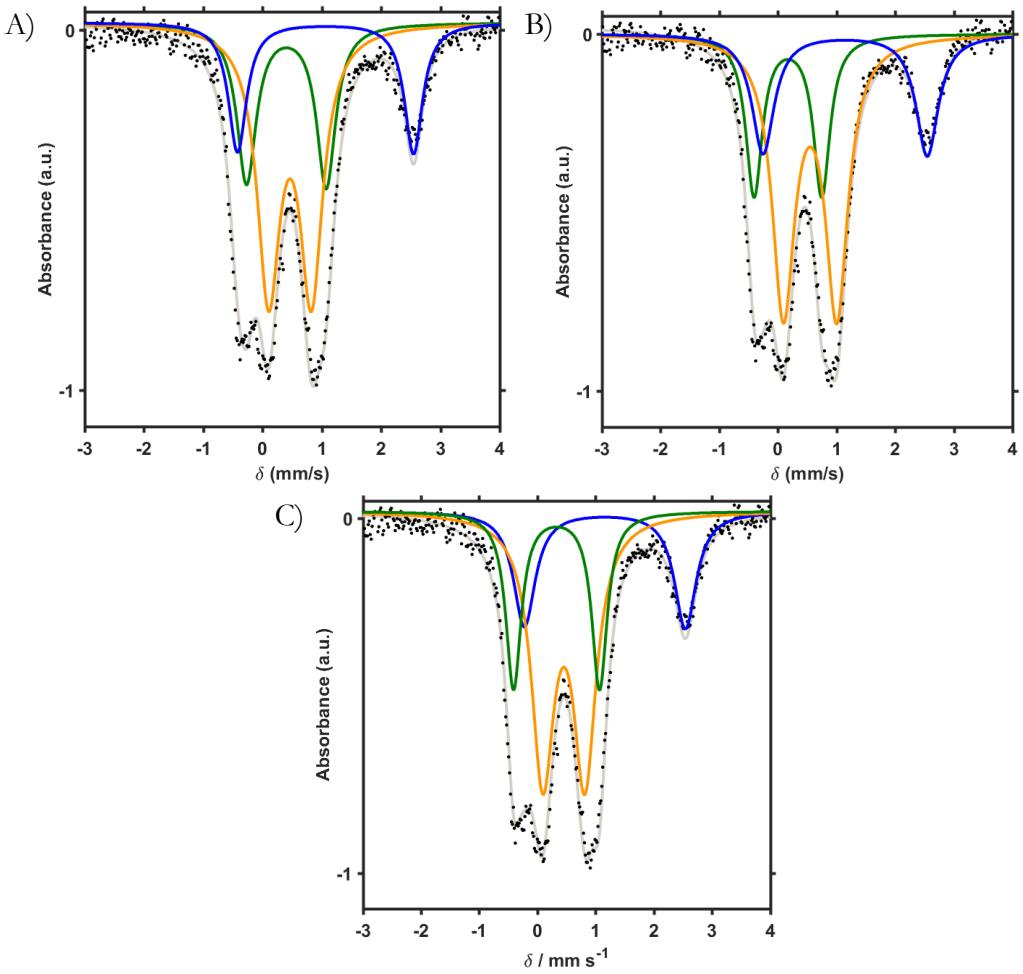

Figure 51. Mössbauer spectrum of **5** (black dots) fit with three doublets in ~ 1:1:2 ratio (gray trace) with parameters (A) δ = 0.463 mm/s; ΔE_q = 0.722 mm/s (green trace), δ = 0.401 mm/s; ΔE_q = 1.343 mm/s (orange trace), and δ = 1.062 mm/s; ΔE_q = 2.969 mm/s (blue trace), (B) δ = 0.171 mm/s; ΔE_q = 1.154 mm/s (green trace), δ = 0.549 mm/s; ΔE_q = 0.910 mm/s (orange trace), and δ = 1.147 mm/s; ΔE_q = 2.800 mm/s (blue trace), and (C) δ = 0.331 mm/s; ΔE_q = 1.478 mm/s (green trace), δ = 0.456 mm/s; ΔE_q = 0.723 mm/s (orange trace), and δ = 1.161 mm/s; ΔE_q = 2.766 mm/s (blue trace).

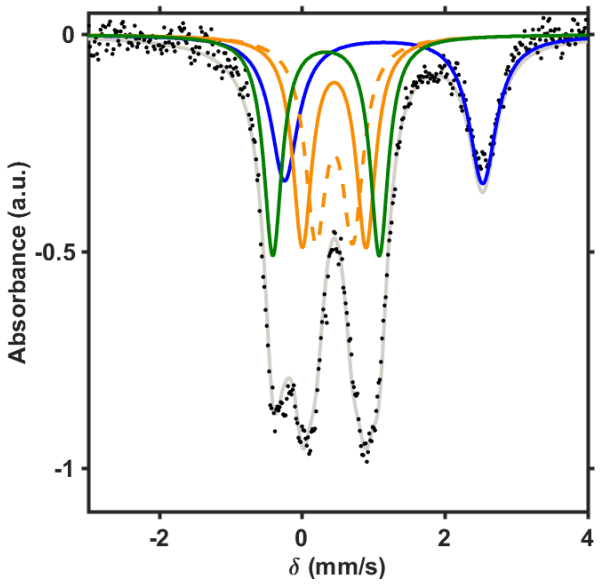

	δ (mm/s)	$\lvert\Delta E_q\rvert$ (mm/s)	Rel. %
	1.145	2.778	25
	0.452	0.893	25
	0.454	0.519	25
	0.339	1.493	25

Figure 52. Zero applied field Mössbauer spectrum of **5** (black dots) fit with four quadrupole doublets. The blue trace is assigned to high-spin Fe(II), the orange traces are assigned to high-spin Fe(III), and the green trace is assigned to the apical Fe(III).

Simulation details for $[(LFe_3O(Pz)_3Fe)_2O][OTf]_4$ (6): The spectrum displays four discernable peaks corresponding to three quadrupole doublets in ~ 1:1:2 ratio. The parameters of the most intense peak are consistent with a high-spin Fe(III) assignment, and the remainder of the signal can be fit a number of ways (Figure 53). Figure 53C gives parameters most consistent with an apical Fe(III) and high-spin Fe(II) in the tri-iron core. The final fit split the large doublet into two equal signals (Figure 54).

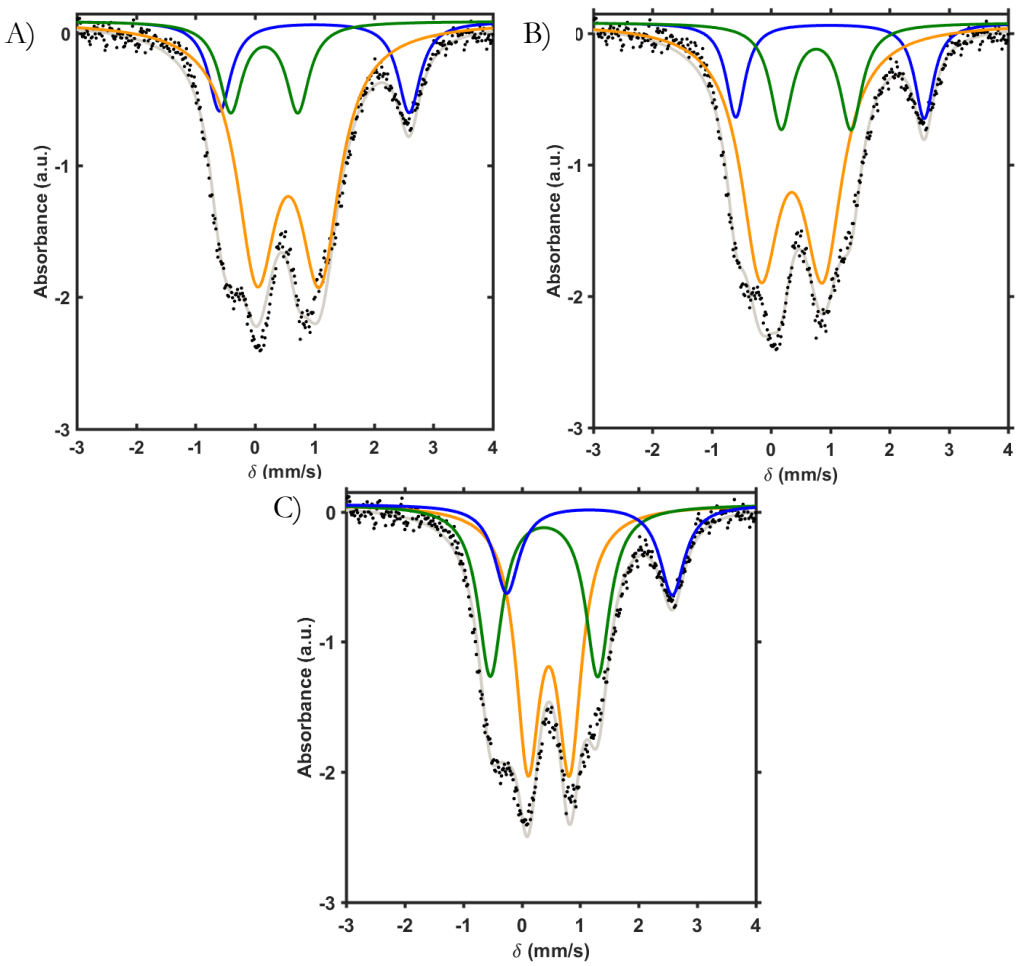

Figure 53. Mössbauer spectrum of **6** (black dots) fit with three doublets in ~ 1:1:2 ratio (gray trace) with parameters (A) $\delta = 0.156$ mm/s; $\Delta E_q = 1.128$ mm/s (green trace), $\delta = 0.560$ mm/s; $\Delta E_q = 1.057$ mm/s (orange trace), and $\delta = 0.999$ mm/s; $\Delta E_q = 3.188$ mm/s (blue trace), (B) $\delta = 0.762$ mm/s; $\Delta E_q = 1.176$ mm/s (green trace), $\delta = 0.350$ mm/s; $\Delta E_q = 1.049$ mm/s (orange trace), and $\delta = 0.995$ mm/s; $\Delta E_q = 3.180$ mm/s (blue trace), and (C) $\delta = 0.382$ mm/s; $\Delta E_q = 1.835$ mm/s (green trace), $\delta = 0.463$ mm/s; $\Delta E_q = 0.711$ mm/s (orange trace), and $\delta = 1.160$ mm/s; $\Delta E_q = 2.827$ mm/s (blue trace).

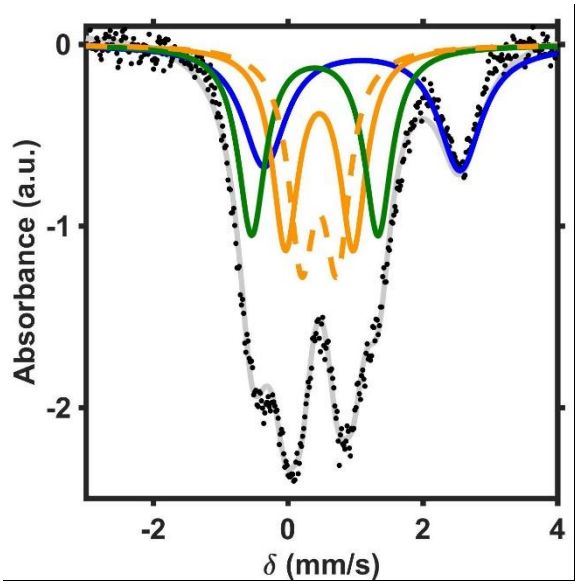

	δ (mm/s)	$\lvert\Delta E_q\rvert$ (mm/s)	Rel. %
	1.099	2.909	25
	0.645	1.005	25
	0.464	0.530	25
	0.398	1.875	25

Figure 54. Zero applied field Mössbauer spectrum of **6** (black dots) fit with four quadrupole doublets. The blue trace is assigned to high-spin Fe(II), the orange traces are assigned to high-spin Fe(III), and the green trace is assigned to the apical Fe(III).

Simulation details for putative intermediate of 2 and sPhIO: Based on variable temperature 1H NMR data, the putative intermediate is the major species at low temperature, with a small (~20%) impurity of **5**. The parameters for **5** in Figure 63 were used to model this amount of impurity, and was subtracted out (Figure 55). The remaining spectrum displays three discernable peaks corresponding to three quadrupole doublets in ~ 1:1:2 ratio. It was modeled with parameters similar to **6**, based on its similar match to the data (Figure 56).

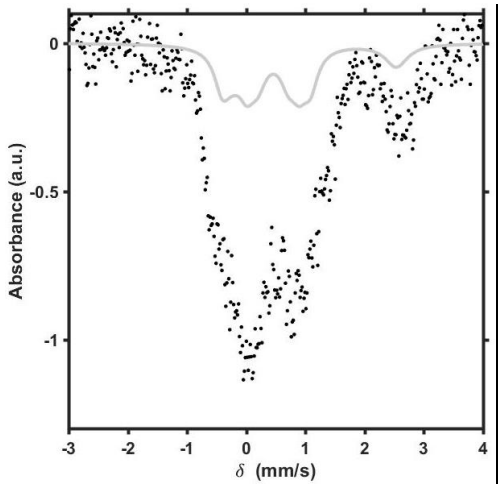

Figure 55. Mössbauer spectrum of putative intermediate between **2** and sPhIO, with ~ 20% of an impurity, **5** (black dots). The signal attributed to the impurity was subtracted from the data (gray trace).

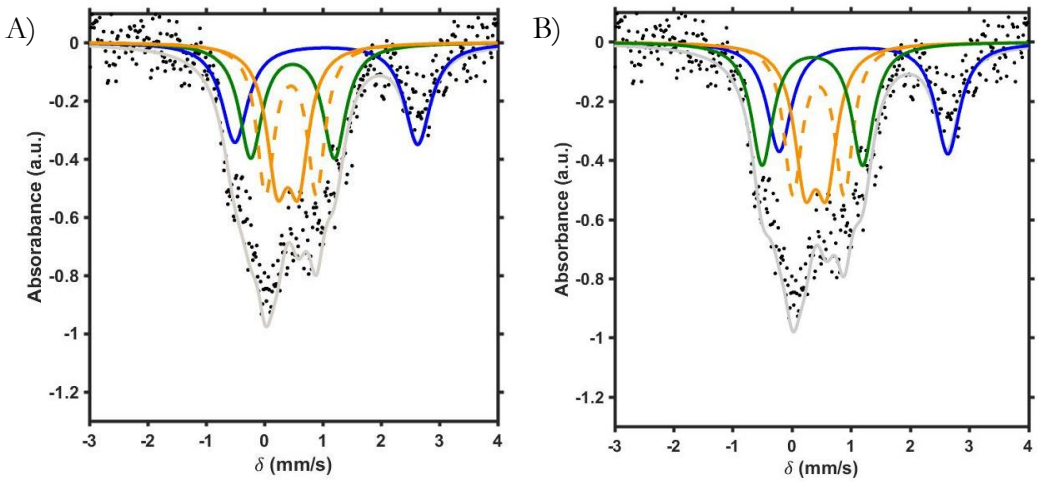

Figure 56. Mössbauer spectrum of putative intermediate between **2** and sPhIO (black dots) fit with four equally abundant quadrupole doublets (gray trace). Two potential fits with the following parameters: (A) (i) δ = 1.21 mm/s, $|\Delta E_q|$ = 2.83 mm/s (blue trace), (ii) δ = 0.41 mm/s, $|\Delta E_q|$ = 0.36 mm/s (solid orange trace), and (iii) δ = 0.45 mm/s, $|\Delta E_q|$ = 0.87 mm/s (dashed orange trace), (iv) δ = 0.35 mm/s, $|\Delta E_q|$ = 1.70 mm/s (green trace), and (B) (i) δ = 1.06 mm/s, $|\Delta E_q|$ = 3.13 mm/s (blue trace), (ii) δ = 0.40 mm/s, $|\Delta E_q|$ = 0.36 mm/s (solid orange trace), and (iii) δ = 0.46 mm/s, $|\Delta E_q|$ = 0.87 mm/s (dashed orange trace), (iv) δ = 0.49 mm/s, $|\Delta E_q|$ = 1.44 mm/s (green trace).

MISCELLANEOUS CRYSTAL STRUCTURES

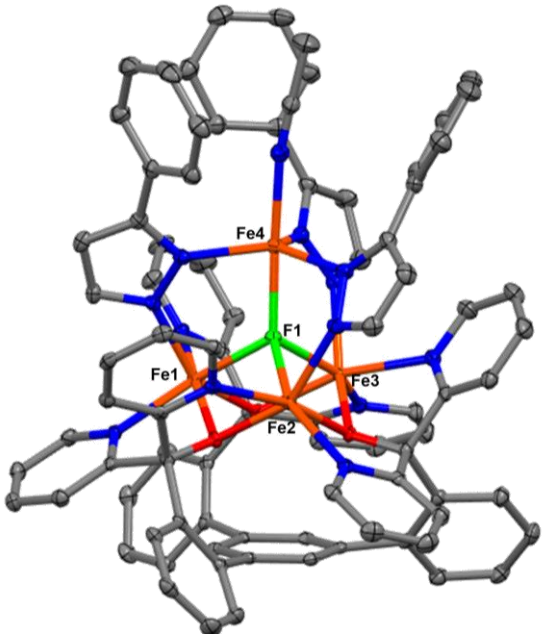

Figure 1. Structure of $[LFe_3F(PhPz)_3Fe(MeCN)][OTf]$, obtained via recrystallization of $[LFe_3F(PhPz)_3Fe][OTf]$ in $MeCN/Et_2O$ vapor diffusion.

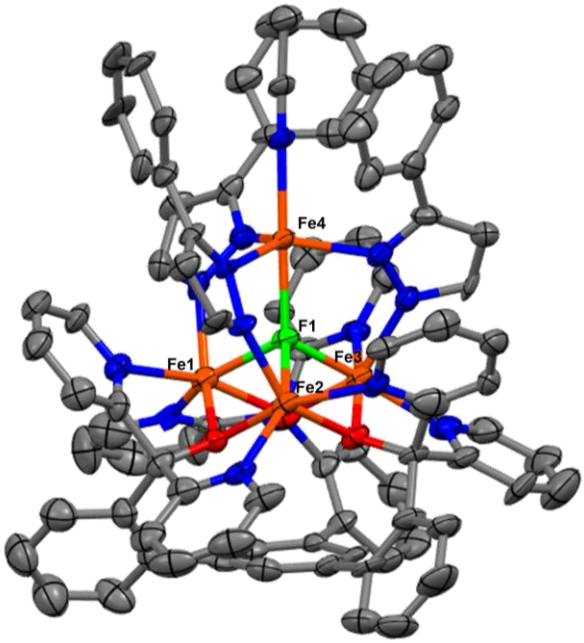

Figure 2. Structure of $[LFe_3F(PhPz)_3Fe(MeCN)][OTf]_2$, obtained via recrystallization of $[LFe_3F(PhPz)_3Fe][OTf]_2$ in $MeCN/Et_2O$ vapor diffusion.

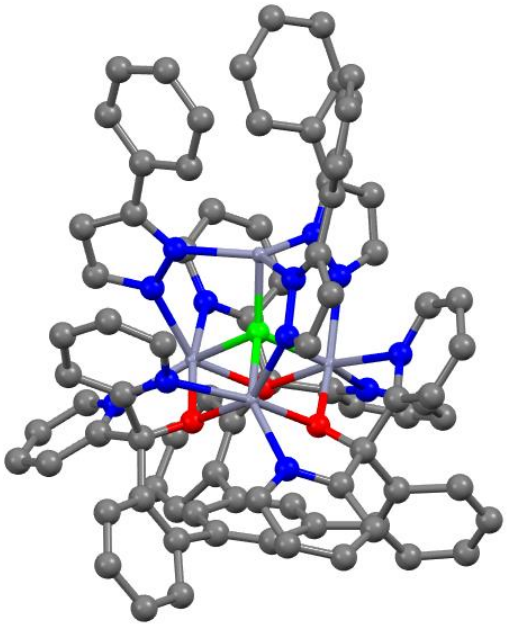

Figure 3. Structure of $[LM_3F(PhPz)_3M][OTf]$, from $LZn_3(OTf)_3$ and $Fe(N(SiMe_3)_2)_2$. The occupancies of the metals are similar at each site: ~130% Fe and ~105% Zn. This is rationalized as Fe scrambling to each position in the cluster.

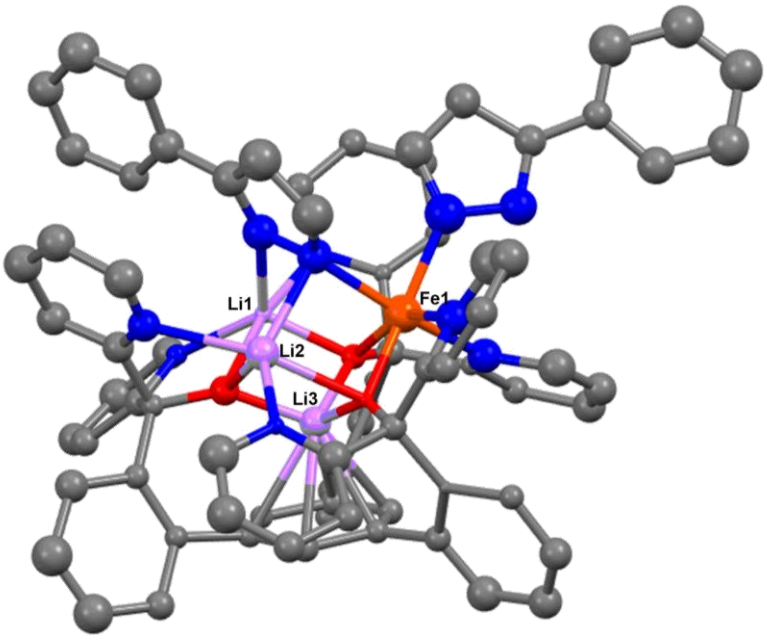

Figure 4. Structure of $LLi_3Fe(PhPz)_2$ (tentative assignment), obtained as a decomposition product of $[NEt_4][Fe_4N_2Cl_{10}]$ (Bennett, et al. *J. Am. Chem. Soc.* **127**, 12378), KPhPz, and LLi_3 in THF. The Et_2O soluble product is pink, and gives this structure.

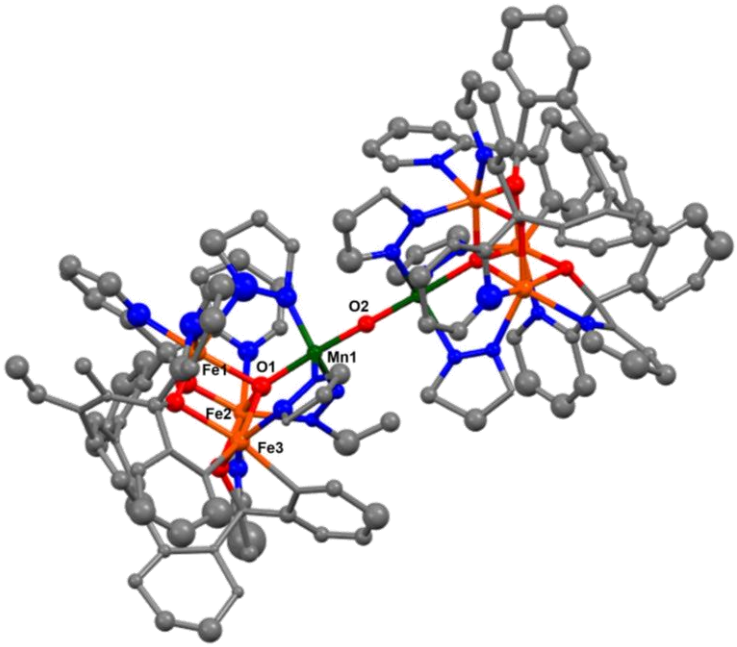

Figure 5. Structure of $[(LFe_3O(Pz)_3Mn)_2O][OTf]_2$, obtained from decomposition of $[LFe_3O(Pz)_3Mn(OH)][OTf]$.

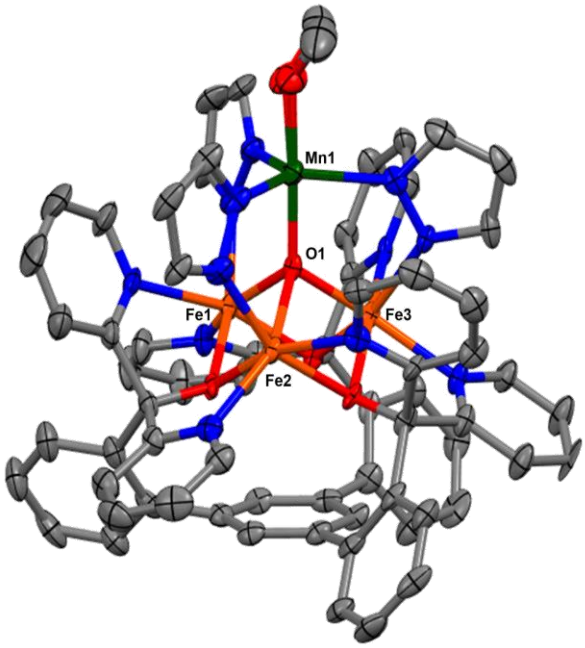

Figure 6. Structure of $[LFe_3O(Pz)_3Mn(OMe)][OTf]$, obtained from addition of methanol solution of sodium methoxide to . $[LFe_3O(Pz)_3Mn][OTf]_2$.

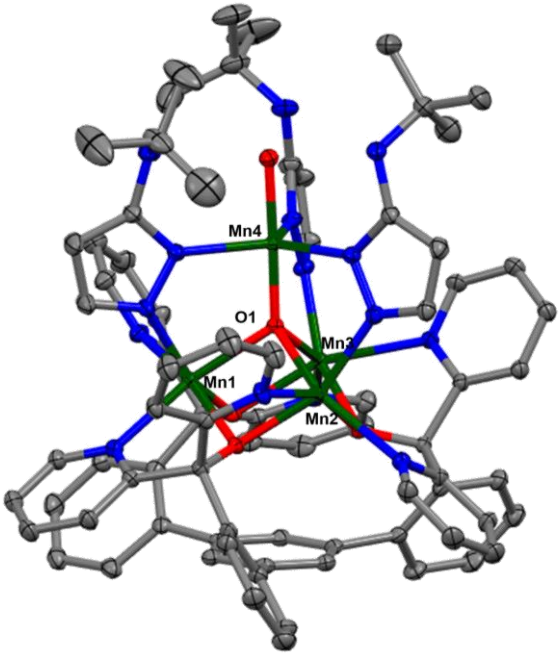

Figure 7. Structure of $LMn_3O(PzNHtBu)_3Mn(OH)$, obtained from the same synthetic route as $LFe_3O(PzNHtBu)_3Fe(OH)$, starting from LMn_3OTf_3 and $Mn(OTf)_2$ • 2 MeCN.

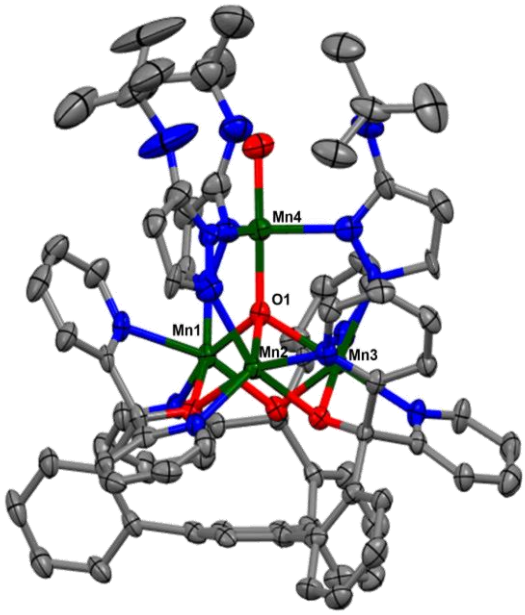

Figure 8. Structure of $[LMn_3O(PzNHtBu)_3Mn(OH)][OTf]$, obtained from oxidation of $LMn_3O(PzNHtBu)_3Mn(OH)$ with [Fc][OTf].

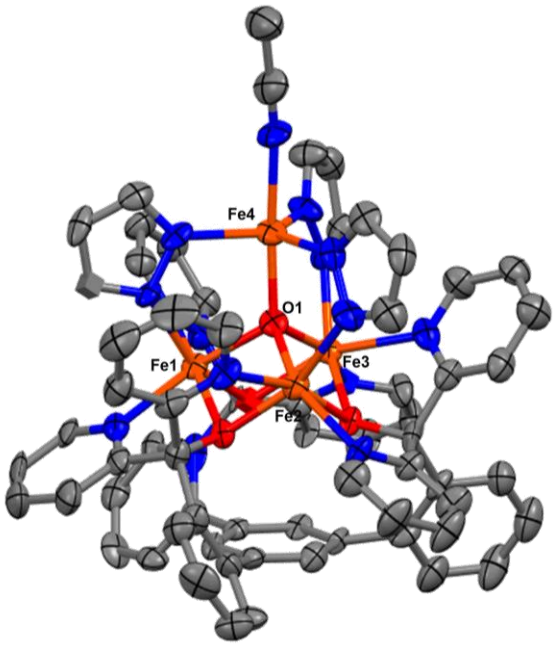

Figure 9. Structure of $[LFe_3O(Pz)_3Fe(MeCN)][OTf]$, obtained from recrystallization of $[LFe_3O(Pz)_3Fe][OTf]$ by MeCN/Et2O vapor diffusion.

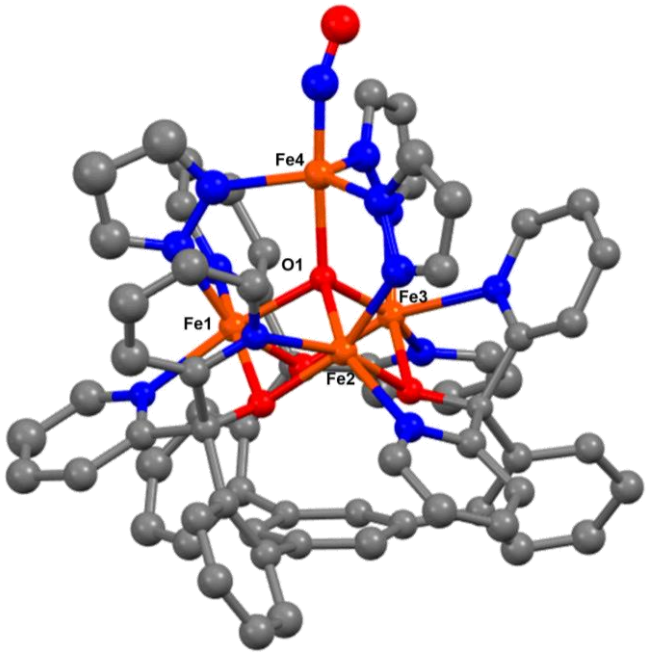

Figure 10. Structure of $[LFe_3O(Pz)_3Fe(NO)][OTf]_2$, obtained from addition of one equivalent NO gas to $[LFe_3O(Pz)_3Fe][OTf]_2$.

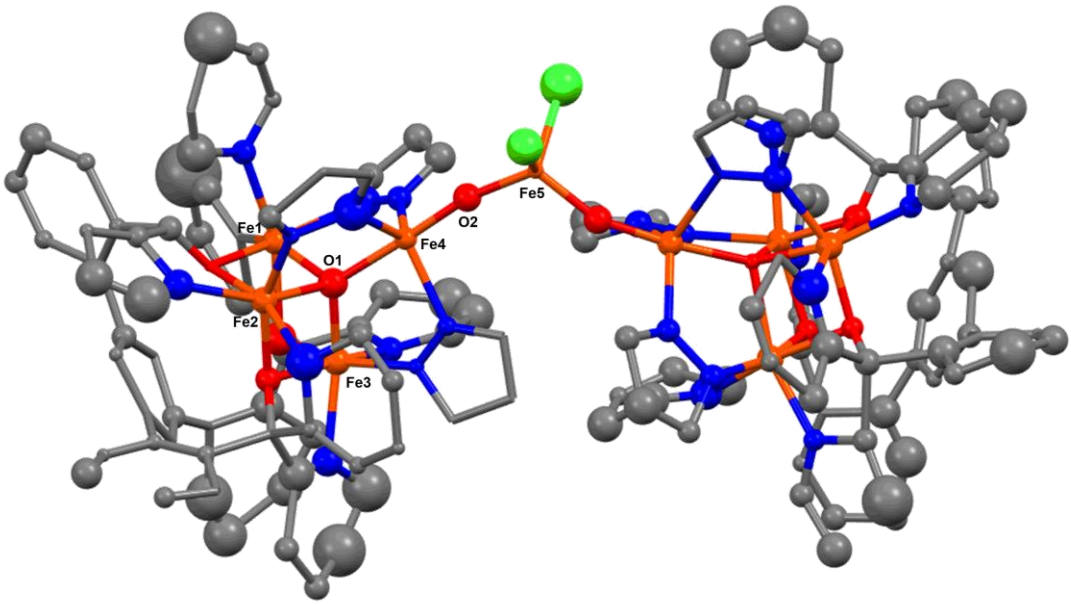

Figure 11. Structure of $[(LFe_3O(Pz)_3FeO)_2FeCl_2]$ (tentative assignment), obtained from addition of one equivalent $[NBu_4][IO_4]$ to $[LFe_3O(Pz)_3FeCl][OTf]$ in THF.

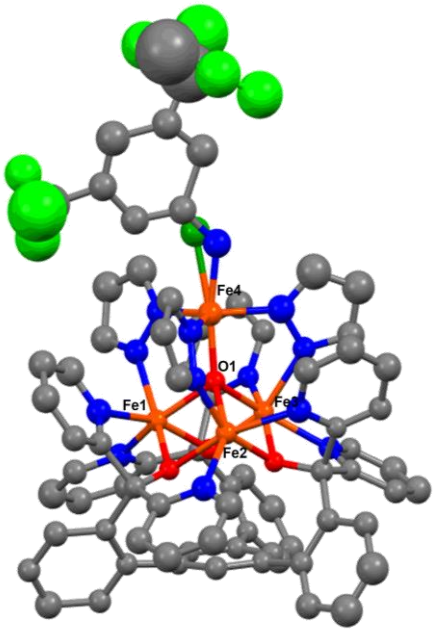

Figure 12. Structure of $[LFe_3O(Pz)_3Fe(NHAr/Cl)][OTf]$ (Ar = 3,5-CF_3-Ph; ~6:4 amide to chloride), obtained from partial decomposition of the reaction product between $[LFe_3O(Pz)_3Fe][OTf]$ and ArN_3.

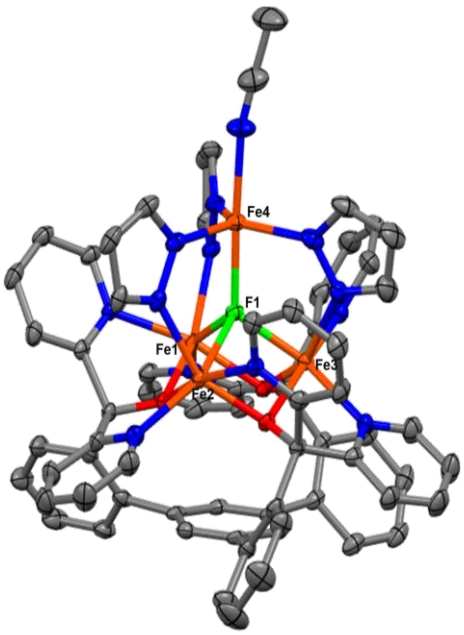

Figure 13. Structure of $[LFe_3F(Pz)_3Fe(MeCN)][OTf]$, obtained by recrystallization of $[LFe_3F(Pz)_3Fe][OTf]$ in $MeCN/Et_2O$ vapor diffusion.

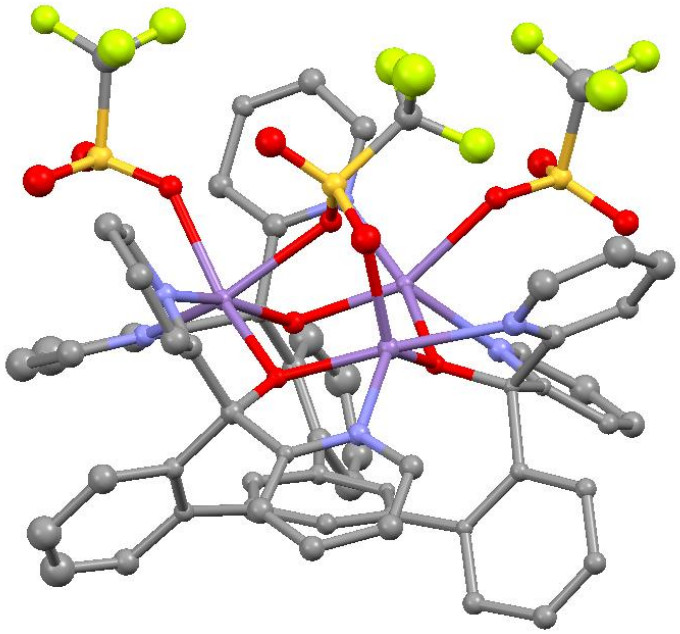

Figure 14. Structure of $LMn_3(OTf)_3$, obtained by an analogous synthesis to that of $LFe_3(OTf)_3$ ($LFe_3(OAc)_3$ and 10 equivalents Me_3SiOTf; Arnett, et al. *J. Am. Chem. Soc.* **140**, 5569).

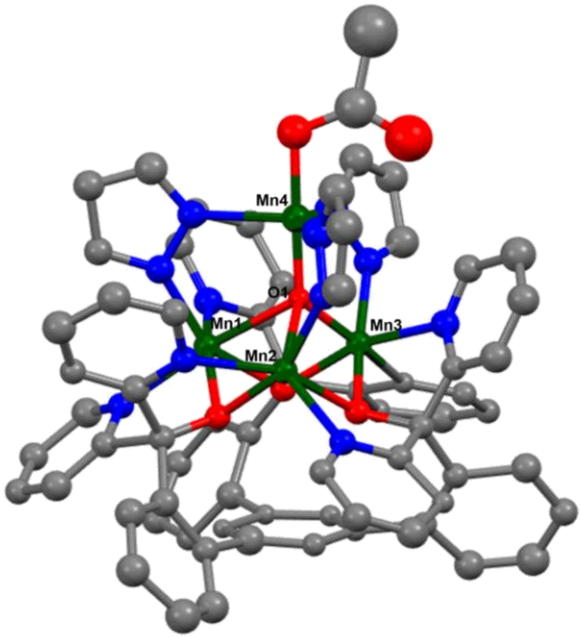

Figure 15. Structure of $[LMn_3O(Pz)_3Mn(OAc)][OTf]$, obtained by an analogous synthesis to that of $[LFe_3O(Pz)_3Fe(OAc)][OTf]$.

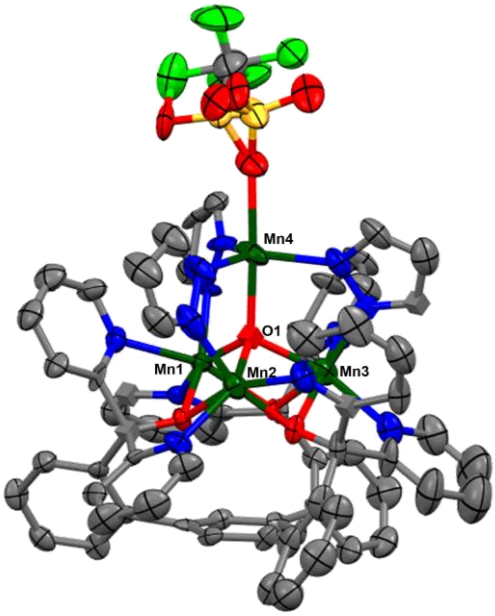

Figure 16. Structure of $[LMn_3O(Pz)_3Mn][OTf]_2$, obtained by an analogous synthesis to that of $[LFe_3O(Pz)_3Fe][OTf]_2$.

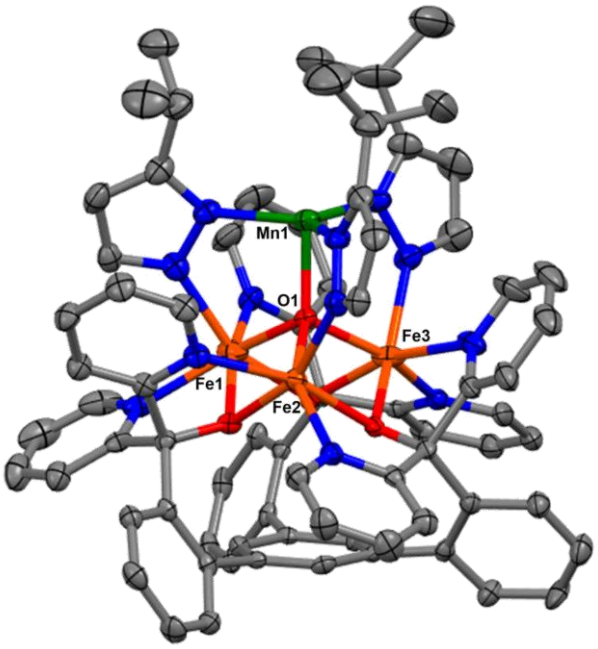

Figure 17. Structure of $[LFe_3O(iPrPz)_3Mn][OTf]_2$, obtained by addition of KiPrPz, PhIO, and $Mn(OTf)_2$ • 2 MeCN to $LFe_3(OTf)_3$.

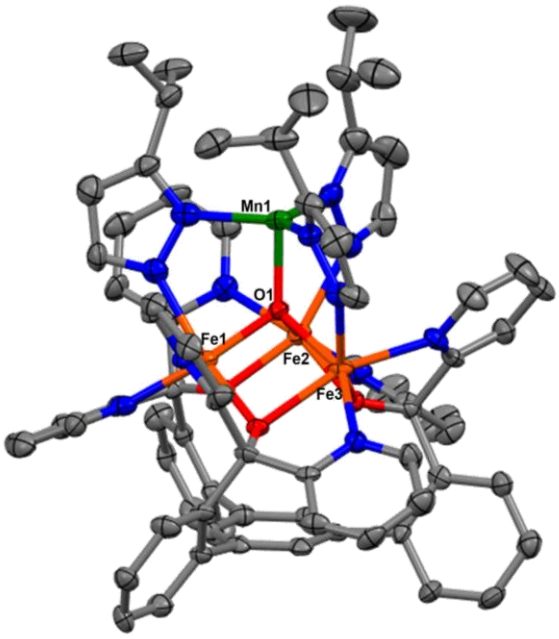

Figure 18. Structure of $[LFe_3O(iPrPz)_3Mn][OTf]$, obtained by reduction of $[LFe_3O(iPrPz)_3Mn][OTf]_2$ with $CoCp_2$.

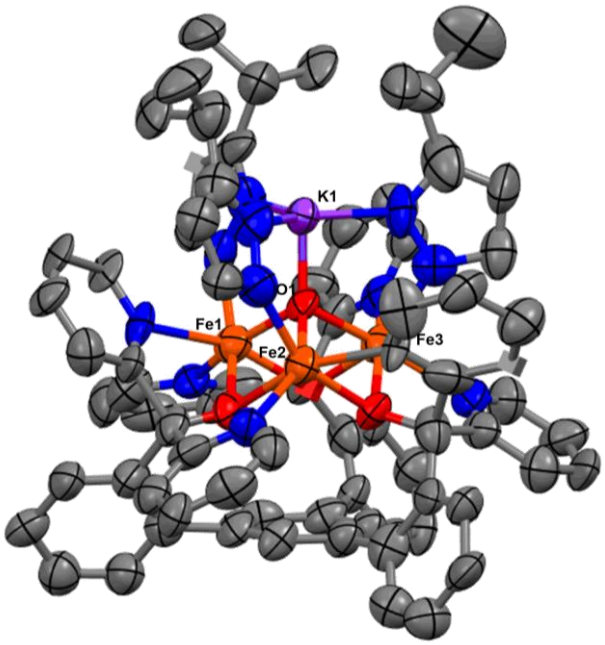

Figure 19. Structure of $[LFe_3O(iPrPz)_3K][OTf]$, obtained by addition of KiPrPz, PhIO, and $Fe(OTf)_2$ to $LFe_3(OTf)_3$. Full metalation of Fe was not observed by NMR, and this byproduct was crystalized out instead of the desired compound.

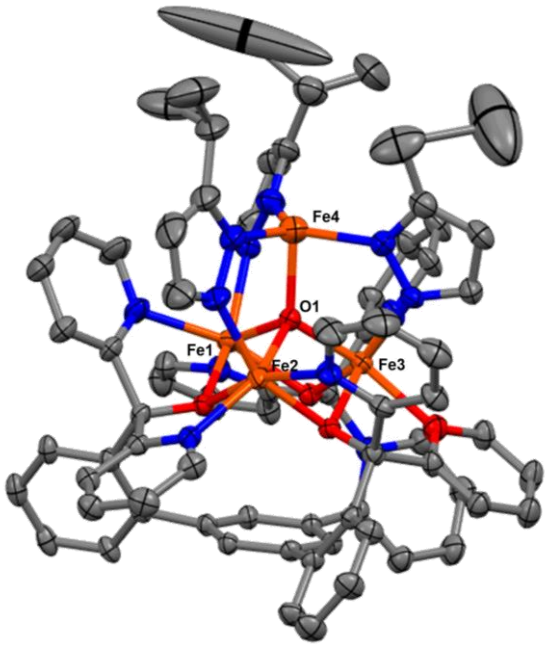

Figure 20. Structure of $[LFe_3O(iPrPz)_3Fe][OTf]_2$, obtained by addition of KiPrPz, PhIO, and $Fe(OTf)_2$ • 2 MeCN to $LFe_3(OTf)_3$. Full metalation of Fe was observed with this reagent by NMR.

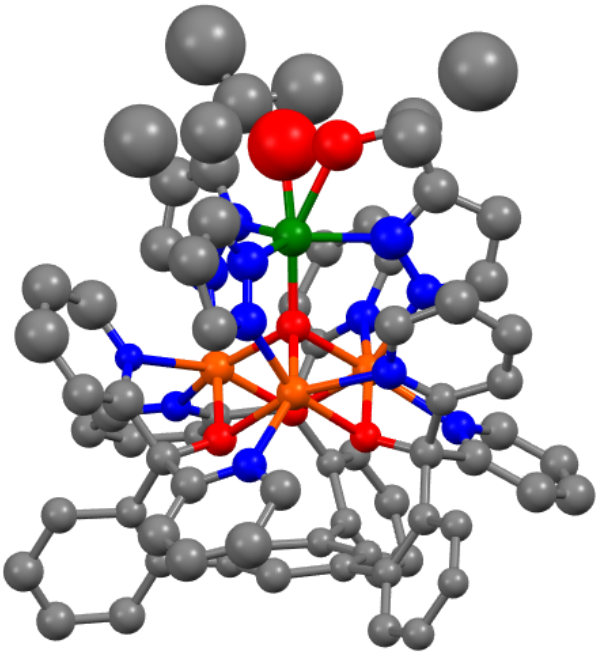

Figure 21. Structures of a mixture of $[LFe_3O(iPrPz)_3Mn(OH)][OTf]$ and $[LFe_3O(iPrPz)_2(OiPrPz)Mn][OTf]$ (roughly 50:50; tentative assignments), obtained by addition of (2-tert-butyl-sulfonyl)-iodosylbenzene to $[LFe_3O(iPrPz)_3Mn][OTf]$.

ABOUT THE AUTHOR

Christopher John Reed was born in Boise, ID on July 2nd, 1991. He, and his brother Alexander Reed, were raised in Idaho by their mother, Freda Reed. He attended Mountain View High School and graduated in 2009. Then, he moved to Pocatello, ID to attend Idaho State University for undergraduate. During his time at ISU, he worked in the 'extreme biochemistry' laboratory of Prof. Caryn Evilia where he studied protein structure and stability of halophilic microorganisms using circular dichroism spectroscopy. In the summer of 2012, he completed a research internship at Utah State University, in the protein crystallography lab of Prof. Sean Johnson. Chris graduated from ISU in 2014 with a B.S. in Chemistry and Biochemistry; he received the ISU Outstanding Student Achievement Award from the College of Science and Engineering (Science Division). He completed his Ph. D. studies in the lab of Prof. Theodor Agapie at the California Institute of Technology in 2019. In 2017, he received a Resnick Sustainability Institute Graduate Fellowship to support the remainder of his graduate studies. He is currently planning to start his post-doctoral studies with Prof. Yi Lu at University of Illinois, Urbana-Champaign.